

# Characterisation of Tip Wear during AFM Probe-Based Nanomachining



Thesis submitted in fulfilment of the requirement for the degree of

**Doctor of Philosophy**

By

**Nur Farah Hafizah Mukhtar**

Cardiff School of Engineering

Cardiff University

Cardiff, Wales

United Kingdom

2017

## ABSTRACT

Atomic force microscope (AFM) probe-based mechanical nanomachining has been considered as a potential low-cost alternative method for the generation of nanoscale features on the surface of components and devices. Therefore, it is important to understand the factors that influence the tip wear of AFM probes in order to achieve reliable and accurate machining operations when implementing this process. Despite the fact that the basic applicability of AFM probe-based machining has been demonstrated for many years, studies focussing on the wear of the tips as a function of processing conditions are relatively scarce. In addition, the accuracy and practical suitability of in-situ techniques to monitor the condition of AFM probes is not adequately acknowledged.

To address these issues, a series of experimental studies were conducted in this PhD research when implementing the AFM probe-based machining process on a single crystal copper workpiece at selected values of applied normal loads, machining distances and for different machining directions. First, the assessment of the wear of AFM silicon probes was carried out based on two dimensional (2D) tip profile data. This particular study also presented a simple method for improving the accuracy of the tip wear assessment procedure when conducted on 2D profiles. Next, AFM silicon probes with diamond-coated tips were used as cutting tools for a different range of applied normal loads and along various processing directions. For this particular study, the AFM probes wear assessment relied on two different three dimensional (3D) in-situ measurement techniques, namely the ultra-sharp tip scan approach and the reverse imaging method. Reliability and practical suitability aspects between these two in-situ techniques were also assessed and discussed. For each set of experiments, different qualitative and quantitative

wear metrics were observed and analysed. Particularly, from the qualitative perspective, the evolution of the AFM tip apex profiles along selected machining distances and directions was considered. As for the quantitative measurement, tip radius and tip volume loss measurements were estimated.

The most important findings reached in this study are given as follows. First, it was shown that the error associated with the traditional method of assessing the tip volume from 2D profiles could be 26% in comparison with the simple method proposed here. In addition, among the 3D in-situ AFM probe characterisation methods considered, the reverse imaging approach was judged to be the most reliable technique. This study also showed that tips in silicon were very prone to initial tip fracture during the AFM probe-based nanomachining process. This phenomenon could also take place, albeit to a lesser extent, when silicon tips coated with diamond were utilised. When the nanomachining process is not in control due to such tip fracture, it is difficult to extract firm conclusions about the influence of the processing parameters on the tip wear. Besides, this rules out the application of a design of experiments approach where the minimisation of the tip wear volume may be the objective. The study also showed that the AFM probe-based nanomachining process was more likely to be in control when using silicon tips coated with polycrystalline diamond with no nitrogen doping. In this case, a much reduced likelihood of tip fracture could be achieved accompanied with negligible tip wear. In addition, the associated results suggested that the evolution of the tip wear was not equal in all machining directions investigated, with the largest wear occurring in a direction parallel and away to the cantilever long axis. The reason for this should be due to the fact that this was also the direction where the process was most likely to be conducted in the ploughing-dominated regime. Finally, when the nanomachining process was realised in

control, the wear volume was seen to increase with the increase in the normal load for all directions considered.

## **ACKNOWLEDGEMENTS**

First and foremost, my praise is to ALLAH (my Lord), the Almighty, the greatest of all, on whom ultimately that I depend for sustenance and guidance. I would like to thank Almighty Allah for giving me opportunity, determination and strength to do my research. His continuous grace and mercy was with me throughout my life and ever more during the tenure of my research.

Now, I would like to thank and express my deep and sincere gratitude to my supervisor Dr. E. B. Brousseau, Senior Lecturer, School of Engineering, Cardiff University for his continuous support, guidance and encouragement. In addition to being an excellent supervisor, he is a man of principles and has immense knowledge of research in general and his subject in particular. I appreciate all his contributions of time, support and ideas as well as his quick feedback and constructive comments were really inspiring and helpful.

I would also like to express my gratitude to my co-supervisor Mr. P. Prickett, Senior Lecturer, School of Engineering, Cardiff University for his valuable guidance and suggestions. I also appreciate my colleagues and friends for discussions, suggestions and positive criticism.

I am very grateful to Majlis Amanah Rakyat (MARA) Malaysia and University Kuala Lumpur (UniKL) for the supported funds. And I would also like to thank to my former dean of UniKL MITEC, Professor Dr. Khairanum Subari for encouraging me to get a Ph.D. degree and believing in me.

I owe everything to my family who encouraged and helped me at every stage of my personal and academic life and longed to see this achievement come true. I dedicate this work to my dearly husband who had sacrifice his dream for me to pursue my study, my sincere and generous father and my loving mother. Every breath of my life and drop of blood in my body is dedicated to my family. I love you all.

## **DECLARATION**

This work has not been submitted in substance for any other degree or award at this or any other university or place of learning, nor is being submitted concurrently in candidature for any degree or other award.

Signed ..... (N. F. H. Mukhtar) Date .....

### **STATEMENT 1**

This thesis is being submitted in partial fulfilment of the requirements for the degree of PhD

Signed ..... (N. F. H. Mukhtar) Date .....

### **STATEMENT 2**

This thesis is the result of my own independent work/investigation, except where otherwise, and the thesis has not been edited by third party beyond what is permitted by Cardiff University's policy on the Use of Third Party Editors by Research Degree Students. Other sources are acknowledged by explicit references. The views expressed are my own.

Signed ..... (N. F. H. Mukhtar) Date .....

### **STATEMENT 3**

I hereby give consent for my thesis, if accepted, to be available for photocopying and for inter-library loan, and for the title and summary to be made available to outside organisations.

Signed ..... (N. F. H. Mukhtar) Date .....

## TABLE OF CONTENTS

|  |              |
|--|--------------|
| <b>ABSTRACT .....</b>                              | <b>i</b>     |
| <b>ACKNOWLEDGEMENTS.....</b>                       | <b>iv</b>    |
| <b>DECLARATION.....</b>                            | <b>vi</b>    |
| <b>TABLE OF CONTENTS.....</b>                      | <b>vii</b>   |
| <b>LIST OF FIGURES .....</b>                       | <b>xiii</b>  |
| <b>LIST OF TABLES .....</b>                        | <b>xxi</b>   |
| <b>LIST OF ACRONYMS .....</b>                      | <b>xxiii</b> |
| <b>NOMENCLATURE.....</b>                           | <b>xxiv</b>  |
| <br>   |              |
| <b>CHAPTER 1: INTRODUCTION.....</b>                | <b>1</b>     |
| 1.1    Background and motivation .....             | 2            |
| 1.2    Research hypothesis and objectives .....    | 5            |
| 1.3    Thesis Organisation .....                   | 6            |
| <br>   |              |
| <b>CHAPTER 2: LITERATURE REVIEW.....</b>           | <b>8</b>     |
| 2.1    Overview .....                              | 9            |
| 2.2    AFM probe-based fabrication processes ..... | 9            |
| 2.2.1    Force-assisted AFM nanolithography .....  | 10           |
| 2.2.2    Bias-assisted AFM nanolithography .....   | 15           |
| 2.3    AFM probe-based nanomachining .....         | 19           |
| 2.4    AFM tip characterisation techniques.....    | 25           |

|         |                                      |    |
|---------|--------------------------------------|----|
| 2.4.1   | In-situ techniques .....             | 26 |
| 2.4.1.1 | Scan of specific features .....      | 26 |
| 2.4.1.2 | Ultra-sharp tip scan technique ..... | 33 |
| 2.4.1.3 | Blind tip reconstruction .....       | 37 |
| 2.4.1.4 | Wear metrics.....                    | 40 |
| 2.4.2   | Ex-situ measurements .....           | 43 |
| 2.5     | Summary .....                        | 46 |

**CHAPTER 3: ASSESSMENT OF WEAR FOR AFM SILICON PROBES USING  
TWO DIMENSIONAL TIP PROFILE DATA .....50**

|       |   |    |
|-------|---|----|
| 3.1   | Overview .....                            | 51 |
| 3.2   | Experimental set-up and methodology.....  | 52 |
| 3.2.1 | AFM system.....                           | 52 |
| 3.2.2 | Workpiece preparation .....               | 57 |
| 3.2.3 | AFM probes .....                          | 57 |
| 3.2.4 | Cutting conditions .....                  | 61 |
| 3.3   | Methodology for tip wear assessment ..... | 64 |
| 3.3.1 | Two-dimensional profile extraction .....  | 64 |
| 3.3.2 | Area and volume loss measurement.....     | 66 |
| 3.3.3 | Tip radius measurement .....              | 69 |
| 3.3.4 | Assessment of groove topography .....     | 70 |
| 3.4   | Analysis of the results .....             | 72 |

|       |   |    |
|-------|---|----|
| 3.4.1 | Area and volume loss measurements ..... | 72 |
| 3.4.2 | Tip radius measurements.....            | 80 |
| 3.4.3 | Machined grooves .....                  | 83 |
| 3.5   | Conclusions .....                       | 89 |

**CHAPTER 4: ASSESSMENT OF WEAR FOR AFM SILICON PROBES WITH  
DIAMOND-COATED TIPS USING THE IN-SITU ULTRA SHARP TIP SCAN  
METHOD .....**

|         |   |     |
|---------|---|-----|
| 4.1     | Overview .....  | 93  |
| 4.2     | Experimental set-up and methodology.....                        | 94  |
| 4.2.1   | AFM system and workpiece preparation .....                      | 94  |
| 4.2.2   | AFM probes .....  | 94  |
| 4.2.3   | Experimental procedure .....                                    | 96  |
| 4.2.4   | Cutting conditions .....  | 98  |
| 4.3     | Methodology for tip wear assessment .....                       | 99  |
| 4.3.1   | Ultra-sharp tip scan technique.....                             | 99  |
| 4.3.2   | Tip radius measurements.....                                    | 99  |
| 4.3.3   | Volume loss measurement .....                                   | 101 |
| 4.3.4   | Assessment of groove topography .....                           | 107 |
| 4.4     | Analysis of the results .....                                   | 107 |
| 4.4.1   | Tip radius measurements.....                                    | 107 |
| 4.4.1.1 | Effect of the selected vertical interval from the tip apex..... | 107 |

|         |  |     |
|---------|--|-----|
| 4.4.1.2 | Analysis of measured tip radius values ..... | 111 |
| 4.4.2   | Volume loss measurement .....                | 119 |
| 4.4.3   | Machined grooves .....                       | 121 |
| 4.5     | Conclusions .....                            | 128 |

**CHAPTER 5: ASSESSMENT OF WEAR FOR AFM SILICON PROBES WITH  
DIAMOND-COATED TIPS USING THE IN-SITU REVERSE IMAGING  
METHOD .....**

|         |  |     |
|---------|--|-----|
| 5.1     | Overview .....   | 132 |
| 5.2     | Experimental set-up and methodology.....   | 133 |
| 5.2.1   | AFM system and workpiece preparation .....   | 133 |
| 5.2.2   | Comparison of two AFM probe inspection techniques for three-dimensional tip characterisation ..... | 133 |
| 5.2.3   | Nanomachining process .....  | 136 |
| 5.2.4   | Cutting conditions for the nanomachining experiments .....   | 138 |
| 5.2.5   | AFM DT-NCHR-10 probes .....  | 141 |
| 5.3     | Comparison of two AFM probe inspection techniques for 3D tip assessment ....                       |     |
|         | .....  | 141 |
| 5.4     | Methodology for tip wear assessment .....  | 147 |
| 5.5     | Analysis of the results .....  | 148 |
| 5.5.1   | Tip radius measurements.....   | 148 |
| 5.5.1.1 | Effect of the selected vertical interval from the tip apex.....                                    | 148 |

|         |  |     |
|---------|--|-----|
| 5.5.1.2 | Analysis of measured tip radius values ..... | 150 |
| 5.5.2   | Volume loss measurement .....                | 161 |
| 5.5.3   | Machined grooves .....                       | 166 |
| 5.6     | Conclusions .....                            | 174 |

**CHAPTER 6: CONTRIBUTIONS, CONCLUSIONS AND FUTURE WORK ....176**

|     |                                      |     |
|-----|--------------------------------------|-----|
| 6.1 | Overview .....                       | 177 |
| 6.2 | Contributions .....                  | 177 |
| 6.3 | Conclusions .....                    | 180 |
| 6.4 | Recommendations for future work..... | 181 |

|                    |  |            |
|--------------------|--|------------|
| <b>Appendix A:</b> | <b>Comparison between two discretisation schemes for tip volume calculations from 2D profile data.</b> | <b>183</b> |
|--------------------|--|------------|

|                    |   |            |
|--------------------|---|------------|
| <b>Appendix B:</b> | <b>Fitness agreement for AFM tip profile.....</b> | <b>186</b> |
|--------------------|---|------------|

|                    |  |            |
|--------------------|--|------------|
| <b>Appendix C:</b> | <b>SEM micrograph of AFM silicon tip after breakage occurrence. ....</b> | <b>188</b> |
|--------------------|--|------------|

|                    |  |            |
|--------------------|--|------------|
| <b>Appendix D:</b> | <b>SEM micrograph of AFM silicon diamond coated tip after breakage occurrence.....</b> | <b>189</b> |
|--------------------|--|------------|

|                    |  |            |
|--------------------|--|------------|
| <b>Appendix E:</b> | <b>Evolution of tip radius, area and volume loss value for silicon tip nanomachining experiments. ....</b> | <b>191</b> |
|--------------------|--|------------|

|   |            |
|---|------------|
| <b>Appendix F: Evolution of tip radius and volume loss value for silicon diamond coated tip with nitrogen doping nanomachining experiments.....</b>     | <b>193</b> |
| <b>Appendix G: Evolution of tip radius and volume loss value for silicon diamond coated tip without nitrogen doping nanomachining experiments. ....</b> | <b>194</b> |
| <b>REFERENCES.....</b>  | <b>196</b> |
| <b>PUBLICATIONS AND PRESENTATIONS.....</b>  | <b>214</b> |

## LIST OF FIGURES

|   |    |
|---|----|
| Figure1.1: Schematic of the principle for the AFM probe-based mechanical machining process (from Brousseau <i>et al.</i> 2010).....   | 3  |
| Figure 2.1: (a) Force assisted and (b) bias assisted nanolithography (from Xie <i>et al.</i> 2006) .....  | 11 |
| Figure 2.2: Force-assisted AFM nanolithography processes: (a) schematic of the AFM-based nano indentation process (from Chen 2014), (b) schematic of AFM scratching (also known as AFM probe-based machining) (from Jiang <i>et al.</i> 2012), (c) thermomechanical writing (from Vettiger <i>et al.</i> 2002), (d) AFM-based nano-manipulation (from Yano <i>et al.</i> 2013) and (e) schematic diagram of the din-pen nanolithography (DPN) process (from Rozhok <i>et al.</i> 2003).....   | 13 |
| Figure 2.3: Bias-assisted AFM nanolithography processes: (a) AFM local oxidation scheme (from Losilla <i>et al.</i> 2010), (b) AFM image of a gold-dot array written on SiO <sub>2</sub> film 34 Å thick by field evaporation process (from Koyanagi <i>et al.</i> 1995), (c) schematic sketch of the experimental setup for electrochemical deposition (from Li <i>et al.</i> 2001), (d) CNT on an oxide layer imaged in tapping-mode AFM (i) before and (ii) after cutting by applying two voltage pulses (from Park <i>et al.</i> 2002), (e) schematic representation of the electrostatic field formation between an AFM tip and a conductive layer with a polymer film spin-coated onto the conductor (from Lyuksyutov <i>et al.</i> 2004), (f) polymer patterning by nano-explosion (from Ponzoni <i>et al.</i> 2006), and (g) the application of charge deposition for nanofabrication (from Mesquida and Stemmer 2001)..... | 17 |
| Figure 2.4: (a) Rapid initial wear followed by a slower linear wear and (b) sudden blunting of the tip (from Gozen and Ozdoganlar 2014). ....   | 24 |
| Figure 2.5: (a) A simulation of an AFM tip scanning over a columnar thin film surfaces (from Westra <i>et al.</i> 1993), (b) a scanning electron microscope image of the silicon grating  |    |

|  |    |
|--|----|
| TGT01 model from NT-MDT (Neto and Craig, 1995), (c) schematic of the principle for the AFM probe-based characterisation method using sharp pin-like asperities (Bloo <i>et al.</i> 1999). ....   | 29 |
| Figure 2.6: SEM micrograph of copper thin film prepared by MOCVD showing a pin-like structure with a height of more than 300 nm and a radius of less than 120 nm (from Atamny and Baiker 1995). ....   | 30 |
| Figure 2.7: (a) Colloidal gold particles imaged with a commercial AFM probe (from Vesenka <i>et al.</i> 1993) and (b) schematic diagram of the structure used by Griffith and co-workers for characterising probe tips (from Griffith <i>et al.</i> (1991)).....   | 34 |
| Figure 2.8: (a) Illustration of the AFM tip characterisation technique using an ultra-sharp tip, (b) an example of a 3D AFM image obtained (c) a cross-sectional AFM image extracted from the 3D data (from Gozen and Ozdoganlar 2014).....                        | 36 |
| Figure 2.9: AFM topography images of the ultra nanocrystalline UNCD surfaces acquired by (a-c) a Si tip, (d-f) a SiNx-coated Si tip, (g-i) a sharpened SiNx tip, and (j-l) an unsharpened SiNx tip (from Liu <i>et al.</i> 2010). ....                             | 39 |
| Figure 2.10: Comparison of the tip profiles measured by TEM and blind reconstruction (“BR”) for (c) the SiNx-coated Si probe and (d) the unsharpened SiNx before use, after acquiring 20 images, and after acquiring 100 images (from Liu <i>et al.</i> 2010)..... | 39 |
| Figure 2.11: Illustration of the method employed by Cheng and co-workers. Depending of the degree of tip bluntness, an increase or decrease in the resonance frequency of the transmitted acoustic waves may be detected (from Cheng <i>et al.</i> 2011).....      | 41 |
| Figure 2.12: (a) SEM image of the tip before the wear experiment and (b) SEM image of tip after the wear experiment (from Bloo <i>et al.</i> 1999). ....   | 44 |

|  |    |
|--|----|
| Figure 2.13: A TEM image demonstrating the contrast between the thin coating of diamond-like carbon and the single-crystal silicon probe underneath (from Jacobs <i>et al.</i> 2015). ....                             | 44 |
| Figure 3.1: XE-100 AFM instrument from Park Systems. ....  | 53 |
| Figure 3.2: Schematic diagram of the AFM tip-based nanomachining principle (adapted from Brousseau <i>et al.</i> 2013). ....   | 54 |
| Figure 3.3: Illustration of the possible effect of the tilt on the groove depth when conducting the AFM tip-based nanomachining operations with the “ <i>z-scanner</i> ” mode. ....                                    | 56 |
| Figure 3.4: Workpiece preparation procedure. ....  | 58 |
| Figure 3.5: SEM micrographs of a typical NSC15 probe. ....   | 59 |
| Figure 3.6: The investigated three machining directions with respect to the long axis of the cantilever. ....  | 63 |
| Figure 3.7: Tip wear assessment procedure. ....  | 65 |
| Figure 3.8: SEM images of (a) the unused tip, (b) the tip after machining for a distance of 0.5 mm during Trial 5; corresponding 2D profiles, (c) before alignment, (d) after completing the alignment procedure. .... | 65 |
| Figure 3.9: Frustum of a right circular cone. ....   | 68 |
| Figure 3.10: <i>H/D ratio</i> ....   | 71 |
| Figure 3.11: (a) AFM topography image of a groove and (b) cross section of a groove profiles after 0.5 mm of machining distance. ....  | 73 |
| Figure 3.12: SEM micrographs of the six NSC 15 silicon tips used in this chapter prior to the start of the experimental trials. ....   | 74 |
| Figure 3.13: Tip profiles at different stages of machining for each trial conducted for each NSC 15 silicon probes. ....   | 75 |

|   |     |
|---|-----|
| Figure 3.14: Evolution of the tip area loss as a function of the machining direction for the different values of set normal force considered for NSC 15 silicon probes. ....                          | 76  |
| Figure 3.15: Evolution of the tip volume loss as a function of the machining direction for the different values of set normal force considered NSC 15 silicon probes. ....                            | 77  |
| Figure 3.16: Generated grooves on the Cu surface at different magnifications for Trial 3 (set applied force: 80 $\mu$ N; machining direction: 3). ....  | 81  |
| Figure 3.17: Evolution of tip radii as a function of the machining direction for the different values of set normal force considered NSC 15 silicon probes.....                                       | 82  |
| Figure 3.18: Groove profiles obtained when machining with NSC 15 silicon probes. ..   | 86  |
| Figure 4.1: SEM micrographs of a typical DCP20 probe. ....  | 95  |
| Figure 4. 2: Experimental procedure.....  | 97  |
| Figure 4.3: (a) schematic diagram of the ultra-sharp tip scan approach; (b) SEM micrographs of an ultra-sharp tip and of a diamond-coated tip at the same magnifications. ....                        | 102 |
| Figure 4.4(a): four different cross section drawn on an AFM probe topography image for an unused DCP20 tip and (b) corresponding profiles from the cross sections shown in (a). ....                  | 103 |
| Figure 4.5: (a) 3D AFM topography image of a silicon diamond-coated probe, (b) correspond 2D AFM topography image; (c) Pixel discretisation of the selected area in the 2D AFM topography image. .... | 104 |
| Figure 4.6: Tip volume estimation procedure based on 3D data obtained using the ultra-sharp tip scan method.....  | 106 |
| Figure 4.7: Example of a 3D AFM topography image of the produced grooves.....   | 108 |
| Figure 4.8: Radius measurements as a function of different vertical intervals considered from the tip apex for DCP 20 diamond-coated silicon probes.....  | 110 |

|  |     |
|--|-----|
| Figure 4.9: SEM micrographs of the six DCP 20 silicon tips coated with diamond, which were used in this chapter prior to the start of the experimental trials. ....                                    | 113 |
| Figure 4.10: Tip profiles before and after the completion of the machining trials for each DCP 20 diamond-coated silicon probe. ....   | 114 |
| Figure 4.11: Comparison of the radius measurements obtained from ultra-sharp tip scan data and SEM data for machining distances of 0.0 mm and 5.0 mm. The error bars show the standard deviation. .... | 115 |
| Figure 4.12: Evolution of tip radii as a function of the machining direction for the different values of set normal force considered for DCP 20 diamond-coated silicon probes. ....                    | 117 |
| Figure 4.13: Evolution of the tip volume loss as a function of the machining direction for the different values of set normal force considered for DCP 20 diamond-coated silicon probes. ....          | 120 |
| Figure 4.14: Groove profiles obtained when machining with DCP 20 diamond-coated silicon probes. ....   | 125 |
| Figure 5.1: Comparison of two AFM probe inspection technique for 3D tip characterisation procedure. ....   | 134 |
| Figure 5.2: (a) Schematic diagram of the reverse imaging approach; (b) SEM micrographs of a diamond-coated tip and the sharp pin-like asperities (model TGT1). ....                                    | 135 |
| Figure 5.3: Illustration of the concept of profile area difference between SEM data and the considered 3D tip characterisation techniques. ....  | 137 |
| Figure 5.4: Experimental procedure followed during the nanomachining experiments. ....   | 139 |
| Figure 5.5: SEM micrographs of a typical DT-NCHR-10 probe.....   | 142 |

|   |     |
|---|-----|
| Figure 5.6: Qualitative profile comparisons between SEM data and the corresponding cross sections obtained with the ultra-sharp tip scan profile characterisation technique for new tips .....  | 143 |
| Figure 5.7: Qualitative profile comparisons between SEM data and the corresponding cross sections obtained with the reverse imaging characterisation technique for new tips. ....   | 144 |
| Figure 5.8: Average difference for radius measurements between SEM data and the 3D tip characterisation techniques .....  | 146 |
| Figure 5.9: Discrepancies in the profile area difference data between the SEM inspection and the 3D tip characterisation techniques .....   | 146 |
| Figure 5.10: Radius measurements as a function of different vertical intervals considered from the tip apex. The inset plot for each graph shows the profiles obtained with the SEM and the reverse imaging method for a fixed vertical distance of 80 nm. .... | 149 |
| Figure 5.11: SEM micrographs of the six DT-NCHR-10 silicon tips coated with diamond used for machining at applied loads of 100 $\mu\text{N}$ and 60 $\mu\text{N}$ prior to the start of the experimental trials.....  | 151 |
| Figure 5.12: Tip profiles before and after the completion of the machining trials for each DT-NCHR-10 diamond-coated silicon probe used for machining at applied loads of 100 $\mu\text{N}$ and 60 $\mu\text{N}$ .....  | 152 |
| Figure 5.13: SEM micrographs of the six DT-NCHR-10 silicon tips coated with diamond used for machining at applied loads of 20 $\mu\text{N}$ and 10 $\mu\text{N}$ prior to the start of the experimental trials.....   | 153 |
| Figure 5.14: Tip profiles before and after the completion of the machining trials for each DT-NCHR-10 diamond-coated silicon probe used for machining at applied loads of 20 $\mu\text{N}$ and 10 $\mu\text{N}$ .....   | 154 |

|   |     |
|---|-----|
| Figure 5.15: Comparison of the radius measurements obtained from the reverse imaging technique and SEM inspection for machining distances of 0.0 mm and 3.0 mm. The error bars show the standard deviation. ....          | 157 |
| Figure 5.16: Evolution of tip radii as a function of the machining direction and distance for different values of set normal force considered for DT-NCHR-10 diamond-coated silicon probes. ....                          | 158 |
| Figure 5.17: Evolution of tip radii as a function of the machining direction and distance for different values of set normal force considered for DT-NCHR-10 diamond-coated silicon probes. ....                          | 159 |
| Figure 5.18: Evolution of the tip volume loss as a function of the machining direction for the different values of set normal force considered for DT-NCHR-10 diamond-coated silicon probes with standard deviation. .... | 162 |
| Figure 5.19: Evolution of the tip volume loss as a function of the machining direction for the different values of set normal force considered for DT-NCHR-10 diamond-coated silicon probes with standard deviation. .... | 163 |
| Figure 5.20: Grooves profiles. ....   | 169 |
| Figure 5.21: Grooves profiles. ....   | 171 |
| Figure A.1: Circular disk.....  | 183 |
| Figure A.2: Comparison between two discretisation schemes for tip volume calculations from 2D profile data.....   | 184 |
| Figure B.1: Profile of the polynomial of degree two fitted to profile of the AFM probe .....  | 186 |
| Figure D.1: SEM micrographs of the DCP 20 silicon diamond coated tips with nitrogen doping after machining at 0.5 mm. ....  | 189 |

Figure D.2: SEM micrographs of the DT-NCHR 10 silicon diamond coated tips without nitrogen doping after machining at 0.5 mm at set applied force 100  $\mu$ N. .... 190

Figure D.3: A part of silicon polycrystalline diamond coated tip without nitrogen doping stuck on the surface of single crystal copper workpiece..... 190

## LIST OF TABLES

|  |     |
|--|-----|
| Table 3.1: Probe specification for the NSC15 model. ....   | 60  |
| Table 3.2: Selected AFM tip-based nanomachining parameters. ....   | 63  |
| Table 3.3: Probe specification for the CSG30 model. ....   | 71  |
| Table 3.4: Rate of change of the radius values based on the plots in Figures 3.13, 3.14 and 3.16.....  | 84  |
| Table 3.5: <i>H/D ratios</i> for NSC 15 silicon probes. ....   | 87  |
| Table 3.6: SEM micrographs of grooves at the considered machining distances for NSC 15 silicon probes. Scale bars: 13 $\mu\text{m}$ .....                | 88  |
| Table 4.1: Probe specifications for the DCP20 model from NT-MDT.....   | 95  |
| Table 4.2: Selected AFM tip-based nanomachining parameters. ....   | 100 |
| Table 4.3: Rate of change of the radius values based on the plots in Figure 4.12. ....   | 118 |
| Table 4.4: Rate of change of volume loss based on the plots in Figures 4.13. ....  | 123 |
| Table 4.5: SEM micrographs of grooves at the considered machining distances for DCP 20 diamond-coated silicon probes. Scale bars: 10 $\mu\text{m}$ ..... | 124 |
| Table 4.6: <i>H/D ratios</i> for DCP 20 diamond-coated silicon probes.....   | 126 |
| Table 5.1: Selected AFM tip-based nanomachining parameters. ....   | 140 |
| Table 5.2: Probe specifications for the DT-NCHR-10 model from NANONSENSORS <sup>TM</sup> . ....  | 142 |
| Table 5.3: Rate of change of the radius values based on the plots in Figure 5.16. ....   | 160 |
| Table 5.4: Rate of change of the radius values based on the plots in Figure 5.17. ....   | 160 |
| Table 5.5: Rate of change of volume loss based on the plots in Figure 5.18.....  | 164 |
| Table 5.6: Rate of change of volume loss based on the plots in Figure 5.19.....  | 164 |

|  |     |
|--|-----|
| Table 5.7: SEM micrographs of grooves at the considered machining distances for set applied force of 100 $\mu\text{N}$ and 60 $\mu\text{N}$ . Scale bars: 10 $\mu\text{m}$ ..... | 168 |
| Table 5.8: SEM micrographs of grooves at the considered machining distances 20 $\mu\text{N}$ and 10 $\mu\text{N}$ . Scale bars: 10 $\mu\text{m}$ .....                           | 170 |
| Table 5.9: <i>H/D ratios</i> for set applied force 100 $\mu\text{N}$ and 60 $\mu\text{N}$ .....  | 172 |
| Table 5.10: <i>H/D ratios</i> for set applied force 20 $\mu\text{N}$ and 10 $\mu\text{N}$ .....  | 172 |
| Table D.1: Evolution of tip radius measurement for silicon tip.....  | 191 |
| Table D.2: Evolution of tip area loss measurement for silicon tip.....   | 191 |
| Table D.3: Evolution of tip volume loss measurement for silicon tip.....   | 192 |
| Table E.1: Evolution of tip radius measurement for silicon tip.....  | 191 |
| Table E.2: Evolution of tip area loss measurement for silicon tip.....   | 191 |
| Table E.3: Evolution of tip volume loss measurement for silicon tip.....   | 192 |
| Table F.1: Evolution of tip radius measurement for silicon diamond coated tip with nitrogen doping. ....   | 193 |
| Table F.2: Evolution of tip volume loss measurement for silicon diamond coated tip with nitrogen doping. ....  | 193 |
| Table G.1: Evolution of tip radius measurement for silicon diamond coated tip without nitrogen doping. ....  | 194 |
| Table G.2: Evolution of tip volume loss measurement for silicon diamond coated tip without nitrogen doping. ....   | 195 |

## **LIST OF ACRONYMS**

|        |  |
|--------|--|
| AFM:   | Atomic Force Microscopy                          |
| SEM:   | Scanning Electron Microscopy                     |
| TEM:   | Transmission Electron Microscopy                 |
| HRTEM: | High Resolution Transmission Electron Microscopy |
| DPN:   | Dip-Pen Nanolithography                          |
| DNA:   | Deoxyribonucleic acid                            |
| PSPD:  | Position Sensitive Photodiode Detector           |
| BTR:   | Blind Tip Reconstruction                         |
| Ra:    | Roughness Average                                |
| PDMS:  | Polydimethylsiloxane                             |
| N:     | Nitrogen   |

## NOMENCLATURE

|                      |   |
|----------------------|---|
| $R$ :                | Radius of curvature   |
| $A$ :                | Area  |
| $h_i$ :              | Height of a AFM tip profile extracted at regular interval   |
| $l_i$                | Regular interval  |
| $V_f$ :              | Volume of frustum for a right circular cone   |
| $h_f$ :              | Height of frustum for a right circular cone   |
| $R_f$ :              | Radius of the base of frustum for a right circular cone   |
| $r_f$ :              | Radius of the top face of frustum for a right circular cone                                       |
| $h_1$ :              | Pile-up heights measured on left side of a machined groove  |
| $h_2$ :              | Pile-up heights measured on right side of a machined groove                                       |
| $d$ :                | Depth of a machined groove  |
| $V_p$ :              | Volume of the AFM tip   |
| $k$ :                | Number of pixel   |
| $z_k$ :              | Height of the AFM tip $k^{\text{th}}$ pixel   |
| $\Delta x$ :         | Value of changes in the distance between two pixels along the $x$ axis                            |
| $\Delta y$ :         | Value of changes in the distance between two pixels along the $y$ axis                            |
| $V_{\text{error}}$ : | The AFM probe volume error associated with the discretisation using circular disk-shaped elements |

$V_{average}$ : Average AFM probes volume values

$H/D\ ratio$ : Ratio between the sum of the pile-up heights measured on each side of a machined groove.

# **CHAPTER 1:**

## **INTRODUCTION**

# CHAPTER 1

## INTRODUCTION

### 1.1 Background and motivation

The Atomic Force Microscope (AFM) was invented in 1986 by Binning and co-workers to directly image the surface topography of specimens with atomic level resolution by relying on the interactions between the tip of a probe and the specimen surface (Bining *et al.* 1986). Since then, the AFM technology has attracted substantial interest not only as a microscope but also as an instrument for the characterisation of different mechanical, electrical and magnetic properties of materials. In recent years, the AFM has also been employed increasingly as an enabling tool for the development of a variety of micro and nanofabrication processes (Tseng *et al.* 2005). As a result, AFM instruments are widely used in academic and industrial research studies.

Among many fabrication techniques based on the AFM technology, AFM probe-based machining (also referred to as AFM scratching or scribing), which is illustrated in Figure 1.1, has been derived as a simple alternative to vacuum-based technologies for the creation of nanoscale features (Gozen and Ozdoganlar 2012). This process allows material removal from a workpiece as a result of the direct contact between the probe tip and the specimen surface. AFM probe-based machining has been demonstrated for a number of applications. For example, it has shown potential for producing nanostructured replication masters, which can subsequently be used for small and medium series production of polymer components (Brousseau *et al.* 2010).

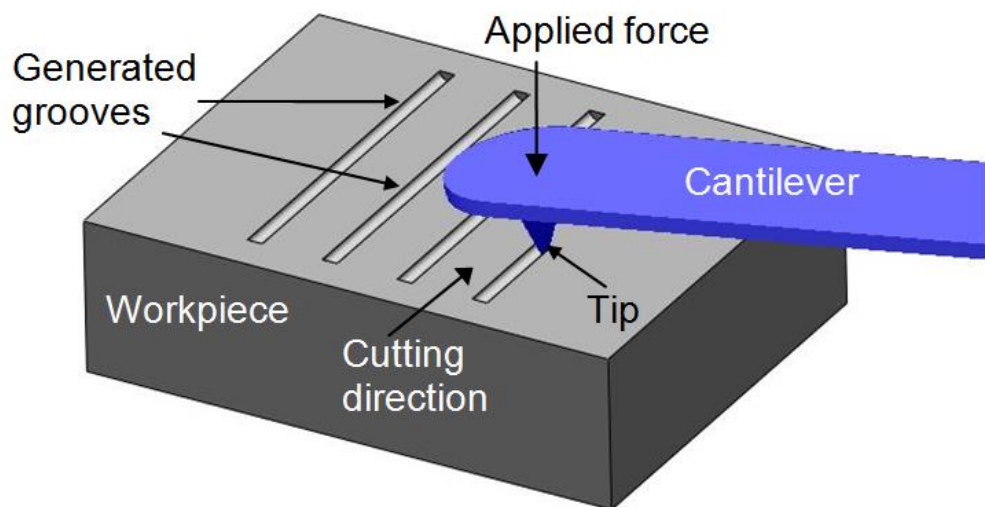


Figure 1.1: Schematic of the principle for the AFM probe-based mechanical machining process (from Brousseau *et al.* 2010)

In parallel, there is a growing market demand for the reduction of the size of products leading to the need of micro and nanoscale features and components (Chau *et al.* 2005) such that light weight, low power consumption and reduced material requirements can be achieved (Mostofa *et al.* 2013). Such a trend makes the AFM to be a potential future low-cost technique for nanoscale pattern formation, structuring, fabrication and replication (Quate 1997 and Snow and Campbell 1994). In addition, most AFM-based techniques can be performed at room temperature and in ambient environment and can benefit from the concurrent application of mechanical, electrical, thermal, chemical and photonic phenomena on either conducting or non-conducting surfaces.

In the field of mechanical machining, both at macro and micro scales, the quality of the produced parts can be significantly affected by the condition of the cutting tool used. In particular, tool wear and tool breakage not only affect the obtained surface finish and dimensional accuracy of machined parts, but also would impact the production process by reducing the productivity, reliability and efficiency of a machining system. Such concerns also do exist when machining is performed with the tip of an AFM probe. The condition of AFM probe tips is also of critical importance when an AFM is used for its primary purpose, i.e. imaging. Indeed, the resolution of AFM-based measurements is dependent on the geometry of the tip apex and is strongly affected by the degradation of the tip through processes such as wear (Liu *et al.* 2010). In this case, tip wear could lead to the obtained topography image to be different from the real surface features of an inspected specimen (Atamny and Baiker 1995 and Edwards *et al.* 1998).

For these reasons, the analysis of the wear evolution of the AFM tip geometry for the processes of imaging and machining have taken on a greater importance recently. Particularly, in the context of AFM imaging such tip characterisation studies are numerous. A single probe may be used numerous times and scanned over distances of millimetres to kilometres during its life (Liu *et al.* 2010 and Griffith *et al.* 1991). Therefore, the geometry of the AFM tip should be controlled carefully and its dimensions must be accurately known if the true profile of the surface is to be determined. However, tip wear investigations are still scarce in the field of AFM probe-based machining for which typical cutting forces lie between a few and tens of  $\mu\text{N}$  and where the intended process phenomena are different from those occurring during AFM imaging. Thus, the main motivation behind this research is the need to gain a further understanding of the influence of different process factors on the wear of AFM tips when performing AFM probe-based mechanical nanomachining operations.

## 1.2 Research hypothesis and objectives

The overall aim of this research was to investigate the tip wear of AFM probes when implementing the AFM probe-based mechanical nanomachining process. In particular, to achieve the overall aim of the research, the following two main objectives were set:

- To investigate experimentally the influence of different process parameters, namely the tip material, the machining direction and the applied load on the wear of AFM tips.
  
- To investigate the accuracy and the reliability of different in-situ techniques for characterising the apex geometry of the AFM tips.

### 1.3 Thesis Organisation

**Chapter 2:** a literature review is conducted in this chapter to identify knowledge gaps relevant to the context of the thesis. This chapter begins with an introduction to AFM nanolithography techniques. In particular, the basis of the force-assisted and bias-assisted nanolithography approaches and the operational principles of various derived techniques were discussed. Then, the AFM probe-based nanomachining process is reviewed in more details. The chapter then moves on to present literature on AFM tip characterisation techniques. Specifically, in-situ and ex-situ measurement approaches are discussed. Finally, the chapter is concluded with a summary of research issues in the study of tip wear for AFM probe-based nanomachining and in the investigations of techniques monitoring the conditions for the AFM probes.

**Chapter 3:** this chapter presents an experimental study where AFM silicon tips were employed to machine a relatively soft workpiece material, namely single crystal copper. First, the chapter describes the experimental methodology used, which includes the machining conditions considered together with the analytical approach utilised to assess the tip wear when using 2D profile data extracted from SEM micrographs of the tips. Then, results are assessed using different tip wear metrics and are discussed.

**Chapter 4:** a similar of AFM probe-based machining set up to that reported in Chapter 3 is employed in this chapter. However, silicon diamond-coated probes are employed for the nanomachining trials in this case. In addition, this particular chapter uses different wear metrics because an in-situ method, namely the ultra-sharp tip scan approach, is employed to obtain 3 dimensional (3D) data of the shape of the AFM tips.

**Chapter 5:** this chapter starts by investigation experimentally the accuracy and practical suitability of two different 3D in-situ measurement techniques for tip characterisation, namely the ultra-sharp tip san method and reverse imaging method, which is described in more details in Chapter 2. Then, a further experimental study of the wear of diamond-coated tips in silicon is conducted during the AFM probe-based machining process. In particular, this chapter considers a different type of probe and a wider range of normal applied loads in comparison with the study reported in Chapter 4.

**Chapter 6:** this final chapter reiterates the knowledge gaps identified in the literature review conducted in Chapter 2 and presents the contributions of this research in the light of these gaps. In addition, key conclusions reached as well as identified future work, as a result of the research carried out in this thesis, are described.

**Appendix A** shows a comparison between two discretisation schemes for tip volume calculations from 2D profile data that extracted from SEM micrographs.

## **CHAPTER 2:**

## **LITERATURE REVIEW**

## CHAPTER 2

## LITERATURE REVIEW

### 2.1 Overview

In this chapter, a review of the state of the art and its analysis is presented in the areas of AFM probe-based manufacturing and AFM tip characterisation techniques. The chapter is organised as follows. The next section introduces different AFM probe-based nanofabrication approaches by grouping them into the two categories, i.e. force-assisted and bias-assisted nanolithography. Following this, particular focus is given to the specific process of AFM probe-based machining. Then, existing AFM probe characterisation techniques, which can be used to assess the wear of the tip, are reviewed. In addition, a comparison of the relative merits of these characterisation techniques. Finally, the chapter is concluded with a summary of the open research issues when assessing the tip wear in the context of AFM probe-based machining.

### 2.2 AFM probe-based fabrication processes

The applicability of conventional mask-based and vacuum-based nanofabrication techniques can be limited by their high capital investment and operating cost, multiple-step processes and limited accessibility. Several other methods appear to be flexible alternatives for nanoscale patterning and fabrication such as AFM probe-based fabrication, nano-imprint lithography and soft lithography. Among these, AFM nanolithography has shown itself to be a unique tool for material structuring and patterning with nanometre resolution. In this case, localised nanostructures are generated through physical modifications and/or chemical reactions of the surface of materials. In addition, using an AFM instrument as a platform for nanoscale pattern formation has

potential for the development of future low cost manufacturing techniques (Tseng 2011, Quate 1997 and Campbell *et al.* 1996). Moreover, AFM nanolithography possesses the versatility for patterning a wide range of materials including metals, semiconductors, polymers and biological molecules in different media (Takahata 2013). As a result, numerous AFM based lithographic techniques have been developed in the last two decades. Generally, these could be classified into two general groups, namely force-assisted and bias-assisted nanolithography depending on their mechanistic and operational principles. A simplistic illustration to describe the main difference between these two groups is illustrated in Figure 2.1. Different processes have been demonstrated by researchers within each category. These are now elaborated further in the following sub-sections.

### **2.2.1 Force-assisted AFM nanolithography**

In force-assisted AFM nanolithography, a relatively large load is applied by the tip for pattern fabrication on the workpiece. In particular, the range of forces employed in this case are larger than those used for AFM imaging (Xie *et al.* 2006). Figure 2.2 illustrates the different force-assisted AFM nanolithography processes. These include mechanical indentation and scratching (also referred to as machining or scribing), thermomechanical writing, manipulation and dip-pen nanolithography. Indentation is a single structure formation approach for which the tip is first located at a specific surface site and a large force is then applied by the tip to indent the surface in a single vertical motion of the probe. AFM-based scratching can be realised either via static or dynamic ploughing. In the case of static ploughing, the tip operates in contact mode. It is scanned with a load large enough to induce plastic deformation of the substrate material across the surface to define features, which are typically in the shape of lines, or rectangles and

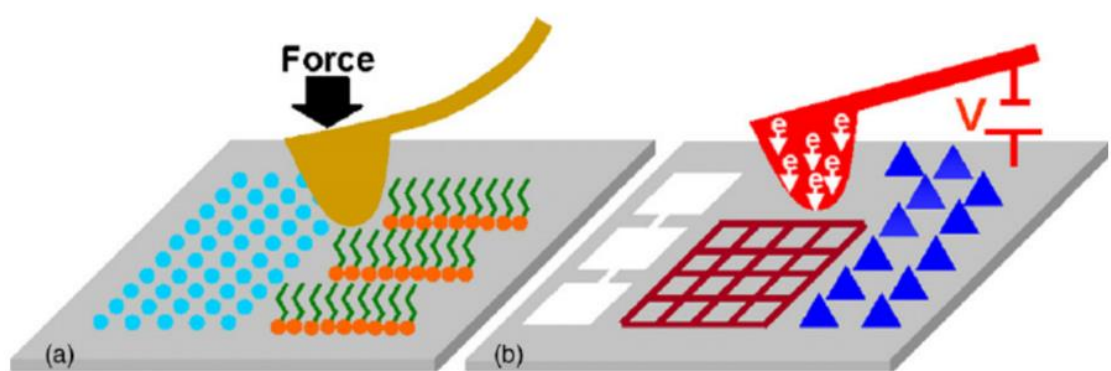
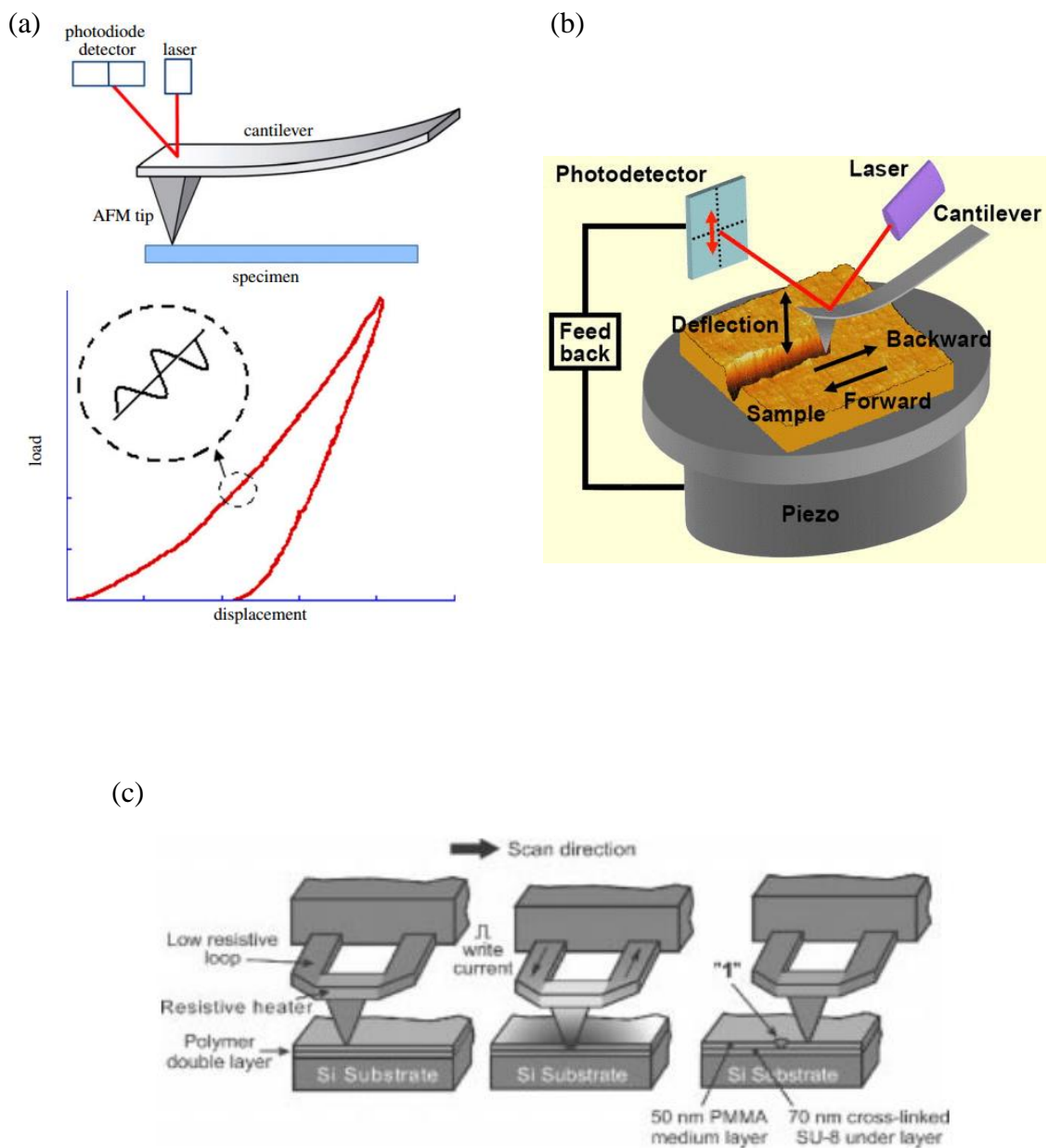


Figure 2.1: (a) Force assisted and (b) bias assisted nanolithography (from Xie *et al.* 2006)



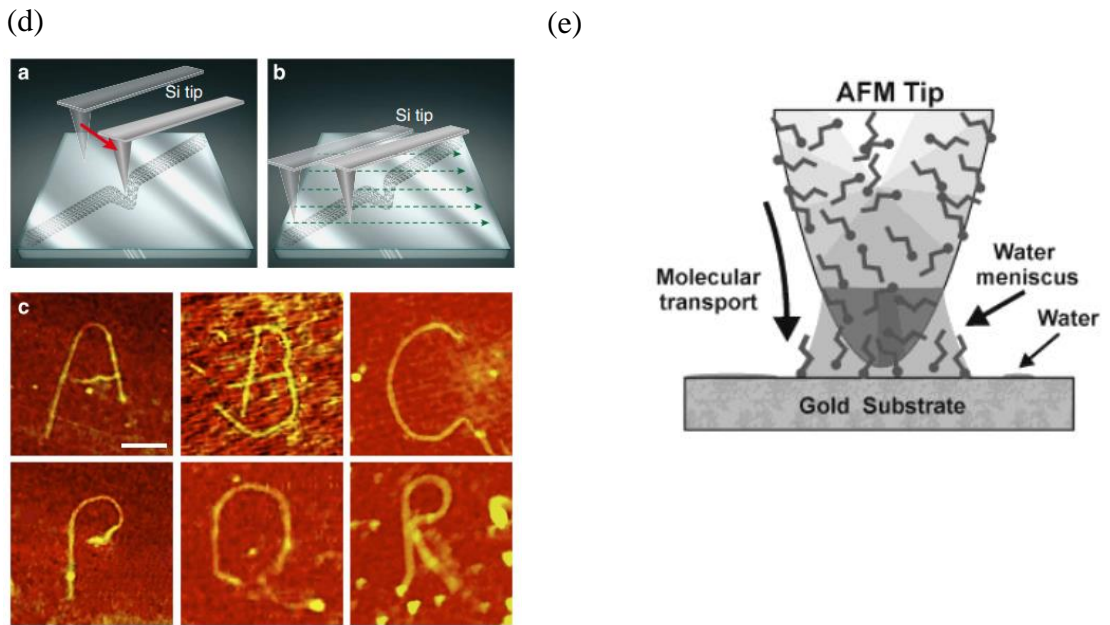


Figure 2.2: Force-assisted AFM nanolithography processes: (a) schematic of the AFM-based nano indentation process (from Chen 2014), (b) schematic of AFM scratching (also known as AFM probe-based machining) (from Jiang *et al.* 2012), (c) thermomechanical writing (from Vettiger *et al.* 2002), (d) AFM-based nano-manipulation (from Yano *et al.* 2013) and (e) schematic diagram of the din-pen nanolithography (DPN) process (from Rozhok *et al.* 2003)

squares cavities when the tip generates a series of linear parallel grooves. Dynamic ploughing involves scratching the surface with a vibrating tip in tapping mode. The force applied by the tip onto the substrate is modulated by adjusting the amplitude of the cantilever oscillations. In addition to implementing direct AFM indentation or scratching, numerous groups have reported indirect approaches based on transfer of the mechanically-generated patterns through follow-up wet-etching of lift-off techniques (Klehn and Kunze 1999, Snow *et al.* 1996 and Sugimura 2008).

Thermomechanical writing is also considered as a type of force-assisted AFM nanolithography process. In this case the AFM tip is also heated to write patterns over a polymer surface. The combined heat and mechanical force caused by the tip result in the polymer to soften and flow. This technique was first developed by IBM Zurich research group to facilitate the high density writing of data bits in a storage medium (King *et al.* 2001). This approach has also led to the development of the so-called “Millipede” technology, which relies on an entire array of probe cantilevers that are brought into contact with the storage medium (Mamin and Rugar, 1992 and Ried *et al.* 1997).

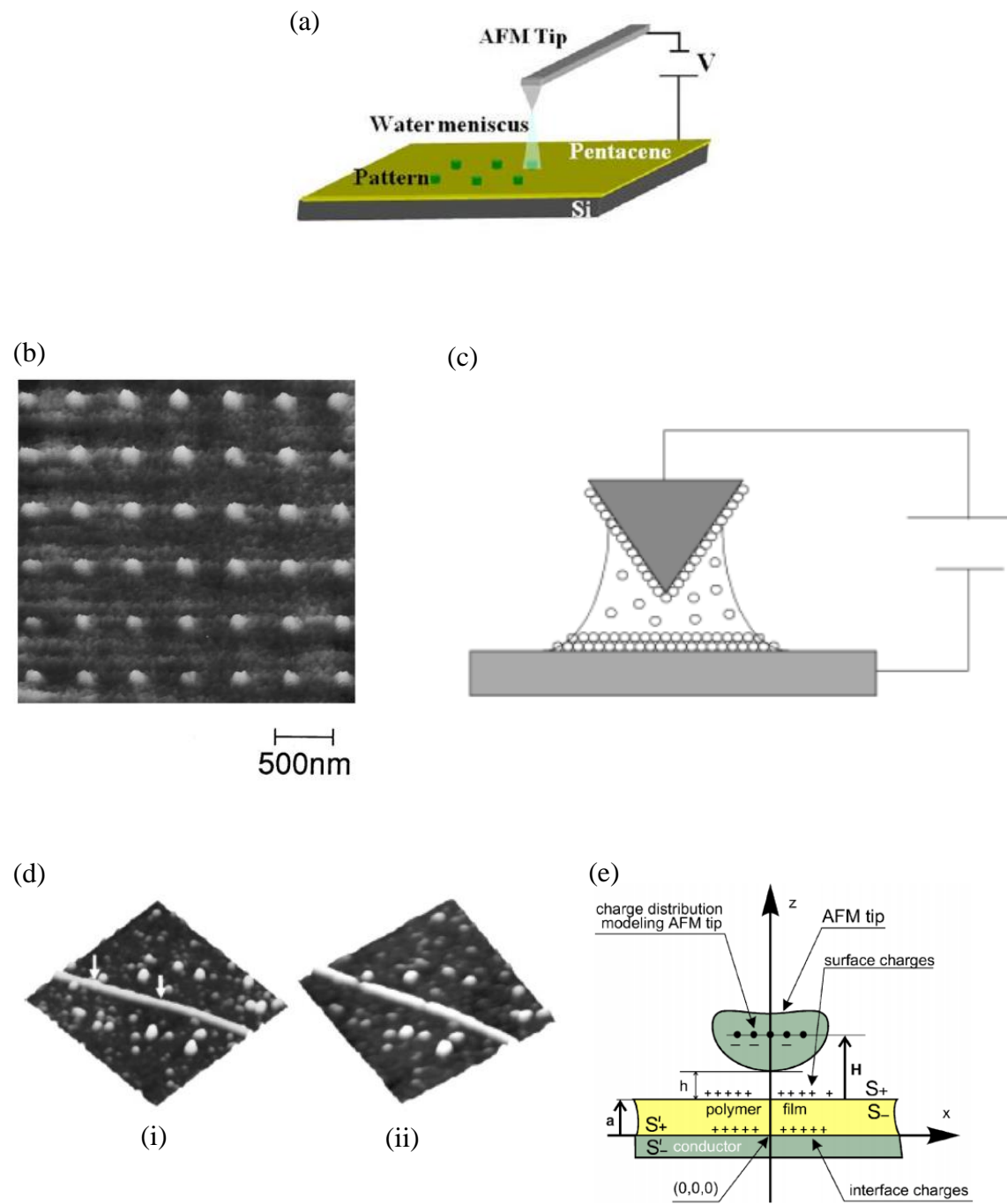
AFM-based manipulation relies on the tip to mechanically cut, push and transport, substances to form desired patterns on a substrate. The type of materials that have been processed via this approach range from single atoms, nanoparticles, nanocrystals and nanotubes to biological molecules such as DNA (Junno *et al.* 1995). The manipulation can be operated in contact, tapping and non-contact modes with the feedback loop either on or off (Requicha *et al.* 2001). The last force-assisted AFM nanolithography technique reported here is dip-pen nanolithography (DPN), which was invented by Mirkin’s group in 1999 (Piner *et al.* 1999). DPN is used to deliver collections of molecules in a printing

mode. Thus, it is an AFM-based direct write lithographic technique in which the AFM probe is used as a pen to directly deliver ink materials to a nanoscopic region on a target substrate.

### **2.2.2 Bias-assisted AFM nanolithography**

For this second group of AFM-based nanofabrication techniques, a bias is applied to the AFM probe to create a localised electric field in the nanometre-sized tip-sample gap. Since the gap is usually less than a few nanometres, a moderate tip bias of several volts generates a field of  $10^8$  V/m to  $10^{10}$  V/m. Such an extremely high electric field can initiate various physical and chemical processes, which facilitate pattern formation through field emission, charge injection, Joule heating, electrostatic attraction, explosive discharge and electrochemical reactions (Xie *et al.* 2006). Figure 2.3 illustrates the existing bias-assisted AFM nanolithography processes. Such techniques encompass probe anodic oxidation, field evaporation, electrochemical deposition and modification, electrical cutting and nicking, electrostatic deformation and electro-hydrodynamic nano-fluidic motion, nano-explosion and shock wave generation, and charge deposition and manipulation. These are briefly introduced below.

Local anodic oxidation is one of the earliest and most extensively studied techniques for bias-assisted AFM nanolithography. Through the application of a bias between the tip and a sample, the local electro-physical properties of the surface can be changed. In particular, the application of a voltage to conductive cantilever probes stimulates the electrochemical process on the surface under the probe tip and a metallic layer can be oxidised (Lemeshko *et al.* 2001). The field evaporation process is used for



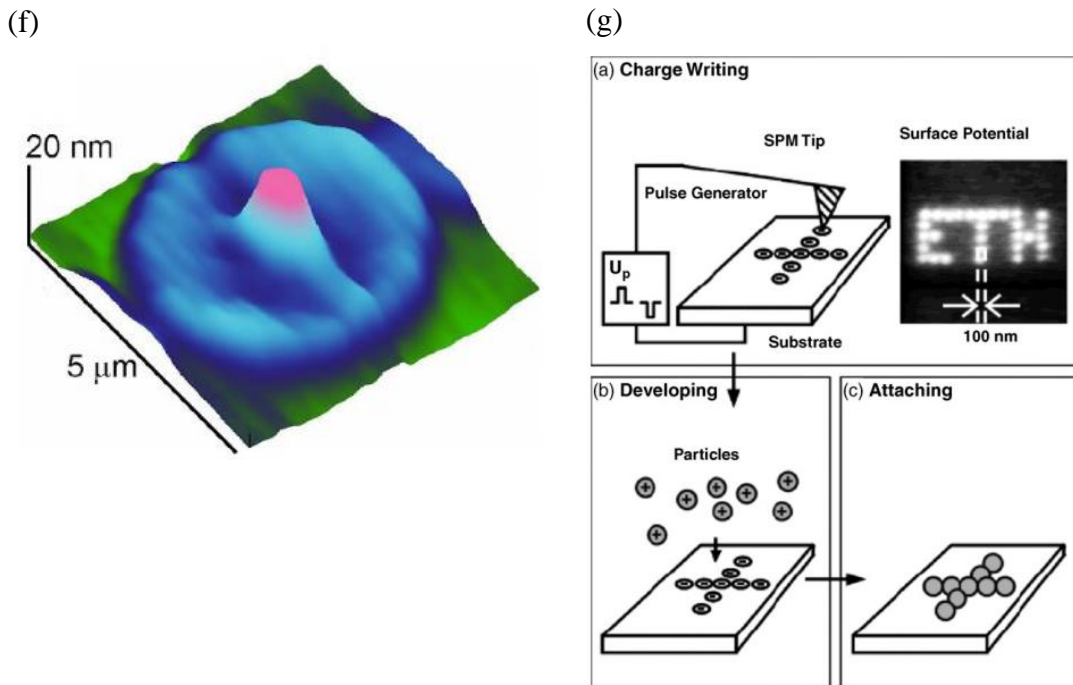


Figure 2.3: Bias-assisted AFM nanolithography processes: (a) AFM local oxidation scheme (from Losilla *et al.* 2010), (b) AFM image of a gold-dot array written on SiO<sub>2</sub> film 34 Å thick by field evaporation process (from Koyanagi *et al.* 1995), (c) schematic sketch of the experimental setup for electrochemical deposition (from Li *et al.* 2001), (d) CNT on an oxide layer imaged in tapping-mode AFM (i) before and (ii) after cutting by applying two voltage pulses (from Park *et al.* 2002), (e) schematic representation of the electrostatic field formation between an AFM tip and a conductive layer with a polymer film spin-coated onto the conductor (from Lyuksyutov *et al.* 2004), (f) polymer patterning by nano-explosion (from Ponzoni *et al.* 2006), and (g) the application of charge deposition for nanofabrication (from Mesquida and Stemmer 2001).

atomic manipulation, as it makes it possible to remove and deposit an individual atom or a cluster of atoms to surface complexes formed between a metal atom and an adsorbed gas atom. The process is usually a multi-step process, which involves the initial escape of the surface atom or complex. Then, it is further ionised as it moves away from the surface. During the escape, the atom or complex breaks the bonds holding it to the surface, by crossing an activation-energy barrier (Forbes, 1995).

Electrochemical deposition is an electrochemical version of DPN utilising meniscus formation and tip bias application during ink position (Li *et al.* 2001). By applying a bias to a tip, it is also possible to induce electrochemical surface transformation of certain functionalised self-assembled monolayers, while fully preserving the overall monolayer structural integrity. Depending on the nature of the transformations, such locally modified monolayer surfaces can be used to induce site-selective self-assembly of a number of different materials (organic, metal, semiconductor), according to a predefined geometric pattern and pre-selected type of chemical modification (Maoz *et al.* 2000).

Cutting and etching of nanostructures can also be realised by an electrically biased AFM tip. The nicking principle is similar to cutting, but the applied tip bias voltage is smaller than that used in cutting, so the nanostructure is not completely cut (Park *et al.* 2002). For the electrostatic deformation and electro-hydrodynamic nano-fluid motion techniques, the current flow generated by the tip bias produces effective Joule heating, which locally softens the polymer film. The extremely non-uniform electric field gradient polarizes the viscoelastic polymer and attracts it towards the tip apex, leading to the formation of protruding structures on the film (Lyuksutov *et al.* 2003). Xie *et al.* (2005) reported an observation of nano-explosion and shock wave generation in a nanometre-

sized air/water media induced by a biased AFM probe. In this case, the electric field exceeds the breakdown strength of the dielectrics, initiating the explosive discharge of the air/water media in the tip-substrate gap. Moreover, such nano-explosions could trigger transient shock waves, which propagate parallel to the substrate surface. The propagation of the shock waves helps to significantly expand the trajectory of discharged species out of the explosion zone, thus leading to the formation of an outer ring surrounding the entire structure. Several investigations have been reported for the charge deposition and manipulation technique. For example, Crook *et al.* (2003) introduced an erasable electrostatic lithography technique based on this method. In this implementation, patterns of charges are deposited on a device surface with a negatively biased scanning probe at low temperature and in a high vacuum environment. This technique may be particularly useful for the construction of a solid state scalable quantum computer, where the required level of uniformity between quantum components is hard to achieve using other schemes.

In the next section, an overview of the state of the art in AFM probe-based nanomachining is realised given that this is the process of interest in this research.

### **2.3 AFM probe-based nanomachining**

AFM probe-based machining is one of the force-assisted AFM nanolithography techniques. As stated in the previous chapter, AFM probe-based machining has been acknowledged as a simple, reliable, and versatile scheme for the fabrication of a fairly wide range of nanoscale devices and systems (Tseng *et al.* 2009). By controlling the contact force between the AFM tip and the sample, desired nano-patterns can be created (Klehn and Kunze 1999). In particular, when implementing this process, the tip is first forced into the surface of the specimen until a specified cantilever deflection is reached.

Then, the tip is moved laterally across the surface of the processed sample according to a pre-set length, speed and direction. The main difference to AFM imaging in contact mode is that the load applied by the tip at the free end of the cantilever probe is purposely set to be large enough to induce plastic deformation on the surface of the specimen. Thus, the probe is effectively employed as a cutting tool to carry out material removal operations through chip formation or to induce plastic deformation from a ploughing action. Initial reports of research studies implementing AFM probe-based nanomachining operations were published just six years after the invention of the AFM instrument (Jung *et al.* 1992, Jin and Unertl 1992 and Kim and Dornfeld 2000). Examples of applications of the technique have demonstrated the manufacture of nanostructures for nanoelectronic (Notargiacomo *et al.* 1999 and Schumacher *et al.* 2000) and bio-sensors (Ngunjiri and Garno 2008) devices for instance.

The process can also be used to assess properties of specimen surfaces such as the scratch hardness (Beegan *et al.* 2007) or the scratch resistance of thin films (Sundararajana and Bhushan 2001). Such studies are generally only concerned with the generation of single grooves and do not focus on the process outcome from a manufacturing point of view. When AFM probe-based scratching is employed for nanofabrication purposes however, studies report the production of more complex structures such as curvilinear grooves (Bourne *et al.* 2010) or pockets machined as a result of the probe tip cutting parallel and adjacent lines (Fang and Chang 2003). Such pockets can also display complex three dimensional features by varying the load applied by the tip along the machined grooves as the work reported by Yan *et al.* (2010).

This section does not intend to provide a comprehensive review of all the studies about the implementation of the AFM probe-based nanomachining process as a number of state-of-the art review papers have been published recently to this effect by Tseng (2011), Yan *et al.* (2015) and Yan *et al.* (2016). However, it is still worth mentioning the recent efforts of a number of researchers in the micro and nano manufacturing community to address some limitations associated with AFM probe-based nanomachining. Particularly, it is known that, in its most basic implementation, only a relatively small area (i.e. generally smaller than 100 µm by 100 µm) can be processed and that relatively low cutting speeds (i.e. normally less than 1 mm/min) are reported. To tackle these issues, Bourne *et al.* (2010) and Yan *et al.* (2007) tried to enhance the machining area and speed by implementing the process with multi-axes precision motion platforms. In addition, Gozen and Ozdoganlar (2012) and Zhang and Dong (2012) attempted to increase the cutting velocity via the generation of piezoelectric-based kHz rotational lateral motions between the tip and the workpiece. Among the studies where additional piezoelectric actuators were fitted to a basic AFM instrument for enhancing the process, the work of Park *et al.* (2014) and Zhang *et al.* (2013) should also be mentioned. In particular, these researchers conducted vibration-assisted cutting with the aim of reducing the tip wear through high-frequency vertical motions generated with such actuators.

As acknowledged by researchers in the micro and nanomanufacturing community (Yan *et al.* 2015, Gozen and Ozdoganlar 2014, Tseng 2011, Fang and Chang 2003, Notargiacomo *et al.* 1999 and Zhao *et al.* 2001), the wear of the probe tip during machining operations is an important issue as it affects the reliability and repeatability of the process. Particularly, a blunt tip apex not only influences the achieved resolution but also, due to changes of the cutting edge radius and the rake angle of the tip, this leads to

changes of the cutting conditions at the interface between the tip and the material. Regarding the influence of the cutting edge radius, it is well-known in the micro machining literature that it is important for the tool to be sharp enough to ensure that cutting take place via chip formation (Liu *et al.* 2004). This is due to the minimum chip thickness effect. More specifically, this effect means that when the engagement depth of the tip into the material (which is normally referred to as the uncut chip thickness in the machining literature) is less than the minimum chip thickness, no chip can be formed through the shearing of the workpiece material. In this case, no material is removed from the processed specimen. However, provided that the applied load is large enough, ploughing of the workpiece material via plastic deformation can still take place. In particular, the ploughing regime is characterised by some of the workpiece material being pushed out on the edges of a machined groove and some being compressed under the tip and recovering back after the tip passes (Elkaseer and Brousseau 2014). A number of methods have been investigated by researchers in the micro machining area to estimate the normalised minimum chip thickness for a given material (Elkaseer and Brousseau 2014). These are beyond the scope of this review. However, it is worth stating that the minimum chip thickness value is normally expressed as a percentage of the cutting edge radius of a tool depending of the material processed (Liu *et al.* 2006). Thus, it is obvious that blunting of the tip through wear during AFM probe-based machining could affect the machining conditions via a transition from cutting with chip formation to ploughing.

Thus, in the specific context of employing AFM probe-based machining for fabrication purposes, it is somewhat surprising that investigations focussing on the study of the wear of the tip as a function of processing conditions are relatively scarce. To the best knowledge of the author, such studies have only been reported on a few occasions

by Zhao *et al.* (2001) and Gozen and Ozdoganlar (2014). Zhao and co-workers studied the wear of a diamond tip when machining polished single crystal silicon. The characterisation of the worn tip was performed by scanning it with sharper AFM probes at different stages of the machining process. The experimental data were used to compute the wear rate of the diamond tip and to observe the evolution of the depth of the generated cavities as a function of the machining time. In particular, it was found that this depth gradually decreased under constant applied force. This was attributed to the fact that, as the tip wear increases over the machining time and thus, the tip radius becomes larger, the contact stress between the tip and the silicon surface decreases. In the study from Gozen and Ozdoganlar (2014) wear measurements were also performed for diamond AFM probes, which were employed to process single crystal silicon. This study enabled the authors to quantify the volumetric wear and to analyse its evolution as a function of the length of cut. As shown in Figure 2.4, a fast initial wear occurred during the first few millimetres of processing and this was followed by a slower linear wear increase until a sudden blunting of the tip after about 30 mm of machining. The reported experimental study also investigated the repeatability of the wear behaviour between different AFM probes from the same manufacturer under identical processing conditions. Interestingly, the observed results showed a large variation of the initial wear in the first few millimetres of cutting. This was attributed to possible variations in the crystallographic structure around the apex of the tip leading to variable initial wear behaviour, which is likely to be characterised by a sudden breakage of the tip.

The analysis of the literature reported above reveals that, despite the increased attention on AFM probe-based machining, the study of the wear of tips, when employed as nano-scale cutting tools, remains an area where further research is required.

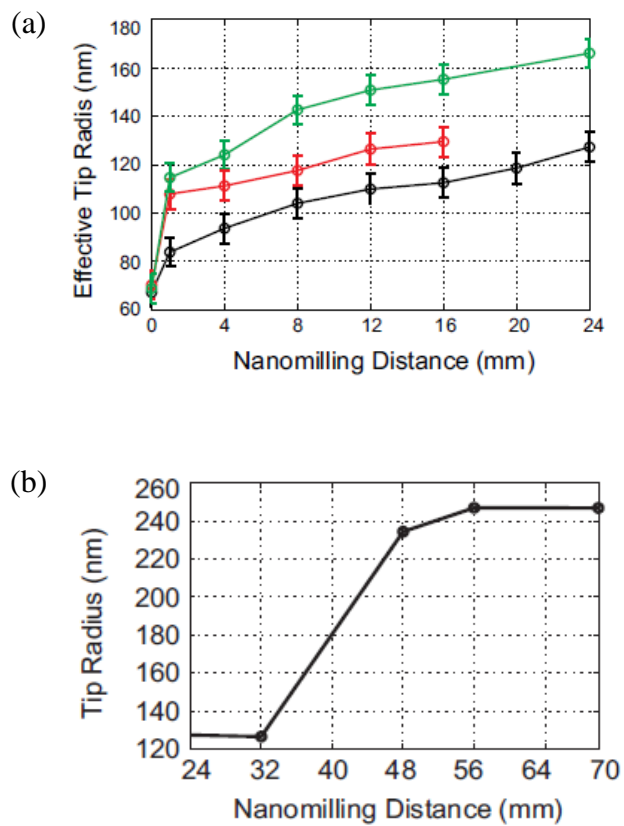


Figure 2.4: (a) Rapid initial wear followed by a slower linear wear and (b) sudden blunting of the tip (from Gozen and Ozdoganlar 2014).

In particular, the influence of different machining parameters, such as the machining direction, force applied and tip material, on the wear of AFM tips has not been the focus of systematic experimental studies. Thus, the main objective of the research reported in this thesis aims to provide additional research data and analysis towards the establishment of a more comprehensive understanding of the process factors contributing to the wear of AFM probes study. To achieve such aims, implementation of an effective and reliable technique for the characterisation of the shape of the tip apex becomes a key enabler. For this reason, the next section will provide a review of such characterisation techniques.

## 2.4 AFM tip characterisation techniques

When an AFM instrument is employed for its primary purpose, i.e. as a microscope for imaging the surface topography of specimen at nano-scale, it is widely recognised that assessing and understanding the wear of AFM tips is of primary importance. This is due to the fact that tip wear can strongly affect the quality of the imaging results. Therefore, numerous researchers have acknowledged the importance of acquiring and examining tip apex data accurately and efficiently. Liu *et al.* (2010), reported that typical silicon and silicon nitride AFM probes underwent significant shape change even under the sole action of adhesive forces. Therefore, it is natural to anticipate that, in the case of AFM probe-based nanomachining, the tip may suffer significant wear. Indeed, the applied loads are typically comprised between a few  $\mu\text{N}$  to a few tens of  $\mu\text{N}$ . In comparison, these are about 1000 times larger than those used for typical AFM imaging in contact mode (i.e. a few  $\text{nN}$  to a few tens of  $\text{nN}$ ). A relatively large number of studies have been reported in the literature for assessing the wear of AFM tips. The measurement techniques employed to extract geometrical data about the tip apex can generally be categorised into two groups, namely in-situ and ex-situ techniques. The in-situ techniques employ instrumentation or

set-ups that can be utilised on an AFM system, while ex-situ measurements rely on methods which cannot be conducted on an AFM instrument.

### **2.4.1 In-situ techniques**

There is a wide range of in-situ techniques for AFM tip characterisation. Some of them take advantage of the convolution effect. As illustrated in the next section, this effect is associated with the fact that the probe geometry determines the resolution of AFM imaging (Gan 2009). Particularly, it is a well-known fact that the tip geometry will be convoluted with the shape of the sample (Pelz and Koch, 1990 and Montelius and Tegenfeldt, 1992). This effect provides an opportunity to characterise an AFM tip apex by scanning the probe over specific features such as sharp pin-like asperities, pillars and holes. The blind tip reconstruction technique is another in-situ characterisation approach, which takes advantage of the convolution effect (Montelius *et al.* 1993). In addition, several reports investigated the characterisation of the tip apex by employing an ultra-sharp tip as a probe. In this case, the assessed tip is positioned on the AFM stage with its apex facing upward toward the ultra-sharp tip. A number of indirect, but still in-situ, techniques also proposed to apply wear indices and adhesion tests to assess the condition of AFM probe tips. The following sub-sections provide further description about each of these in-situ techniques.

#### **2.4.1.1 Scan of specific features**

Many studies reported the direct imaging of the tip shape (also known as reversed imaging or inverse AFM mode) by conducting an AFM scanning operation over specific structures with the tip to be assessed left in position in the AFM head. Westra *et al.* (1993) presented a study on tip artefacts obtained when scanning AFM images of thin films as

shown in Figure 2.5(a). Particularly, the scanned films had asperities with a radius quoted as 160 Å to 300 Å. In this way, the authors estimated the radius of the AFM tip apex by assuming that the end of the tip was spherical. Thus, the approximate radius of curvature of the probe tip could be found by calculating the radius of a truncated sphere with the same height and width of the features of the thin film surfaces. Similarly, Neto and Craig (2001) described a method making use of reverse AFM imaging to characterise the tip apex. In this case however, a spherical colloid particle was attached to the tip. Thus, the objective for these authors was to characterise the colloid probe. To achieve this, the probe was scanned over a commercially available test structure displaying sharp pin-like asperities (model TGT01 from ND-MDT) (see Figures 2.5 (b) and (c)). As illustrated in Figure 2.5(c), this structure consists of an array of sharp asperities in silicon with full cone angles less than 30° and with radii of curvature less than 10 nm. Following the scan, the author used the same technique as Westra *et al.* (1993) to estimate the radii of the AFM probe. In addition, SEM micrographs were also used to act as references. The radii obtained with the reverse imaging method were found to be in good agreement with those obtained from the SEM images. In particular, the difference in the radii measured with the two techniques was approximately 4%.

Bloo *et al.* (1999), Bushan and Kwak (2007) and Bykov *et al.* (1998) also presented work that characterised the AFM probe tip by scanning over the same commercial test structure made of sharp pin-like asperities. Bloo *et al.* (1999)'s study, the test structure displayed an array of sharp tips where the cone angle was 20°, instead of 30°. Both types of samples are commercially available and thus, are easy to acquire for AFM practitioners. Bykov *et al.* (1998) noted that scanning the tip over such structures provided an inverted image of the tip itself, and therefore that it was a mirror transformation of the

real tip shape. As in the case of Bloo *et al.* (1999) and Bushan and Kwak (2007), the obtained three-dimensional data were also used by Bykov *et al.* (1998) to calculate the wear volume. More specifically, Bloo *et al.* (1999) estimated the wear volume by using the Archard wear equation. In the case of Bushan and Kwak (2007), the wear volume was estimated by assuming that the probe had a conical shape. The assumption has certain limitation because AFM probes tend to be asymmetric (Allen *et al.* 1992 and Gruter *et al.* 1992). Asymmetries can be easily detected even for specimens only a few nanometres tall (Vesenka *et al.* 1993). Maw *et al.* (2002) also used a similar array of sharp spikes as in Figures 2.5(b) and 2.5(c). The tip images were used by these authors to determine the area of the worn tip by counting the number of pixels at a series of height increments above a set baseline.

Sheiko *et al.* (1993), Montelius and Tegenfeldt (1993), Atamny and Baiker (1995) and Bao and Li (1998) also implemented the reversed tip imaging method by scanning specific sharp structures. The difference, in comparison with the studies reported above, is that these authors fabricated their own specific samples in order to characterise the tip apex. Montelius and Tegenfeldt (1993) prepared their samples using aerosol-produced metal particles that were deposited on the sample surface in a subsequent ECR (electron cyclotron resonance) plasma. Sheiko *et al.* (1993) utilised a nanometre-scale stepped surface of a SrTiO<sub>3</sub> crystal. Atamny and Baiker (1995) prepared samples with spike-like protrusions present on copper films deposited on quartz by metal organic chemical vapour deposition (MOCVD) (see Figure 2.6). Bao and Li (1998) used hydrothermal deposition to prepare a ZnO thin film, which exhibited a large number of sharp crystallites oriented normal to the substrate. Sheiko *et al.* (1993), Bao and Li (1998) and Montelius and Tegenfeldt (1992) agreed that such sharp pin-like structures are suitable for imaging the

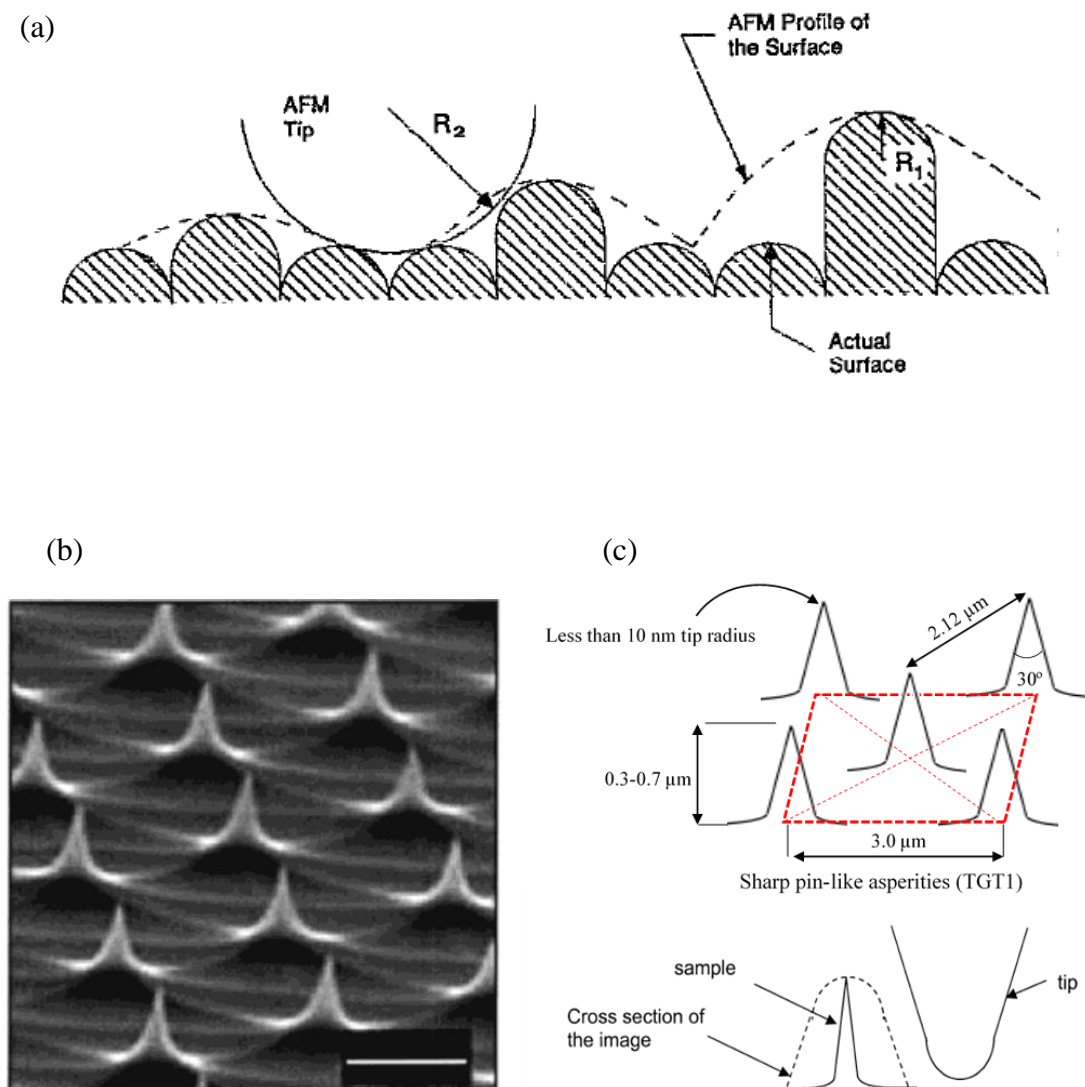


Figure 2.5: (a) A simulation of an AFM tip scanning over a columnar thin film surfaces (from Westra *et al.* 1993), (b) a scanning electron microscope image of the silicon grating TGT01 model from NT-MDT (Neto and Craig, 1995), (c) schematic of the principle for the AFM probe-based characterisation method using sharp pin-like asperities (Bloo *et al.* 1999).

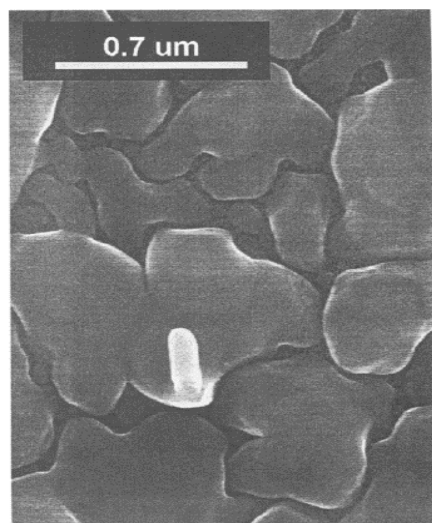


Figure 2.6: SEM micrograph of copper thin film prepared by MOCVD showing a pin-like structure with a height of more than 300 nm and a radius of less than 120 nm (from Atamny and Baiker 1995).

AFM probe to gain information about the tip geometry. Atamny and Baiker (1995) confirmed this by observing the shape of the tip profile using three different cross-sections from the scanned data and showing that the results from all profiles were similar. However, these authors also pointed out that the effectiveness of using the convolution effect for this purpose depends on the sharpness of the specific feature scanned.

The above studies show the advantage of using the reverse tip imaging technique to obtain two- and three dimensional data of the tip apex. Implementing this technique can be relatively straight forward particularly if a commercial test structure is already available to AFM users. In subsequent analyses, the data obtained in this way can be exploited based on qualitative and/or quantitative approaches to assess the tip condition. In addition, the method appears relatively fast to implement as there is no need to remove the tip under investigation from the AFM head. Another advantage related to this method is that such an approach should be less prone to lead to tip damage, which may otherwise result from probe handling operations.

It is also worth mentioning that employing colloidal particles is another approach, which has been used by researchers to implement the in-situ reversed imaging technique. In particular, Vesenka *et al.* (1993) conducted an experiment where colloidal gold particles (see Figure 2.7(a)) were imaged by the AFM tip to be assessed. Specifically, the nominal diameter of the used particles was between 10 nm to 24 nm. The spherical and incompressible nature of the particles could be exploited effectively to characterise the tip geometry. This could be seen from the experimental data reported in this study as the obtained tip radius measurements between the spherical particles and TEM profile images of the probe showed an excellent agreement. In this study, a simple 2D geometric

relationship was used to relate the scanned width and height of the particles with the radius of the tip. From the TEM profile, the radius of the tip was estimated by superimposing a sphere on the tip image. Similarly, in the study from Miller *et al.* (1995), the tip profile was assessed using colloidal gold particles. The diameter values of these particles were between 10 nm and 20 nm so almost similar to those used by Vesenka *et al.* (1993). A mathematical model was developed and a solution was proposed to enable the 3D reconstruction of the tip geometry based on the scanned data. The reconstructed tip was superimposed over a TEM image of the same tip in order to examine the accuracy of the extracted profile. The agreement was seen to be good to within a nanometre except near the edge of the reconstructed tip. The authors noted that the accuracy of the probe reconstruction method depends on the image noise and numerical derivative approximations.

In a similar way, Odin *et al.* (1994) proposed that the tip apex radius of curvature and its cone angle could be obtained by scanning the probe over a monolayer of rigid latex balls. The used latex balls mean diameter was 176 nm with a standard deviation of 2 nm. To obtain the tip radius, the ball dimension was required. This study assumed two different types of tip geometries: a conical tip with spherical apex and a parabolic tip. A formula was presented to estimate the tip radius. The author suggested that the half-angle of the tip should be known before estimating the tip radius. Hence, when implementing the proposed method, the authors discovered that the radius measurements would be influenced by noise errors caused by the quality of the tip and the scanned image.

Other types of specific features have been used to implement the reverse tip imaging approach. Griffith *et al.* (1991), Grigg *et al.* (1992) and Griffith and Grigg (1993)

measured the geometry of AFM tips by extracting their shape from the scan of pillars displaying a slight undercut (as shown in Figure 2.7 (b)). This undercut ensured that an obtained profile reflected the tip apex shape as it travelled down the side of the pillar during scanning. Griffith and Grigg (1993) showed that the shape of the imaged profiles along the undercuts corresponded well to the shape of the tip when observed with an SEM instrument. In order to measure the total width of the probe, the width of the scanned pillar must be known in advance and thus, determined by other means. According to the authors, sources of error with this approach come from the quality of the pillars. In particular, the roughness on the top of pillars could produce waviness on the edges of the pillar. In comparison with imaging very sharp asperities, such features require more complex post-processing of the scanned data to reconstruct the probe tip image.

Finally, Glasbey *et al.* (1994) estimated the tip profile by scanning a wide range of holes present on various samples made off polyethylene glycol methacrylate copolymers. These holes had walls which were steeper than the angle of the tip. From the scanned data, tip radii were assessed using the radius of curvature formula and the tip angle could be estimated by measuring the slope of the scanned hole profiles.

#### **2.4.1.2 Ultra-sharp tip scan technique**

With this technique, the tip itself is used as the inspected sample. In this case, the AFM probe is removed from the head of the AFM instrument and positioned on the stage with its tip facing up so that its apex can then be scanned by a sharper tip. Khurshudov and Kato (1995) and Khurshudov *et al.* (1996) were the first to use this principle to analyse the wear of an AFM probe. However, the tip employed in their studies was of the same type as the probe under investigation. Thus, these authors did not use the ultra-sharp

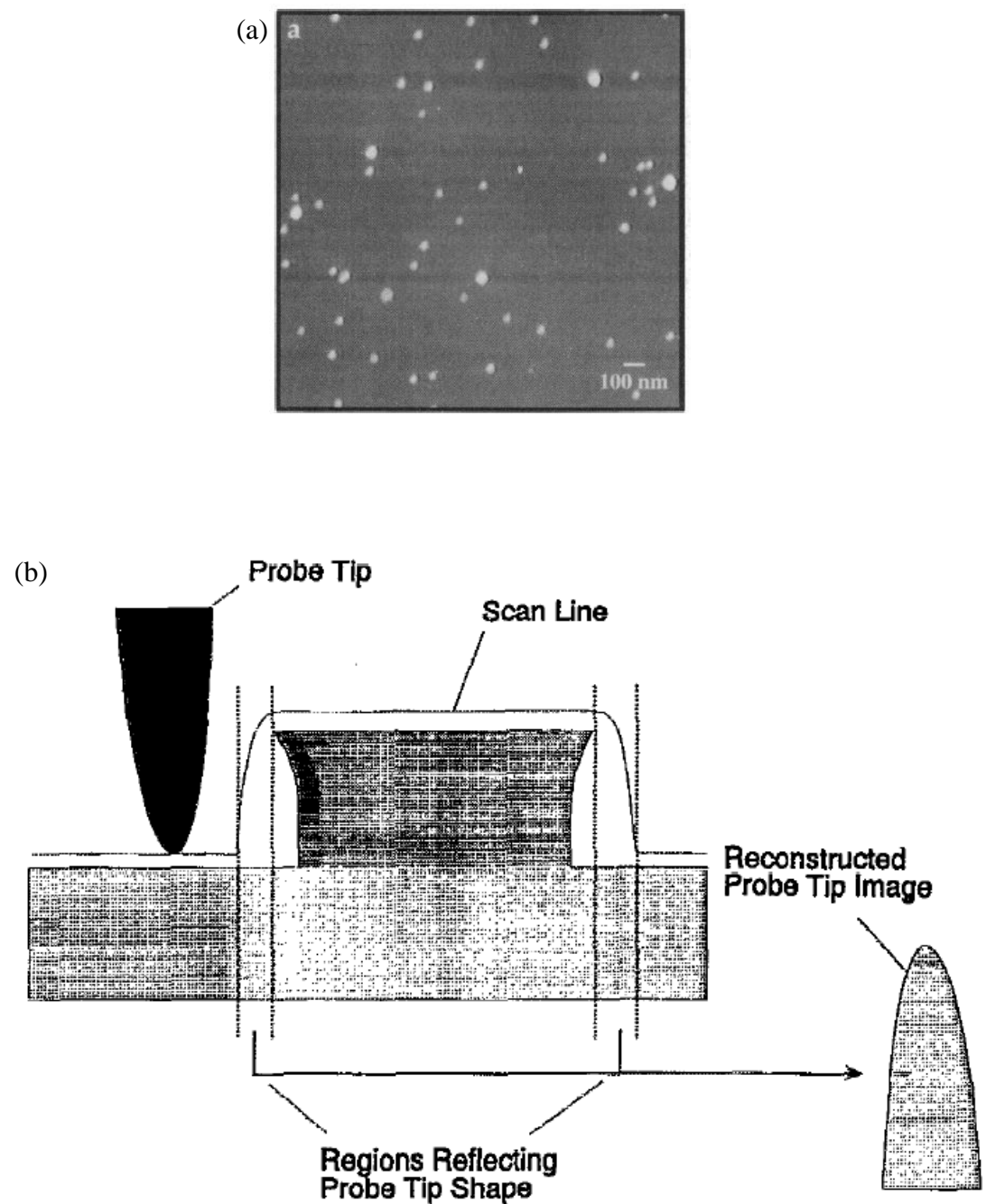


Figure 2.7: (a) Colloidal gold particles imaged with a commercial AFM probe (from Vesenka *et al.* 1993) and (b) schematic diagram of the structure used by Griffith and co-workers for characterising probe tips (from Griffith *et al.* (1991)).

tip approach in the strict sense of the term. Nevertheless, signs of wear on the inspected probe could still be observed although the authors did acknowledge that the data may be partly affected by the tip convolution effect (Khurshudov and Kato, 1995). In another study by Khurshudov *et al.* 1996), such direct tip imaging technique was employed to superimpose and compare cross sectional profiles of AFM tips between their unused and their worn states. In this way, the wear volume could be estimated. In addition to using the direct tip imaging, the authors also monitored the wear from the decrease in scratch depth, when processing a silicon sample, with the increasing number of cycles.

The ultra-sharp tip approach was used by Gozen and Ozdoganlar (2014). The inspected tip was measured using a commercially available ultra-sharp tip (see Figure 2.8). In this work, the condition of ultra nanocrystalline diamond AFM tips were characterised at different stages of so-called “nanomilling” operations. Data about the 3D geometry of such probes was extracted through non-contact AFM measurements performed by the ultra-sharp tip. The obtained data were used to determine the progression of the tip wear by assessing four different metrics, namely the wear volume, the wear area, the tip radius and the change in tip height after different machining distances. The scanned 3D AFM image for a given diamond probe was first aligned with its 3D topography obtained prior to the start of the machining operation, i.e. in its unworn state. The volume of a worn tip was calculated through the discrete integration of the heights of its 3D coordinates of points, obtained from the ultra-sharp tip scan, within a given region. The worn volume was estimated by subtracting this volume from the volume of the unworn tip bounded by the same region. To determine the tip radius at any stage of the experiment, cross sectional height data sets were extracted within a predetermined apex region. Subsequently, a sphere was fitted to this profile data using a

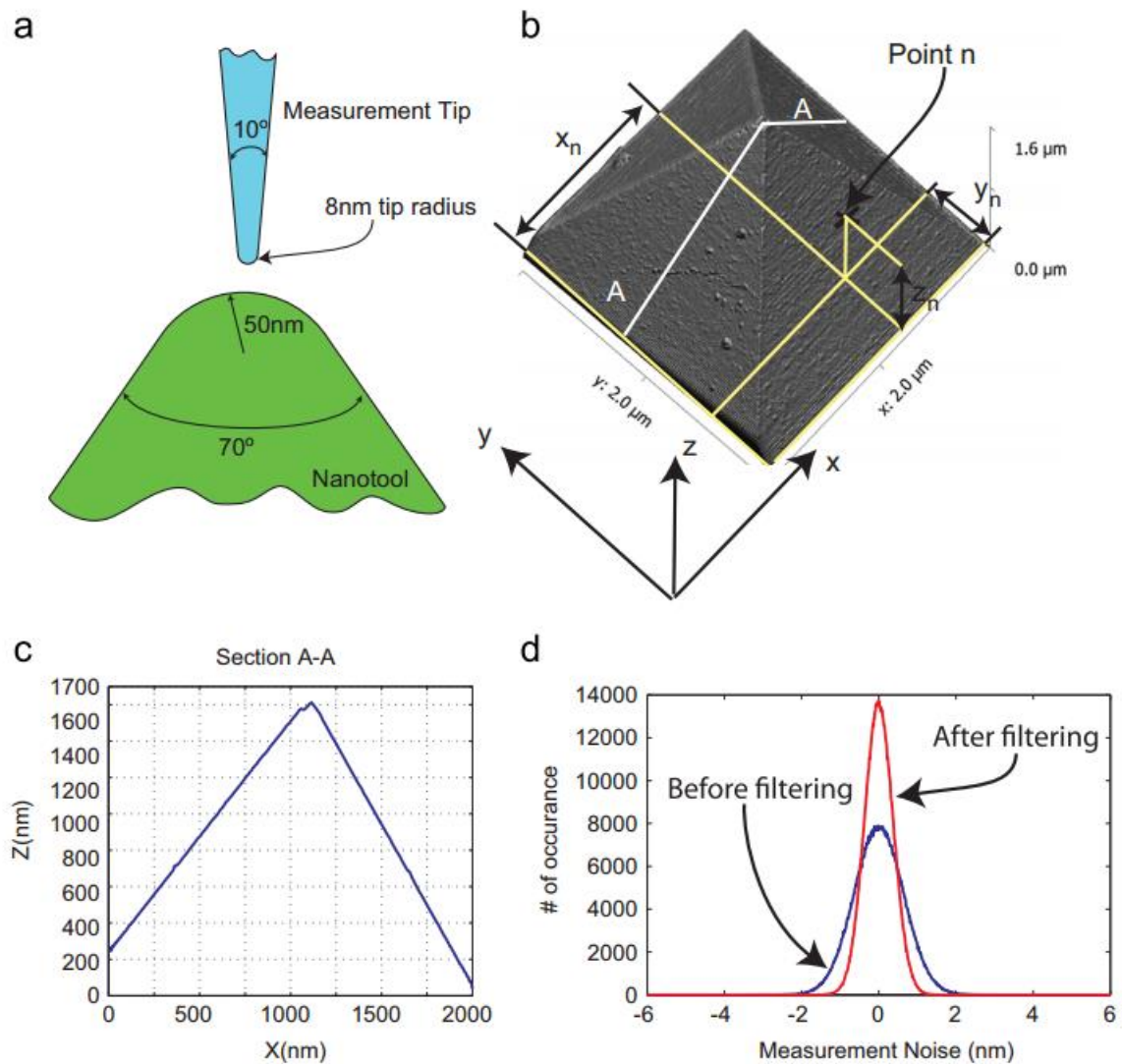


Figure 2.8: (a) Illustration of the AFM tip characterisation technique using an ultra-sharp tip, (b) an example of a 3D AFM image obtained (c) a cross-sectional AFM image extracted from the 3D data (from Gozen and Ozdoganlar 2014).

least-square approach and the tip radius was determined to be equal to the radius of the fitted sphere.

#### 2.4.1.3 Blind tip reconstruction

The blind tip reconstruction (BTR) method is a technique established by Villarubia (1994). BTR allows the determination of an outer envelope that describes the tip geometry from the AFM image data of the roughness of a surface obtained by scanning the tip over it without a priori knowledge of the surface actual geometry. The derivation of such an outer bound by this method may closely approximate parts of the tip that were in contact with the surface during the scanning process (Villarubia 1996).

Dongmo *et al.* (2000) carried out an experimental investigation to characterise AFM probes using the BTR technique. In this study, two different probes were tested. One of them had a relatively smooth shape and the other displayed a more complicated profile. In this work, SEM scans of the probe tips were also performed. These profiles were used as a reference against the cross sectional profiles of the tips extracted from the BTR data. Based on a qualitative analysis, it was shown that the SEM and BTR profiles agreed well within about 600 nm from the apex. Outside this range, the BTR results overestimated the tip envelope. In this study, the obtained data were also used to calculate the tip radii. This was done by finding the parabola  $y = x^2/2r$  that best fitted the profile near the apex where  $r$  is the radius.

Liu *et al.* (2010) performed experiments to analyse the nanoscale wear of AFM tips. Four types of commonly used and commercially available AFM probes were scanned on an ultra nanocrystalline (UNCD) sample surface in contact mode under adhesion forces

alone. Figure 2.9 shows the obtained AFM scans for different tips at various stages of wear. These authors used the BTR technique along with TEM observations and pull-off force measurements. The extracted BTR profiles were compared against TEM profiles of the same tips (as shown in Figure 2.10). Similarly, to the findings reported by Dongmo *et al.* (2000), a good agreement was found close to the tip apex but not for the whole tip profile. The data extracted from the BTR technique were also used to assess the tip radii and also to calculate the volume loss wear. In this case, the tip volume was calculated by assuming that the tip could be described by a stack of circular disk-shaped elements with a diameter equal to the measured tip width.

Wan *et al.* (2014) presented a theoretical study with the aim of investigating the sources of errors that resulted from implementing the BTR technique in practice. This study was motivated by the recognition that BTR can lead to a reconstructed tip envelope that exhibits large errors if the scanned surface, or tip characteriser, used is not appropriate. Among the different recommendations made in this study, it was noted that the cone angle of the features used as tip characteriser must be smaller than the cone angle of the tip to be reconstructed. In addition, the authors advised that the height of the features on the tip characteriser should be higher than the height of the region of interest to be reconstructed from the tip apex.

In addition to some limitations of the BTR technique mentioned above, according to Yan *et al.* (2016), the method is very sensitive to spikes in the data (i.e. noise). These may occur during the imaging process as a result of external interferences and the scanning parameter settings. These authors reported that these spikes lead to an underestimated tip radius.

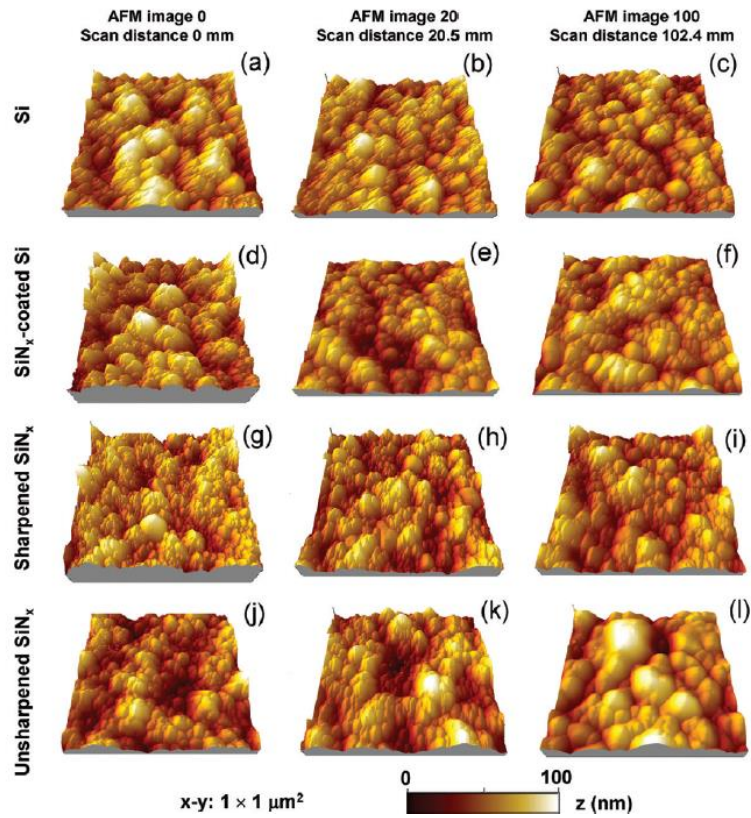


Figure 2.9: AFM topography images of the ultra nanocrystalline UNCD surfaces acquired by (a-c) a Si tip, (d-f) a SiNx-coated Si tip, (g-i) a sharpened SiNx tip, and (j-l) an unsharpened SiNx tip (from Liu *et al.* 2010).

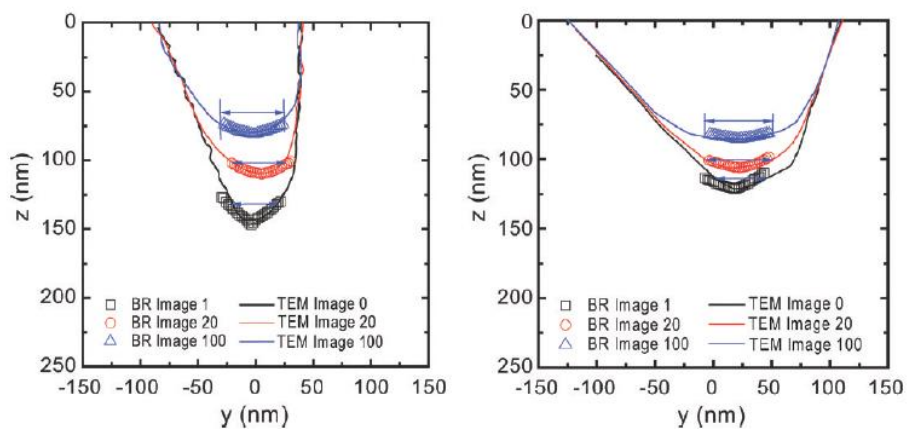


Figure 2.10: Comparison of the tip profiles measured by TEM and blind reconstruction (“BR”) for (c) the SiNx-coated Si probe and (d) the unsharpened SiNx before use, after acquiring 20 images, and after acquiring 100 images (from Liu *et al.* 2010).

#### 2.4.1.4 Wear metrics

A number of other approaches can be implemented on an AFM instrument to assess the tip wear. However, these do not lead to the direct extraction of geometric information from the tip. Instead, these approaches enable the assessment of different wear metrics, which can still be used to evaluate the condition of an inspected tip.

Cheng *et al.* (2011) developed a method, which requires the utilisation of an acoustic transducer mounted on the top of an AFM tip. The principle of the technique is illustrated in Figure 2.11. It relies in the transmission of acoustic waves to the AFM tip at GHz frequencies. Thus, tip bluntness was determined by monitoring the shift in the resonance frequency in comparison with the resonance frequency value of an unworn tip. This technique enables the in-situ and non-contact monitoring of nanometre changes at the tip end. However, in order to implement this approach in practice, the main drawback is that the tip needs to be fabricated on a thin piezoelectric membrane and thus, standardised and commercially available probes cannot be used in this case.

Bhaskaran *et al.* (2010) studied the wear of ultra-sharp tips made of diamond-like carbon with silicon when sliding them on a SiO<sub>2</sub> surface using applied loads less than 20 nN, which are typical loads for AFM imaging in contact mode. To assess the tip shape, adhesion tests between the tips and the surface were performed. In this case, an increase in adhesion corresponds to an increase in the contact area between the tip and the substrate. Thus, measuring the force required to pull the tip off the surface can be used as an indicator of wear. In the reported experiments, the authors observed a tip wear rate of one atom per micrometre of sliding. Using the obtained experimental data, these authors were also able to demonstrate that the classical wear law of Archard did not describe

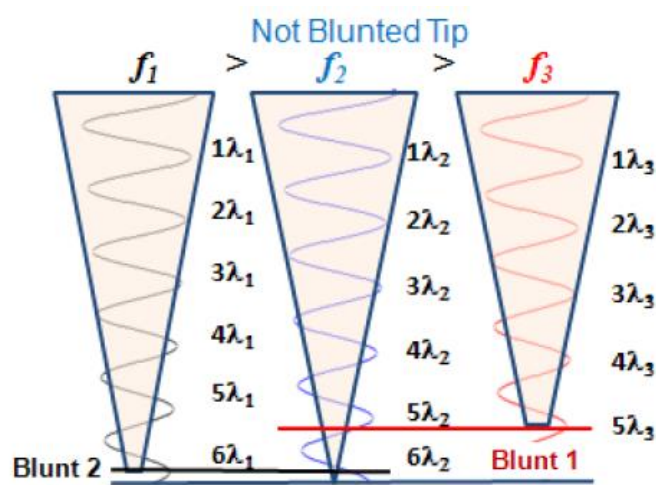


Figure 2.11: Illustration of the method employed by Cheng and co-workers. Depending of the degree of tip bluntness, an increase or decrease in the resonance frequency of the transmitted acoustic waves may be detected (from Cheng *et al.* 2011).

appropriately the tip wear at such small scale and for such small values of applied load. Instead, they suggested that atom by atom attrition dominated the wear mechanisms. Prior to this study, Gotsmann and Lantz (2008) also used such adhesion tests to study the wear of sharp silicon tips when sliding on a polymer surface at relatively low loads (i.e. between 5 nN and 100 nN). These authors also observed that Archard's law did not fit the experimental data obtained.

Schmutz *et al.* (2010) proposed to measure changes in the resonance frequency of the oscillating AFM probe and to relate this frequency shift to a change in mass of the tip. This idea was implemented using different combinations of probe and sample materials used to carry out scratching experiments. In particular, colloid probes were employed in this study, which consisted of small spheres of a few micrometres in diameter attached to the tip. According to the authors, with this approach it is possible to measure the increase or decrease of the tip mass down to a few picograms.

Huang *et al.* (2013) studied the effect of different scanning parameters on the tip wear when operating the AFM instrument in tapping mode. In this work, Si and diamond-coated Si probes were used. The specimen scanned was a commercially available sample specially designed for assessing the condition of AFM tips as it displayed shallow but sharp nanostructures on its surface. Based on the AFM topography data obtained by scanning these samples, the arithmetical mean roughness ( $R_a$ ) was extracted. The evolution of the calculated  $R_a$  values as a function of the tip scanning time was considered as a tip-wear index. The blind tip reconstruction method was also applied to the AFM scans to estimate the diameter of the probe. A good correlation was found between the variations in the diameters of the tip and of the  $R_a$  values as a function of the scanning

time. Based on this, the authors indicated that the assessment of the Ra metric could be considered as a possible tip-wear index.

### 2.4.2 Ex-situ measurements

In the context of characterising and assessing AFM tips, ex-situ measurement techniques are defined as those where the probe needs to be removed from the AFM instrument such that the tip can be inspected with another microscopy method. In all cases, ex-situ measurements are realised using an electron microscopy approach, either SEM, transmission electron microscopy (TEM), Scanning TEM (STEM) or high resolution TEM (HRTEM). It is evident from the literature that numerous studies used ex-situ techniques for characterising AFM probes. Such studies used electron microscopy techniques either on their own or as a way to confirm the reliability of the data obtained with an in-situ method. In this section, a few examples of such studies are reported and the advantages and limitations of using electron microscopy are discussed.

Bloo *et al.* (1999) used an SEM instrument to obtain qualitative and quantitative information on the geometry of AFM tips as shown in Figure 2.12. Qualitative data which can be observed from SEM inspections include contamination of the tip for instance. In the study by Bloo *et al.* (1999) adhesive wear was reported as shown in Figure 2.12 (b) where extra material can be observed around the tip apex. The authors claimed that such contamination could not be detected without the utilisation of electron microscopy. Along with the completion of adhesion tests, Gotsmann and Lantz (2008) also used an SEM equipment to analyse the effects of tribochemical wear of silicon tips when scanned on a polymer surface. Other examples of investigations of AFM probe wear using SEM can be found in the work from Chung and Kim (2003) and Pugno *et al.* (2009) for instance.

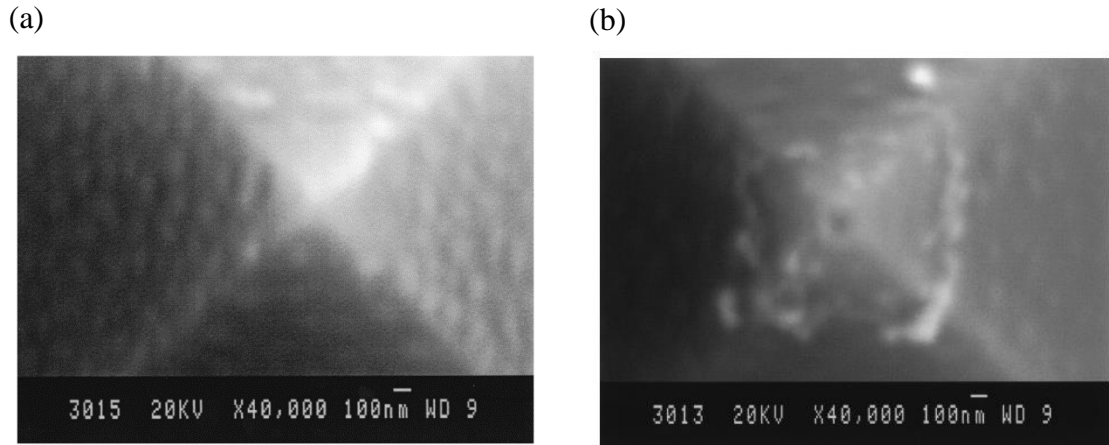


Figure 2.12: (a) SEM image of the tip before the wear experiment and (b) SEM image of tip after the wear experiment (from Bloo *et al.* 1999).

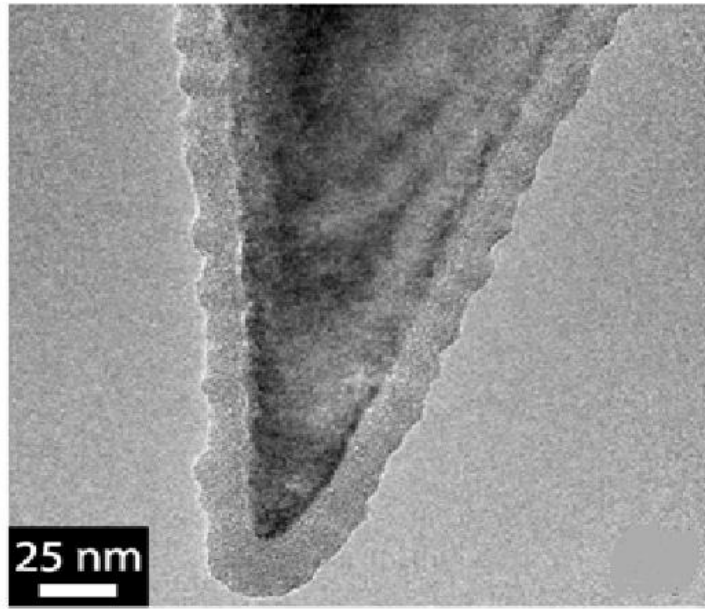


Figure 2.13: A TEM image demonstrating the contrast between the thin coating of diamond-like carbon and the single-crystal silicon probe underneath (from Jacobs *et al.* 2015).

Particularly, the profiles of the tips before and after sliding tests were analysed in these studies.

As mentioned above, another electron-based microscopy technique used to analyse and characterise the AFM tip apex is TEM. TEM micrographs can show regions of a specimen with different contrasts as a result of differences in composition (atomic number) and crystal structure between those regions as illustrated in Figure 2.13. Imperfections or small pieces of contamination on the side of a probe can also be easily observed using TEM inspection. Jacobs *et al.* (2016) used both SEM and TEM to determine and analyse the geometry of AFM probe tips. In a previous study involving adhesions tests realised with AFM probes, the same authors recreated the 3D profiles of tips from their 2D profiles obtained with HRTEM (Jacobs *et al.* 2015). To do this, the authors had to assume that the observed tips had circular profiles at each resolved height increment. Based on the analysis of TEM images of tips obtained at different tilt angles, the authors reported that this was a reasonable assumption in the context of their study as they restricted their observation within a region less than 10 nm from the tip apex, which is where the adhesion forces took place. Liu and Chen (2011) also examined AFM probes using a combination of TEM and SEM depending on the resolution required. Changes in tip profiles before and after AFM scan tests were analysed by overlapping pre-scan and post-scan images of the same probes at the same magnification and at the same viewing angle.

Chung *et al.* (2005a) also used HRTEM images to characterise AFM tip profiles. The main purpose of this work was to understand the nature of silicon tip wear when sliding such tips on DLC and silicon surfaces for applied loads comprised between 10 nN

and 100 nN. The authors assumed that the Archard's wear law held true for their study and thus, they aimed to calculate the wear coefficient from Archard's wear equation. This required the estimation of the worn volume of the tips. Regrettably, the authors did not describe how this volume was calculated from the HRTEM data.

An important advantage of employing an ex-situ electron microscopy approach is that direct imaging of the tip can be realised. In the case of TEM or HRTEM, this can be achieved to a very high degree of resolution, down to the atomic level and thus, enabling the lattice structure to be observed. With this approach, it is also straight-forward to inspect if there is any extra material on the tip and thus, to determine if the probe suffered from contamination during experiments. However, due to the ex-situ nature of using electron microscopy, there is an increased risk of tip damage as a result of having to remove the probe from the AFM instrument. Another drawback of electron microscopy is that SEM and TEM images provide only two dimensional data for the inspected tips. Thus, assumptions have to be made when recreating the 3D volume of the tip. Nevertheless, such electron-based approaches appear essential as a tool to complement and confirm the validity of in-situ techniques, particularly in the initial stage of implementing a given or novel in-situ method.

## 2.5 Summary

As highlighted in section 2.3, despite the importance of tip wear in the specific context of AFM probe-based nanomachining, research in this area is still relatively scarce. Although a number of tip wear studies have been reported when a tip was used to perform scratching against a surface, these studies did not focus particularly on the process from a nano-scale machining point of view. Thus, these do not address some of the practical

issues that face AFM users when implementing AFM probe-based nanomachining. In particular, some of the knowledge gaps that still exist in this area are as follows:

- It is not clear whether the tip wear may vary significantly as a function of different nanomachining parameters and particularly, as a function of the tip material, machining direction and applied load. This represents the overarching theme for this research and is considered in Chapters 3, 4 and 5.
- The estimation of the radius of AFM tips is a commonly employed metric in tip characterisation studies. However, in the context of using an AFM probe for the controlled removal of material from the surface of a workpiece, no study has been devoted to analysing the information content of such a metric. Thus, it is not clear whether radius measurements are reliable for determining the condition of AFM tips when used to machine a workpiece. For this reason, radius measurements will be conducted in Chapters 3, 4 and 5 with the aim of providing sufficient experimental evidence to confirm or reject the suitability of tip radius data during AFM tip-based nanomachining.
- Despite the limitations of electron microscopy techniques, these still appear to be a very important tool to assess the conditions of AFM probes. However, when recreating the 3D volume of a tip from the 2D profile of a SEM or TEM image, the assumption that a tip is made of a stack of circular disks may be seen as too simplistic. Rather, it should be better to describe the tip as a stack of frustums of right circular cones. This alternative representation will be investigated in Chapter 3.
- For monitoring the conditions of AFM probes in practice, the literature review indicates that the implementation of an in-situ technique still appears to be a more

preferable solution over an ex-situ approach. This is due to the fact it can result in the acquisition of 3D data, while enabling all operations to be conducted within a unique instrument, i.e. the AFM system itself. However, the identification of the best in-situ 3D measurement techniques in terms of accuracy and practical suitability when implementing AFM probe-based nanomachining represents a line of research that needs systematic investigations. This aspect is considered in Chapter 5.

Based on the knowledge gaps reported above, the common focus of Chapters 3, 4 and 5 is on analysing the influence of different parameters on the wear of various types of AFM probes during tip-based nanomachining operations. For each chapter, different methods are used to characterise the AFM probe geometry. More specifically, in Chapter 3, the tip apex of Si probes is characterised using only scanning electron microscopy. In this chapter, three wear metrics, namely the tip radius, the area loss and the volume loss are extracted from the 2D SEM data and estimated as a function of the machining distance, the machining direction and the applied force. Next, the objective of Chapters 4 and 5 is to analyse the influence of these parameters on the wear of diamond-coated Si probes during tip-based nanomachining. In both chapters, the radius and volume wear loss are estimated based the acquisition of 3D data from the tip apex. In particular, for Chapter 4, the ultra-sharp tip scan approach is employed for this purpose while for Chapter 5, both the ultra-sharp tip scan and reverse imaging techniques are utilised. This also allows to conduct a comparative study about the reliability of these in-situ approaches in this chapter. Analyses of the topography of the machined grooves are also carried out in all three chapters in order to gain further insight into the machining regime that

occurred during the experiments. Finally, Chapter 6 presents the conclusions, contributions and proposed future work from this research.

**CHAPTER 3:**

**ASSESSMENT OF WEAR FOR AFM SILICON**

**PROBES USING TWO DIMENSIONAL TIP**

**PROFILE DATA**

## CHAPTER 3

# ASSESSMENT OF WEAR FOR AFM SILICON PROBES USING TWO DIMENSIONAL TIP PROFILE DATA

### 3.1 Overview

From the literature reviewed in Chapter 2, it was identified that there has been no detailed experimental study so far about the influence of different parameters on the wear of AFM probes during tip-based nanomachining. Thus, the motivation for this chapter is to conduct such an investigation when employing AFM probes having silicon tips to machine a relatively soft workpiece material, namely single crystal copper. Such probes are widely used for scanning the surface topography of samples with an AFM instrument. Thus, the study conducted in this chapter also aims to assess to which extent this type of probes may be used in the context of AFM tip-based nanomachining. In addition, silicon tips tend to be sharper than those made in silicon nitride ( $\text{Si}_3\text{N}_4$ ) and those that are coated with diamond. Therefore, this characteristic is of potential interest with respect to the obtained resolution of the process. To achieve this aim, the characterisation of the two-dimensional (2D) profile of a number Si tips was performed on geometric data acquired by Scanning Electron Microscopy (SEM).

Another objective for this chapter is to propose the utilisation of a novel and simple method for improving the accuracy of the tip wear assessment procedure when conducted on 2D profiles. The remainder of the chapter is organised as follows. First, the experimental set-up and methodology are described. In particular, the selected machining

parameters and the rationale behind their selection is explained. Next, the analytical methods adopted to extract different tip wear metrics from 2D profile data are presented. Then, the experimental results obtained are discussed in the context of the wear assessed along different machining directions. Finally, conclusions and recommendations for the following chapters are drawn.

## **3.2 Experimental set-up and methodology**

### **3.2.1 AFM system**

In this study, the AFM tip-based nanomachining operations were conducted on the XE-100 AFM model from Park Systems. The actual AFM instrument utilised is shown in Figure 3.1. This AFM is positioned on an active anti-vibration table (model TS 150 from Table Stable Ltd). In addition, it is located inside a full acoustic enclosure. This AFM system has individual X, Y and Z piezoelectric actuators. The X and Y actuators generate displacements of the stage along the  $x$  and  $y$  axes with sub-micrometre resolution, while the Z actuator defines the vertical displacement of the AFM probe along the  $z$  axis. Figure 3.2 illustrates the principle of the AFM tip-based nanomachining process. The basic steps for its implementation are described as follows. The tip of the AFM probe is first brought into contact with a sample/workpiece until a predefined load is reached. Then, the workpiece is moved relative to the tip via the displacements of the stage along the  $x$  and  $y$  axes. The normal force applied by the tip on the workpiece depends on the deflection of the probe cantilever in the normal direction at the tip position. For most AFM systems, this deflection is conventionally measured by projecting a laser beam on the back of cantilever and by monitoring the displacement of the beam reflection with a position sensitive photodiode (PSPD). The

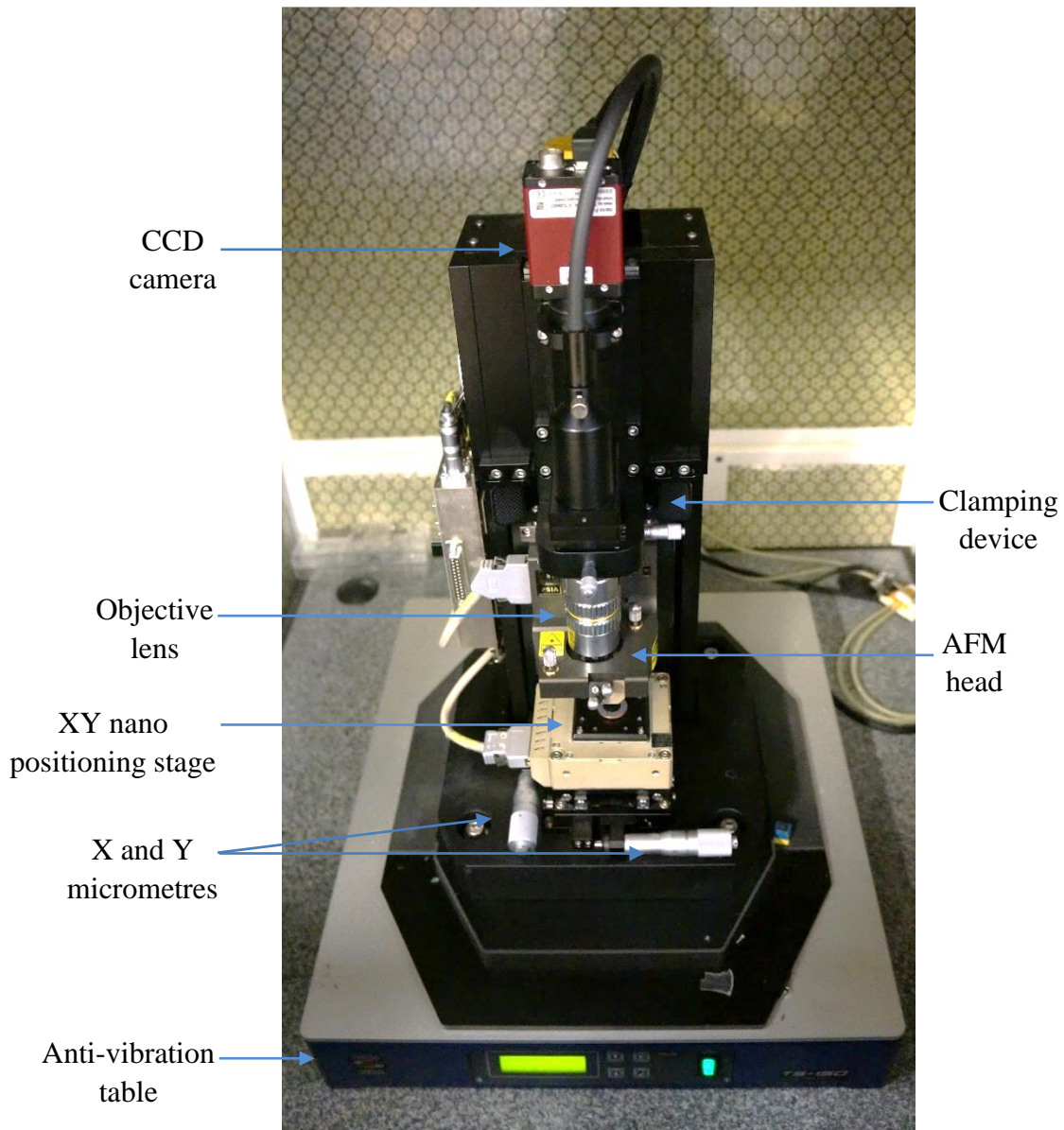


Figure 3.1: XE-100 AFM instrument from Park Systems.

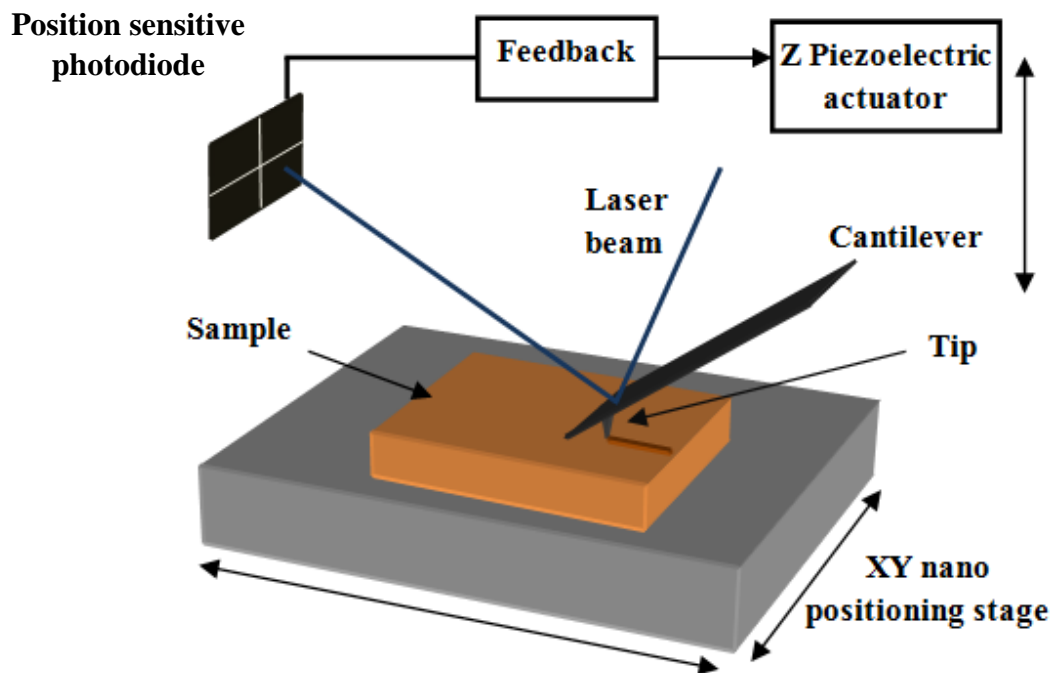


Figure 3.2: Schematic diagram of the AFM tip-based nanomachining principle (adapted from Brousseau *et al.* 2013).

PSPD output signal can be used to implement a feedback loop, which ensures that the value of this signal output is maintained as the probe tip is moved along the surface of a sample. This is achieved by adjusting constantly the vertical displacement of the probe with the Z piezoelectric actuator on which it is mounted.

In this research, to conduct the AFM tip-based nanomachining process, the “XEL” software from Park Systems was used. This software enables the user to define customised tip trajectories. In addition, two different modes of operations may be detected to implement the nanomachining process, namely the “*set-point*” and the “*z-scanner*” modes. The “*set-point*” mode requires the user to specify a particular value for the applied load. Thus, this mode relies on the feedback loop of the AFM instrument, which ensures that the position of the reflected laser spot on the PSPD is kept constant, as mentioned above. The “*z-scanner*” mode allows the user to define a specific vertical displacement of the AFM probe towards the sample prior to the start of machining. Thus, in the “*z-scanner*” mode, the feedback loop of the AFM instrument is not utilised to control the vertical position of the probe, as this position is fixed during a machining operation. Therefore, compared to “*set-point*”, the “*z-scanner*” mode enables the application of a higher load onto the sample. This is due to the fact that the maximum value of tip deflection is not limited by the dimensions of the PSPD in this case. However, it is important to note that nanomachining conducted with the “*z-scanner*” mode do not compensate for the tilt of the processed surface as illustrated in Figure 3.3. Indeed, if the surface is inclined at an angle, “ $\theta$ ” with respect to the  $x$  axis, then the obtained depth of the grooves may not be constant along a cut. In this research, initial trials revealed that the load applied by the tip using the “*set-point*” mode was not always sufficient to induce

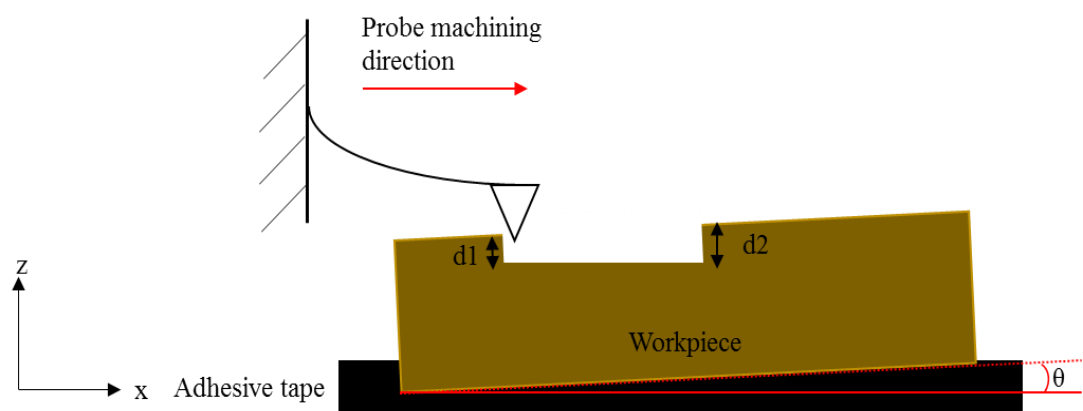


Figure 3.3: Illustration of the possible effect of the tilt on the groove depth when conducting the AFM tip-based nanomachining operations with the “*z-scanner*” mode.

plastic deformation into the workpiece. Therefore, the “*z-scanner*” mode was employed throughout the experiments.

### **3.2.2 Workpiece preparation**

A single crystal copper sample with 99.999 % purity was used as a workpiece. Figure 3.4 shows the complete workpiece preparation procedure prior to the nanomachining experiments. The sample, which had a diameter of 12 mm, was cut to a length of 12.5 mm using micro wire Electrical Discharge Machining (EDM). Next, the sample was polished using a procedure tailored for soft materials as described in Figure 3.4. The roughness achieved after polishing was Ra 4 nm as measured with the AFM instrument.

### **3.2.3 AFM probes**

Silicon probes (model NSC15 from MikroMasch) were used for the experiments conducted in this chapter. Figure 3.5 shows a SEM micrograph of such type of probe. These probes are normally designed for AFM imaging tasks in non-contact mode. The nominal radius value for tip apex of such probes is specified as 8 nm by the manufacturer. The probe cantilever is designed such that it has a nominal normal spring constant,  $k$ , of 40 N/m. The complete set of specifications for this AFM probe is given in Table 3.1. Given the traditional large uncertainty associated with the actual  $k$  value of AFM probes, a calibration procedure was systematically carried out to assess the normal spring constant of each probe used in the experimental trials. The particular procedure adopted to perform this calibration was that proposed by Sader *et al.* (1999) for rectangular cantilevers.

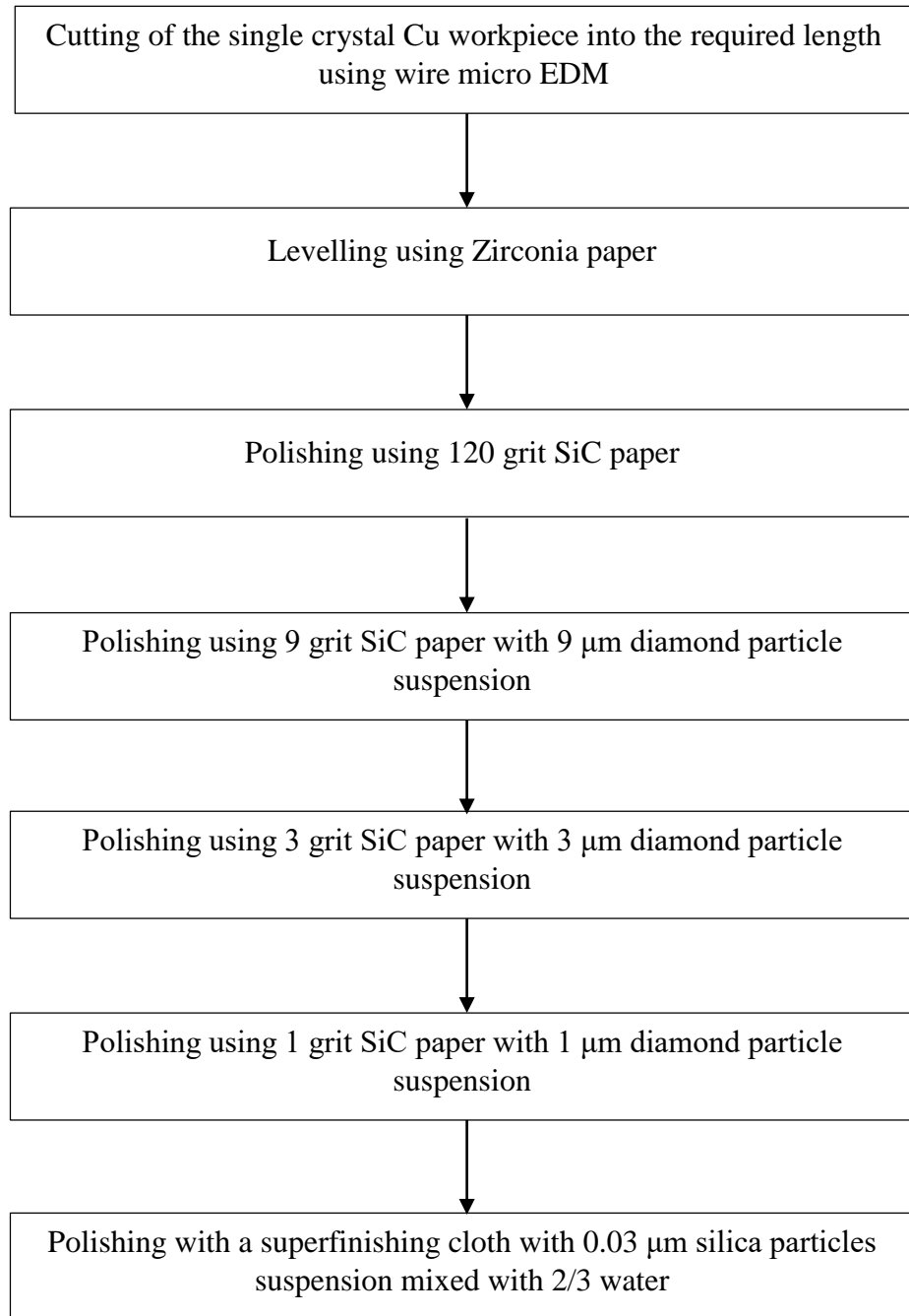


Figure 3.4: Workpiece preparation procedure.

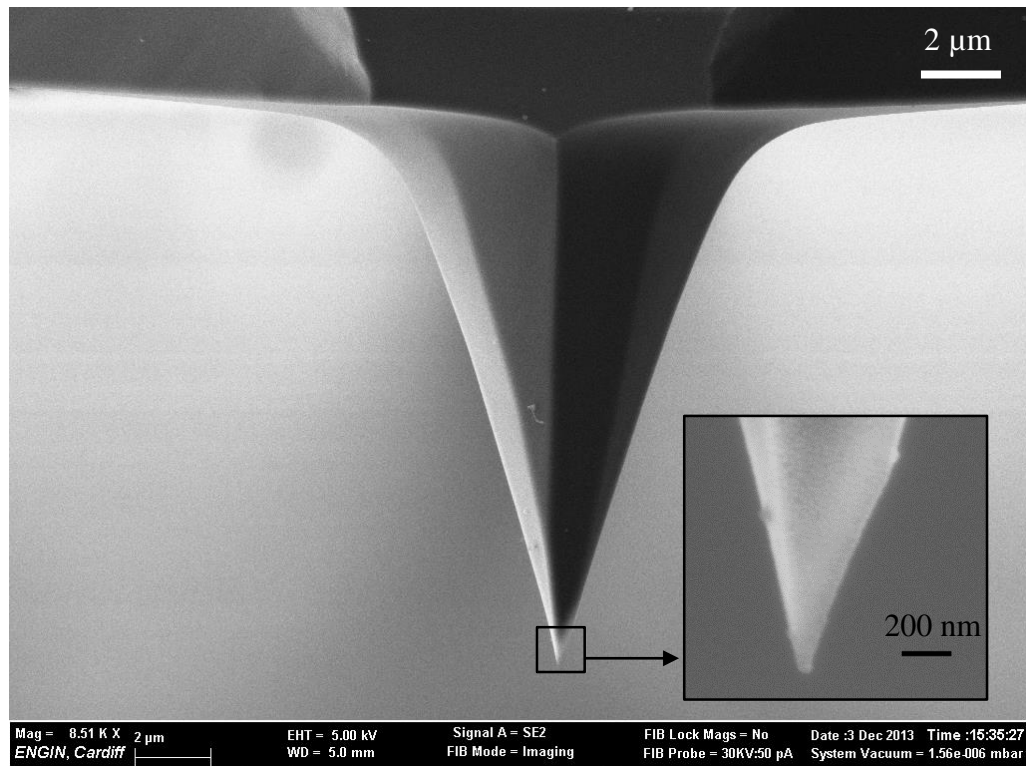
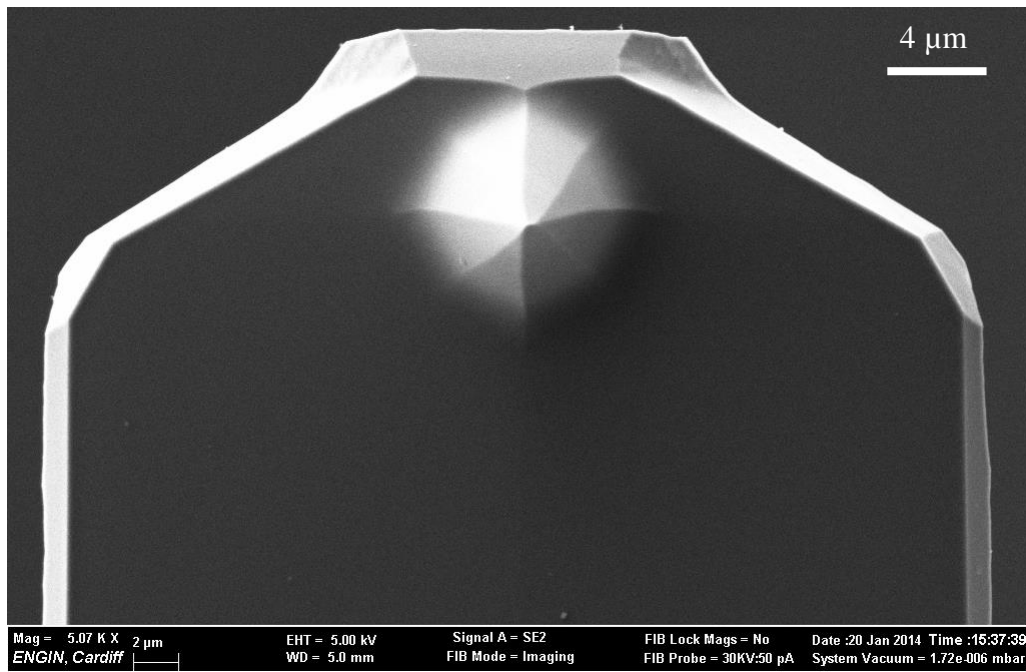


Figure 3.5: SEM micrographs of a typical NSC15 probe.

| Probe | Resonance frequency (kHz) |         |     | Force constant (N/m) |         |     | Cantilever                           |                                     |   |
|-------|---------------------------|---------|-----|----------------------|---------|-----|--------------------------------------|-------------------------------------|---|
|       | min                       | nominal | max | min                  | nominal | max | Length<br>$l$<br>$\pm 5 \mu\text{m}$ | Width<br>$w$<br>$\pm 3 \mu\text{m}$ | Thickness<br>$t$<br>$\pm 0.5 \mu\text{m}$ |
|       | NSC15 series              | 265     | 325 | 410                  | 20      | 40  | 80                                   | 125                                 | 30  |

Table 3.1: Probe specification for the NSC15 model.

### 3.2.4 Cutting conditions

In this experimental study, it was decided to vary only two process parameters as follows:

- *Set applied normal force:* This value is defined by the AFM user prior to performing an AFM machining operation. It corresponds to the normal force applied by the tip on a specimen when the tip is engaged vertically into the material without any lateral displacement of the probe with respect to the sample. As pointed out in Brousseau *et al.* (2013), due to the particular implementation of AFM instruments and the fact that during AFM machining operations, an additional horizontal cutting force acts on the tip, the actual normal force value is not known during processing unless a specific data acquisition system is implemented to assess it as described in Malekian *et al.* (2010). In this study, it was decided to use two different values of applied normal force, 80 µN and 40 µN.
- *Machining direction:* A large number of machining directions can be implemented, for example when cutting curvilinear grooves. However, in the majority of studies on AFM tip-based machining, mainly four different directions are utilised. As described in Tseng *et al.* (2011), these can be parallel to the long axis of the cantilever while towards to, or away from, the probe as well as perpendicular to the cantilever. The machining directions selected in this study are illustrated in Figure 3.6. They correspond to the possible two directions parallel to the cantilever, namely towards (*Direction 1*) and away from (*Direction 2*) the cantilever as well as perpendicular to it (*Direction 3*). In practice, for conventional AFM systems, the probe cantilever is not parallel to the surface of the specimen but mounted at an

angle such that the probe is slightly pointing towards the sample. For example, this inclination angle is  $12^\circ$  for the XE-100 AFM instrument used in this study. Due to this inclination, *Direction 1* results in a different rake angle compared to *Direction 2* for which machining is conducted away from the probe. Only one direction perpendicular to the long axis of the cantilever was considered (i.e. *Direction 3* shown in Figure 3.6) because it is assumed that the tip configuration is symmetrical with respect to the long axis of the cantilever.

In addition, it should be noted that recent molecular dynamics simulation studies of a diamond tip cutting silicon (Goel *et al.* 2012) and copper (Geng *et al.* 2015) suggest that the tip wear mechanism is affected by the crystal orientation of the workpiece. Thus, in this study, the copper sample was rotated in the appropriate direction before each machining trial to make sure that the parameter “machining direction” was only representative of the potential influence of the tip and probe orientation with respect to the specimen without the introduction of a possible effect from the crystal orientation of the copper workpiece. Table 3.2 summarises the set-up used to perform each of the six machining trials that could be designed based on the selected process parameter values. The machining speed was kept constant at  $5 \mu\text{m/s}$  in all experiments. The total machined distance for each experiment was 3 mm. The assessment of the tip wear was performed at different points across this total distance, namely after 0.5 mm, 1 mm, 1.5 mm and finally 3 mm of machining. The particular approach used to assess the wear of the tips is described in the next section.

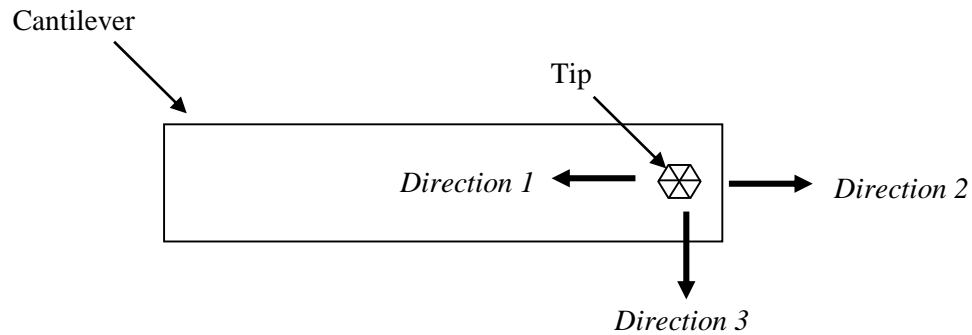


Figure 3.6: The investigated three machining directions with respect to the long axis of the cantilever.

| Trial number | Set normal force ( $\mu\text{N}$ ) | Machining direction | Machining speed ( $\mu\text{m/s}$ ) | Machining distance (mm) |
|--------------|------------------------------------|---------------------|-------------------------------------|-------------------------|
| 1            | 80                                 | 1                   |                                     |                         |
| 2            | 80                                 | 2                   |                                     |                         |
| 3            | 80                                 | 3                   | 5                                   | 3                       |
| 4            | 40                                 | 1                   |                                     |                         |
| 5            | 40                                 | 2                   |                                     |                         |
| 6            | 40                                 | 3                   |                                     |                         |

Table 3.2: Selected AFM tip-based nanomachining parameters.

### 3.3 Methodology for tip wear assessment

#### 3.3.1 Two-dimensional profile extraction

As reported in Chapter 2 earlier, a number of techniques can be used to characterise the geometry of AFM tips. It is common for many researchers to employ SEM equipment for this purpose. Therefore, in this chapter, it was decided to assess the wear of the tips used for machining based on 2D profile data obtained with SEM inspections. Figure 3.7 demonstrates the particular procedure adopted in this chapter to assess the wear of the NSC15 tips. At each selected point along the overall cutting length, an SEM image of the tip was obtained at a set magnification, which was the same for each tip inspected. In order to quantify the wear at a given state of the machining distance, the SEM image obtained at that particular state (worn tip image) is compared to the one obtained before the experimentation (unused tip image). This comparison requires the alignment of the two images such that the unworn regions of each image coincide, revealing the regions that have been subjected to wear. Next, Figure 3.8 provides an example that illustrates the procedure for extracting the tip profile information in practice. In particular, Figures 3.8(a) and 3.8(b) show the SEM image of a new tip and that of the same tip after machining for 0.5 mm, respectively. Particularly, an automatic tip edge detection procedure was applied on the SEM data using an image processing software (Image J). Then, the 2D coordinates of the detected points on a tip profile were exported into a text file that could be further processed with the Excel software. The unused tip profile was aligned with the profile of the worn tip. Principally, the aligned profiles are obtained by offsetting the coordinates the worn tip profiles as illustrated in Figure 3.8(c). When the unused tip and the worn tip images are superimposed within this common coordinate system, the worn region can be identified as depicted in Fig. 3.8(d).

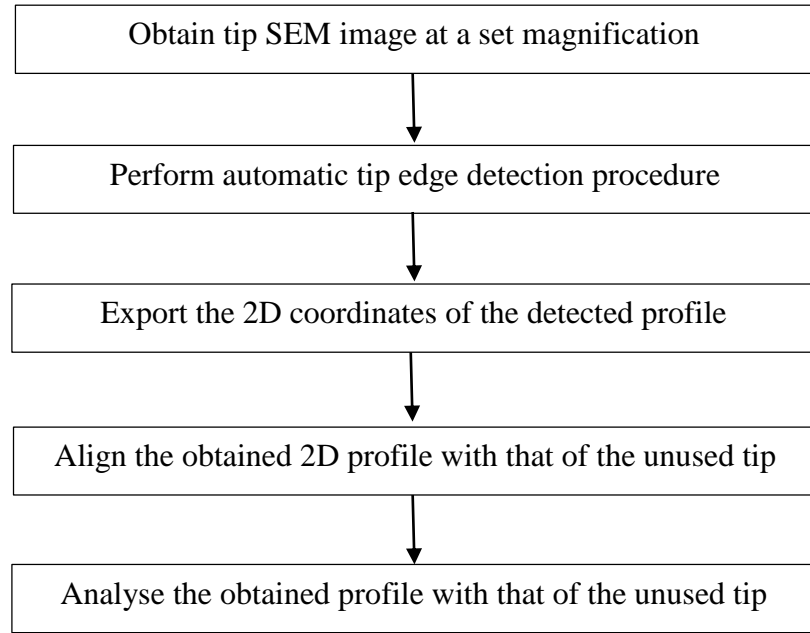


Figure 3.7: Tip wear assessment procedure.

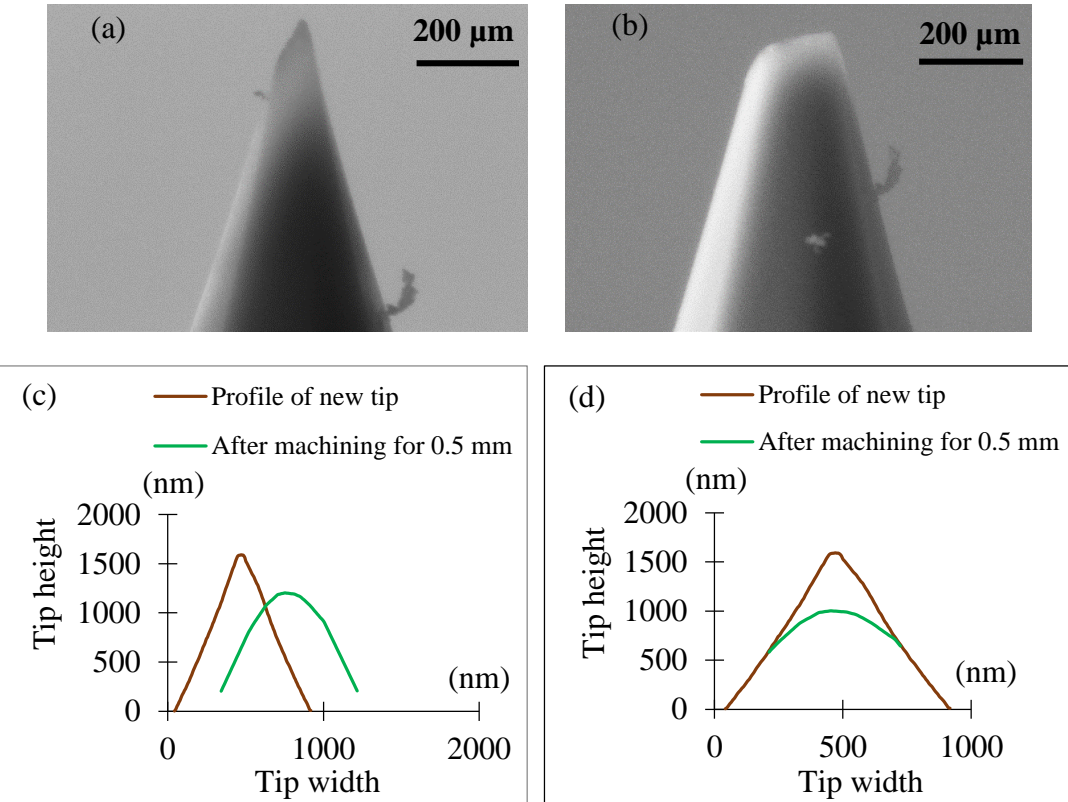


Figure 3.8: SEM images of (a) the unused tip, (b) the tip after machining for a distance of 0.5 mm during Trial 5; corresponding 2D profiles, (c) before alignment, (d) after completing the alignment procedure.

Based on the 2D profile information for a given probe, the assessment of the tip wear at a selected machining distance was performed via the calculation of three different metrics, which could then be compared between the profile of the unused tip and its current profile. The particular wear metrics considered are presented in the following sections. These consists in the area and volume loss measurement as well as the assessment of the tip radius.

### 3.3.2 Area and volume loss measurement

As discussed in the previous section, the assessment of the AFM tip wear was conducted after performing the procedure of extracting and aligning profile data from the SEM images. Based on this 2D information for a given probe, the first wear metric considered was the measurement of the area loss between the profile of the unused tip and its profile obtained at a selected machining distance. This was achieved as follows. First, the height,  $h_i$ , of a profile was extracted at regular interval,  $l_i$ . The maximum  $h_i$  value was determined by considering the area of the profile which is affected by the wear. This was performed following the alignment of the profiles as in Figure 3.8 (d). Next, each of the height values was multiplied by the length of the interval considered. Finally, the area,  $A$ , under a given profile was estimated by adding all the rectangular areas calculated during the previous step as expressed in the following equation:

$$A = \sum_{i=1}^n h_i \cdot l_i \quad (3.1)$$

where  $n$  represents the number of intervals. Characteristically in this study, there were about 100 to 150 intervals considered along the tip profile. It is acknowledged that this approach has an error associated with it. However, this error can be minimised by using a small interval value. The interval employed in this work was 5.8 nm. In particular, the interval was defined according to the resolution of the SEM micrograph, thus the distance

between each pixel. This value generally corresponded to about 0.5% of the overall distance over which a profile was extracted. Finally, the wear metric “*area loss*” could then be obtained by subtracting the area under the tip at a given machining distance from the area under the profile of the same tip in its unused condition:

$$\text{area loss} = A_{\text{unused tip}} - A_{\text{tip after machining}} \quad (3.2)$$

The second wear metric considered is referred to as “*volume loss*”. The procedure followed to compute this metric is inspired by that reported by Liu *et al.* (2010). Based on 2D profile data, these authors assumed that the tip was comprised of a stack of circular disk-shaped elements where the diameter of each element corresponded to the measured tip width at regular intervals along the tip vertical axis. In this way, the volume for a given tip could be calculated by adding the volumes of all elements. In this work, it is proposed to discretise a tip into a stack of frustums of right circular cones instead. It is expected that this approach should lead to a better fit to the real shape of a tip in comparison with assuming a stack of circular disk-shaped elements. The geometry of a frustum for a right circular cone is illustrated in Figure 3.9. The formula used to express the volume,  $V_f$ , of such an element is given below.

$$V_f = \frac{\pi h_f}{3} (R_f^2 + R_f r_f + r_f^2) \quad (3.3)$$

where  $h_f$  is the height,  $R_f$  is the radius of the base and  $r_f$  is the radius of the top face as shown in Figure 3.9. Finally, the volume for a particular tip and the “*volume loss*” metric could be obtained from equation (3.4) and (3.5), respectively.

$$V = \sum_{j=1}^m V_{fj} \quad (3.4)$$

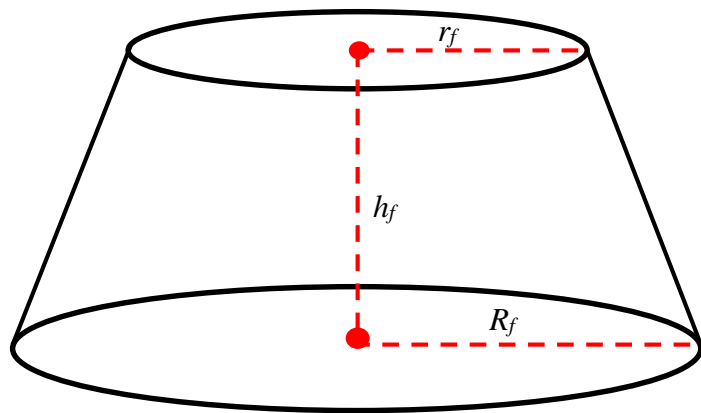


Figure 3.9: Frustum of a right circular cone.

where  $m$  represents the number of intervals considered along the tip profile. In this study stacks of about 200 frustum of right circular cones were used.

$$\text{volume loss} = V_{\text{unused tip}} - V_{\text{tip after machining}} \quad (3.5)$$

In this study, the value of the interval used along the tip vertical axis to discretise a tip profile was 10 nm. The interval was considered according to the resolution of the AFM tip SEM micrograph. Based on the experimental data obtained in this chapter, a comparison between the approach of Liu *et al.* (2010) and that proposed here showed that the error associated with the discretisation using circular disk-shaped elements was 26% (see appendix A).

### 3.3.3 Tip radius measurement

As reported in Chapter 2, calculating the radius of the apex of an AFM tip is a procedure commonly employed by researchers to assess the tip condition. Thus, in this chapter, the third wear metric is the estimation of the tip radius,  $R$ . To achieve this, a polynomial was first fitted to the extracted 2D profile data. Similarly, to Odin *et al.* (1994),  $R$  was then estimated by calculating the radius of curvature at the maximum point of the fitted polynomial based on the following formula:

$$R = \frac{\left[1 + \left(\frac{dy}{dx}\right)^2\right]^{3/2}}{\frac{d^2y}{dx^2}} \quad (3.6)$$

For all analysed tips, a polynomial of degree two was fitted to the data to implement equation (3.6). Based on the obtained experimental results, the fitness agreement between the tip and a polynomial of degree two was between 88% to 95% (see appendix B). A better level of fitness could be achieved with higher degree polynomials. However, initial

investigations revealed that such polynomials were more sensitive to very localised and sudden changes along the tip profile. In turn, this higher sensitivity tended to lead to erroneous estimations of the tip radius because such local irregularities are not representative of the overall radius of the tip apex along a specific tip width.

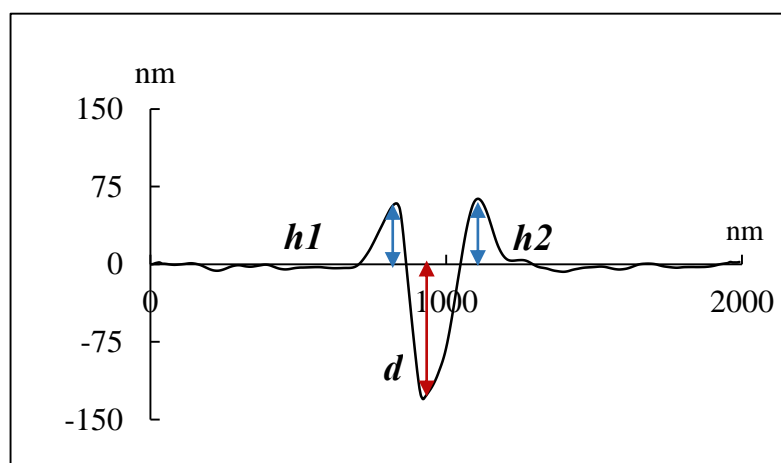
### 3.3.4 Assessment of groove topography

The generated grooves on the single crystal copper workpiece were inspected with an SEM instrument (model XB1540 from Carl Zeiss) and with the XE-100 AFM from Park Systems. In particular, the SEM micrographs were used to observe the formation, or otherwise, of chips during machining. Specifically, a SEM image was obtained for the set of grooves produced after each considered machining distance, namely 0.5 mm, 1 mm, 1.5 mm and 3 mm. The AFM was employed in contact mode with an applied force of 20 nN using a single crystal silicon probe to obtain 3D scans of individual grooves. The specific probe utilised was the CSG 30 model from NT-MDT. Such probes have a nominal tip radius of 10 nm. The complete set of specifications for this type of probe is given in Table 3.3. Such AFM scans were taken for grooves generated during the trials conducted for the first (i.e. 0.5 mm) and the last (i.e. 3.0 mm) machining distance. From the obtained AFM data, the cross section of grooves could be analysed. This analysis was performed based on the method reported in Ahn and Lee (2009). As suggested by these authors, which completed AFM tip-based nanomachining experiments on a brittle material (i.e. silicon), the ratio between the sum of the pile-up heights measured on each side of a machined groove,  $h_1$  and  $h_2$ , and the depth of this groove,  $d$ , as illustrated in Figure 3.10 was used to detect the machining regime. This ratio is referred to the *H/D ratio* and it is expressed as follows:

$$H/D \text{ ratio} = \frac{h_1 + h_2}{d} \quad (3.7)$$

| Probe        | Resonance frequency (kHz) |         |     | Spring constant (N/m) |         |     | Length<br>$l$<br>$\pm 5$<br>μm | Width<br>$w$<br>$\pm 3$<br>μm | Thickness<br>$t$<br>$\pm 0.5$ μm |
|--------------|---------------------------|---------|-----|-----------------------|---------|-----|--------------------------------|-------------------------------|----------------------------------|
|              | min                       | nominal | max | min                   | nominal | max |                                |                               |                                  |
| CSG30 series | 26                        | 48      | 76  | 0.13                  | 0.6     | 2   | 190                            | 30                            | 1.5                              |

Table 3.3: Probe specification for the CSG30 model.

Figure 3.10: *H/D ratio*

According to Ahn and Lee (2009), when the *H/D ratio* is more than unity, i.e. more than 1, it could be assumed that machining is taking place in the ploughing-dominated regime. Inversely, when this ratio is less than 1, it may be assumed that machining occurs in the cutting-dominated regime, i.e. with chip formation. In this study, seven cross sections for each grooves were measured as illustrated in Figure 3.11 to calculate the average value of the *H/D ratio*.

### 3.4 Analysis of the results

#### 3.4.1 Area and volume loss measurements

SEM images of the tips employed to complete the six experimental trials are given in Figure 3.12. Each image shown corresponds to the tip condition prior to the start of the experiments. It can be easily noticed that the geometry of each tip apex is relatively different despite the fact that the probes were fabricated by the same manufacturer. Such observations about variations in tip conditions were also recently reported by Jacobs *et al.* (2016). Based on the procedure described in Figure 3.7, each tip profile could be extracted during the machining trials as shown in Figure 3.13. In particular, each graph in this figure combines the profile of an unused tip with its subsequent profiles at each selected machining distance. In addition, Figures 3.14 and 3.15 show the evolutions of single measurement of the area and volume losses between the profile of an unused tip and those of the same tip at selected machining lengths (see Appendix E

From Figures 3.14 and 3.15, it can be observed that both wear metrics, area loss and volume loss, show a similar generic trend for all six experimental conditions. In particular, the initial wear of the tip is relatively large in the first 0.5 mm of machining. Following this, the wear rate reduces and generally tends to follow a linear behaviour.

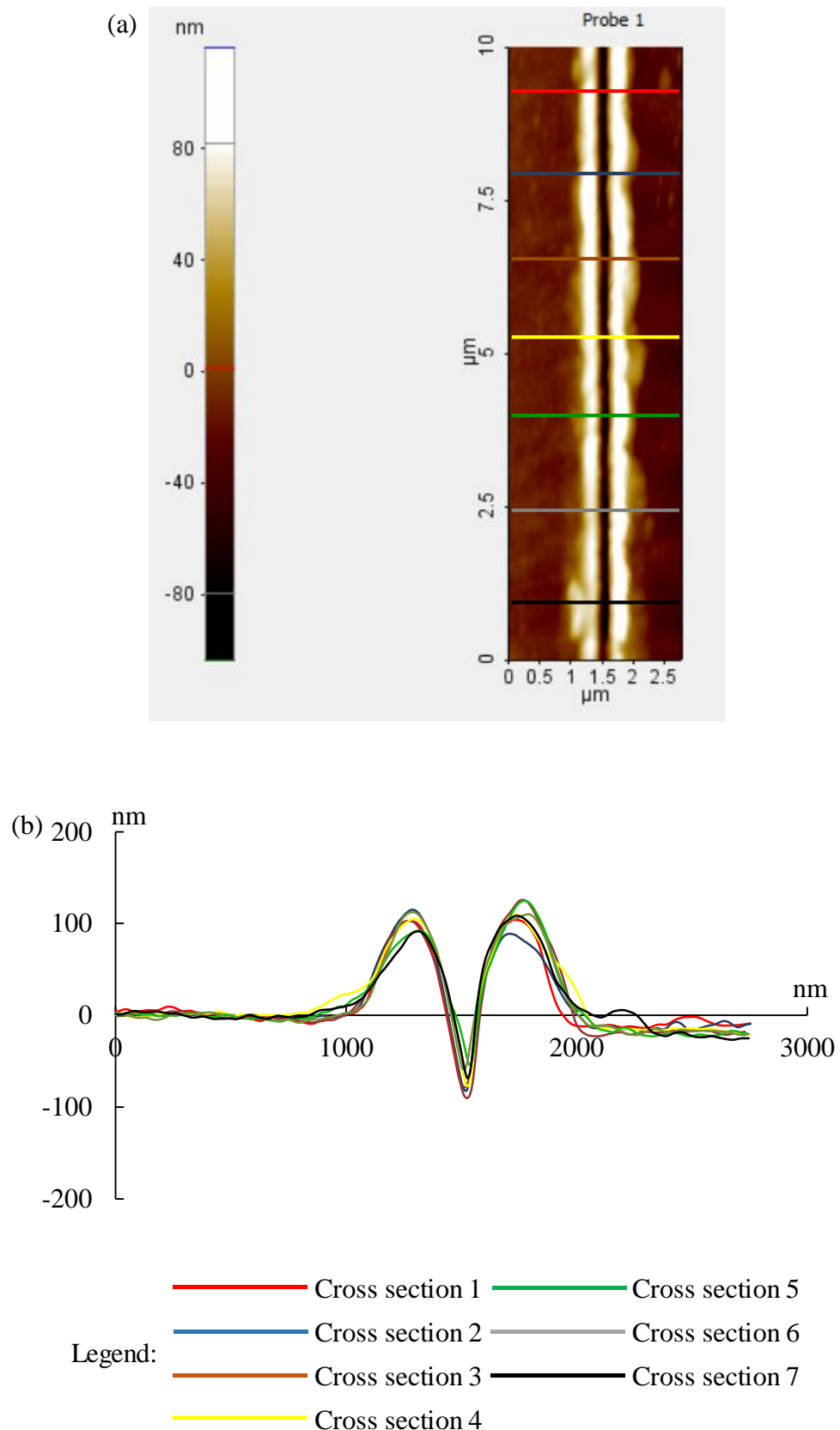


Figure 3.11: (a) AFM topography image of a groove and (b) cross section of a groove profiles after 0.5 mm of machining distance.

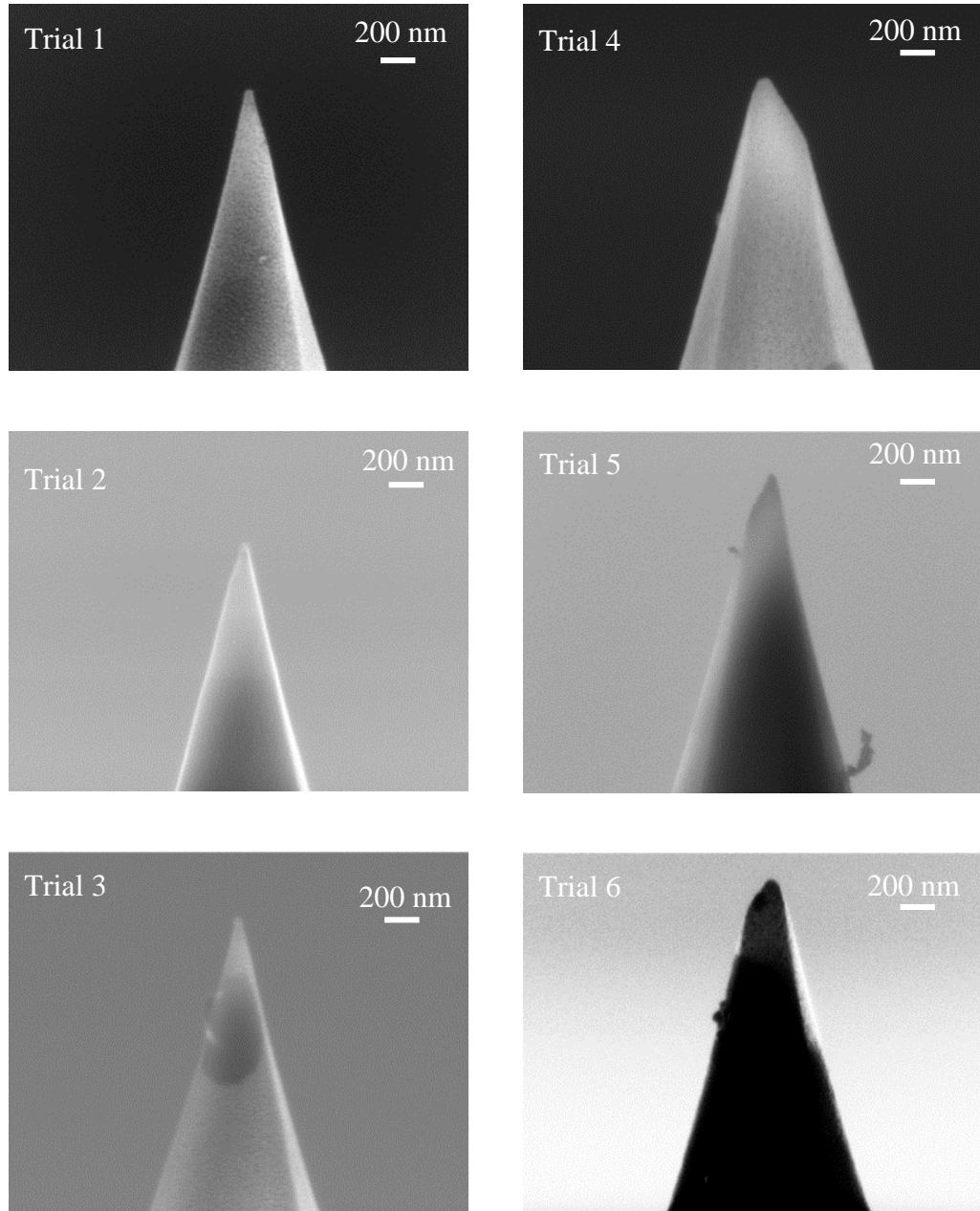


Figure 3.12: SEM micrographs of the six NSC 15 silicon tips used in this chapter prior to the start of the experimental trials.

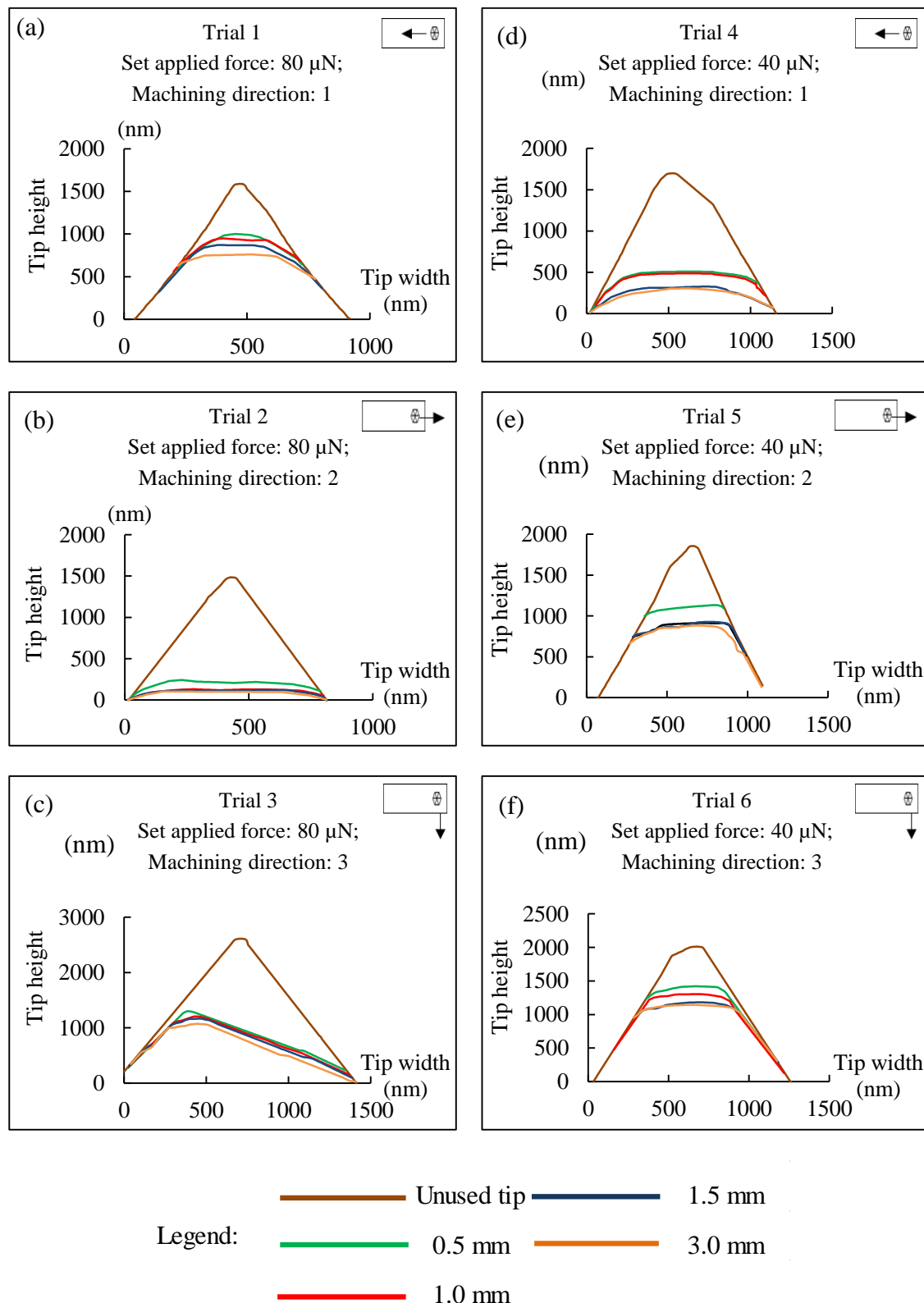


Figure 3.13: Tip profiles at different stages of machining for each trial conducted for

each NSC 15 silicon probes.

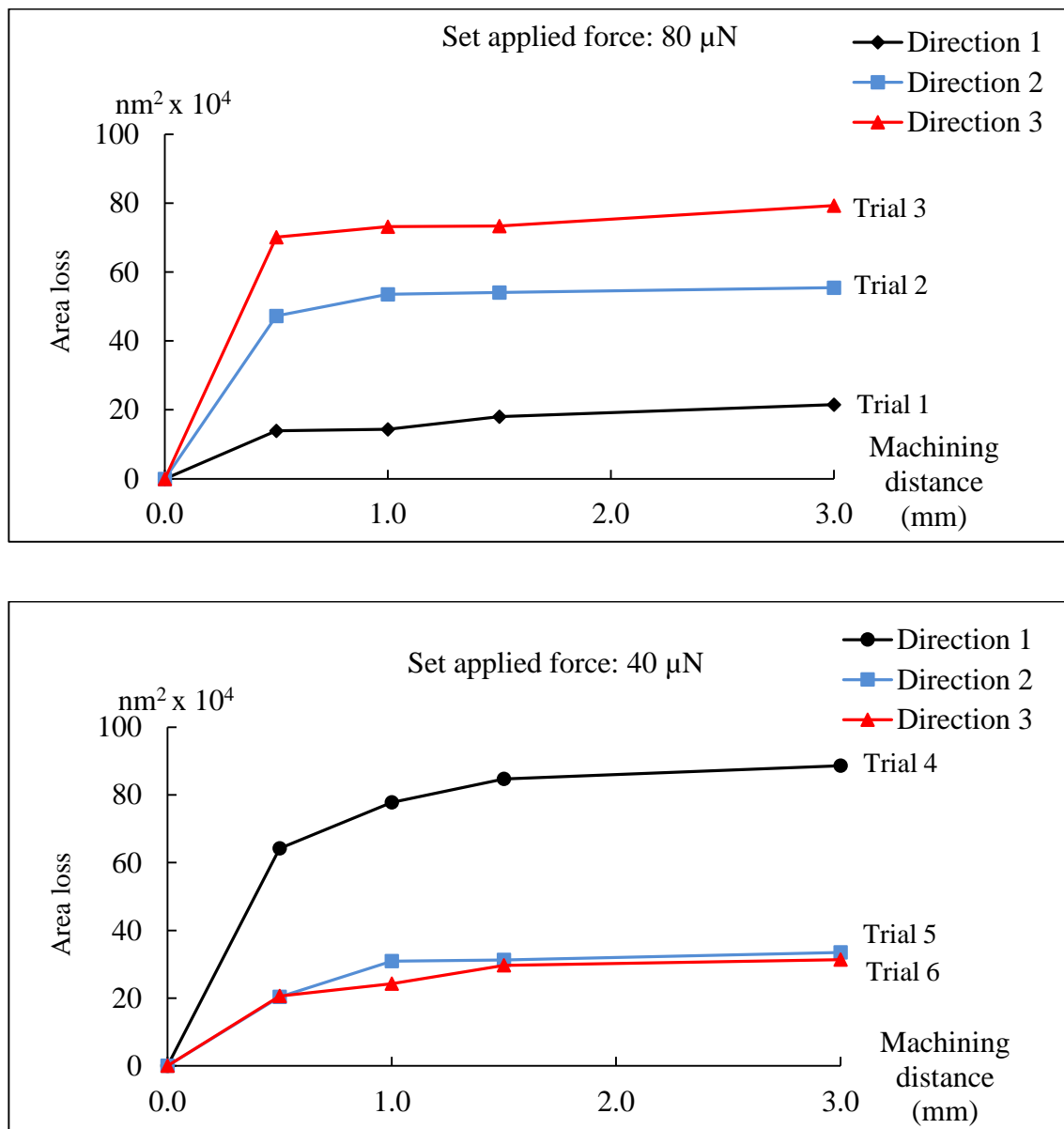
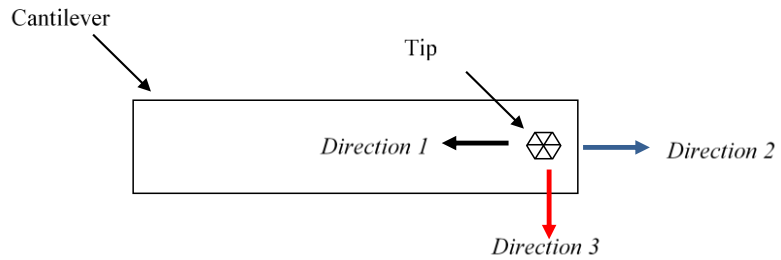


Figure 3.14: Evolution of the tip area loss as a function of the machining direction for the different values of set normal force considered for NSC 15 silicon probes.

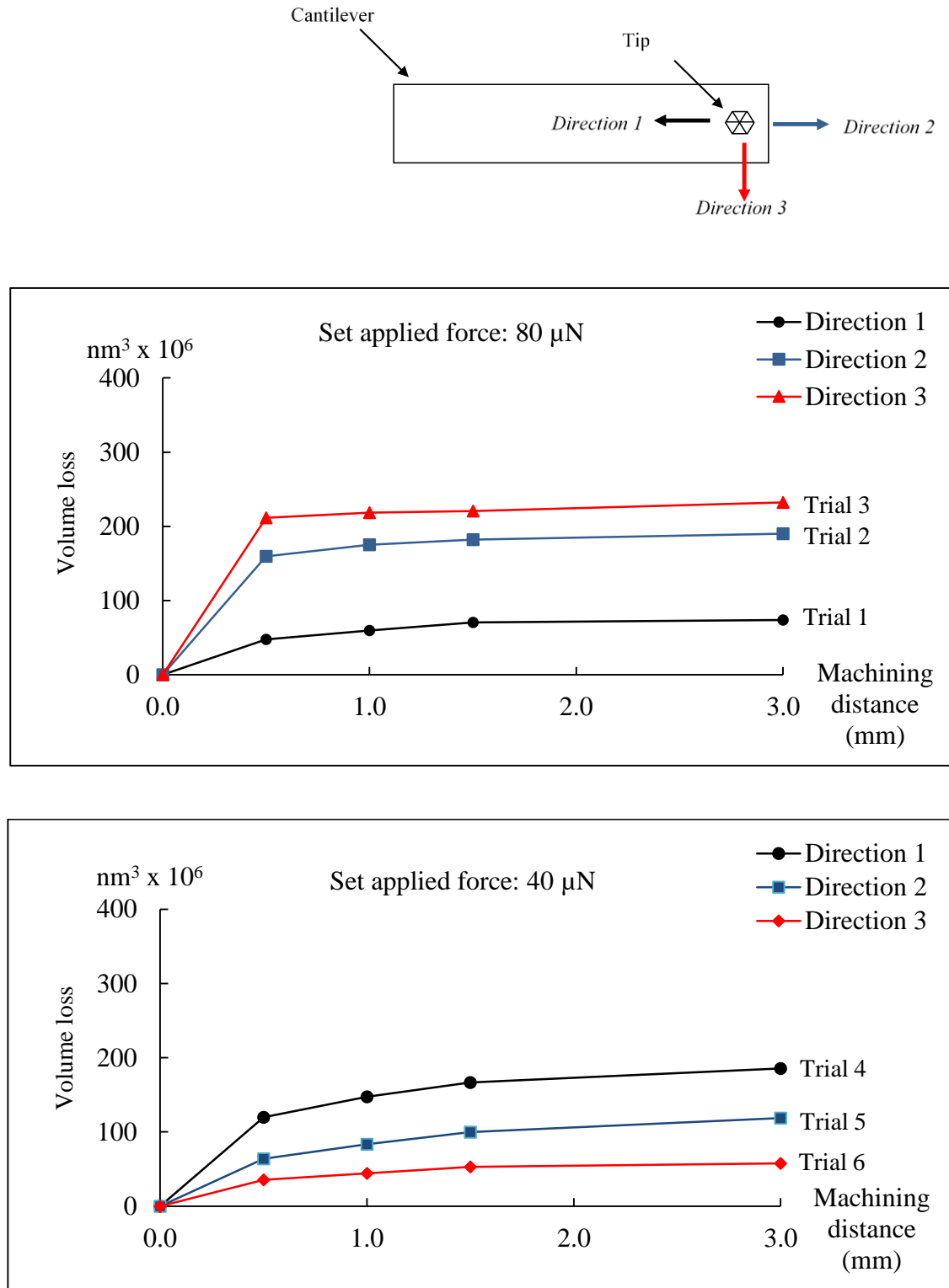


Figure 3.15: Evolution of the tip volume loss as a function of the machining direction for the different values of set normal force considered NSC 15 silicon probes.

Similar observations were presented in Gozen and Ozdoganlar (2014) where the initial wear of diamond tips was reported to be due to a sudden breakage of the sharp tip due to increased stress concentration (see Appendix C). Small but early fractures of silicon tips have also been observed in studies from Liu *et al.* (2010) and Villarubia (1997) where much lighter normal forces, i.e. in the order of a few nN, had been applied. Thus, it is immediately apparent that this behaviour represents an important limitation when employing Si tips for AFM probe-based machining. It is expected that, following fracture, the gradual wear evolution is due to mechanisms involving the progressive removal of atoms in small clusters through local bond breaking (Liu *et al.* 2010).

The second observation that can be drawn from Figures 3.14 and 3.15 is that the amount of material removed from the tip during the initial fracture seems to be dependent on the magnitude of the applied force. In particular, a higher applied normal force (80  $\mu$ N) led to a larger portion of removed tip material for two of the considered machining directions (i.e. *Directions 2* and *3*). This is not observed for the tip used to machine along *Direction 1*. However, it must be noted that the tip used to perform the trial 1, i.e. along *Direction 1* and at 80  $\mu$ N of applied force, was from a different box of probes. Thus, this particular tip could have been manufactured from a different batch and as a consequence, it may possess a different crystallographic structure. Therefore, it was decided that the data from this particular trial should not be taken into account when analysing the results.

The plots given in Figures 3.14 and 3.15 can be used to compare the rate of wear between different experiments after the first 0.5 mm of machining when the wear evolution has reached a steadier state. More specifically, this can be done by fitting a linear function to the data points for a given trial and then by examining the slope of this

regression line. In this way, it is observed that for both *Directions 2* and *3*, the wear rate is slightly higher for a lower amount of applied force. Although this result seems counterintuitive, hypotheses can be put forward to explain it based on the examinations of both the geometry of the tips after fracture and the topography of the generated grooves. More specifically, the tip geometry reveals the degree of bluntness and thus, the extent of the contact area between the sample and the tip. A blunter tip leads to a higher contact area and thus, a reduced contact stress, which in turn is expected to decrease the rate of wear for the tip.

Another conclusion that can be made from Table 3.4, when comparing rate of change of volume loss, the Trials in machining in *Direction 2* is always higher than machining the probe in *Direction 3*. The reason that can put forward is that different machining directions lead to different rake angles. Particularly, the stiffness of the cantilever whether in torsional or normal deflection may influences the rake angle. Thus, it is expected that for a given value of applied normal force, different machining directions will result in different loads acting on the tip, which in turn should influence the wear rate. This has been observed by other researchers where a reduction of tip wear rate was correlated with an increase in the tip size, thus indicating the role that stress plays in nano-scale wear (Liu *et al.* 2010). This phenomenon is most likely at play regarding the wear rate results obtained for *Direction 2*. In particular, the comparison between Figure 3.13(b) and Figure 3.13(e) reveals that the tip after fracture is blunter for the trial conducted at 80  $\mu\text{N}$ . Thus, the larger contact area for this trial contributes to lessen the wear rate compared to the corresponding experiment in which a smaller force was applied. In the case of the results obtained for *Direction 3*, a different phenomenon is probably taking place given that the same conclusion with respect to the area of contact cannot be drawn. In particular,

from Figure 3.13(c), it can be seen that, after fracture, the tip has retained a relatively high degree of sharpness compared to the corresponding tip profile shown in Figure 3.13(f), which was for the trial conducted in the same cutting direction but with a lower force. The inspection of the generated grooves clearly indicates the formation of chips when machining with the sharper tip as illustrated in Figure 3.16. Such chip formation was not observed for the experiment carried out at 40  $\mu\text{N}$ , which means that machining in this case was ploughing-dominated. In the field of micro machining, it has been reported by Biermann and Kahnis (2010) that cutting forces increase when machining is conducted in the ploughing-dominated regime compared to the cutting regime with formation of chips. Thus, in the case of the results observed for *Direction 3*, it is hypothesised that the lowest rate of wear for the trial with a higher normal force is driven by the fact that machining is taking place in the cutting-dominated regime.

### 3.4.2 Tip radius measurements

In Figure 3.17, the evolution of tip radius measurements for all machining trials is plotted (see Appendix E). In-line with the previous section, this figure suggests that the initial wear of the tip increases rapidly. It could be expected that the radius should gradually become larger as the machined distance increases. However, the results shown in Figure 3.17 suggest that this is not always the case. In particular, if the radius evolution of the tip used for trial 5 (i.e. *Direction 2* and 40  $\mu\text{N}$ ) is considered, it can be observed that it slightly reduces after 1 mm of machining. Based on the tip profile data provided earlier in Figure 3.13(e), this is attributed to the fact that the initial tip fracture resulted in a tip profile close to that of a flat punch. Further machining with this tip led to the rounding of the edges first and thus, to a reduced tip radius compared to that of a flat punch geometry.

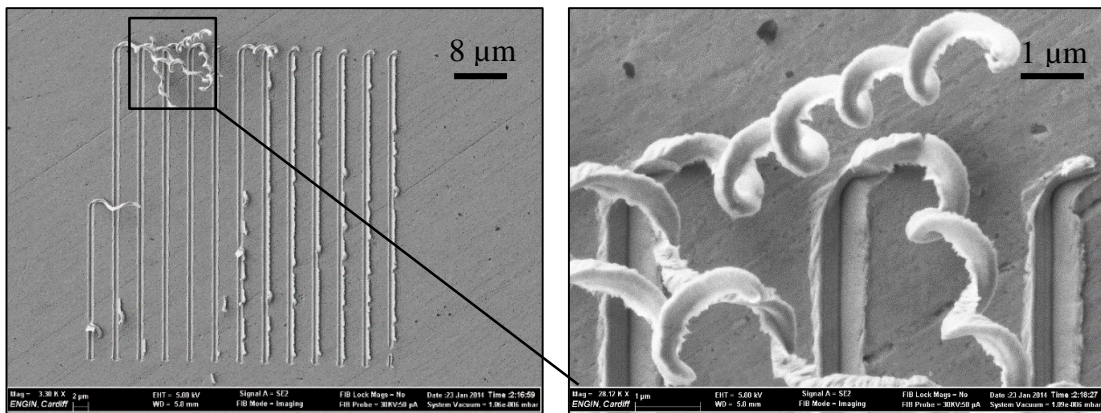


Figure 3.16: Generated grooves on the Cu surface at different magnifications for Trial 3  
(set applied force: 80  $\mu$ N; machining direction: 3).

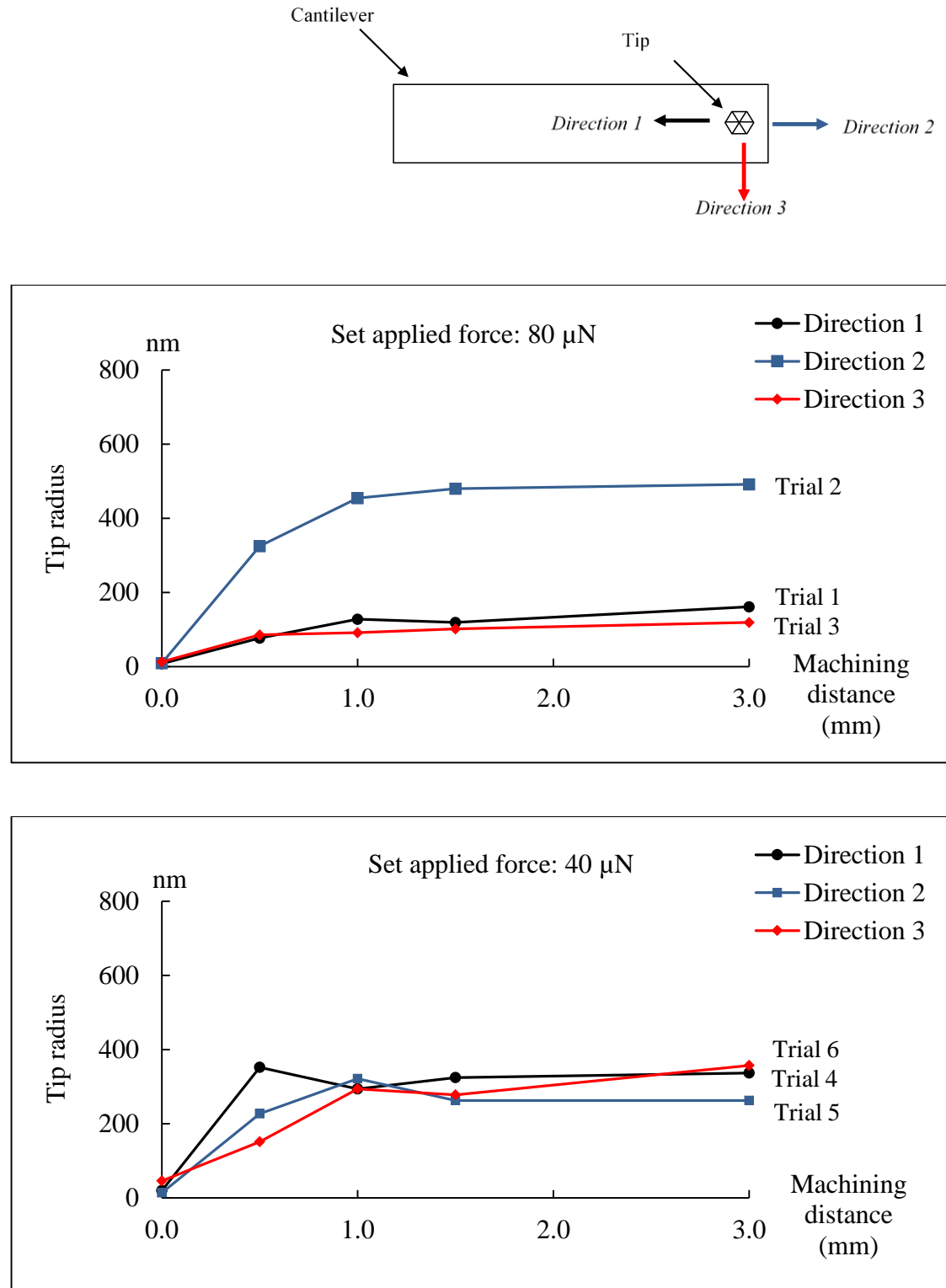


Figure 3.17: Evolution of tip radii as a function of the machining direction for the different values of set normal force considered NSC 15 silicon probes.

In addition, it was noted in the previous section that for both *Directions 2* and *3*, the wear rate was observed to be slightly higher for a lower amount of applied force. However, when calculating the rate of change for the radius measurements in these directions, the opposite outcome is obtained (see Table 3.4). It is also observed from Figure 3.17 that the application of a larger force does not necessarily lead to a larger tip radius. Instead, for a given applied force and processing direction, the tip radius evolution seems to be strongly determined by the radius value achieved after 0.5 mm and thus, by the shape of the probe after initial fracture. Thus, these observations indicate that the analysis of the tip radius could provide information for the occurrence of fracture. However, such data alone have limitations for drawing meaningful conclusions about tip wear.

### **3.4.3 Machined grooves**

The cross section profiles of machined grooves are shown in Figure 3.18 for all trials at two different machining distances, namely 0.5 mm and 3.0 mm. In the majority of cases, protuberances or ridges (also referred to as pile-ups in the AFM-based literature) which accumulate on the edges of the grooves can be observed. Tseng *et al.* (2009) suggested that such pile-ups are formed when the process is conducted in the ploughing-dominated regime. In particular, they are the result of the material being plastically squeezed or deformed by the stress generated by the tip during machining. Tseng *et al.* (2009) indicated that the height of the squeezed protuberances can be as large as the depth of the indentation. In conventional machining, the height of such protuberances (also referred to as burrs) when the process is conducted in the cutting-dominated regime is smaller than those observed in the ploughing regime (Kim and Dornfeld, 2000).

| Machining direction | Trial | Applied normal force ( $\mu\text{N}$ ) | Rate of change of area loss<br>( $\text{nm}^2 \times 10^4 / \text{mm}$ ) | Rate of change of volume loss<br>( $\text{nm}^3 \times 10^6 / \text{mm}$ ) | Rate of change of tip radius<br>( $\text{nm} / \text{mm}$ ) |
|---------------------|-------|--|--|--|---|
| 1                   | 1     | 80                                     | 3.2  | 9.4  | 28.9  |
|                     | 4     | 40                                     | 8.5  | 24.3   | 1.9   |
| 2                   | 2     | 80                                     | 2.6  | 10.8   | 53.1  |
|                     | 5     | 40                                     | 4.1  | 20.7   | 1.9   |
| 3                   | 3     | 80                                     | 3.5  | 7.9  | 13.3  |
|                     | 6     | 40                                     | 4.1  | 8.2  | 67.7  |

Table 3.4: Rate of change of the radius values based on the plots in Figures 3.15, 3.16 and 3.18.

In Section 3.4.1, it was suggested that the particular results observed for Trial 3 were due to the fact that machining was taking place in the cutting-dominated regime. In order to verify this hypothesis, the *H/D ratio*, which was defined in eq. (3.7), can be calculated. In addition, SEM micrographs of the produced grooves can be obtained to observe the presence, or otherwise, of chips. These quantitative (i.e. *H/D ratio* calculations) and qualitative (i.e. SEM inspections) assessments were conducted for all trials (see Tables 3.5 and 3.6, respectively). For Trial 3, Table 3.5 shows that the *H/D ratio* is 2.97 for the first 0.5 mm of machining distance. This suggests that ploughing was occurring during this interval. Indeed, referring to Table 3.6, it is also noticed that no chip was generated for the first 6 grooves. However, during the 7<sup>th</sup> groove, a chip started to form. Following this, a chip was formed for all grooves in Trial 3 until the last machining interval, i.e. until a distance of 3 mm. It is also interesting to note that the *H/D ratio* for Trial 3 in this case is found to be 0.96. This is consistent with the SEM observations.

From the values reported in Table 3.5, a similar phenomenon was found for Trial 2. However, the depth of the grooves during the cutting distance until 3.0 mm was shallower than that achieved during the first 0.5 mm (refer to Figure 3.18(b)). This shows that the groove depth alone does not indicate whether machining is taking place in the cutting or ploughing dominated regime. It is also worth noticing that the profile of the tip used in this trial was already found to be relatively blunt (see Figure 3.13(b)). This appears to be in contradiction with the suggestion that machining took place in the cutting-dominated regime. However, the profiles shown in Figure 3.12 only present 2D information. Thus, it may be possible that the cutting edge of the cross section perpendicular to that shown in Figure 3.14(b) was still relatively sharp. This observation provides further evidence that using 2D SEM micrographs has limitations when assessing

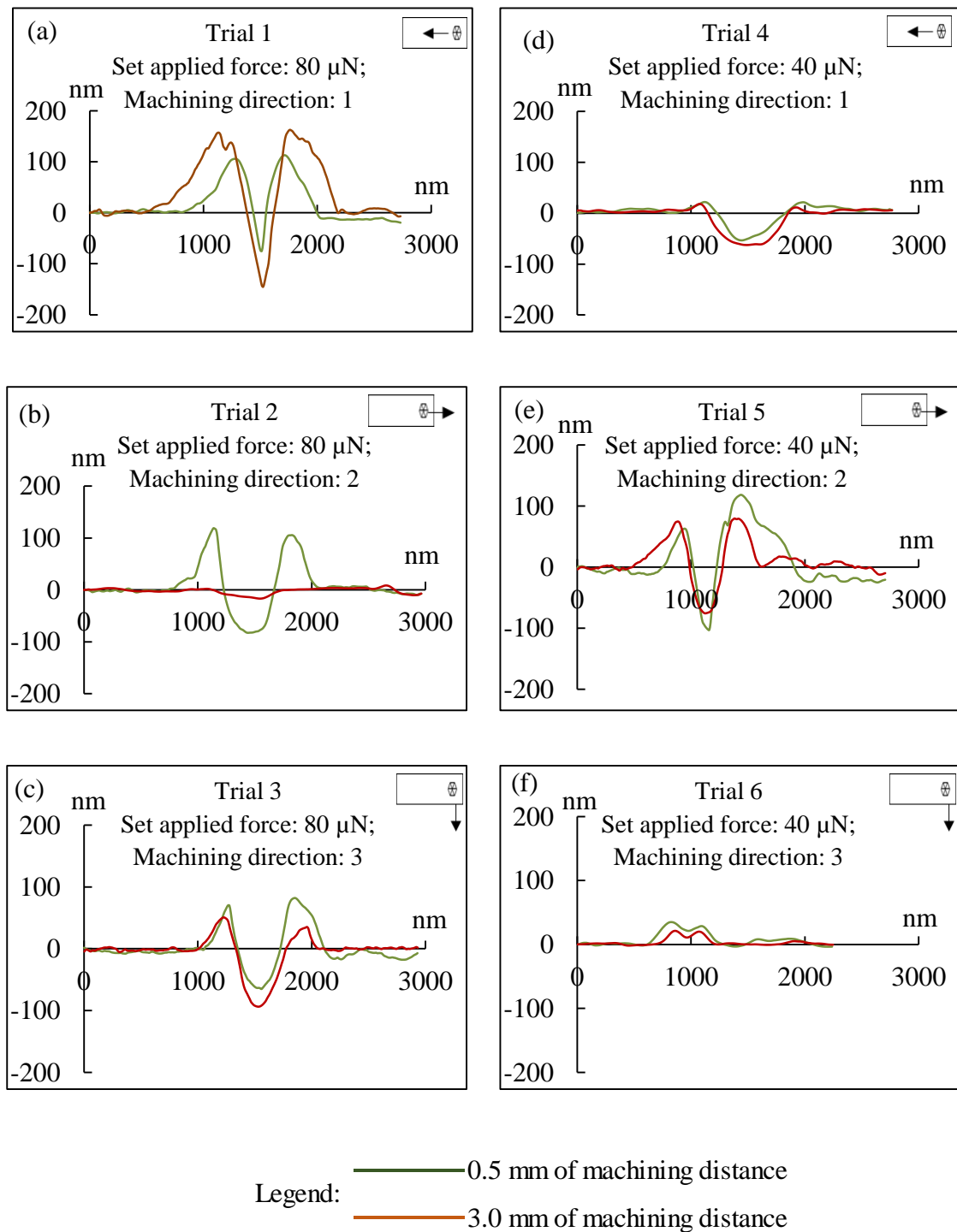


Figure 3.18: Groove profiles obtained when machining with NSC 15 silicon probes.

| Trial | Applied<br>normal force<br>( $\mu\text{N}$ ) | <i>H/D ratio</i> with standard deviation |  |
|-------|--|--|--|
|       |  | During machining trial<br>until 0.5 mm   | During machining trial<br>until 3.0 mm |
| 1     | 80   | $3.23 \pm 0.22$                          | $2.04 \pm 0.13$                        |
| 2     |  | $3.00 \pm 0.73$                          | $0.77 \pm 0.19$                        |
| 3     |  | $2.97 \pm 0.84$                          | $0.96 \pm 0.06$                        |
| 4     | 40   | $0.67 \pm 0.20$                          | $0.58 \pm 0.22$                        |
| 5     |  | $2.37 \pm 0.27$                          | $2.06 \pm 0.44$                        |
| 6     |  | $7.23 \pm 2.17$                          | $1.74 \pm 0.47$                        |

Table 3.5: *H/D ratios* for NSC 15 silicon probes.

| Trial | Set applied force ( $\mu\text{N}$ ) | SEM micrographs of grooves |        |        |        |
|-------|-------------------------------------|----------------------------|--------|--------|--------|
|       |                                     | 0.5 mm                     | 1.0 mm | 1.5 mm | 3.0 mm |
| 1     | 80                                  |                            |        |        |        |
| 2     |                                     |                            |        |        |        |
| 3     | 40                                  |                            |        |        |        |
| 4     |                                     |                            |        |        |        |
| 5     | 40                                  |                            |        |        |        |
| 6     |                                     |                            |        |        |        |

Table 3.6: SEM micrographs of grooves at the considered machining distances for NSC

15 silicon probes. Scale bars: 20  $\mu\text{m}$ .

the bluntness of AFM tips. A similar phenomenon can be reported for Trial 4. In this case, the *H/D ratio* values at the start and the end of this trial were both less than one. The SEM micrographs displayed in Table 3.6 corroborate this as chips were found on the workpiece surface for all the machining distances. However, the SEM profile extracted for this trial again suggest that the probe was quite blunt (see Figure 3.12(d)). The fact that this tip still managed to machine in the cutting-dominated regime is also most likely due to the fact that the cutting edge radius for the profile perpendicular to that reported in Figure 3.12 is still relatively sharp.

For Trials 1, 5 and 6, it is believed that the machining was taking place only in the ploughing-dominated regime throughout as the values of the *H/D ratio* are always more than one. This can be clearly observed in Figures 3.17(a), (e) and (f) as the pile-up are much higher than the groove depth compared to other trials when the machining was carried out in the cutting-dominated regime. Additionally, the SEM micrographs shown in Table 3.6 confirm that for all these three trials no chips were formed. Overall, the observations reported in this section tend to support the method reported in Ahn and Lee (2009) to detect the transition between the ploughing and cutting regime via the assessment of the *H/D ratio* based on the topography of the cross section of machined grooves.

### 3.5 Conclusions

This chapter reported experimentally investigations on the wear behaviour of silicon tips during AFM tip-based machining of single crystal copper. Two machining parameters were varied, i.e. the applied normal force and the machining direction. In the framework of this study, a simple discretisation approach was also proposed to assess the

tip volume based on the knowledge of its 2D profile. In particular, this approach consists in considering the tip into a stack of frustums of right circular cones instead of into a stack of circular elements.

In the reported research, although grooves could be successfully machined over the considered processing distance for each trial, the results obtained highlight the limitation of using silicon probes for such operations. In particular, these probes are very prone to initial tip fracture. This phenomenon makes it difficult to draw firm conclusions about the influence of the studied parameters on the tip wear. Nevertheless, it could still be said that the amount of fractured tip material appears to become larger with the augmentation of the normal applied force. The occurrence of such initial fracture should be avoided as it is very difficult to control and predict the subsequent groove formation mechanism and the wear rate evolution. This is due to the fact that, as the conducted experiments suggest, these process outcomes are dependent on the resulting tip geometry after fracture. More specifically, the tip geometry influences the contact area between the probe and the sample and thus, the stress concentration at the tip apex. The resulting geometry for a fractured tip also plays a role in determining whether machining is taking place in the ploughing-dominated or cutting-dominated regime, which in turn is expected to influence the machining force and thus, the wear.

The combination of measurements used for tip characterisation throughout the wear tests in this work provides a methodology for obtaining a quantitative understanding in the nanoscale degradation of AFM tips with machining. Radius measurements are only best to be used when the probe has no fracture. In comparison, area and volume wear loss metrics and groove measurements are generally in agreement and thus, provide more

representative data about the condition of AFM probe tips. Moreover, despite the fact that measurements via direct SEM imaging of the tip only obtain leads to two dimensional data, these still could provide a detailed picture of the geometry of the tips.

Finally, the combined analysis of the SEM micrographs of the machined grooves and their cross section data obtained from AFM scans indicates that the transition between the ploughing and cutting regime may be detected via the assessment of the *H/D ratio* from Ahn and Lee (2009). In comparison with these authors, a larger range of machining conditions were considered here. However, further experiments should still be conducted to confirm this initial observation.

Based on the results obtained in this study, the following chapter will focus on the investigation of tip wear during AFM probe-based machining using a harder tip material in an attempt to overcome the limitation of Si tips. Additionally, given the limitation of using 2D profiles for assessing the tip wear, in the next chapter, a 3D in-situ technique will be employed, namely the ultra-sharp tip scan method.

## **CHAPTER 4:**

# **ASSESSMENT OF WEAR FOR AFM SILICON PROBES WITH DIAMOND-COATED TIPS USING THE IN-SITU ULTRA-SHARP TIP SCAN METHOD**

## CHAPTER 4

# ASSESSMENT OF WEAR FOR AFM SILICON PROBES WITH DIAMOND-COATED TIPS USING THE IN-SITU ULTRA-SHARP TIP SCAN METHOD

### 4.1 Overview

In Chapter 3, AFM probe tips in silicon were measured and analysed from geometric data acquired by SEM. Although nano-scale grooves could be produced for each considered processing condition on a single crystal copper substrate using such probes, it was observed that these tips were very prone to fracture after a very short machining distance. The important consequence of such tip fracture on the obtained groove topography and processing mechanism was also confirmed and discussed. For this reason, AFM silicon probes with diamond-coated tips were used in this chapter with the aim to overcome the limitation of silicon tips. Considering that diamond-coated tips should be less prone to wear, the studied machining distance was increased by 2 mm in comparison with the previous experimental work conducted in Chapter 3. The set applied normal force and machining speed were also reduced in order to observe and analyse the diamond-coated tip behaviour for conditions thought to decrease the likelihood of tip breakage during the nanomachining process.

In addition, the characterisation of the AFM tips was carried out not only using SEM inspections but also, using an in-situ method, namely the ultra-sharp tip scan approach. This technique was implemented with the aim to enable the analysis of the tip apex geometry based on 3D data rather than solely 2D profiles as was the case in Chapter 3. However, SEM micrographs of the considered tips were still used as a reference against

which the cross sectional profiles extracted from the ultra-sharp tip scan method could be compared. Finally, the influence of considering different vertical distances from the tip apex when selecting profile data for the calculation of the tip radius was also studied in this chapter.

## 4.2 Experimental set-up and methodology

### 4.2.1 AFM system and workpiece preparation

The experimental set-up as well as the machining and workpiece preparation methodologies adopted in this chapter were identical to the work reported in Chapter 3. Thus, the experiments were conducted on the XE-100 AFM using the XEL software and the “*z-scanner*” mode of the AFM instrument. The same single crystal Cu workpiece was also employed. Prior to the start of the machining trials, the polishing procedure for soft materials was repeated on this workpiece to avoid possible prior contamination of its surface.

### 4.2.2 AFM probes

The silicon probes with diamond-coated tips used for these experiments were the model DCP20 from NT-MDT. A SEM micrograph of this type of probes is shown in Figure 4.1. The nominal radius value for tip apex of these probes is specified as 35 nm by the manufacturer. The probe cantilever was not rectangular but displayed a V-shaped geometry. It was designed such that it has a nominal normal spring constant,  $k$ , in the range 28 N/m to 91 N/m. The complete set of specifications for these probes is given in Table 4.1. In this chapter, the calibration procedure carried out to assess the normal spring constant of each probe is that proposed by Neumeister and Ducker (1994) for V-shaped cantilevers.

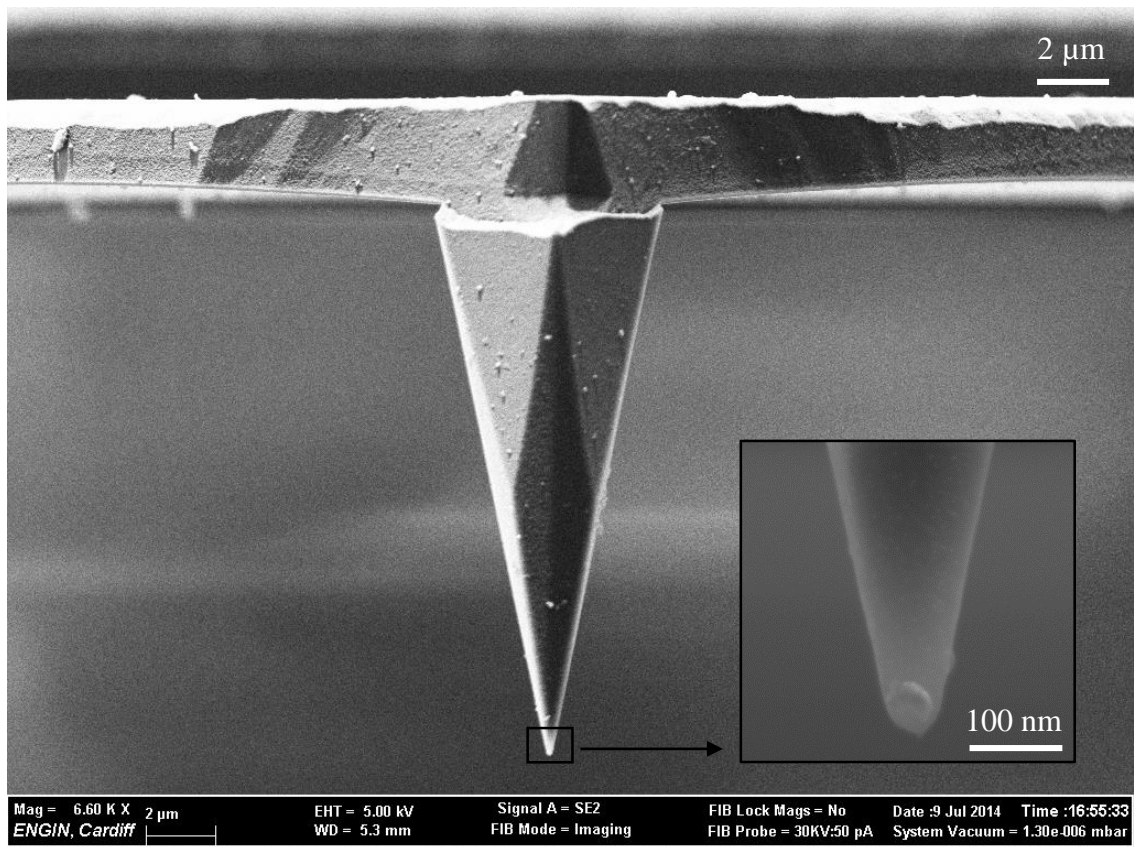


Figure 4.1: SEM micrographs of a typical DCP20 probe.

| Probe         | Resonance frequency (kHz) |         |     | Force constant (N/m) |         |     | Cantilever                 |                           |                        |
|---------------|---------------------------|---------|-----|----------------------|---------|-----|----------------------------|---------------------------|------------------------|
|               | min                       | nominal | max | min                  | nominal | max | Length<br>$l$<br>± 5<br>μm | Width<br>$w$<br>± 3<br>μm | Thickness<br>$t$<br>μm |
| DCP 20 series | 260                       | 420     | 630 | 28                   | 48      | 91  | 90                         | 60                        | 1.7 – 2.3              |

Table 4.1: Probe specifications for the DCP20 model from NT-MDT.

### 4.2.3 Experimental procedure

For each DCP20 probe utilised, Figure 4.2 illustrates the overall procedure implemented to conduct the nanomachining experiments and to acquire data for the subsequent assessment of the tip wear. First, the 2D profile of the unused probe was recorded using SEM. Then, 3D geometric data of its tip apex were obtained prior to machining by implementing the ultra-sharp tip scan method in non-contact mode. To achieve this, ultra-sharp conical probes from Nanoscience Instruments (model ISC 125C40/-R) were utilised. As specified by the manufacturer, these probes have a nominal tip radius less than 5 nm and an included angle less than 5°. The scan direction used was parallel to the long axis of the cantilever. The resolution of the obtained AFM image for inspected tips was set at 256 x 256 pixels. This in-situ method was also performed at different stages of the nanomachining experiments until the overall cutting length of 5 mm was completed. In particular, the assessment of the tip wear using the ultra-sharp tip scan technique was performed at 0.5 mm, 1 mm, 2 mm, 3 mm and finally 5 mm of machining. Once the cutting experiments were completed for a given probe, a final SEM inspection was realised to acquire a second 2D profile of its tip apex. The purpose of obtaining these SEM images was to enable an analysis of the agreement between SEM profiles and cross-section profiles extracted from the 3D geometry of the tip.

In addition, between each machining intervals, and prior to the ultra-sharp tip scan inspection, the probes were cleaned using a two-step indentation process to remove the chips that could be accumulated around its tip apex. This process was the same as that followed by Gozen and Ozdoganlar (2014). In comparison with the overall procedure

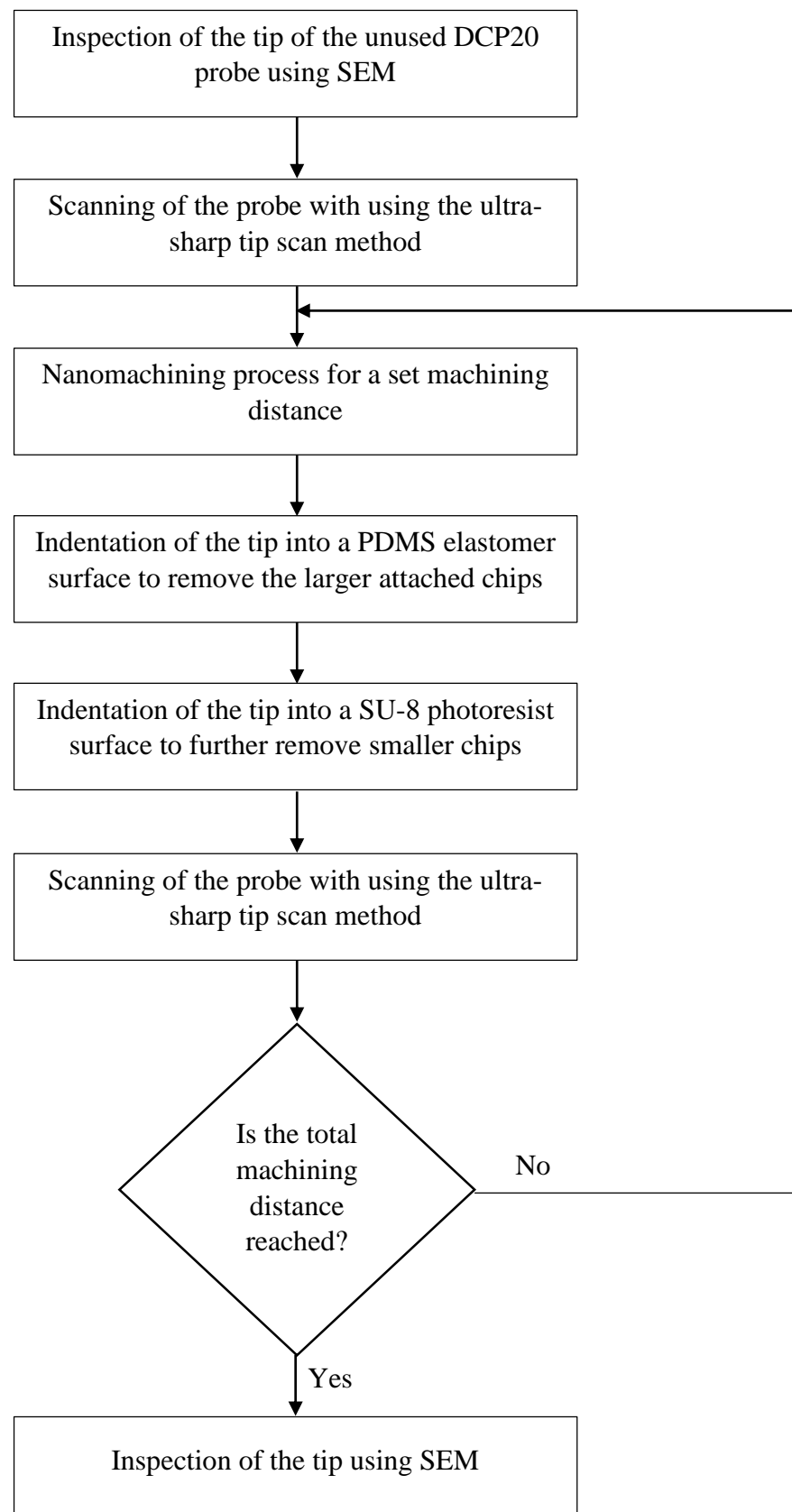


Figure 4. 2: Experimental procedure.

followed in Chapter 3, removing chips from the tip apex was required here as the presence of such chips could affect the quality of the AFM images obtained with the ultra-sharp tip technique. The first step of this cleaning process was to press the tip against an elastomeric polydimethylsiloxane (PDMS) surface. This aimed to remove the larger chips wrapped around its apex. A second indentation step into a soft SU-8 photoresist surface was also implemented to ensure the removal of smaller chips. For both of these steps of the cleaning process, 16 indentations were performed by applying a normal load of 20  $\mu\text{N}$ .

#### 4.2.4 Cutting conditions

In this chapter, it was decided to vary only two process parameters, namely the pre-set applied load and the machining direction, similarly to Chapter 3. However, the particular machining speed used was 2  $\mu\text{m/s}$  while the considered applied loads were 40  $\mu\text{N}$  and 20  $\mu\text{N}$ . The same three different machining directions, as already described in Chapter 3, were used. Due to the fact that the previously studied AFM silicon probes tended to be affected by an initial fracture during the nanomachining operations, in this chapter the values for the machining speed and applied load were selected to reduce the possible occurrence such tip breakage. This was considered in addition to the fact that diamond-coated tips were investigated. One of the selected applied force values was kept at 40  $\mu\text{N}$ , as in Chapter 3, to observe if fracture still occurred for this load. By selecting the second set applied force at 20  $\mu\text{N}$ , the intention was also to observe whether the cutting dominated regime could take place for such a reduced applied force. Finally, the machining distance was increased to 5 mm, in comparison with 3 mm for Chapter 3, in order to maximise the likelihood of being able to detect and measure tip wear. In total,

six machining trials could be designed. The summary of the experimental conditions for each trial is shown in Table 4.2.

### **4.3 Methodology for tip wear assessment**

#### **4.3.1 Ultra-sharp tip scan technique**

In this chapter, the particular implementation of the ultra-sharp tip scan technique to characterise the AFM probe was similar to that reported by Gozen and Ozdoganlar (2014). Figure 4.3(a) provides a schematic illustration of the method. In addition, SEM micrographs of a typical ultra-sharp tip probe and of a typical diamond-coated tip are shown in Figure 4.3(b) to provide a qualitative comparison between the dimensions of both types of probes. It can be observed from this figure that ultra-sharp tips have a significantly lower apex radius and a higher aspect ratio compared to the DCP20 probes. Similarly, to the method followed by Gozen and Ozdoganlar (2012), a low-pass spatial filter was applied on the obtained AFM topography images in order to reduce the possible artefacts and noise that could affect the quality of the scans obtained with the ultra-sharp tip scan method. This filtering procedure resulted in smoothing the overall surface of the scanned AFM images by removing the occurrence of small and sharp spikes while making sure that the overall scanned height of the tip was not affected. This process was conducted using XEI software with the weight ratio of 1.3.

#### **4.3.2 Tip radius measurements**

The apex radius for each tip was estimated using the formula already reported in equation (3.6) in Chapter 3 where the radius of curvature is calculated at the maximum point of a polynomial of degree two fitted on a 2D profile. Additionally, in this chapter, the influence of different vertical heights from the tip apex over which this profile is fitted

| Trial number | Set normal force ( $\mu\text{N}$ ) | Machining direction | Machining speed ( $\mu\text{m/s}$ ) | Machining distance (mm) |
|--------------|------------------------------------|---------------------|-------------------------------------|-------------------------|
| 1            | 40                                 | 1                   |                                     |                         |
| 2            | 40                                 | 2                   |                                     |                         |
| 3            | 40                                 | 3                   |                                     |                         |
| 4            | 20                                 | 1                   | 2                                   | 5                       |
| 5            | 20                                 | 2                   |                                     |                         |
| 6            | 20                                 | 3                   |                                     |                         |

---

*Note: the value for the parameter “machining direction” refers to the definition adopted in Chapter 3 as already described with Figure 3.6.*

Table 4.2: Selected AFM tip-based nanomachining parameters.

was examined first to assess its effect on the obtained radius values. This was done for all six probes considered for both 2D SEM profiles and 2D profiles obtained from the 3D AFM data acquired with the ultra-sharp tip scan technique. This initial study could then be used to determine a constant height value over which all subsequent radius calculations could be applied. This particular analysis will be reported and discussed later in Section 4.4.1.1. Based on the selection of a constant vertical height from the tip apex, the radius for each tip was then calculated as the average value obtained from four different cross sections from the 3D data. As shown in Figure 4.4, it is preferable to consider the average radius based on the analysis of several cross sections as the radius calculated from profile data appear to vary as a function of the cross section selected. In this chapter, the considered angles for extracting cross-sectional data were 1)  $0^\circ - 180^\circ$ , 2)  $90^\circ - 270^\circ$ , 3)  $45^\circ - 225^\circ$  and 4)  $135^\circ - 315^\circ$  (see Figure 4.4).

### 4.3.3 Volume loss measurement

The assessment of the tip volume loss was conducted using 3D data obtained from non-contact mode AFM measurements using the ultra-sharp tip scan technique. The volume of the tip for each selected machining distance was estimated using a pixel discretisation approach as shown in Figure 4.5. Particularly, a 2x2 matrix that stores the height of each pixel within a fixed selected region of the AFM scan of the tip was obtained using the Gwyddion data processing software. From the data contained in this matrix, the volume of the tip,  $V_p$ , within the selected area was estimated using the following equation:

$$V_p = \sum_{k=0}^{k=n} z_k \cdot \Delta x \cdot \Delta y \quad (4.1)$$

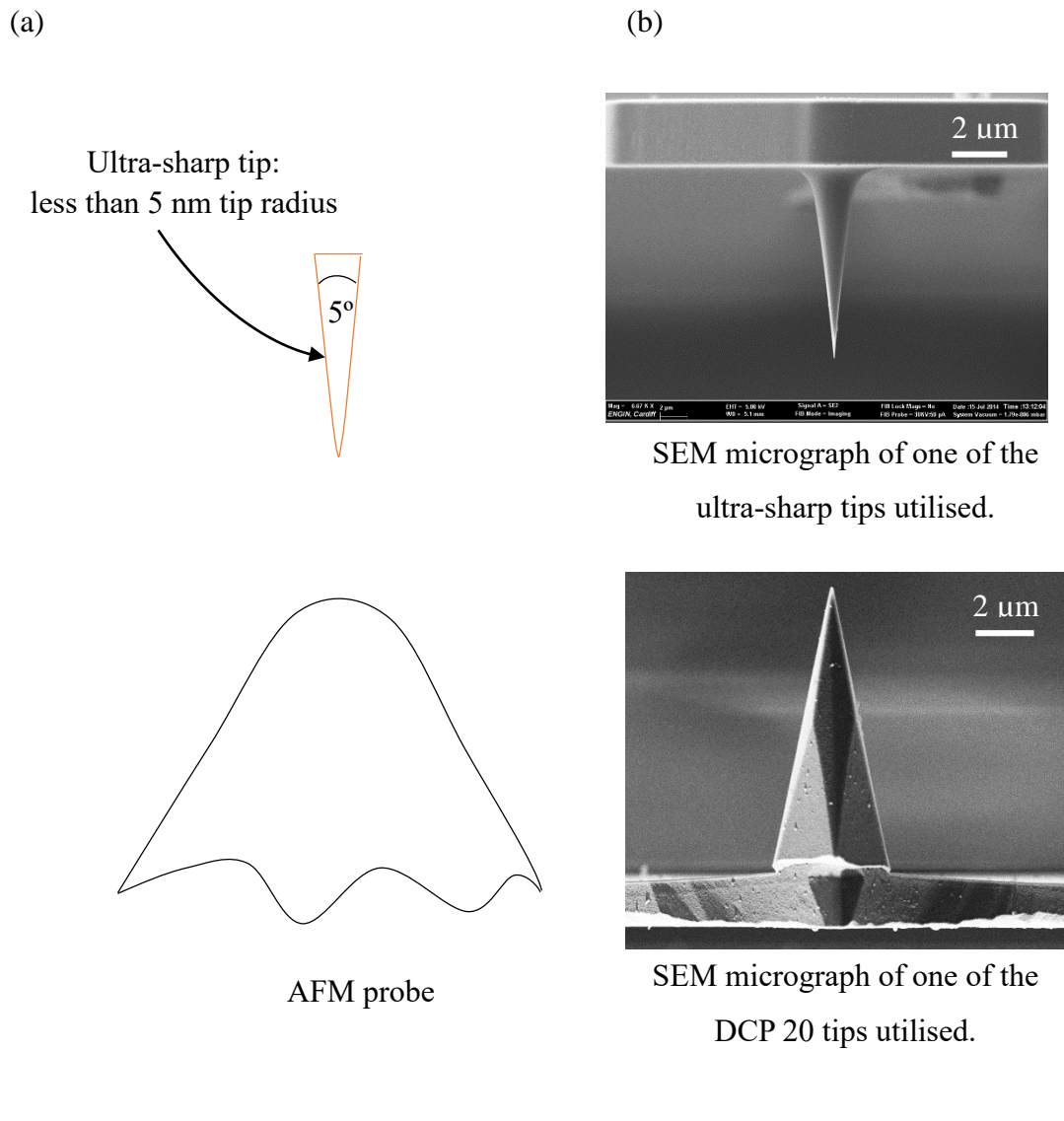


Figure 4.3: (a) schematic diagram of the ultra-sharp tip scan approach; (b) SEM micrographs of an ultra-sharp tip and of a diamond-coated tip at the same magnifications.

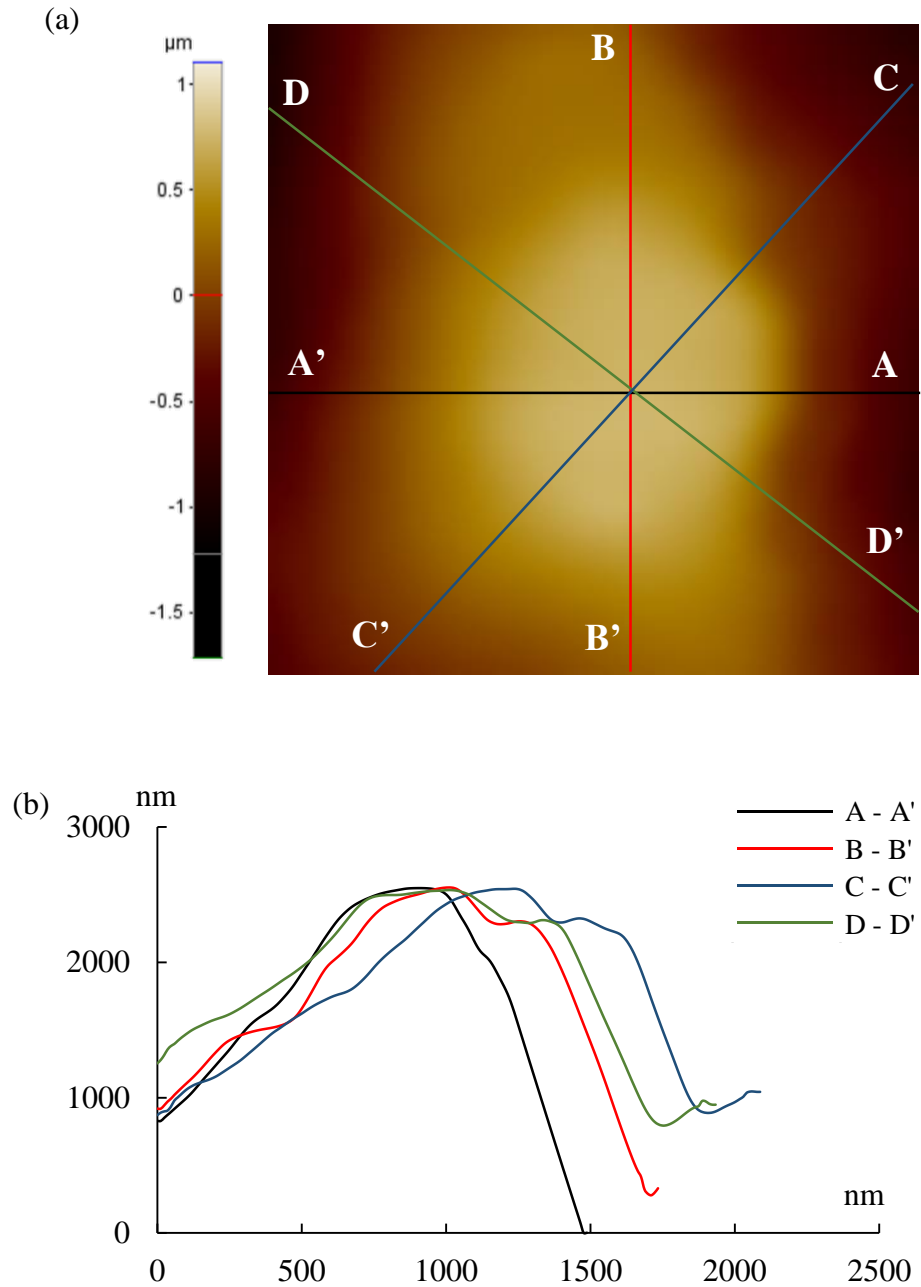


Figure 4.4(a): four different cross section drawn on an AFM probe topography image for an unused DCP20 tip and (b) corresponding profiles from the cross sections shown in (a).

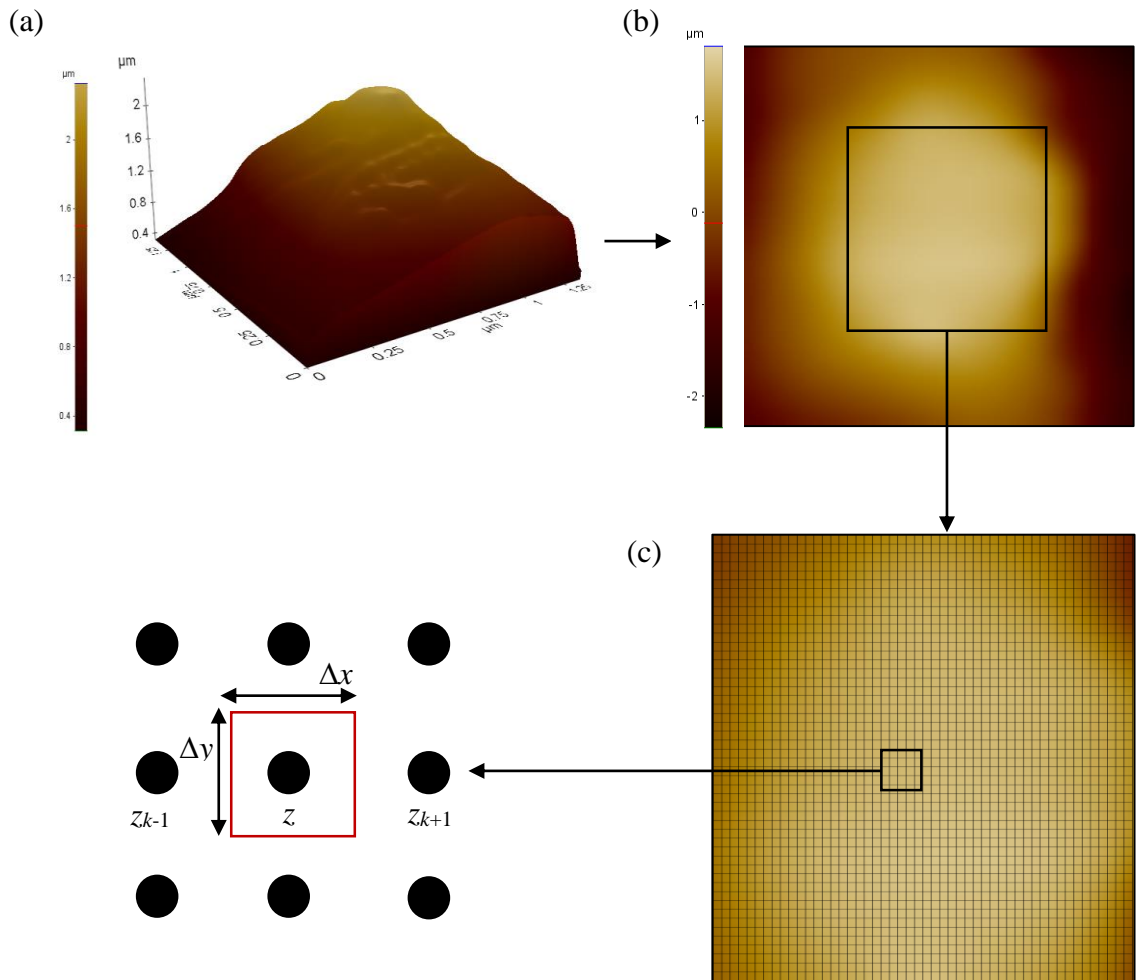


Figure 4.5: (a) 3D AFM topography image of a silicon diamond-coated probe, (b) correspond 2D AFM topography image; (c) Pixel discretisation of the selected area in the 2D AFM topography image.

where  $n$  is the total number of pixels,  $z_k$  is the height of the tip for the  $k^{\text{th}}$  pixel,  $\Delta x$  and  $\Delta y$  represent the resolution of the ultra-sharp tip scan. More specifically,  $\Delta x$  is the distance between two pixels along the  $x$  axis and  $\Delta y$  is the distance between two pixels along the  $y$  axis. In this work,  $\Delta x$  and  $\Delta y$  were both equal to 11.7 nm.

In order to determine over which fixed area the tip volume should be calculated for each probe, an alignment procedure was conducted by comparing the AFM scan of the unused tip and the AFM scan of the same tip after the completion of the experimental trials, i.e. after 5 mm of machining. In this way, it could be ensured that the calculation of the volume of the tip was always carried out over the area which was affected by wear. To perform the alignment of the profiles, the procedure used was similar to the two-dimension profile extraction in Chapter 3 (refer in Section 3.3.1). Particularly, the alignment of the profiles was considered for four different cross sections. Figure 4.6 illustrates the overall procedure followed to estimate the volume loss at each selected machining distance. The “*volume loss*” metric could be obtained from equation 4.2.

$$\text{volume loss} = V_p \text{ unused tip} - V_p \text{ tip after machining} \quad (4.2)$$

The advantage of this volume measurement method is that it can be implemented regardless of the shape of the AFM tip. Thus, it should lead to more accurate results in comparison to other studies where a conical tip shape was assumed (see e.g. Bloo *et al.* 1999 and Yan *et al.* 2016). Indeed, such an assumption may be suitable in the case of unused probes but it should no longer represent appropriately the shape of the tip after using the probe for nanomachining operations. In particular, it is expected that the geometry of the tip apex should be affected by wear and thus, that its profile should become asymmetrical or even display a flat punch surface. The accuracy of the volume

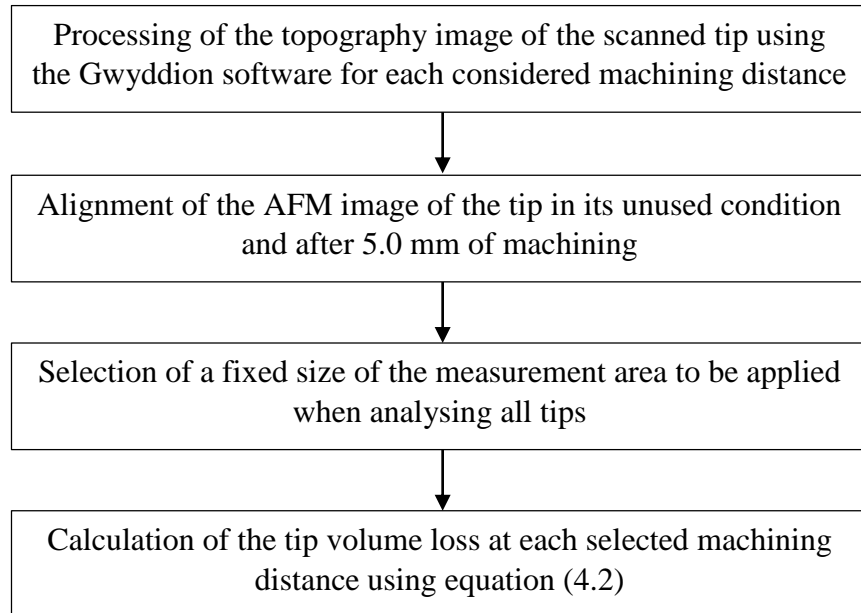


Figure 4.6: Tip volume estimation procedure based on 3D data obtained using the ultra-sharp tip scan method.

loss calculation method followed in this study is influenced by the resolution of the ultra-sharp tip scan. It was considered that a resolution of 11.7 nm was reasonable, because it was about 100 times smaller than the average length of the edges defining the area over which the tip volume was estimated.

#### **4.3.4 Assessment of groove topography**

The same procedure as that reported in Chapter 3 was employed to inspect the generated grooves on the single crystal copper workpiece with both the SEM and AFM instruments. In particular, SEM micrographs were used to provide a qualitative assessment of the grooves and the occurrence of chip formation for all selected machining distances. The groove topography data acquired using the AFM instrument were obtained only for grooves at 0.5 mm and 5.0 mm machining distance. Figure 4.7 illustrates an example of such an AFM scan for a set of three grooves. In order to calculate the average values of the *H/D ratio* at each machining distances, seven cross sections were extracted from the scanned grooves. This was done to determine the machining-dominated regime that took place during the experiments based on the method reported by Ahn and Lee (2009).

### **4.4 Analysis of the results**

#### **4.4.1 Tip radius measurements**

##### **4.4.1.1 Effect of the selected vertical interval from the tip apex**

Radius measurements obtained for all AFM tips under investigation in this chapter are given in Figure 4.8 before the start of the machining experiments. In this figure, the results are given as a function of a vertical distance from the tip apex. This represents the distance, which was considered to extract the tip profile on which the radius calculations

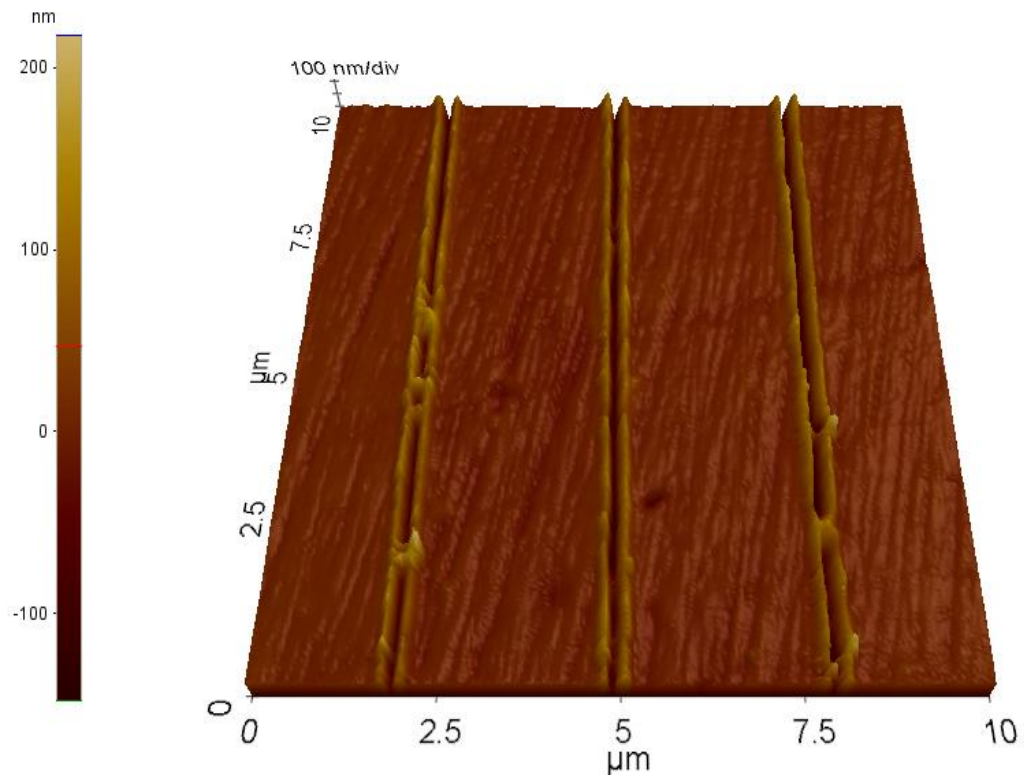


Figure 4.7: Example of a 3D AFM topography image of the produced grooves.

could be performed. In addition, this figure also provides a comparison of the inset graph between the radius estimated from the SEM profile of a tip and the radius obtained from its corresponding cross section based on the scanned 3D data at the vertical distance of 80 nm.

From these results, it is observed that for a selected vertical interval, which is less than 100 nm, the radius values obtained from both characterisation methods generally change rapidly. On the other hand, when considering a distance from the tip apex higher than 200 nm, there is no sudden changes in the calculated radius values. It can also be said that the trend in the evolution of the radius values assessed from both tip characterisation methods agree relatively well. Besides, the values calculated from the ultra-sharp tip scan method are always consistently slightly larger than those obtained with the analysis of SEM profiles. The reason for this can be seen from the observation of the inset graphs of tip profiles provided with each plot in Figure 4.8. Indeed, the cross section profiles obtained with the ultra-sharp tip scan method is always larger than that acquired from an SEM micrograph. This means that the ultra-sharp tip scan method is likely to overestimate the width of an inspected tip. For a region very close to the tip apex, both the SEM and the ultra-sharp tip scan data seem to agree well. It is also worth noting that in the case of Probe 1, the radius values extracted from the 3D data of the tip are actually much larger than those obtained from its SEM profile. This may be due to the fact that the ultra-sharp probe was damaged during the scanning process of this particular tip and thus, suffered significant blunting. In turn, this caused a large error when obtaining the topography of Probe 1.

Apart from the plot for Probe 1, the other graphs indicate that for a selected interval

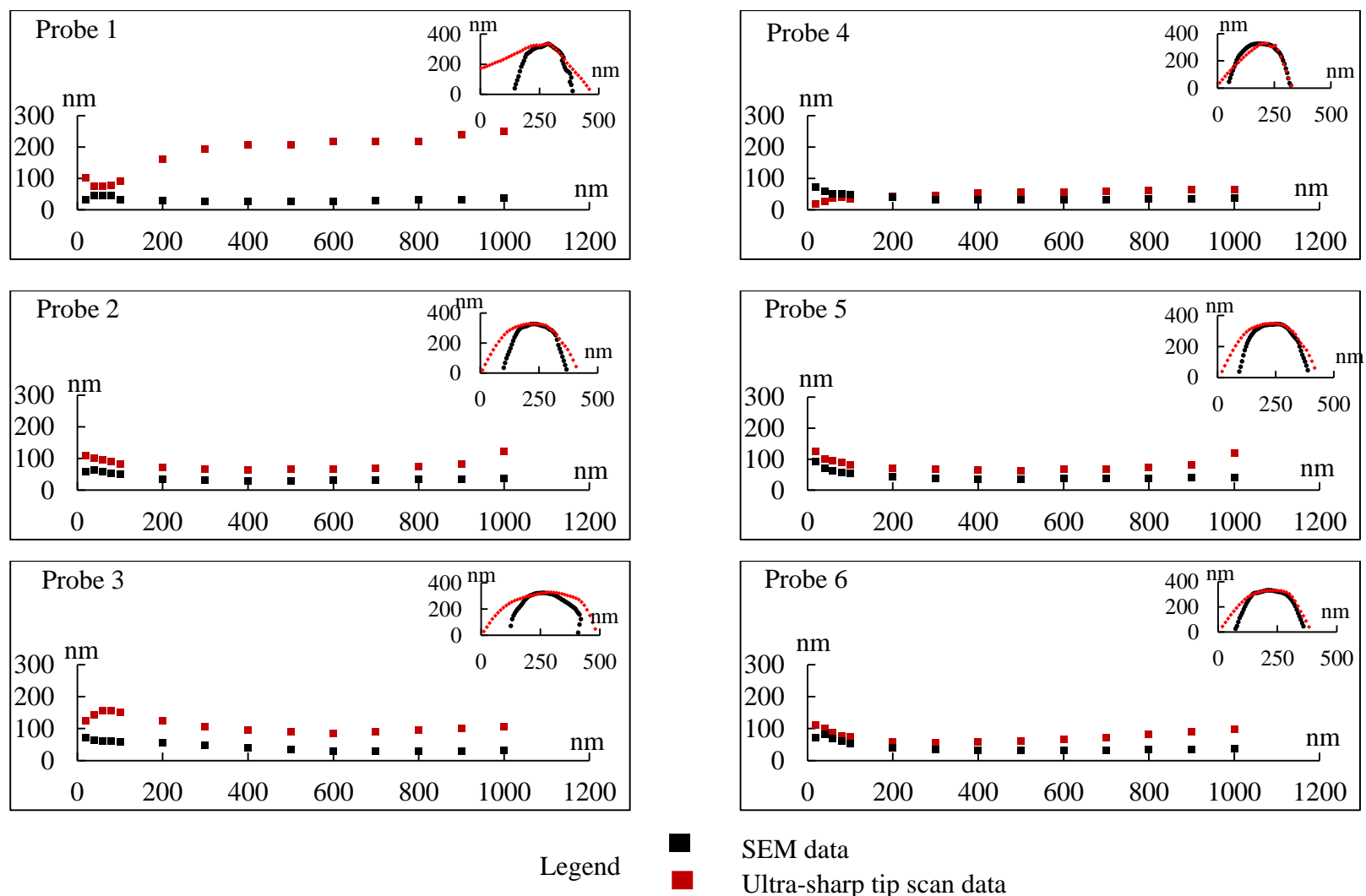


Figure 4.8: Radius measurements as a function of different vertical intervals considered from the tip apex for DCP 20 diamond-coated silicon probes.

higher than 300 nm from the tip apex, the radius measurement can be considered to be stable. Furthermore, in all cases, for a vertical interval higher than 800 nm, the obtained measurements tend to increase slightly. In addition to this observation, it can be argued that considering such a large interval is not appropriate as it is not representative of the tip apex region that is in contact with the workpiece material during AFM tip-based nanomachining operations. Based on these results, it was decided to use a fixed vertical height of 300 nm from the tip apex for all subsequent radius calculations made in this chapter.

#### **4.4.1.2 Analysis of measured tip radius values**

Figure 4.9 shows SEM images of each tip employed prior to the completion of the experimental trials. Based on the procedure described in Chapter 3 to extract the tip profile from a SEM micrograph, Figure 4.10 reports the profiles of each tip in their unused state and also, after 5.0 mm of machining. From this figure, it is argued that a fracture most likely occurred for the tips used for Trials 3 and 4, and that a small tip breakage may also have taken place for Trial 2 (see Appendix D). In addition, Figures 4.11 shows bar graphs to provide a comparison of the radius measurements obtained between the SEM and the ultra-sharp tip scan profiles for 40  $\mu\text{N}$  and 20  $\mu\text{N}$  of applied force. As stated in Section 4.3.2, from an AFM topography image obtained with an ultra-sharp tip scan, the radius was measured for 4 different cross sections. This enabled the calculation of the standard deviation, which is also plotted in Figure 4.11 (see Appendix F).

From the bar graphs shown in Figure 4.11, it is obvious that the radius values obtained from ultra-sharp tip scan profiles are at least twice higher than those acquired from SEM scan profiles. This is consistent with the observation already made earlier with

Figure 4.8. It is believed that the obtained profiles from the ultra-sharp tip scan technique may be affected by the convolution effect. This suggests that the likelihood of damage to the ultra-sharp tip probe, via accidental contacts with the probe under investigation, is not negligible. In fact, experience gained during this work shows that implementing the ultra-sharp tip scan technique is not a straight-forward procedure and requires a very skilled operator. Also, the accurate control of set-up parameters is important for achieving high resolution and truthful AFM topography results (Gan, 2009). In addition, it should be noted that, at a distance of 300 nm from the tip apex, which is the height selected in this chapter to conduct the radius measurement calculations, there should be increased interaction between the sides of both tips (i.e. the tip under investigation and the ultra-sharp tip). This could influence the attractive forces between both surfaces, which in turn would affect the topography obtained when using the ultra-sharp tip scan technique in non-contact mode.

Figure 4.12 presents the radius measurements obtained from ultra-sharp tip scans for all trials at the different selected machining distances (i.e. 0.0 mm, 0.5 mm, 1.0 mm, 2.0 mm, 3.0 mm and 5.0 mm). Based on this, a linear function was fitted to the data points for each trial to calculate the rate of change of the radius values. These results are given in Table 4.3. This was realised using the data points after 1 mm of machining for this set of experiments, which is when the wear evolution has reached a steadier state.

When machining in *Direction 1*, the graphs plotted in Figure 4.12 show that the radius values at the set applied force of 20  $\mu\text{N}$  are always larger than those when machining at 40  $\mu\text{N}$ . This would appear to be counter-intuitive at first. One reason for this result is the fact that, prior to the start of the experiments, the radius of the probe used

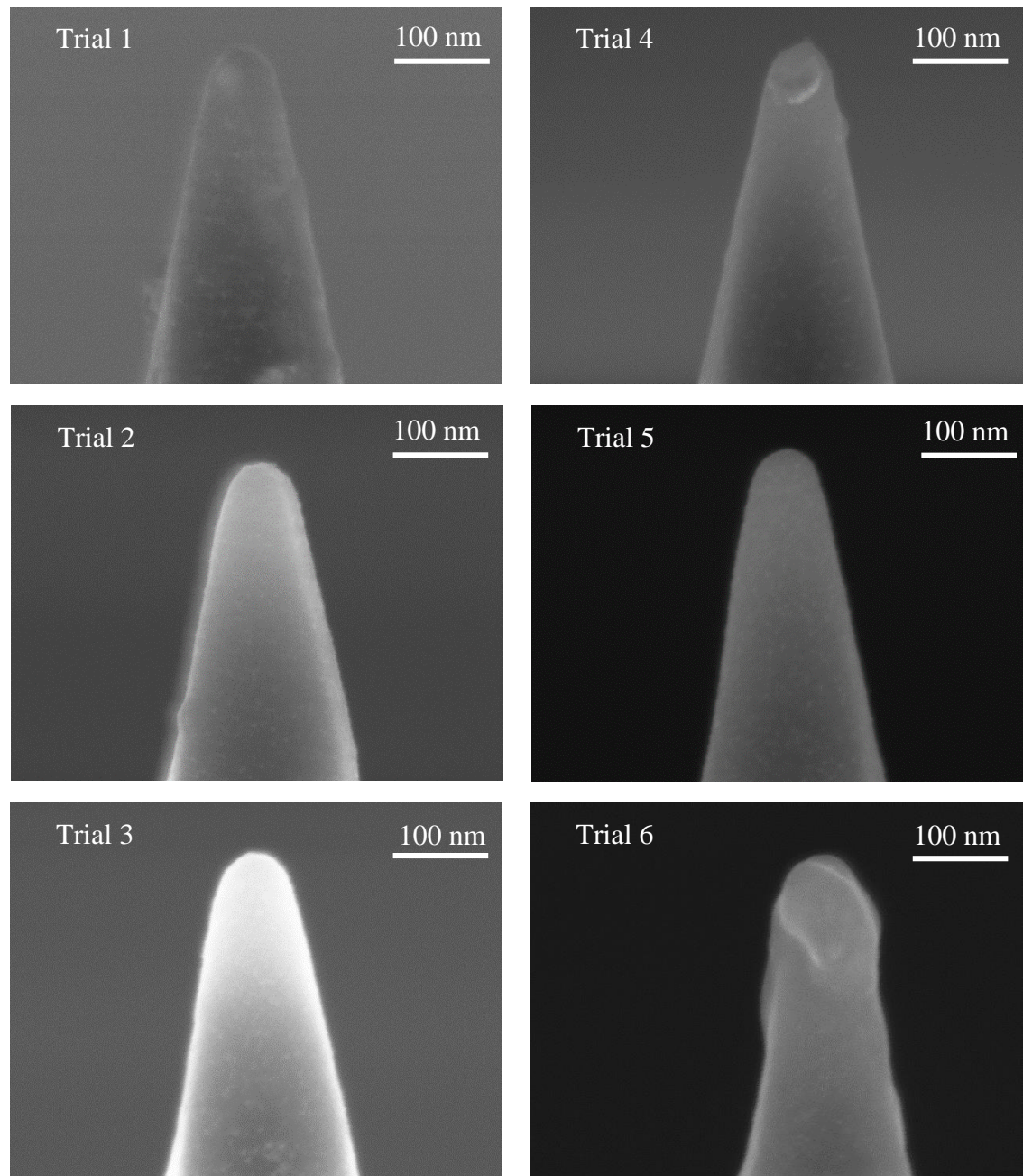


Figure 4.9: SEM micrographs of the six DCP 20 silicon tips coated with diamond, which were used in this chapter prior to the start of the experimental trials.

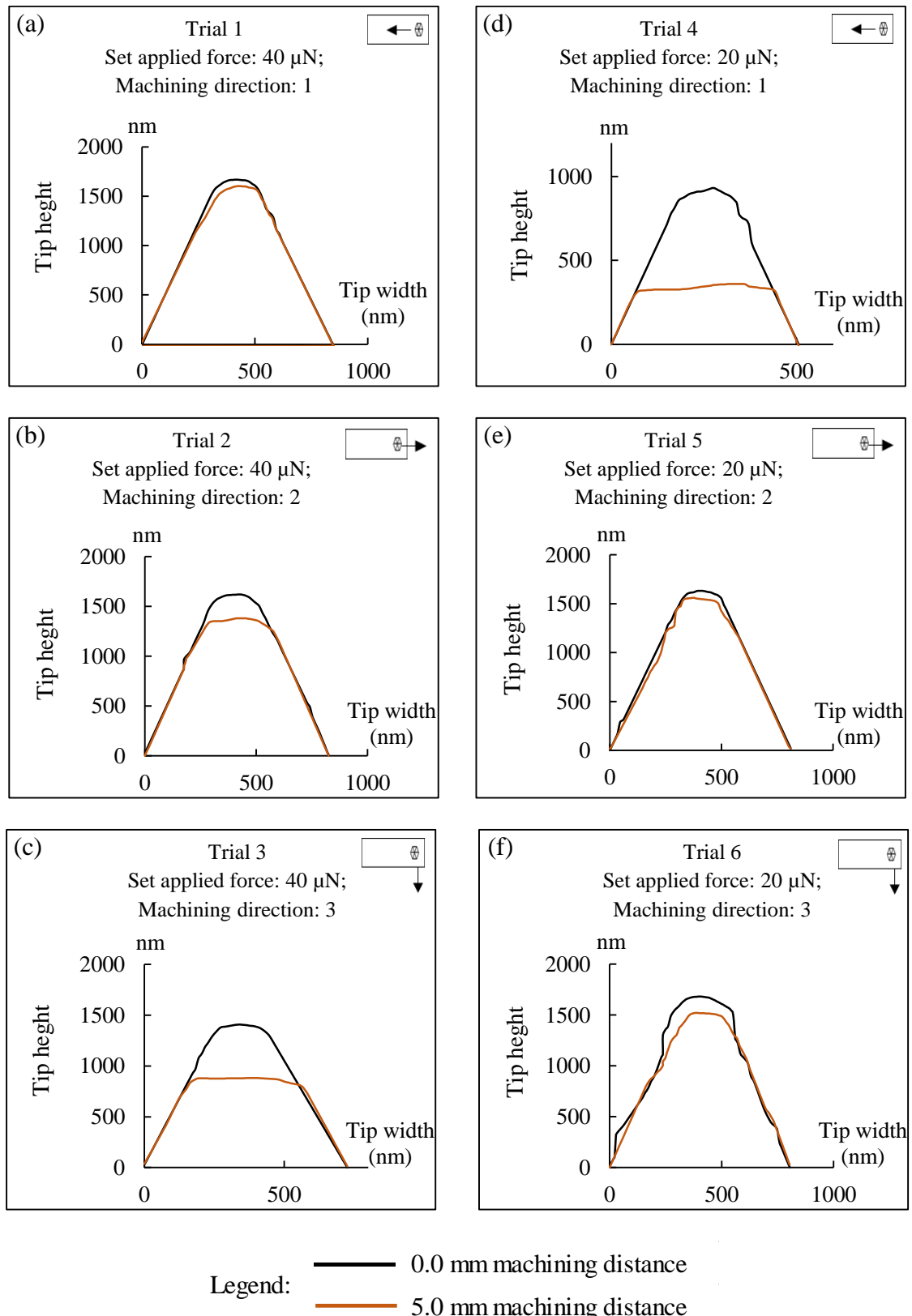


Figure 4.10: Tip profiles before and after the completion of the machining trials for each

DCP 20 diamond-coated silicon probe.

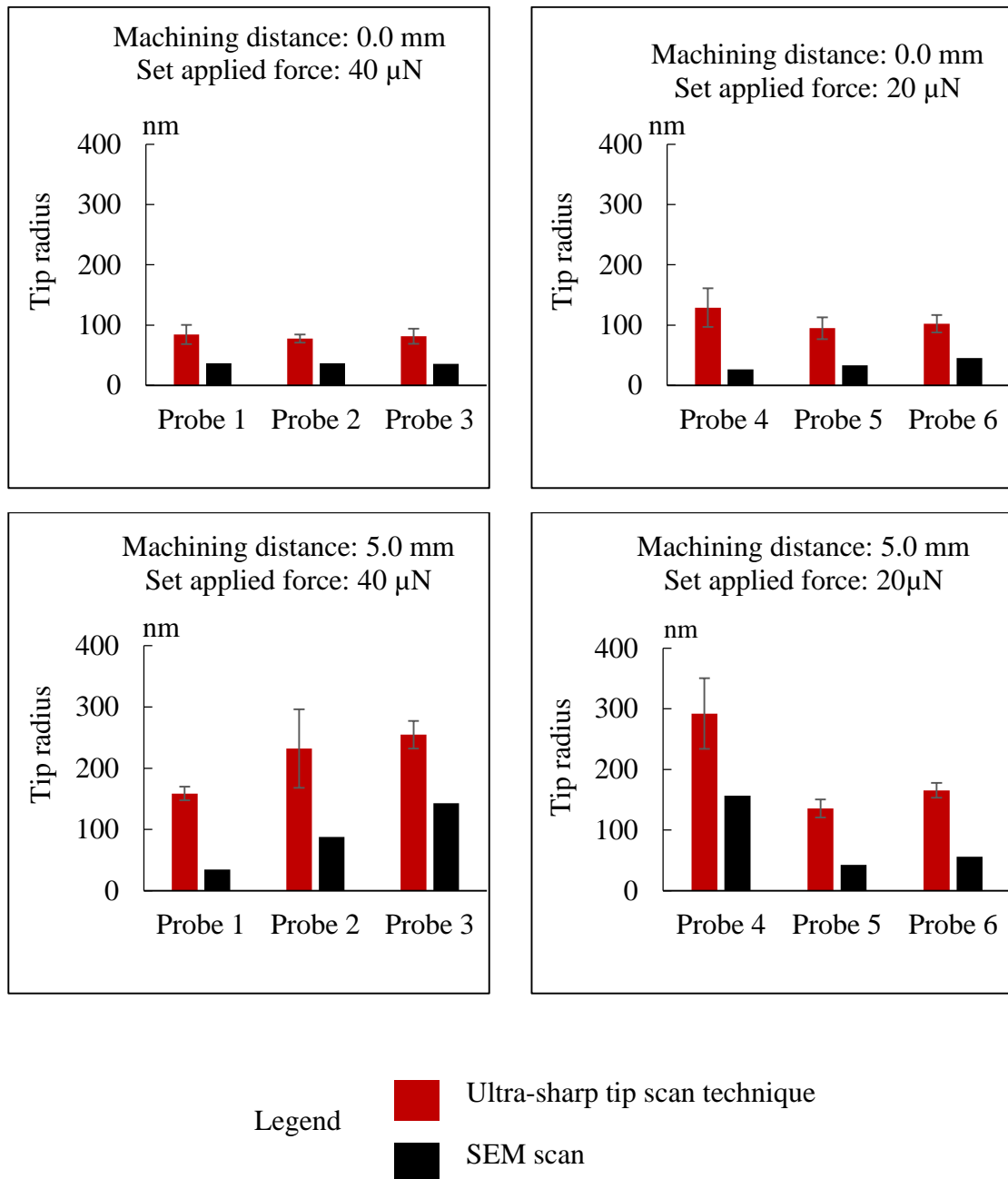


Figure 4.11: Comparison of the radius measurements obtained from ultra-sharp tip scan data and SEM data for machining distances of 0.0 mm and 5.0 mm. The error bars show the standard deviation.

for machining at 20  $\mu\text{N}$  of applied force was already larger than that of the probe used for machining at an applied force of 40  $\mu\text{N}$  (i.e. a radius value of 110 nm against 84 nm). At the same time, it should be noted from Table 4.3 that the rate of change in the tip radius was higher for the smallest applied load along this particular machining direction. This can be explained by the fact that the tip suffered a fracture for the experiments conducted at 20  $\mu\text{N}$  as it displayed a flat punch geometry at the end of the machining operations (c.f. Figure 4.10). Thus, it could be that the machining for Trial 4 (i.e. along *Direction 1* and with 20  $\mu\text{N}$  of applied force) was conducted under the ploughing-dominated regime and thus, that the tip suffered from higher lateral force compared to Trial 1 (i.e. along *Direction 1* and with 40  $\mu\text{N}$  of applied force), which caused its breakage.

For the other two machining directions (i.e. *Directions 2* and *3*), the radius values appear to be directly dependent on the magnitude of the applied force. Particularly, a higher applied normal force (i.e. 40  $\mu\text{N}$ ) led to a larger radius value following the completion of the experimental trials for both considered machining directions. This observation is also accompanied by the fact that, for both of these directions, the rate of change in the radius value is always higher for the set applied force of 40  $\mu\text{N}$  (see Table 4.3). At the same time, it should be noted that both probes used to machine at this higher set applied force seemed to have suffered a fracture (see Figure 4.10).

Finally, when machining along *Direction 2* and for set applied force of 40  $\mu\text{N}$ , the data in Figure 4.12 show that the tip radius decreased between the machining distance from 3.0 mm to 5.0 mm. This should be due to the fact that further nanomachining after 3.0 mm resulted in the tip edges becoming more rounded in comparison with a geometry, which was closer to that of a flat punch until 3 mm of machining. This phenomenon was

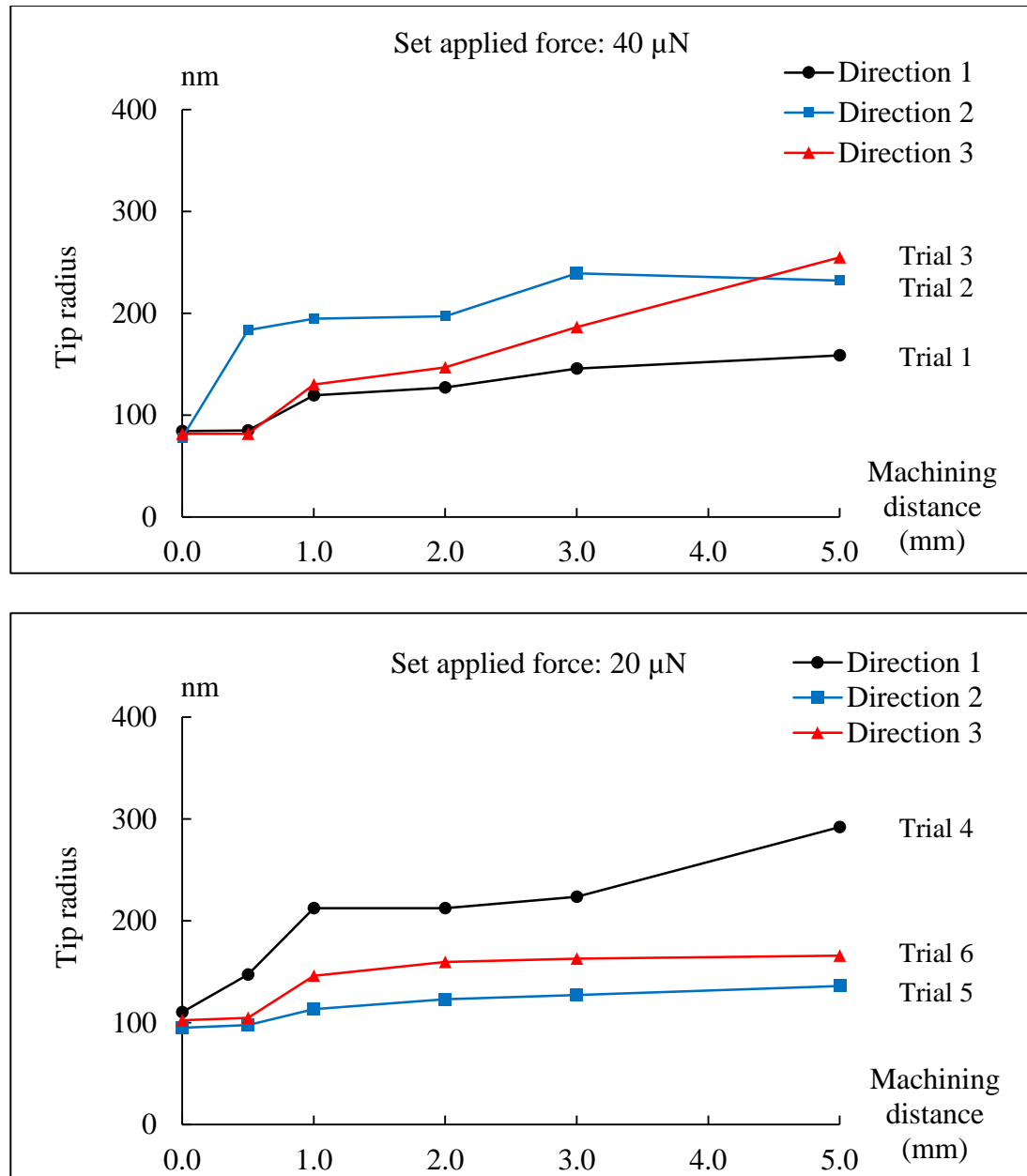
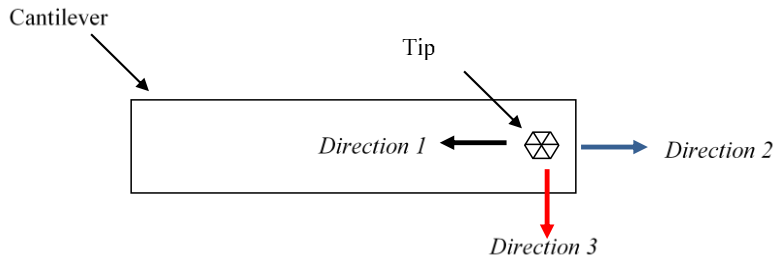


Figure 4.12: Evolution of tip radii as a function of the machining direction for the different values of set normal force considered for DCP 20 diamond-coated silicon probes.

| Machining direction | Trial | Applied normal force ( $\mu\text{N}$ ) | Rate of change of tip radius (nm / mm)<br>between the machining points 1.0 mm until 5.0 mm |
|---------------------|-------|--|--|
| 1                   | 1     | 40                                     | 10.2   |
|                     | 4     | 20                                     | 20.9   |
| 2                   | 2     | 40                                     | 10.7   |
|                     | 5     | 20                                     | 5.4  |
| 3                   | 3     | 40                                     | 32.3   |
|                     | 6     | 20                                     | 4.4  |

Table 4.3: Rate of change of the radius values based on the plots in Figure 4.12.

also observed in Chapter 3 and it could be said that it happened more frequently when using silicon tips. The increased occurrence of such a phenomenon for this type of tips could be due to two main reasons. First, for the same applied load and direction, given that silicon tips should be more brittle than diamond-coated ones, they are more likely to break and thus, to exhibit a flat punch geometry as result. Consequently, this raises the value of the tip radius measured. Second, the subsequent wear of the square edges of such tips should be more prominent with silicon tips, thus reducing the measured radius more readily when completing further machining.

#### 4.4.2 Volume loss measurement

Based on the analysis of the acquired 3D data, Figure 4.13 plots the evolution of the volume loss metric for each tip as a function of the machining length and for both applied loads considered (see Appendix F). In particular, the metric presented for each trials in Figure 4.13 is for a single measurement. The observation of Figure 4.10 earlier suggested that a breakage most likely occurred for the tips used for Trials 3 and 4, and possibly for Trial 2 also. This is confirmed with Figure 4.13. Indeed, as a sharp rise in the volume loss evolution can be seen for Trial 3 between 0.5 mm and 1.0 mm of machining. For Trial 4, this sharp rise took place at some point after 3.0 mm of machining distance. In the case of Trial 2, it is likely that a small fracture occurred indeed between 1.0 mm and 2.0 mm of machining. Based on this combined data from Figure 4.10 and Figure 4.13, it can be said that despite the expected improved durability of diamond-coated silicon tips in comparison with pure silicon tips, these can still be subject to fracture. It is interesting to note that this phenomenon is observed even though the set applied force was the same, i.e. 40  $\mu\text{N}$ , or lower, i.e. 20  $\mu\text{N}$ , than that studied in Chapter 3. However, when comparing the tip profiles obtained in Chapter 3 (c.f. Figure 3.12) and in this chapter (c.f. Figure

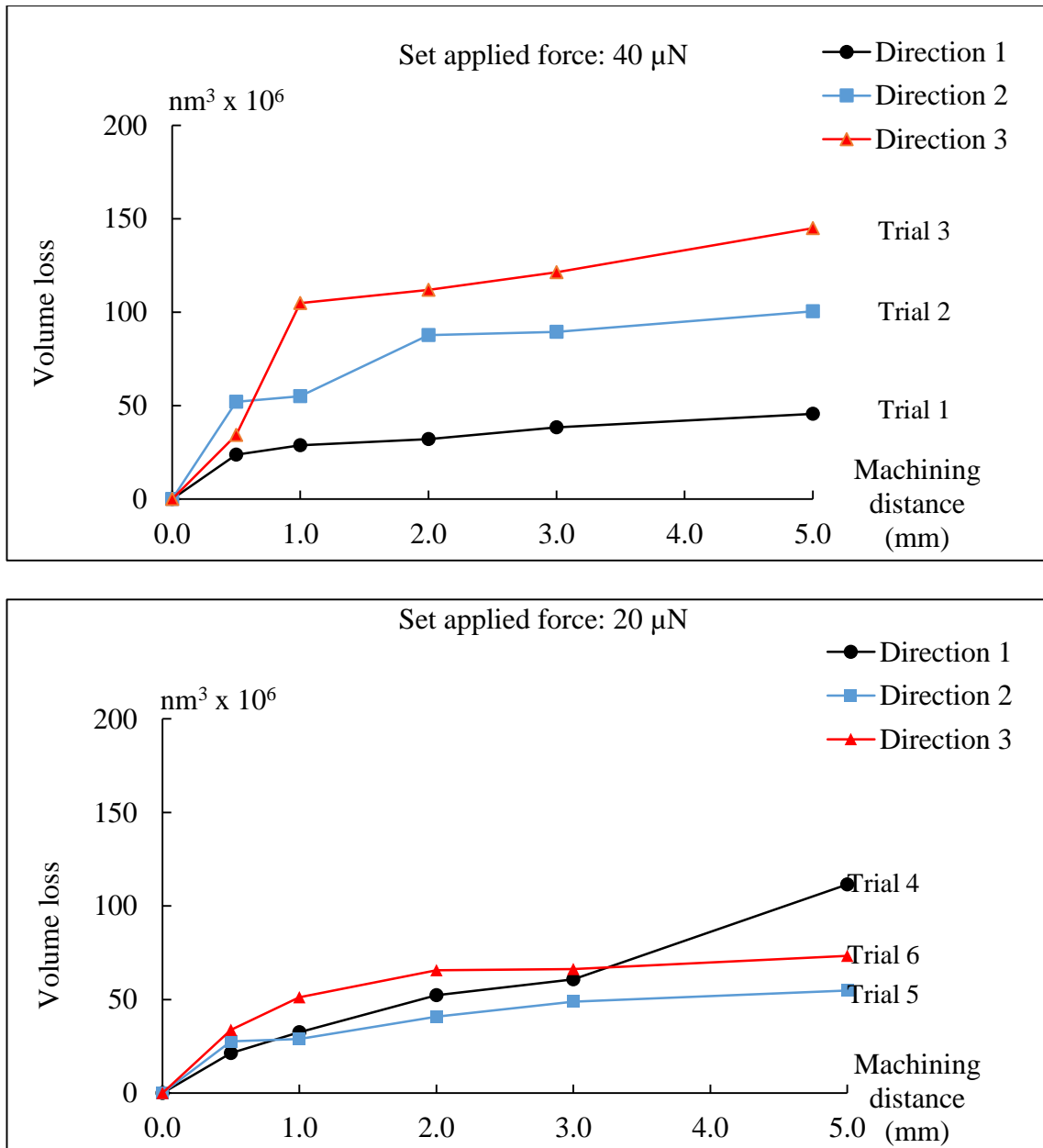
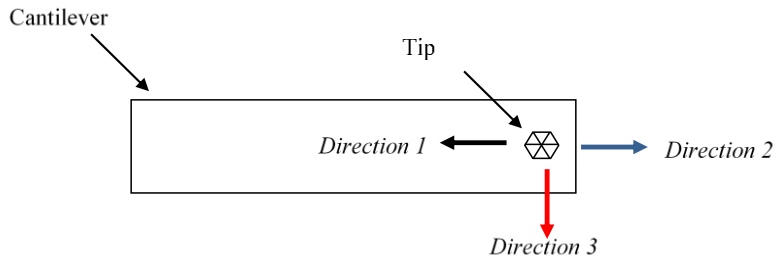


Figure 4.13: Evolution of the tip volume loss as a function of the machining direction for the different values of set normal force considered for DCP 20 diamond-coated silicon probes.

4.10) for the same pre-set applied load (i.e. 40  $\mu\text{N}$ ), it can still be said that the occurrence of a fracture was reduced when using the diamond-coated silicon tips. In particular, while tip breakage happened for all machining directions with the silicon tips, in this chapter, this happened clearly only along the *Direction 3* and to a lesser extend along *Direction 2*.

Overall, the tip volume loss for a pre-set load of 40  $\mu\text{N}$  tends to be marginally smaller than that measured in Chapter 3 (refer to Figure 3.14) at the same machining distance of 3 mm. Besides, the initial wear of the diamond-coated silicon tips after 0.5 mm of machining is also marginally smaller than that of the silicon tips studied in Chapter 3. However, these comments should be taken with caution as different methods were used to calculate the tip volume values between this study and that of Chapter 3. In addition, the amount of material removed from the tip when machining in *Directions 2 and 3* seems to be dependent on the magnitude of the applied force. Indeed, for these experimental trials, the higher applied normal force led to a larger portion of removed tip material. The same conclusion can be reached when comparing the rate of change for the volume loss between an applied load of 40  $\mu\text{N}$  and 20  $\mu\text{N}$  for both of these directions. In particular, a higher applied load results in a faster volume loss. These observations cannot be made for the trials conducted along *Direction 1* (i.e. for Trials 1 and 4). However, this result is in-line with the analysis made earlier when the radius measurements between both trials were compared. In particular, it was proposed that for Trial 4, the tip suffered from higher lateral force compared to Trial 1 because machining could have been conducted under the ploughing-dominated regime in this case. The characterisation of the corresponding grooves, which is the focus of the next section, should enable to confirm, or reject, this hypothesis.

#### 4.4.3 Machined grooves

Table 4.5 shows the SEM micrographs for the set of grooves machined in this chapter along the different considered machining directions. In this table, results are available only for Trials 1, 2, 4 and 5. Indeed, no grooves could be detected with the SEM. Based on the groove topography obtained using the AFM instrument, the *H/D ratio* for each trial was calculated using the formula from Ahn and Lee (2009), which was already reported with equation (3.7) in Chapter 3. These results are given in Table 4.6. From the data in this table and from the obtained SEM micrographs in Table 4.5, it can be said that the machining process was most likely to take place in the cutting-dominated regime for the higher pre-set applied normal force of 40  $\mu\text{N}$ . Particularly, the *H/D ratios* for machining distances of 0.5 mm and 5.0 mm are less than or close to one for both Trials 1 and 2. In addition, the corresponding SEM micrographs of the generated grooves display chip formation on the copper workpiece, except for the last machining distance for Trial 2. The possible reason behind this observation should be due to the gradual change in tip geometry as a result of wear, which led to the ploughing regime becoming the dominant processing mechanism after 3 mm of machining.

On the contrary, for the lower normal applied force of 20  $\mu\text{N}$ , i.e. for Trials 4 and 5, the *H/D ratio* data and SEM micrographs shows that the machining process was mostly realised in the ploughing-dominated regime (neither SEM nor AFM data could be recorded for Trial 6). Thus, these results confirm the hypothesis put forward in the previous section that, for Trial 4, machining was conducted under the ploughing-dominated regime, in comparison with Trial 1. It is also worth mentioning that, along both *Directions 1* and *2* for which grooves could be easily machined, the fact that chip formation took place at the highest applied load means that this load was sufficiently high

| Machining direction | Trial | Applied normal force ( $\mu\text{N}$ ) | Rate of change of volume loss ( $\text{nm}^3 \times 10^6 / \text{mm}$ ) between the machining points 1.0 mm until 5.0 mm |
|---------------------|-------|--|--|
| 1                   | 1     | 40                                     | 4.3  |
|                     | 4     | 20                                     | 19.4   |
| 2                   | 2     | 40                                     | 9.9  |
|                     | 5     | 20                                     | 6.2  |
| 3                   | 3     | 40                                     | 10.2   |
|                     | 6     | 20                                     | 4.9  |

Table 4.4: Rate of change of volume loss based on the plots in Figures 4.13.

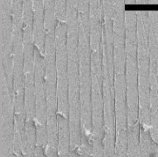
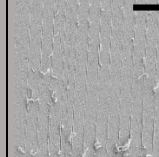
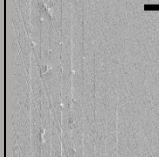
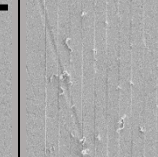
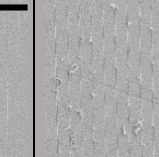
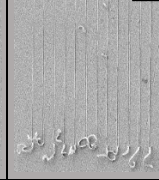
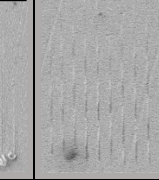
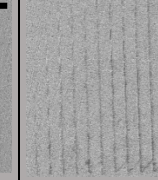
| Trial | Set applied force ( $\mu\text{N}$ )           | SEM micrographs of grooves  |   |  |   |   |
|-------|---|---|---|--|---|---|
|       |   | 0.5 mm  | 1.0 mm  | 2.0 mm   | 3.0 mm  | 5.0 mm  |
| 1     | 40  |    |    |    |    |    |
| 2     |   |    |    |    |    |    |
| 3     | No grooves detected during the SEM inspection |   |   |  |   |   |
| 4     | 20  |  |  | No grooves detected during the SEM inspection  |   |   |
| 5     |   |  |  |  |  |  |
| 6     | No grooves detected during the SEM inspection |   |   |  |   |   |

Table 4.5: SEM micrographs of grooves at the considered machining distances for DCP 20 diamond-coated silicon probes. Scale bars: 12  $\mu\text{m}$ .

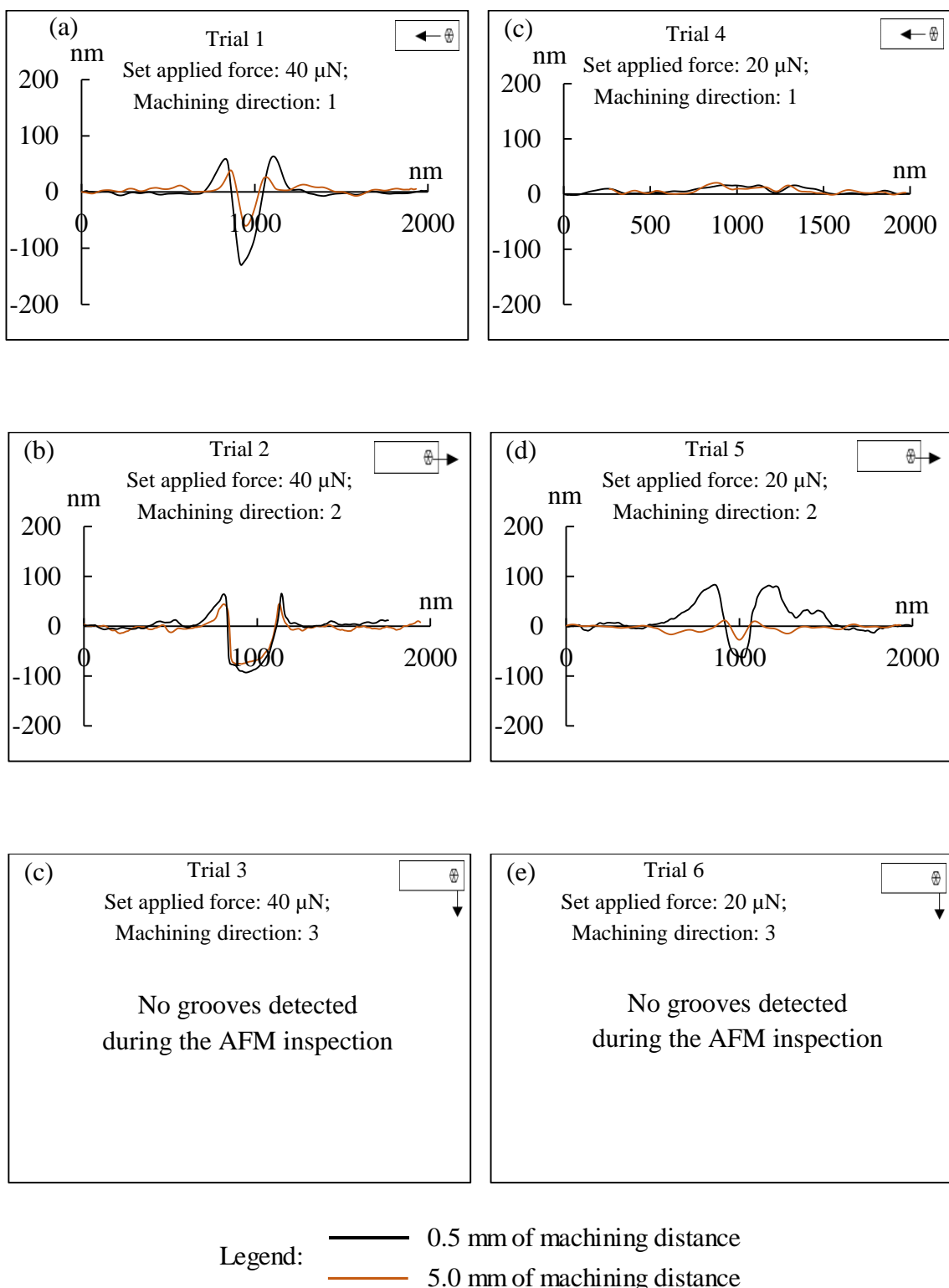


Figure 4.14: Groove profiles obtained when machining with DCP 20 diamond-coated silicon probes.

| Trial | Applied<br>normal force<br>( $\mu\text{N}$ ) | <i>H/D ratio</i> with standard deviation      |  |
|-------|--|---|--|
|       |  | During machining trial<br>until 0.5 mm        | During machining trial<br>until 5.0 mm |
| 1     | 40   | $0.42 \pm 0.16$                               | $0.92 \pm 0.03$                        |
| 2     |  | $0.83 \pm 0.52$                               | $1.06 \pm 0.89$                        |
| 3     |  | No grooves detected during the AFM inspection |  |
| 4     | 20   | $5.41 \pm 0.36$                               | $6.28 \pm 0.37$                        |
| 5     |  | $2.60 \pm 0.07$                               | $5.43 \pm 1.10$                        |
| 6     |  | No grooves detected during the AFM inspection |  |

Table 4.6: *H/D ratios* for DCP 20 diamond-coated silicon probes.

for the engagement depth of the tip into the material to be larger than the minimum chip thickness.

Machining in the cutting-dominated regime could also be observed in the previous chapter when using the silicon probe for *Direction 1* at 40  $\mu\text{N}$  of normal applied force (refer to Trial 4 in Table 3.6, Chapter 3). However, the same conclusion cannot be made if machining with the silicon probe along *Direction 2* with an applied force of 40  $\mu\text{N}$  is considered (refer to Trial 5 in Table 3.6, Chapter 3). Indeed, under such machining conditions, chip formation was observed with the diamond-coated silicon tip while ploughing was the dominant processing mechanism with the silicon tip. This discrepancy should be the result of the different tip geometries in both cases. Particularly, in Chapter 3 the silicon tip was affected by an initial fracture at 0.5 mm of machining distance, which resulted in a flat punch geometry (refer to Figure 3.12(e)).

Finally, when machining along *Direction 3*, grooves could not be detected during both the AFM and SEM inspections regardless of the applied force. This means that the workpiece material was only deformed elastically. In contrast, machining in the ploughing-dominated regime was noted in the previous chapter along this direction at 40  $\mu\text{N}$  of applied load (refer to Trial 6 in Table 3.6, Chapter 3). Two conclusions can be drawn from this observation. First, it would appear that processing along the direction perpendicular to the long axis of the cantilever is generally less favourable for the generation of grooves compared to processing in a direction along the cantilever long axis (i.e. *Direction 1* or *2*). Second, the fact that grooves could not be machined in this chapter for *Direction 3* at 40  $\mu\text{N}$ , while it was possible to do so in Chapter 3, indicates that the torsional stiffness of the V-shape cantilevers used here should be lower than that of the

rectangular cantilevers employed in Chapter 3. Indeed, under the same processing conditions, a lower torsional stiffness would result in a more negative rake angle. According to common knowledge, it is expected that a more negative rake angle should be detrimental to the groove formation process.

## 4.5 Conclusions

The aim of this chapter was to conduct an investigation on the wear of AFM silicon tips with diamond coating when machining a single crystal copper workpiece along different machining distances and directions. Diamond-coated silicon tips were selected with the view to overcome the limitation of the silicon tips, which were employed in the previous chapter. In particular, the silicon tips were prone to breakage after a very short machining distance. In this chapter, in addition to using the SEM instrument for extracting the apex profiles of the employed tips, an in-situ method, namely the ultra-sharp tip scan approach, was implemented to obtain 3D geometric data about the tip apex. In addition, 2D cross sections were extracted from the AFM topography images in order to analyse the agreement between the profiles acquired from the SEM and from the ultra-sharp tip scan approach. The conclusions obtained from the work reported in this chapter are as follows:

- Although the occurrence of tip breakage was reduced when using diamond-coated silicon tips, in comparison with silicon tips, fracture events still affected some trials for this experimental study during the nanomachining process. This observation was made for a set of experimental conditions where the applied loads were equal to, or lower than, those studied in Chapter 3 and for a reduced machining speed. This was perhaps an unexpected result as diamond-coated tips may be considered

to be less prone to wear. The possible explanation for this observation is that fracture may start within the silicon material and propagate through to the diamond coating.

- The machining process was mostly conducted in the ploughing-dominated regime for the lower normal applied force of 20  $\mu\text{N}$ , while the application of a load of 40  $\mu\text{N}$  seemed sufficient to overcome the minimum chip thickness, in particular for processing directions along the long axis of the cantilever.
- SEM and AFM topography images of the processed workpiece surface indicates that the generation of grooves was not so favourable when machining in the direction perpendicular to the long axis of the cantilever for both values of applied load considered.
- The results obtained in this chapter also indicate that the cross section profiles obtained with the ultra-sharp tip scan method are likely to overestimate the width of an inspected tip. However, it can still be said that, for a region very close to the tip apex, there is a good agreement between the profiles extracted from both characterisation techniques implemented (i.e. SEM imaging and ultra-sharp tip AFM scanning).
- Even though the ultra-sharp tip scan technique should, in principle, be more convenient for obtaining topography images of the tip apex, as it does not require the tip to be removed from the AFM system, this approach requires a very skilled operator to be implemented reliably.

Due to the observed drawback of the ultra-sharp tip scan approach, it is worth studying an alternative in-situ method to obtain topography information of the tip of AFM probes. Therefore, one of the aims of the following chapter is to compare the ultra-sharp tip scan approach with the reverse imaging method, which is another in-situ technique that can also be used to acquire 3D geometry data about the tip apex. In addition, a further experimental study of the wear of silicon diamond-coated tips during the AFM probe-based machining process will be conducted in the next chapter, but this time for a wider range of normal applied loads.

**CHAPTER 5:**

**ASSESSMENT OF WEAR FOR AFM SILICON**

**PROBES WITH DIAMOND-COATED TIPS USING**

**THE IN-SITU REVERSE IMAGING METHOD**

## CHAPTER 5

# ASSESSMENT OF WEAR FOR AFM SILICON PROBES WITH DIAMOND-COATED TIPS USING THE IN-SITU REVERSE IMAGING METHOD

### 5.1 Overview

The first objective of this chapter is to investigate the performance and the practical suitability of two different in-situ 3D tip characterisation techniques, namely the ultra-sharp tip scan method and the reverse imaging method. To achieve this, systematic comparative studies were conducted on AFM silicon diamond-coated probes in their unused state. Data obtained from the previous experimental work reported in Chapter 4 were further processed to provide qualitative and quantitative measurements for assessing the ultra-sharp tip scan approach. The reverse imaging technique consisted in obtaining an inverted 3D image of the tip as a result of using it to scan sharp pin-like asperities. Tip profile data obtained with Scanning Electron Microscopy (SEM) were also employed as references to evaluate the quality of the cross sectional profiles extracted from both 3D measurements methods. Moreover, from the obtained data acquired from the reverse imaging technique, the influence of considering different vertical distances from the tip apex, when selecting profile data for the calculation of the tip radius, was studied.

The second objective of this chapter is to conduct a further investigation of the behaviour and performance of silicon diamond-coated probes when machining in a wider range of normal applied loads. Based on the outcome of the study realised to address the first objective of this chapter, it was decided that the 3D geometry of AFM tips should be characterised using the reverse imaging technique for this new set of nanomachining

experiments. In particular, this technique was selected due to its improved practicability and accuracy. The data obtained from the SEM micrographs were used also as a reference against the cross sectional profiles extracted from the acquired 3D measurements, i.e. reverse imaging method. Finally, an attempt is made at drawing useful conclusion about the most influential factor on the wear progression of AFM tips during nanomachining.

## **5.2 Experimental set-up and methodology**

### **5.2.1 AFM system and workpiece preparation**

The same AFM instrument (XE-100 AFM model from Park Systems) was used to conduct the experimental work for this chapter. The workpiece preparation and the nanomachining procedures were operated in the same manner as in Chapters 3 and 4. In addition, the same single crystal copper sample was used as a workpiece. The polishing procedure for soft materials was also repeated here before to the start of the machining trials. This was carried out to prevent the potential detrimental effects of any contamination on the Cu sample.

### **5.2.2 Comparison of two AFM probe inspection techniques for three-dimensional tip characterisation**

As mentioned earlier, the first objective of this chapter is to compare the accuracy and the reliability between the ultra-sharp tip scan approach and the reverse imaging technique. For each of these tip characterisation methods, six unused silicon diamond-coated probes were considered. Figure 5.1 shows the procedure followed for this particular study. As stated earlier, the data measured with the ultra-sharp tip scan method was taken from the previous experimental study in Chapter 4. While for the reverse imaging method, the data was obtained using the procedure illustrated in Figure 5.2. In

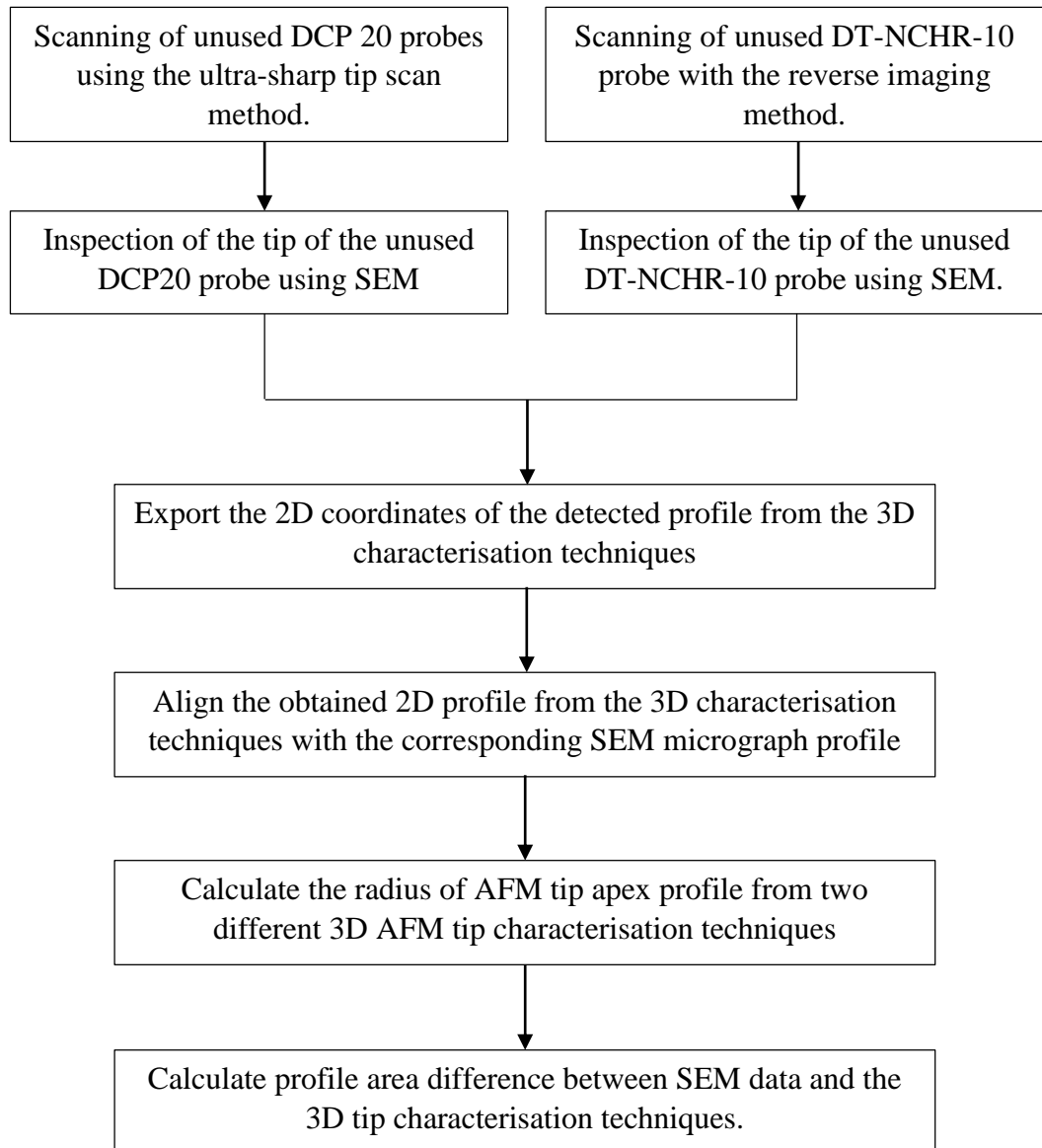


Figure 5.1: Comparison of two AFM probe inspection technique for 3D tip characterisation procedure.

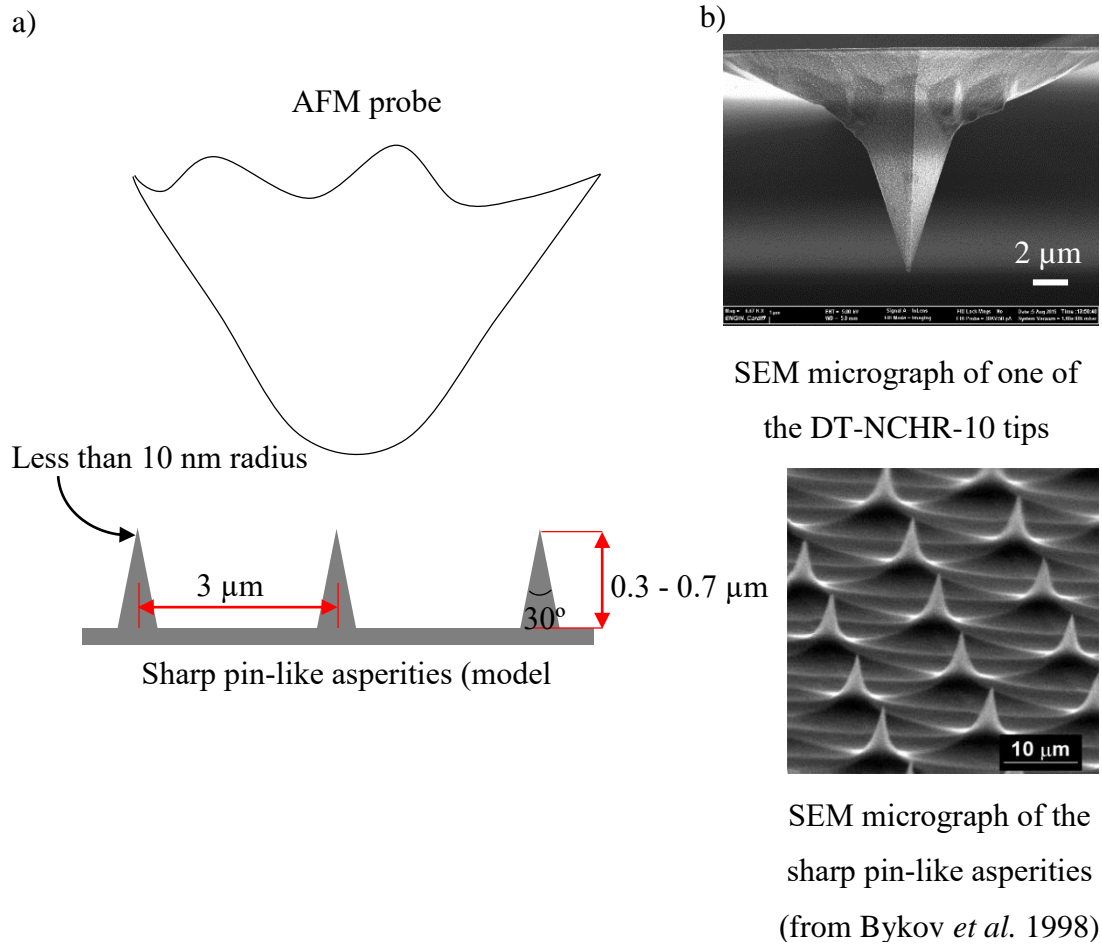


Figure 5.2: (a) Schematic diagram of the reverse imaging approach; (b) SEM micrographs of a diamond-coated tip and the sharp pin-like asperities (model TGT1).

particular, a sample exhibiting an array of sharp pin-like asperities was used to obtain the AFM tip apex topography images. This sample was made by the company NT-MDT and its commercial name is “TGT1”. Next, the 3D tip geometry data acquired from both characterisation techniques were used to estimate the radius of each tip by implementing the procedure already explained in Chapter 3. Prior to that, the radius of each tip was also assessed from the SEM profiles.

In addition to the radius measurements and the average of the metric “profile area difference” between SEM data and the 3D data of the tips was calculated. The meaning of this metric is illustrated in Figure 5.3. Particularly, the profile area difference was calculated using a similar procedure to that employed for assessing the metric “area loss”, which was presented in Chapter 3. However, in this chapter, the alignment process is realised between the 2D profile from a SEM micrograph and of the cross section from a 3D tip characterisation method. In addition, the vertical interval used to process the data from the ultra-sharp-tip scan method and the reverse imaging approach were 300 nm and 80 nm, respectively. The analysis followed for determining this vertical interval value for the data obtained from the ultra-sharp tip scan method was explained in Section 4.4.1.1, while the data that acquired from the reverse imaging technique, this will be reported and discussed in Section 5.5.1.1.

### 5.2.3 Nanomachining process

The most important part of the study reported here is concerned with the further investigation of the performance and the behaviour of the AFM silicon diamond-coated probes when nanomachining with a wider range of normal applied loads (i.e. between 10  $\mu\text{N}$  and 100  $\mu\text{N}$ ) compared to the values considered in previous chapters.

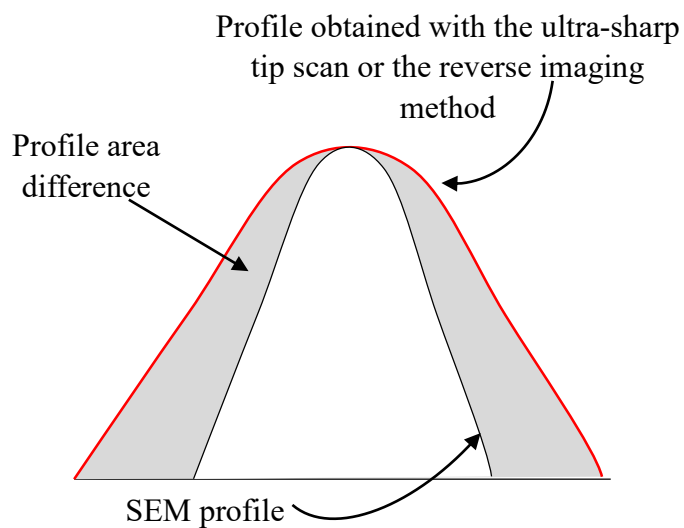


Figure 5.3: Illustration of the concept of profile area difference between SEM data and the considered 3D tip characterisation techniques.

The experimental procedure followed is shown in Figure 5.4. More specifically, this procedure is very similar to that adopted in Chapter 4. The main difference being that the reverse imaging process was utilised here rather than the ultra-sharp tip scan approach for characterising the shape of the tips.

#### **5.2.4 Cutting conditions for the nanomachining experiments**

In this experimental work, similarly to Chapters 3 and 4, it was decided to vary only the value of the pre-set applied load and the machining direction. The summary of the experimental conditions for each trial is shown in Table 5.1. In this chapter, the range of considered applied loads was increased in included values of 100  $\mu\text{N}$ , 60  $\mu\text{N}$ , 20  $\mu\text{N}$  and 10  $\mu\text{N}$ . These load values were selected to observe the behaviour and the performance of the silicon diamond-coated probes when used for nanomachining operations at higher and lower applied forces compared to the experimental study of Chapter 4. It was decided to keep the value of 20  $\mu\text{N}$  to provide further experimental data for studying whether the probe might still suffer from breakage at this particular load during the nanomachining process. The applied normal force was also reduced to 10  $\mu\text{N}$  to investigate whether the probe might be affected by fracture for such a low load. The machining speed was the same as that used in Chapter 4, i.e. 2  $\mu\text{m/s}$ . Finally, the machining distance was decreased to 3 mm in comparison with the consideration of 5 mm in Chapter 4. This decision was made on the basis that the results of Chapter 4 showed that probe fracture was more likely after 3.0 mm of machining distance for a higher applied load. Thus, the idea is to be able to record data which are not affected by tip breakage.

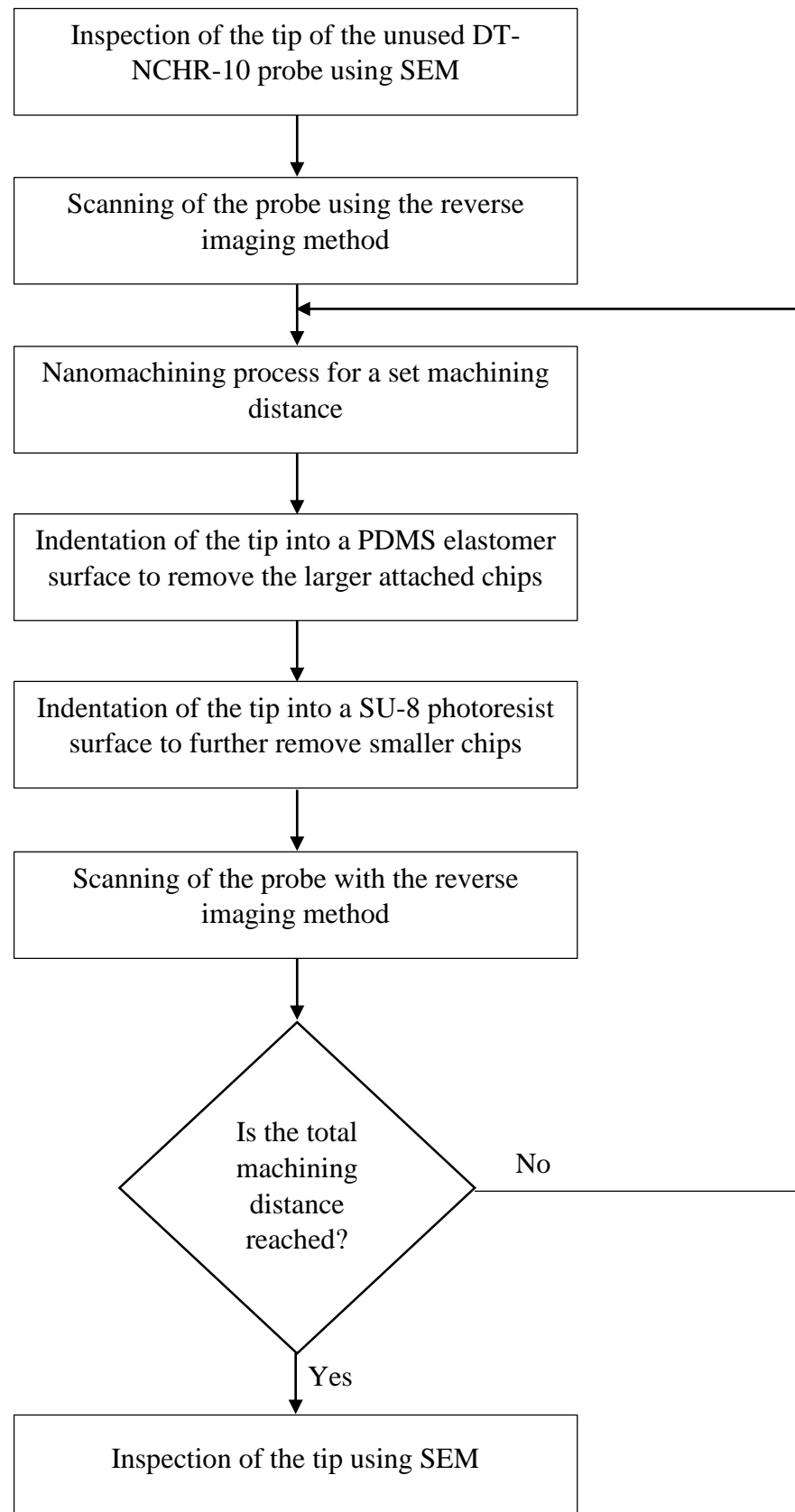


Figure 5.4: Experimental procedure followed during the nanomachining experiments.

| Trial Number | Set normal force ( $\mu\text{N}$ ) | Machining direction | Machining speed ( $\mu\text{m/s}$ ) | Machining distance (mm) |
|--------------|------------------------------------|---------------------|-------------------------------------|-------------------------|
| 1            | 100                                | 1                   |                                     |                         |
| 2            | 100                                | 2                   |                                     |                         |
| 3            | 100                                | 3                   |                                     |                         |
| 4            | 60                                 | 1                   |                                     |                         |
| 5            | 60                                 | 2                   |                                     |                         |
| 6            | 60                                 | 3                   |                                     |                         |
| 7            | 20                                 | 1                   |                                     | 2                       |
| 8            | 20                                 | 2                   |                                     | 3                       |
| 9            | 20                                 | 3                   |                                     |                         |
| 10           | 10                                 | 1                   |                                     |                         |
| 11           | 10                                 | 2                   |                                     |                         |
| 12           | 10                                 | 3                   |                                     |                         |

*Note: the value for the parameter “machining direction” refers to the definition adopted in Chapter 3 and described with Figure 3.6.*

Table 5.1: Selected AFM tip-based nanomachining parameters.

### 5.2.5 AFM DT-NCHR-10 probes

AFM silicon probes with diamond coating (model DT-NCHR-10 from NANOSENSORS<sup>TM</sup>) were employed for this new set of experimental trials. An SEM micrograph of a typical DT-NCHR-10 probe can be seen in Figure 5.5. The nominal radius value for the tip apex of these probes lies between 100 nm and 200 nm as specified by the manufacturer. The cantilever of this type of probe is designed such that it has a nominal normal spring constant,  $k$ , of 80 N/m. The complete set of specifications for such AFM probe is given in Table 5.2. Given that the probe cantilever had a rectangular shape, the particular procedure adopted to perform the assessment of the actual normal spring constant of each probe was that proposed by Sader *et al.* (1999).

## 5.3 Comparison of two AFM probe inspection techniques for 3D tip assessment

Figures 5.6 and 5.7 show tip profiles for the two types of probes considered based on the data acquired with the ultra-sharp tip scan approach and the reverse imaging technique, respectively. Each graph in these figures combines the SEM profile of a tip aligned with its corresponding cross section obtained with a 3D characterisation technique. In particular, both of the profiles obtained from 3D in-situ measurement technique were taken along the cross section of A-A' (refer to Figure 4.4). Thus the profiles corresponded to that observed with the SEM, i.e. that is it perpendicular to the long axis of the cantilever. Thus, both the 2D and 3D profiles are comparable. It should be noted that, for the results extracted from the reverse imaging technique, the data shown represent the average profile based on the scan of five asperities. As stated in the previous chapter, the ultra-sharp tip scan tends to provide reliable data only on a small portion of the tip geometry at its apex (see Figure 5.6). In contrast, the results displayed with Figures 5.7 indicate a better qualitative agreement for the tip apex geometry between the SEM

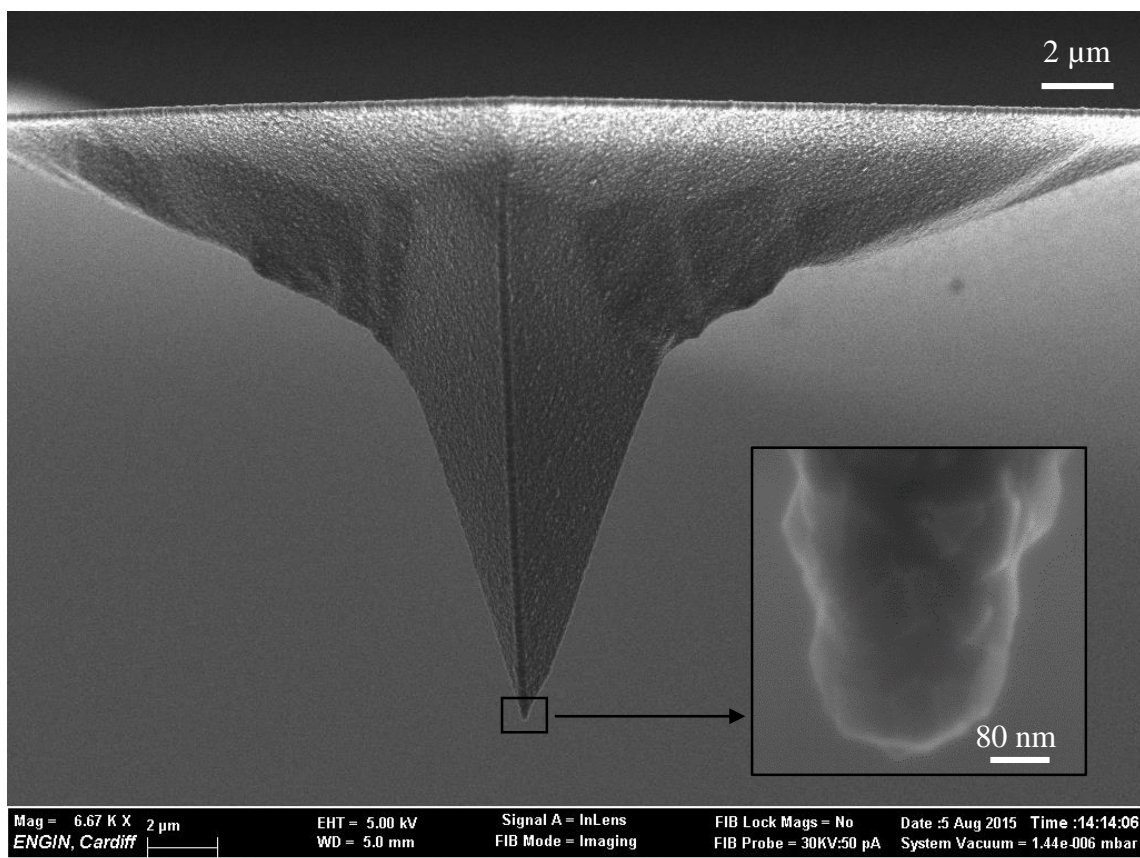


Figure 5.5: SEM micrographs of a typical DT-NCHR-10 probe.

| Probe             | Resonance frequency (kHz) |         |     | Force constant (N/m) |         |     | Cantilever        |                    |                  |
|-------------------|---------------------------|---------|-----|----------------------|---------|-----|-------------------|--------------------|------------------|
|                   | min                       | nominal | max | min                  | nominal | max | Length            | Width              | Thickness        |
|                   |                           |         |     |                      |         |     | $l$<br>± 10<br>μm | $w$<br>± 7.5<br>μm | $t$<br>± 1<br>μm |
| DT-NCHR-10 series | 225                       | 400     | 610 | 23                   | 80      | 225 | 125               | 30                 | 4.0              |

Table 5.2: Probe specifications for the DT-NCHR-10 model from NANOSENSORS™.

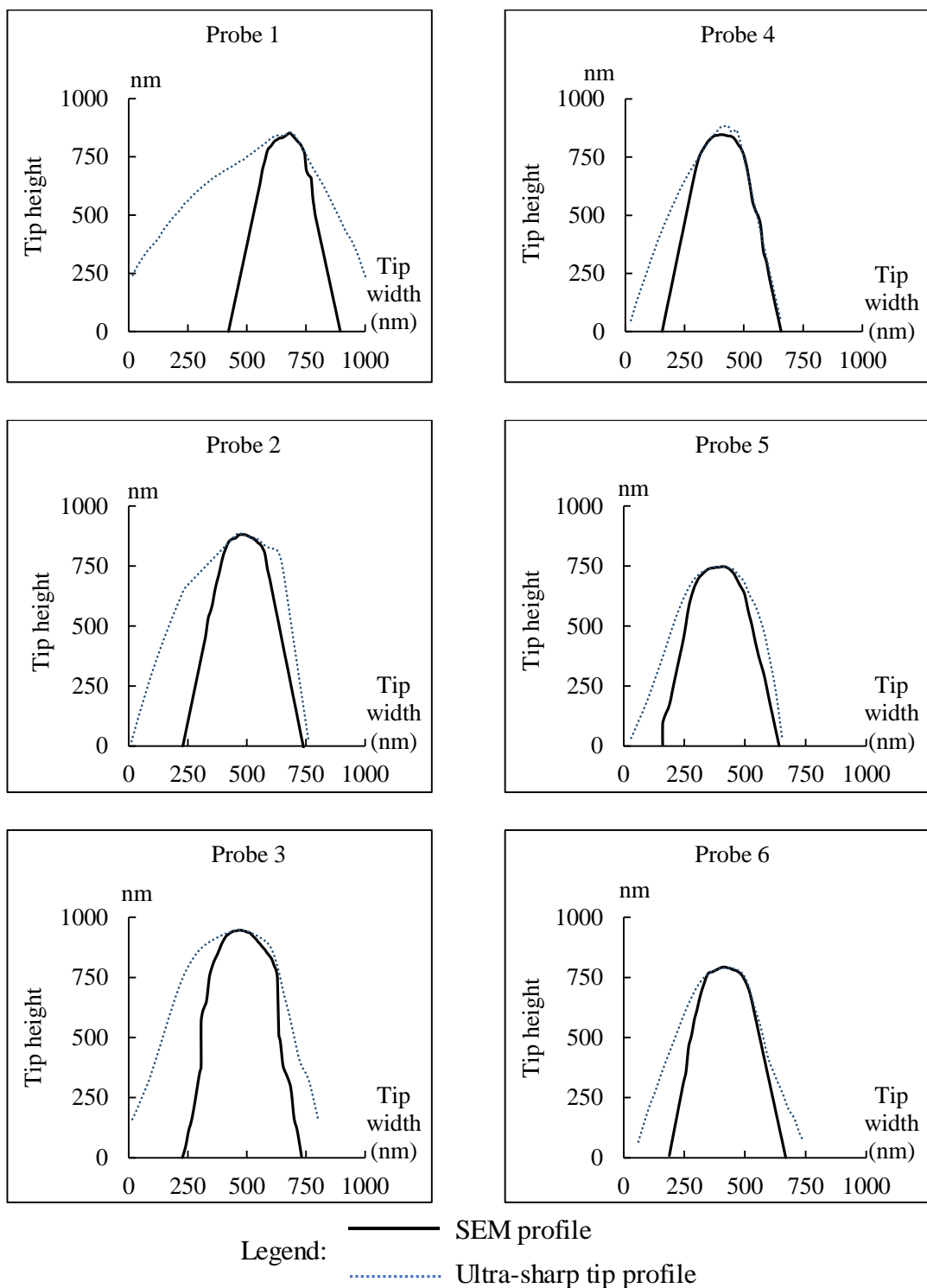


Figure 5.6: Qualitative profile comparisons between SEM data and the corresponding cross sections obtained with the ultra-sharp tip scan profile characterisation technique for new tips.

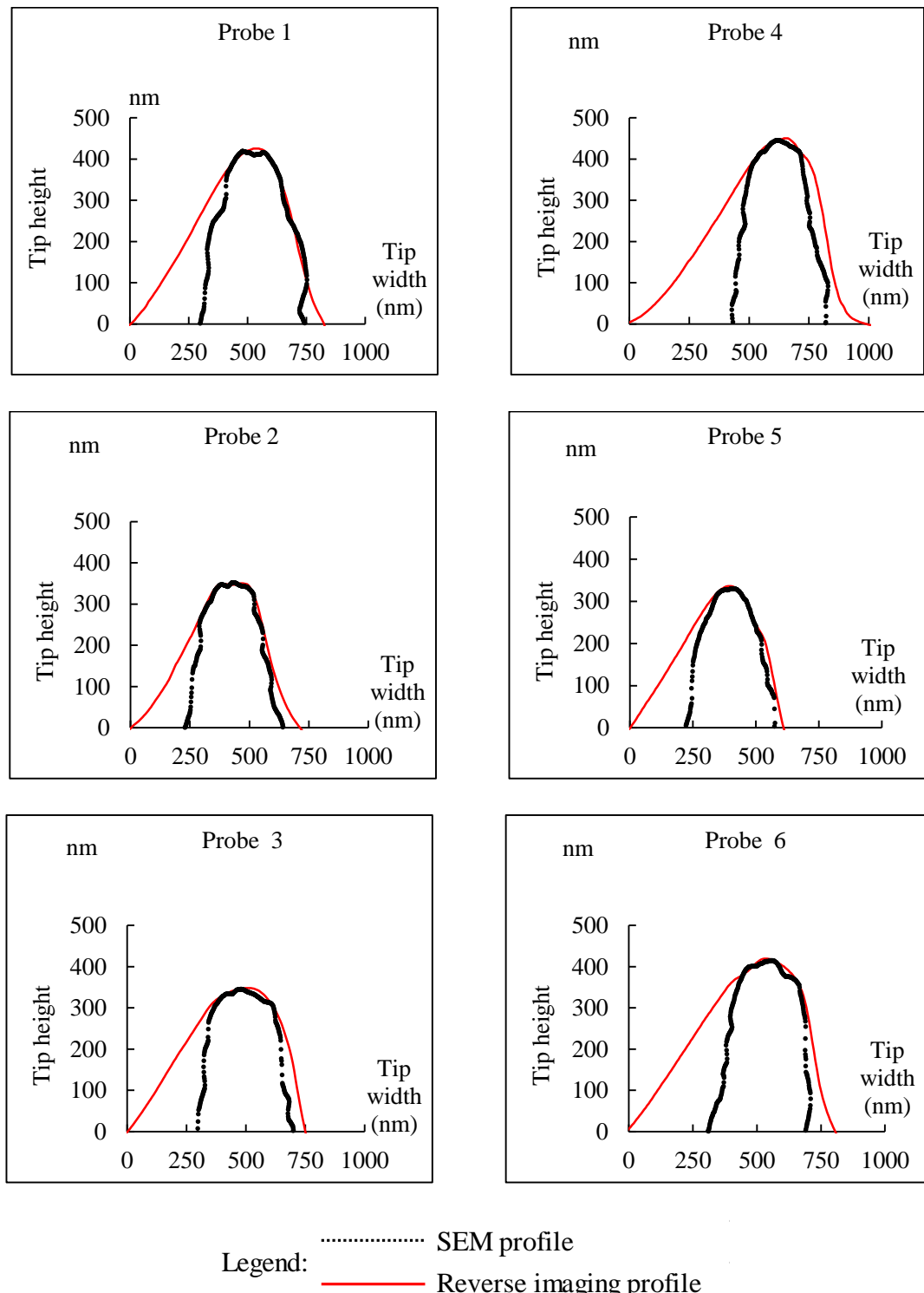


Figure 5.7: Qualitative profile comparisons between SEM data and the corresponding cross sections obtained with the reverse imaging characterisation technique for new tips.

profile and that extracted from reverse imaging scan. From the qualitative observation of these two figures, it may be said that, although the reverse imaging characterisation method is still likely to overestimate the width of an inspected tip, this effect is not as pronounced as when the ultra-sharp-tip scan technique is employed. In order to provide a more quantitative comparison, the average difference in the tip radius extracted from the SEM profile and that obtained from the 3D techniques was estimated as shown in Figure 5.8. From this graph, it can be said that the ultra-sharp tip scan technique exhibits the largest disagreement with the radius evaluated from the SEM data. In addition, Figure 5.9 shows that the reverse imaging technique leads to the lowest value of profile area difference, which is consistent with the results displayed in Figure 5.8.

In summary, from these combined results, it is concluded that tip profiles extracted from the reverse imaging method on sharp pin-like asperities provide a better agreement with those obtained from SEM micrographs. Thus, it could be argued that the tip convolution effect is less detrimental to the quality of the data obtained with this particular 3D characterisation technique. Therefore, the utilisation of a sample with sharp pin-like asperities to obtain an inverted scan of the assessed tip should be the preferred method to implement from this point forward in this research. From a practical point of view, the reverse imaging method is also more straight-forward to carry out compared to the ultra-sharp tip scan technique as there is no need to remove the tip under investigation from the AFM head. In addition, the process of precisely locating an ultra-sharp probe over the inspected tip apex has already been reported in Chapter 4 to be a non-trivial operation, which could sometimes lead to damaging contacts between both tips.

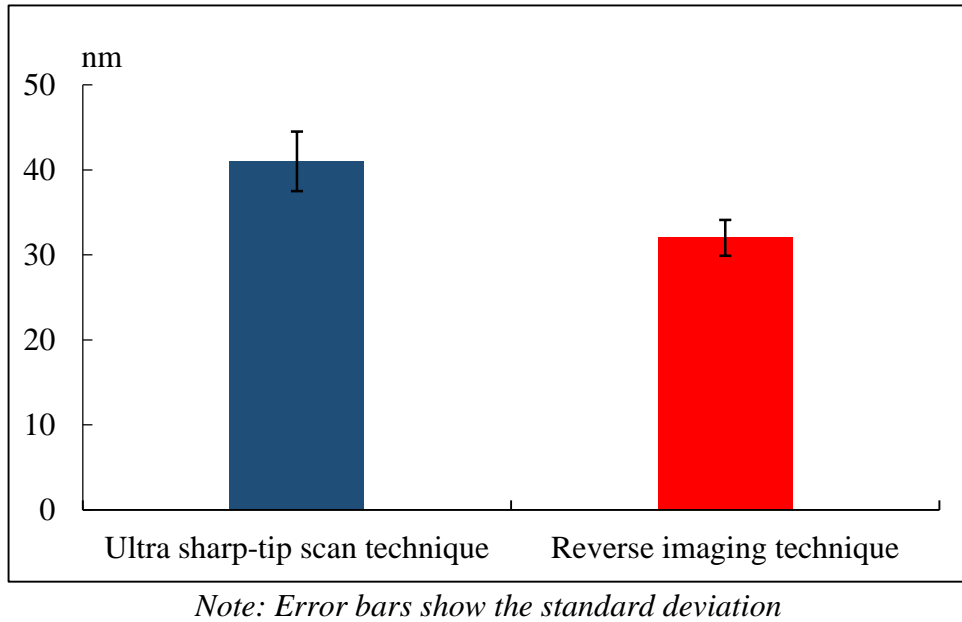
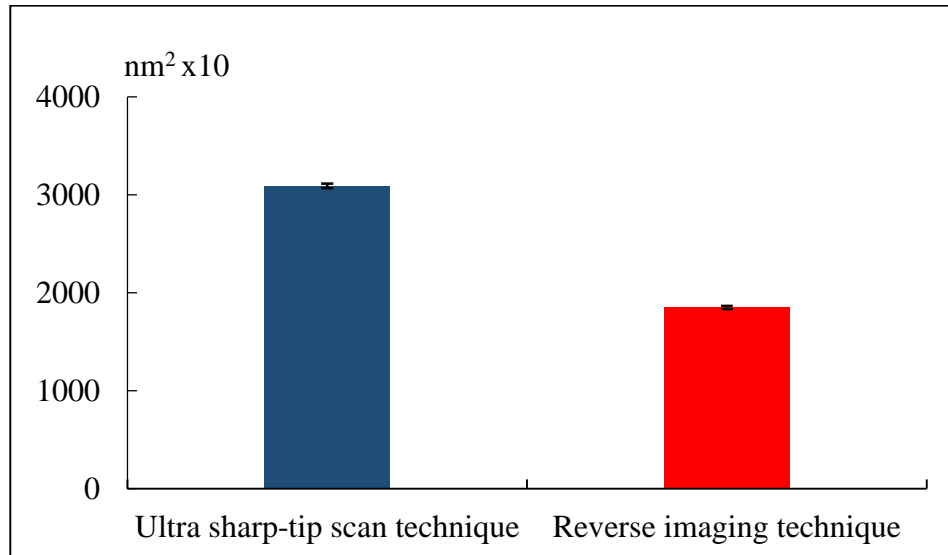


Figure 5.8: Average difference for radius measurements between SEM data and the 3D tip characterisation techniques.



*Note: Error bars show the standard deviation*

Figure 5.9: Discrepancies in the profile area difference data between the SEM inspection and the 3D tip characterisation techniques

#### 5.4 Methodology for tip wear assessment

As a result of the work reported in the previous section, the reverse imaging method was used for the 3D characterisation of the AFM tip apex at different stages of the subsequent nanomachining experiments. Similarly, to the Chapter 4, a low-pass spatial filter with weight ratio of 1.3 was applied on the obtained AFM topography images in order to reduce the noise that could affect the quality of the scans obtained with the reverse imaging method. Care was taken to make sure that this post-processing operation did not affect the overall scanned height of the tip.

From the reverse imaging data, the metrics volume loss and tip radius were assessed based on the procedures explained in Chapter 4 and Chapter 3, respectively. Prior to the start of the machining trials, the profiles of six unused DT-NCHR-10 probes were also considered to analyse the influence of different vertical heights from the tip apex over which the radius calculations should be carried out. Particularly, the radii were measured using both 2D SEM profiles and 2D profiles obtained from the 3D scans. Hence, from this analysis, the determination of a constant vertical height to be applied for all the subsequent radius calculations could be established. It should also be noted that the radius assessed for one tip at one particular machining distance corresponds to the average of 20 radius values as each was obtained from scanning five asperities and from four different cross sections extracted from the 3D data. Thus, given that each tip is assessed at five different machining distances and that 12 experiments were conducted in this chapter, a total of 1200 radius calculations were performed here.

Finally, for the assessment of the machined grooves, the AFM and the SEM instruments were used to inspect the single crystal copper workpiece. SEM micrographs

were used to provide a qualitative assessment of the grooves and the occurrence of chip formation for all selected machining distances. The data obtained from the AFM scans were processed to measure the average values of the *H/D ratio* such that the determination of the machining-dominated regime could be also be conducted in this chapter based on the method reported by Ahn and Lee (2009).

## 5.5 Analysis of the results

### 5.5.1 Tip radius measurements

#### 5.5.1.1 Effect of the selected vertical interval from the tip apex

Figure 5.10 shows the plotted graphs for the radius measurements for six DT-NCHR-10 probes prior to the start of the machining experiments (see Appendix G). The results are given as a function of the considered vertical distance from the tip apex over which the tip profile is extracted. In particular, the figure provides a comparison between the estimated radius obtained from a SEM profile and the average radius from four different cross sections based on the tip 3D data acquired with the reverse imaging method. The plots given in Figure 5.10 shows that in all cases, the radius values for both profile characterisation techniques agree relatively well when the vertical interval considered is comprised between 20 nm and 100 nm. Particularly, for a region very close to the tip apex, both SEM and the reverse imaging data seem to have a good agreement. It should be noted that the same conclusion could not be reached in the previous chapter when the ultra-sharp tip scan method was implemented. It is also noticeable from Figure 5.10 that when the considered vertical interval is higher than 100 nm, then the discrepancy in the radius values obtained from the SEM and the reverse imaging data starts to increase. Thus, such a large interval is judged to be not appropriate for extracting tip radius data. In addition, an interval higher than 100 nm is also not representative of the tip apex region

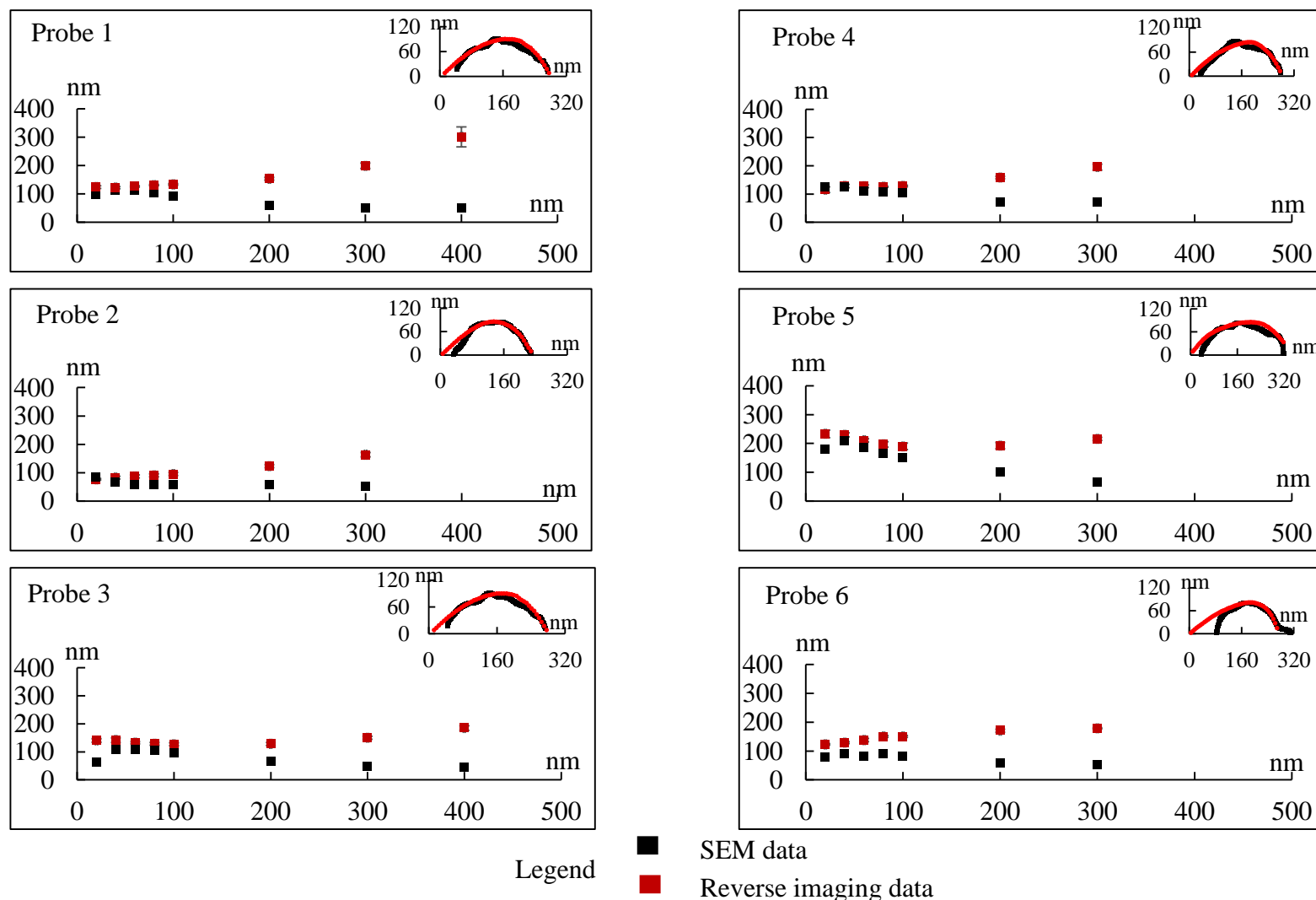


Figure 5.10: Radius measurements as a function of different vertical intervals considered from the tip apex. The inset plot for each graph shows the profiles obtained with the SEM and the reverse imaging method for a fixed vertical distance of 80 nm.

that is in contact with the workpiece material during AFM tip-based nanomachining operations. Although the radius measurements agree well in most cases for a considered vertical distance of 40 nm, the estimation of the tip radius over such a short vertical interval may not fully represent the area affected by wear. Therefore, based on these observations and discussion, it was decided to use a fixed vertical height of 80 nm from the tip apex for all subsequent radius calculations made in this chapter. In addition, the superimposed profiles between the two tip characterisation technique for 80 nm interval generally seem to display a good qualitative agreement (see the inset plots in Figure 5.10).

### 5.5.1.2 Analysis of measured tip radius values

SEM images of the DT-NCHR-10 tips used for the 12 experimental trials are given in Figures 5.11 and 5.13. These SEM micrographs show the condition of the probes prior to the start of the experiments. Based on the procedure reported in Chapter 3 to extract the tip profile from a SEM micrograph, Figures 5.12 and 5.14 reports the corresponding profiles of each tip in their unused state and also, after 3.0 mm of machining. From these profiles, it is interesting to observe that the vast majority of the probes do not show any obvious sign of tip breakage. In fact, only one probe suffered from more pronounced wear (refer to Figures D.2 and D.3 in Appendix D). This was for the probe used from Trial 1 (see Figure 5.12) where the cutting was performed with a set applied load of 100  $\mu\text{N}$  and along *Direction 1* (i.e. towards the fixed end of the cantilever). For this particular trial, it is still difficult to state whether tip fracture definitely occurred. If tip breakage did happen for this probe, then the fracture propagation would seem to be of an intergranular nature given that the resulting surface of the tip is still relatively rough.

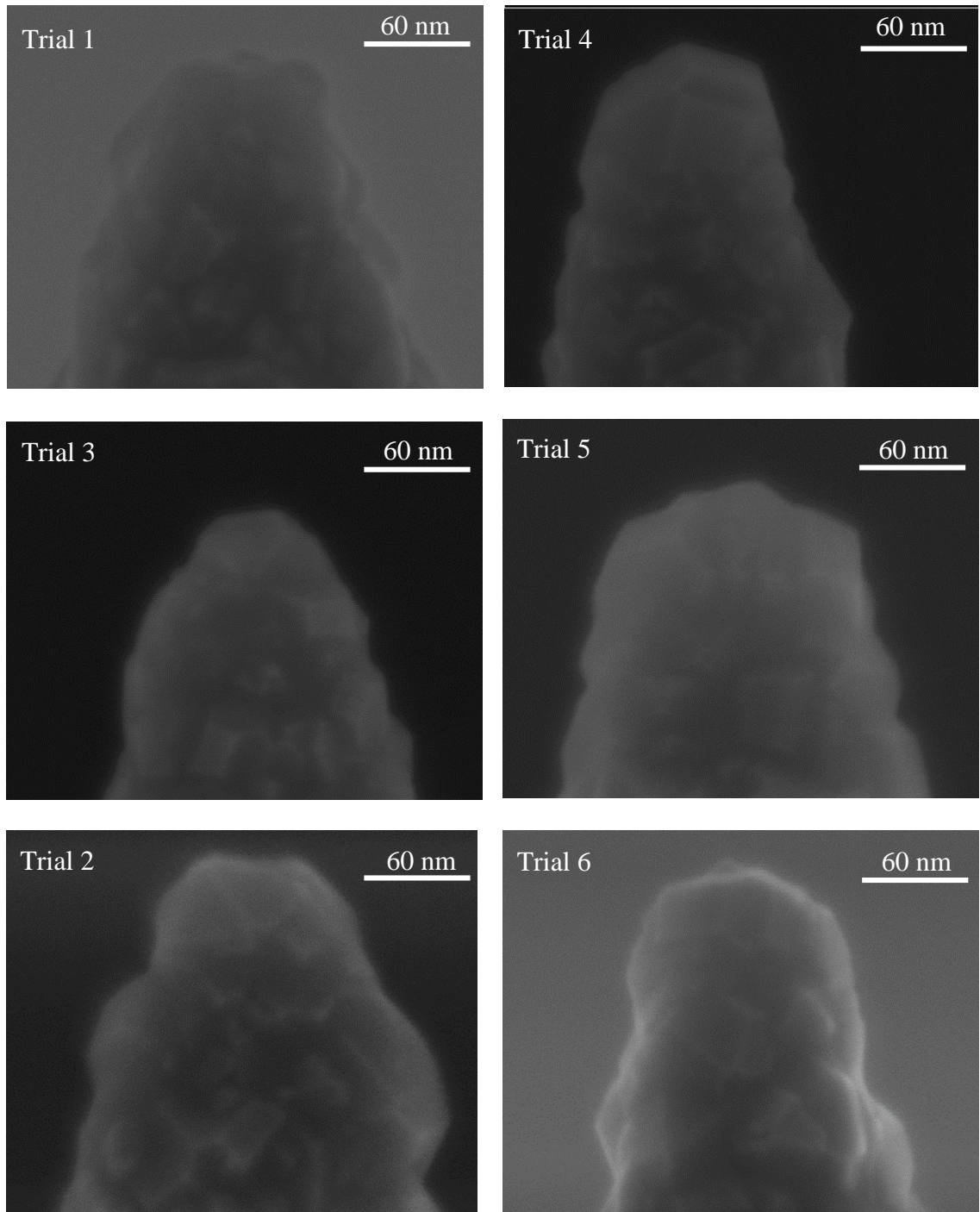


Figure 5.11: SEM micrographs of the six DT-NCHR-10 silicon tips coated with diamond used for machining at applied loads of  $100 \mu\text{N}$  and  $60 \mu\text{N}$  prior to the start of the experimental trials.

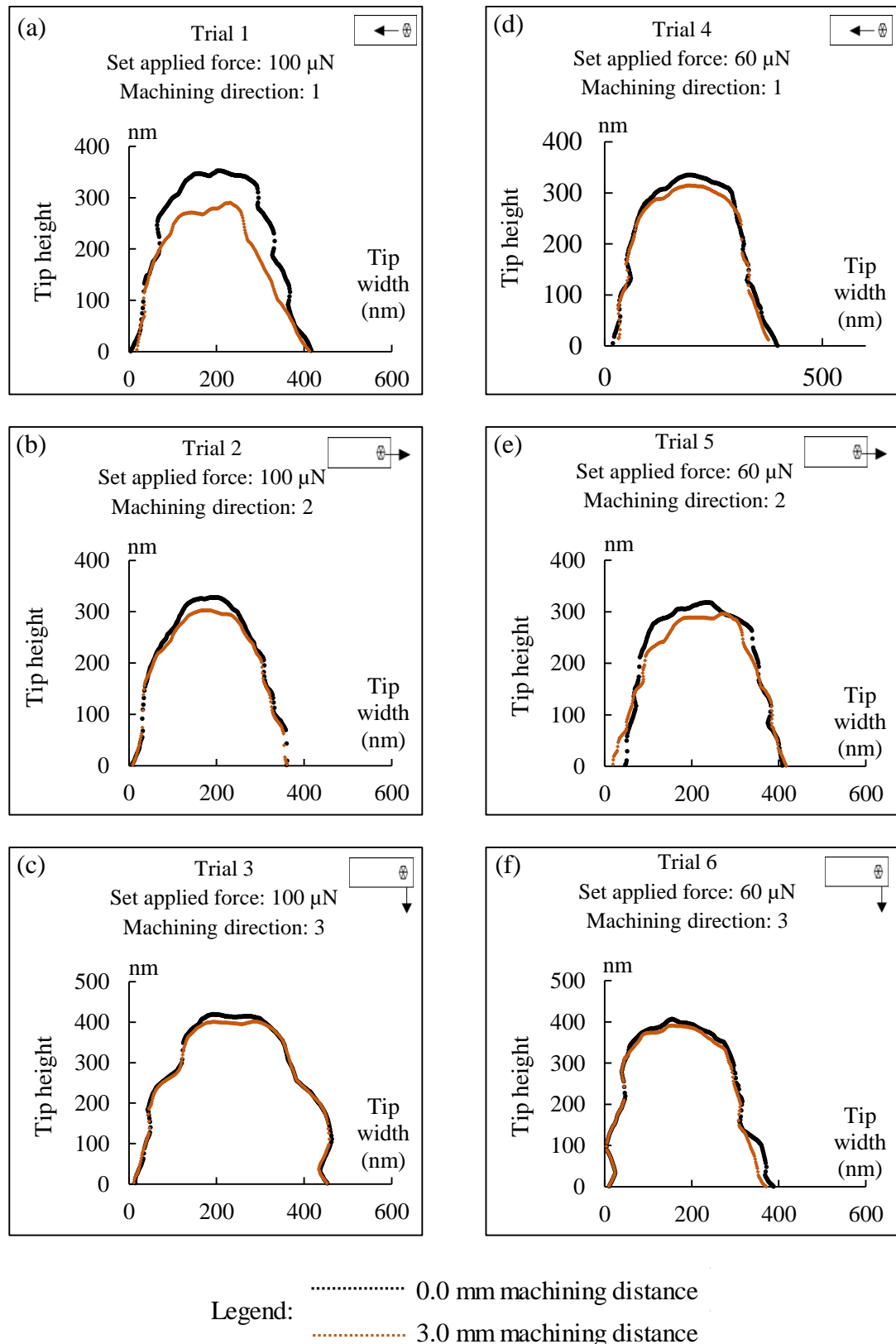


Figure 5.12: Tip profiles before and after the completion of the machining trials for each DT-NCHR-10 diamond-coated silicon probe used for machining at applied loads of 100  $\mu\text{N}$  and 60  $\mu\text{N}$ .

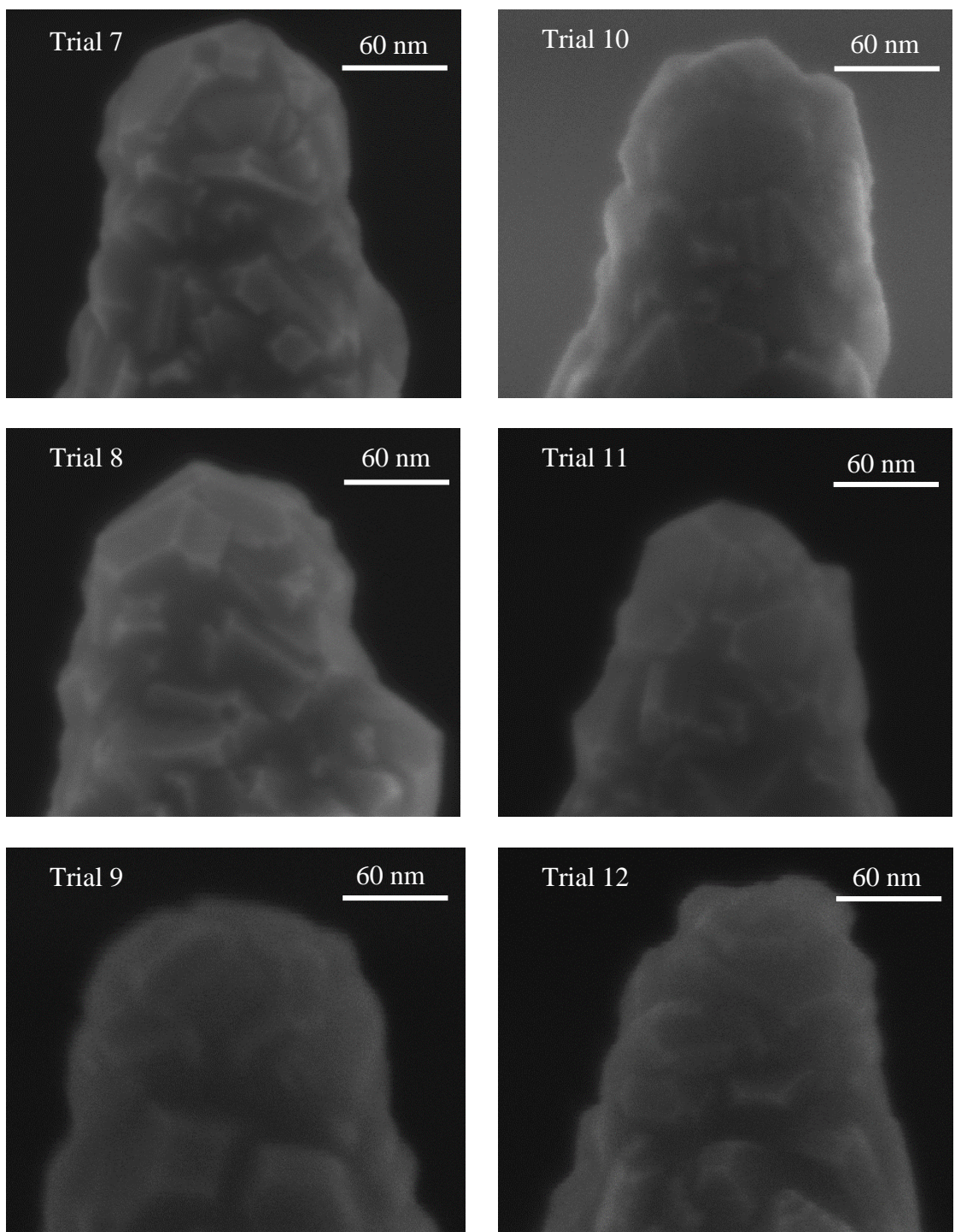


Figure 5.13: SEM micrographs of the six DT-NCHR-10 silicon tips coated with diamond used for machining at applied loads of 20  $\mu\text{N}$  and 10  $\mu\text{N}$  prior to the start of the experimental trials.

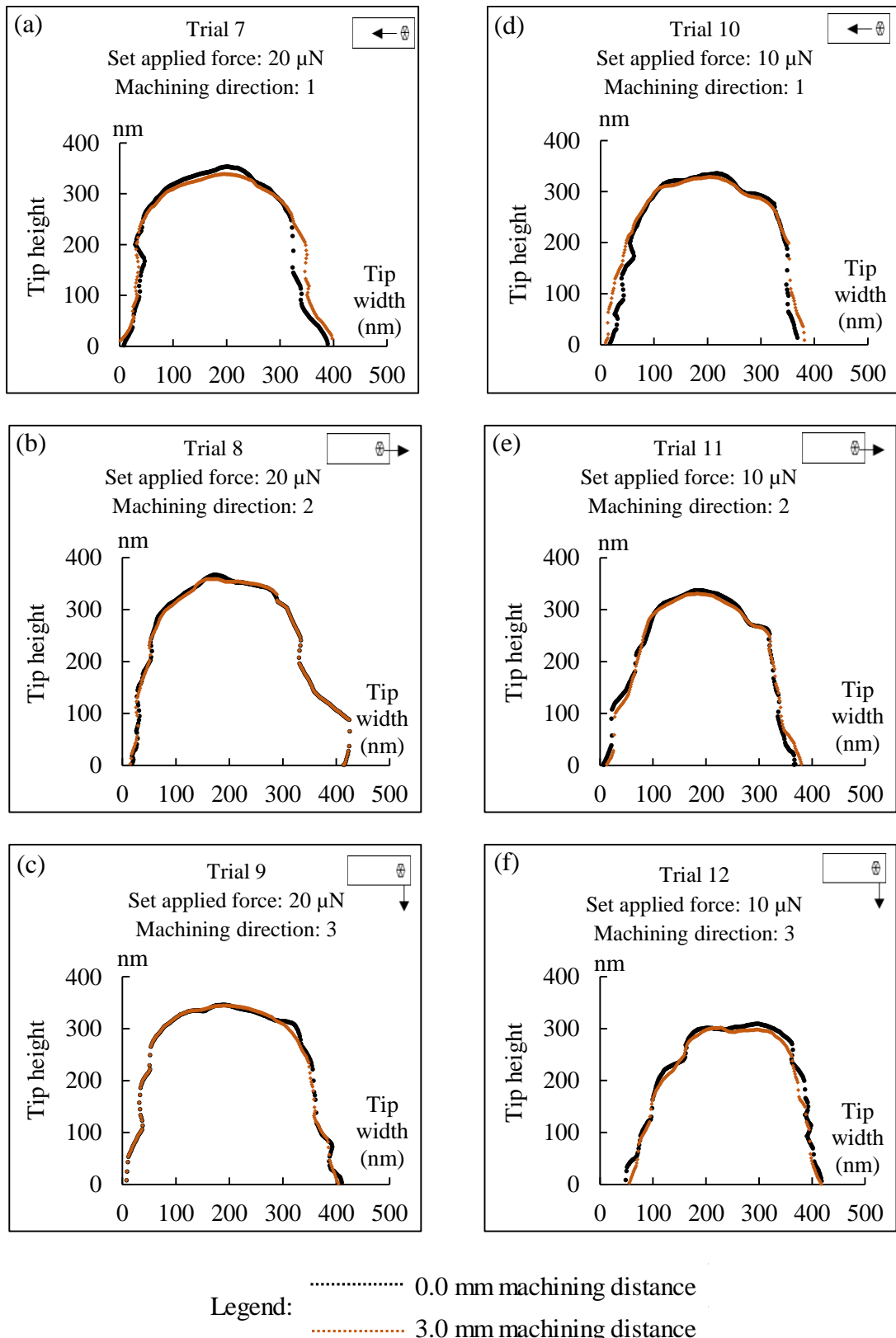


Figure 5.14: Tip profiles before and after the completion of the machining trials for each DT-NCHR-10 diamond-coated silicon probe used for machining at applied loads of 20  $\mu\text{N}$  and 10  $\mu\text{N}$ .

From the qualitative analysis, which can be made from the SEM-based profiles, it is also worth mentioning that about 50% of the diamond-coated probes used in Chapter 4 exhibited a fracture even though the maximum pre-set normal applied force, i.e. 40  $\mu\text{N}$  was in the lower end of the range considered here, which is between 10  $\mu\text{N}$  and 100  $\mu\text{N}$ . The quantitative assessment of the volumetric wear of the probes will be reported later on in Section 5.5.2. However, an initial qualitative analysis suggested that the probes used in the set of experiments reported in this chapter have suffered negligible wear in comparison with the observations made in Chapter 4.

This noticeable difference in the occurrence of fracture and in the wear of the diamond-coated tips between the probes employed in this chapter and those utilised in the previous chapter may be explained as follows. First, the DT-NCHR-10 probes considered here have an average radius of 134 nm in comparison with 95 nm for the DCP 20 probes utilised in Chapter 4. Thus, the radius for these particular probes is approximately 28% larger than the probes used in previous chapter. As already mentioned in Chapter 3, for a given set-applied load, a blunter tip would lead to a higher contact area and thus, a reduced contact stress. For this reason, the wear of the blunter tips may be expected to be lower. Second, the diamond coating of the DCP20 probes used in Chapter 4 is N-doped while the coating of the DT-NCHR-10 probes used in this chapter is not. Recent reports in the literature (see Shen and Chen, 2009 and 2007), suggest that the doping with nitrogen has the effect of reducing the strength of diamond films. Third, based on the manufacturer specification of the DT-NCHR-10 probes, it was calculated that the thickness of the diamond coating for these probes are about 31 % greater than the thickness of the diamond coating for the DCP 20 probes used in Chapter 4. Thus, these combined effect may be the contributing factors to the observed increased likelihood of

tip fracture for the experiments reported in the previous chapter where the DCP20 probes were used.

Figures 5.15 presents bar graphs to provide a comparison of the radius measurements obtained between the SEM and the cross-section profiles acquired from the reverse imaging scan approach. The standard deviation measurement is only given for the reverse imaging scan approach as the radii were estimated in four different cross section. From these bar graphs, it can be said that the estimated radii obtained from the reverse imaging scan method are higher than, but still agree relatively well with, the SEM radius measurement. Thus, this analysis indicates that the reverse imaging technique could be a more reliable approach for obtaining 3D data about the geometry of the probe tip in comparison with the ultra-sharp tip scan approach. Another measurement presented in this section is concerned with the estimation of the radii of the unused tips and those of the same tips at selected machining lengths. These plots are given in Figures 5.16 and 5.17 and rely on data acquired from the reverse imaging method. Based on these plots, the rate of change of the radius values were also calculated and the results are presented in Tables 5.3 and 5.4. As in previous chapters, the rate of change calculation was done by fitting a linear function to the data points for a given trial. In this chapter, this was carried out after 0.5 mm of machining when the wear evolution had reached a steadier state.

When each plot Figures 5.16 and 5.17 are compared with one another, it can be said that the evolution of the tip radius does not seem to be influenced by the machining direction. After completion of the experiments, the largest radius values were measured for the probes used in Trial 5 and Trial 9. However, one should keep in mind that these

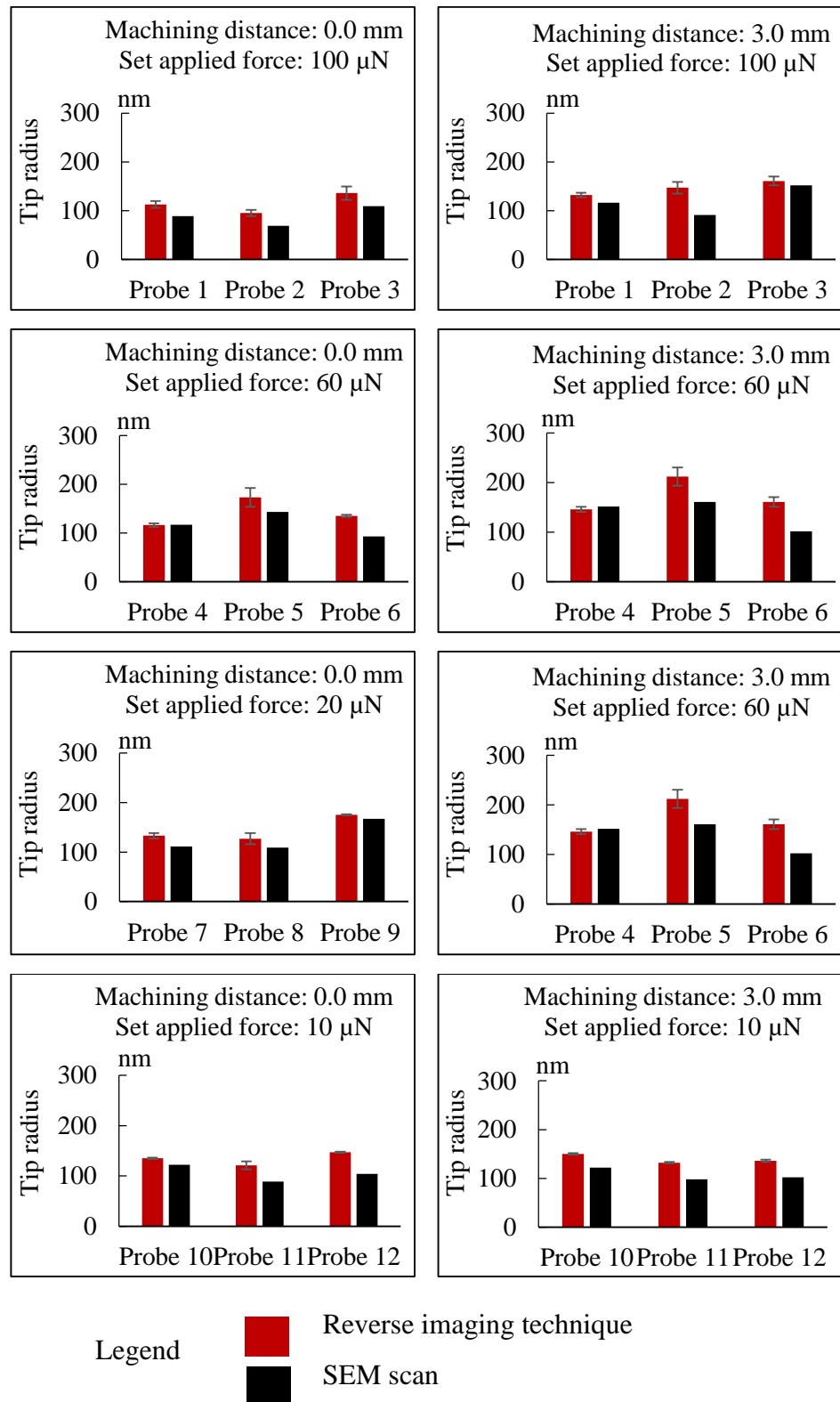


Figure 5.15: Comparison of the radius measurements obtained from the reverse imaging technique and SEM inspection for machining distances of 0.0 mm and 3.0 mm. The error bars show the standard deviation.

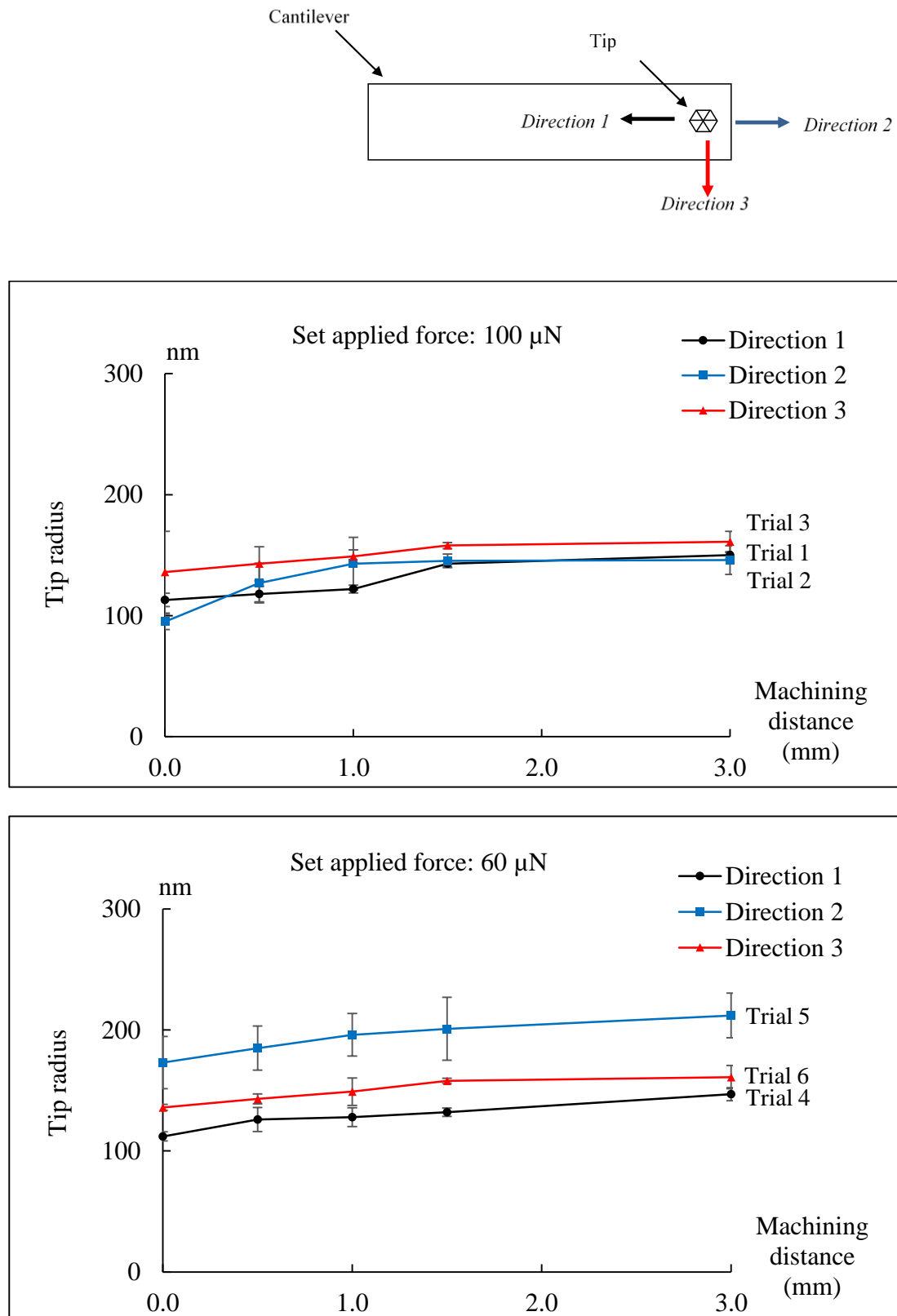


Figure 5.16: Evolution of tip radii as a function of the machining direction and distance for different values of set normal force considered for DT-NCHR-10 diamond-coated silicon probes.

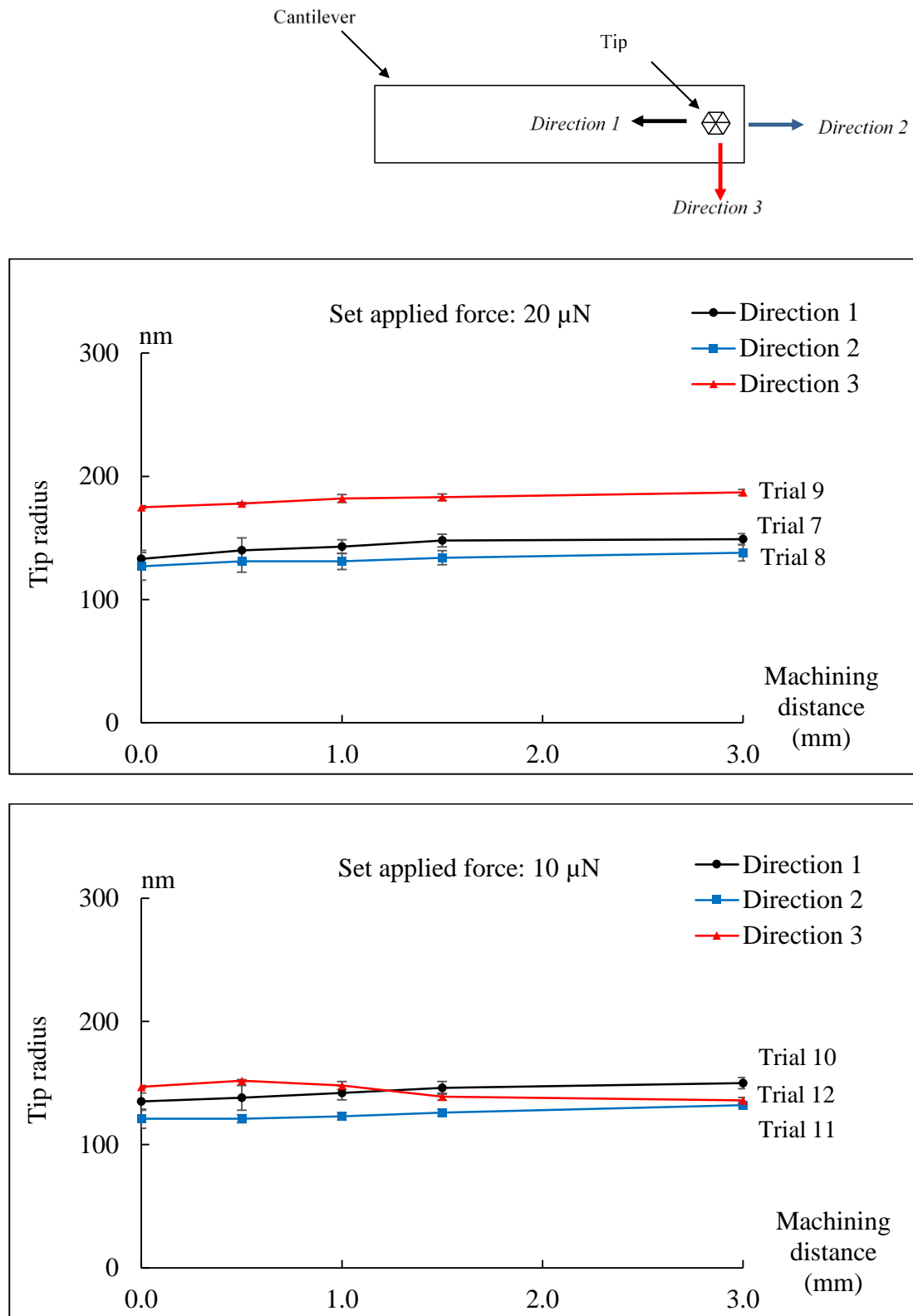


Figure 5.17: Evolution of tip radii as a function of the machining direction and distance for different values of set normal force considered for DT-NCHR-10 diamond-coated silicon probes.

| Machining direction | Trial | Applied normal force ( $\mu\text{N}$ ) | Rate of change of tip radius (nm / mm) between the machining points 0.5 mm until 3.0 mm |
|---------------------|-------|--|---|
| 1                   | 1     | 100                                    | 13.1  |
|                     | 4     | 60                                     | 9.3   |
| 2                   | 2     | 100                                    | 6.4   |
|                     | 5     | 60                                     | 10.0  |
| 3                   | 3     | 100                                    | 6.9   |
|                     | 6     | 60                                     | 6.0   |

Table 5.3: Rate of change of the radius values based on the plots in Figure 5.16.

| Machining direction | Trial | Applied normal force ( $\mu\text{N}$ ) | Rate of change of tip radius (nm / mm) between the machining points 0.5 mm until 3.0 mm |
|---------------------|-------|--|---|
| 1                   | 7     | 20                                     | 3.4   |
|                     | 10    | 10                                     | 4.6   |
| 2                   | 8     | 20                                     | 3.0   |
|                     | 11    | 10                                     | 4.4   |
| 3                   | 9     | 20                                     | 3.3   |
|                     | 12    | 10                                     | -6.3  |

Table 5.4: Rate of change of the radius values based on the plots in Figure 5.17.

probes also displayed the highest radii prior to the start of the nanomachining operations. When comparing the results presented in Tables 5.3 and 5.4, it can be said that the rate of change of tip radius is dependent on the magnitude of the set normal applied force. Particularly, the values of the rate of change of the tip radius for applied forces of 60  $\mu\text{N}$  and 100  $\mu\text{N}$  are larger than those for applied forces of 20  $\mu\text{N}$  and 10  $\mu\text{N}$ . Finally, the rate of change of the radius values for all the machining direction for the set applied normal force of 20  $\mu\text{N}$  in this experimental study is lower compared to that reported in Chapter 4 for the same pre-set normal applied force. This would confirm that the probes used in Chapter 4 might have suffered much more wear as mentioned above.

### 5.5.2 Volume loss measurement

The graph presented in Figures 5.18 and 5.19 show the evolution of the tip volume loss for set applied normal forces of 100  $\mu\text{N}$ , 60  $\mu\text{N}$ , 20  $\mu\text{N}$  and 10  $\mu\text{N}$  (see Appendix G). The measurement for this metric is calculated for the individual trials. From these figures, the rate of change of volume loss between the machining distance of 0.5 mm until 3.0 mm for all the set applied normal loads were also calculated as shown in Tables 5.5 and 5.6. When comparing the plots in Figure 5.18 and 5.19, it is obvious that Trial 1 has the highest tip volume loss. In this case, machining was along *Direction 1* and with a set normal applied force of 100  $\mu\text{N}$ . This result is in line with the observation made earlier regarding the fact that expected the probe for this experiment might have suffered breakage during the machining process. In addition, the rate of change of volume loss for this particular trial also has a greatest value compared to the other trials. It is also interesting to note that the results in Figures 5.19 exhibited much lower tip volume loss when comparing with the results shown in Figure 5.18. It is believed that the tips utilised for this particular set applied loads, i.e. 20  $\mu\text{N}$  and 10  $\mu\text{N}$ , almost had no wear. This can

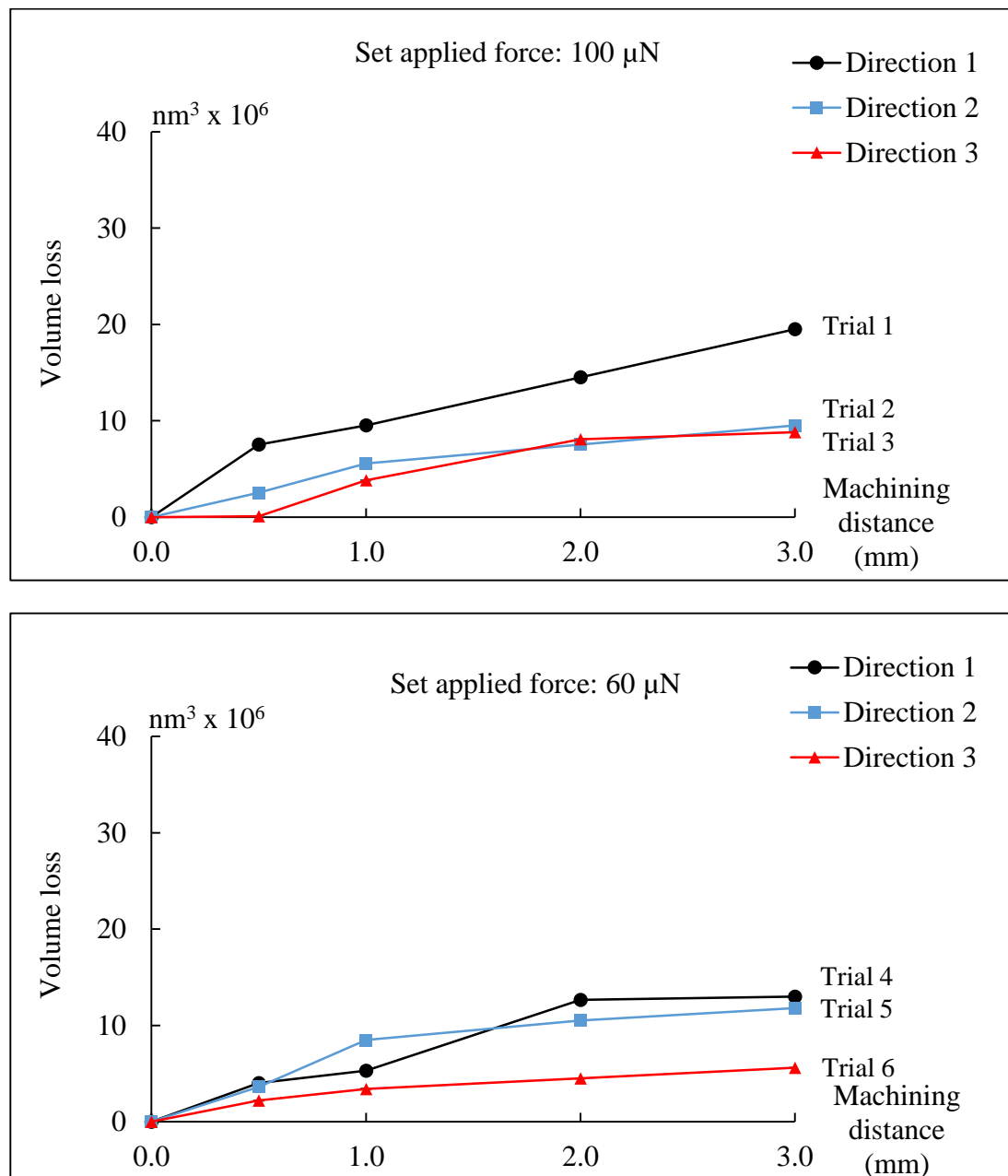
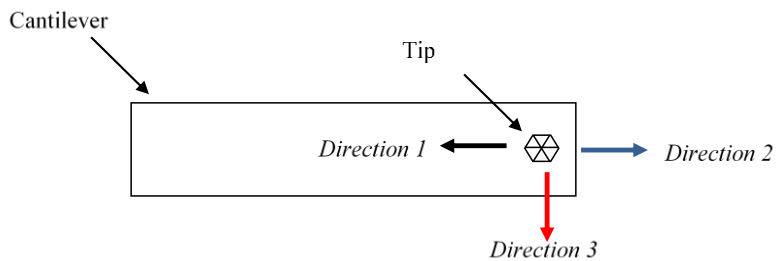


Figure 5.18: Evolution of the tip volume loss as a function of the machining direction for the different values of set normal force considered for DT-NCHR-10 diamond-coated silicon probes with standard deviation.

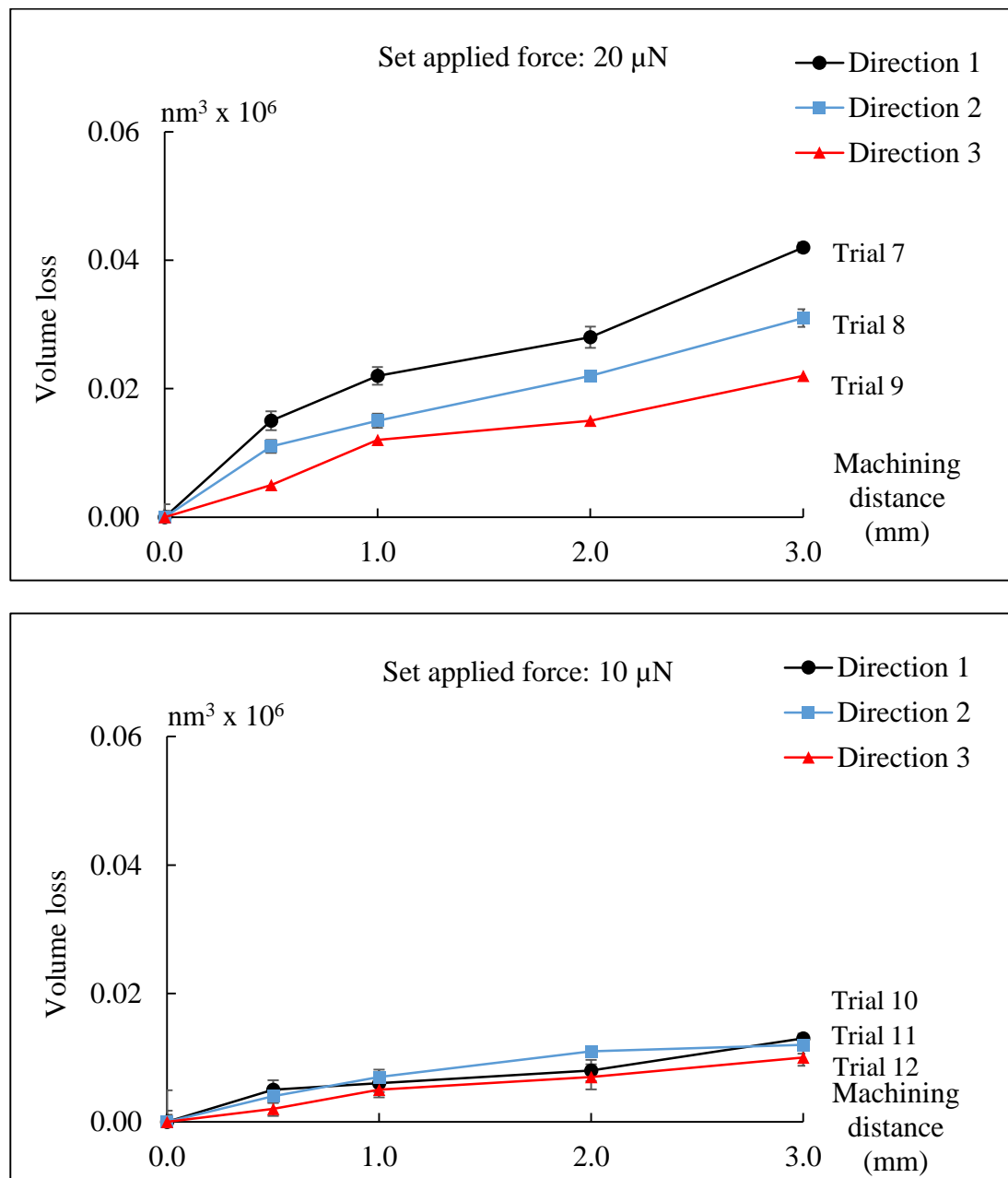
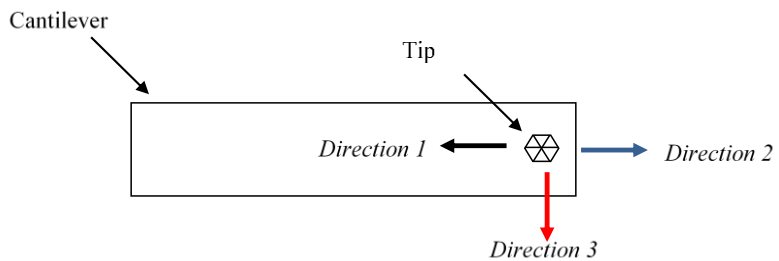


Figure 5.19: Evolution of the tip volume loss as a function of the machining direction for the different values of set normal force considered for DT-NCHR-10 diamond-coated silicon probes with standard deviation.

| Machining direction | Trial | Applied normal force ( $\mu\text{N}$ ) | Rate of change of volume loss ( $\text{nm}^3 \times 10^6 / \text{mm}$ ) between the machining points 1.0 mm until 3.0 mm |
|---------------------|-------|--|--|
| 1                   | 1     | 100                                    | 4.84   |
|                     | 4     | 60                                     | 4.01   |
| 2                   | 2     | 100                                    | 2.60   |
|                     | 5     | 60                                     | 2.93   |
| 3                   | 3     | 100                                    | 3.43   |
|                     | 6     | 60                                     | 1.30   |

Table 5.5: Rate of change of volume loss based on the plots in Figure 5.18.

| Machining direction | Trial | Applied normal force ( $\mu\text{N}$ ) | Rate of change of volume loss ( $\text{nm}^3 \times 10^6 / \text{mm}$ ) between the machining points 1.0 mm until 3.0 mm |
|---------------------|-------|--|--|
| 1                   | 7     | 20                                     | 0.01   |
|                     | 10    | 10                                     | 0.03   |
| 2                   | 8     | 20                                     | 0.08   |
|                     | 11    | 10                                     | 0.03   |
| 3                   | 9     | 20                                     | 0.06   |
|                     | 12    | 10                                     | 0.03   |

Table 5.6: Rate of change of volume loss based on the plots in Figure 5.19.

be observed when comparing profiles of the unused tip and the tip used for machining after completing 3.0 mm of machining distance (see Figure 5.14). This result was similar to that of Gozen and Ozdoganlar (2014), where at the first 3 mm of the nanomachining distance the tip had a volume loss less than  $1.10^6 \text{ nm}^3$ , but in this case ultrananocrystalline diamond AFM tips were employed.

Another result that could be derived from Figures 5.18 and 5.19 is that the tip volume loss seems dependent on the machining direction. Particularly, processing along *Direction 1* always results in the highest tip volume loss at the end of each trial regardless of the normal load applied. In contrast, machining along *Direction 3* leads to the lowest value of tip volume loss. It is interesting to note that such a conclusion could not be made Chapter 3 (refer to Figure 3.14) nor in Chapter 4 (refer to Figure 4.13). The main reason that can be put forward to explain this is the fact that most of the probes used in Chapters 3 and 4 suffered from tip breakage during nanomachining. This means that the wear process could not be considered to be in control as it is affected by sudden discontinuities when a fracture event takes place. This results from the fact that the material of the probes was different between each chapters. For Chapter 3, the tips were in silicon and thus, they were very brittle. In addition, although the probes used for Chapter 4 were diamond coated, their N-doped nature and different geometry seem to be important factors that contributed to tip breakage.

Based on the qualitative analysis of these graphs, it can also be said that the magnitude of the applied force influences the tip volume loss. Indeed, for the majority of results, the larger the load, the highest was the wear volume. In addition, the tip volume loss values are three order of magnitude smaller for 10  $\mu\text{N}$  of applied load in comparison

with 100  $\mu\text{N}$ . The only exception to the observation is for *Direction 2* at applied loads of 100  $\mu\text{N}$  and 60  $\mu\text{N}$ . Indeed, as quantified in Table 5.5 and Table 5.6, this is the only case where the rate of change of volume loss is not directly dependent on the magnitude of the applied force. In other words, these tables confirm that the rate of change of tip volume loss is generally higher for a greater set normal applied force.

Another conclusion can be drawn from Table 5.6, when compared with the results from the previous chapter is that the rate of change of volume loss for the DT-NCHR probes at a fixed load of 20  $\mu\text{N}$  is two orders of magnitude smaller than that for the DCP20 probes utilised previously. This confirms observations made earlier with Figure 5.14 where the cross-section of the profiles obtained from the SEM micrograph show that generally, the AFM probe employed in this chapter suffered less wear at 20  $\mu\text{N}$ . The reason behind this are the same as those mentioned earlier when discussing why the DT-NCHR-10 AFM probes were found to be more durable than the DCP20 probes.

### 5.5.3 Machined grooves

SEM micrographs for the set of grooves machined in this chapter are shown in Tables 5.7 and 5.8 for the different considered machining distances and normal applied forces. In addition, cross section profiles of these grooves are shown in Figures 5.20 and 5.21 for all trials at two different machining distances, namely 0.5 mm and 3.0 mm. These profiles were obtained from the AFM scans of the copper workpiece. Based on these profiles, the *H/D ratio* was calculated using the formula from Ahn and Lee (2009). These results are given in Tables 5.9 and 5.10.

Based on the SEM micrographs of the generated grooves, it can be said that machining along *Direction 1* at the highest value of applied load lead to chip being formed on the surface of the workpiece, except at 3.0 mm of machining distance. This should be caused by the tip breakage that the probe might have suffered as discussed in the previous sections. Thus, such a fracture would have resulted in the geometry of the probe that was not favourable to process the workpiece in a cutting dominated regime. The *H/D ratio* values reported in Table 5.9 are in-line with this observation.

In contrast, when machining along *Direction 2*, machining was realised only in the ploughing-dominated regime as no chips could be found on the sample. In fact, this observation for *Direction 2* also applies for all the different values of normal load investigated. The occurrence of this particular machining state could be confirmed from the *H/D ratio* measurements reported in Table 5.9. Regarding the machining experiments along *Direction 3*, chips were formed only for highest normal applied force, i.e. 100  $\mu\text{N}$  and especially for a machining distance less than 3 mm. The corresponding *H/D ratio* values seen in Table 5.9 tend to corroborate these observations. More specifically, given that the *H/D ratio* is above but still close to one for the smallest machining distance, it is suggested that a mixture of both ploughing and cutting takes place for this processing condition. It is also interesting to note that, in contrast with the results obtained in Chapter 4, processing along *Direction 3* did result in the formation of grooves even for normal applied loads as low as 10  $\mu\text{N}$ , although it is acknowledged that grooves were not consistently machined for lower applied force values. This should be due to the fact that tip breakage was observed in Chapter 4 for one of the loads considered along *Direction 3*. In addition, the difference of torsional stiffness between the probes used in this chapter and in Chapter 4 may also explain the difference in the observed machining outcomes

| Trial | Set up applied force ( $\mu\text{N}$ ) | SEM micrographs of grooves |        |        |        |
|-------|--|----------------------------|--------|--------|--------|
|       |  | 0.5 mm                     | 1.0 mm | 1.5 mm | 3.0 mm |
| 1     | 100                                    |                            |        |        |        |
| 2     |  |                            |        |        |        |
| 3     |  |                            |        |        |        |
| 4     | 60                                     |                            |        |        |        |
| 5     |  |                            |        |        |        |
| 6     |  |                            |        |        |        |

Table 5.7: SEM micrographs of grooves at the considered machining distances for set applied force of 100  $\mu\text{N}$  and 60  $\mu\text{N}$ . Scale bars: 12  $\mu\text{m}$ .

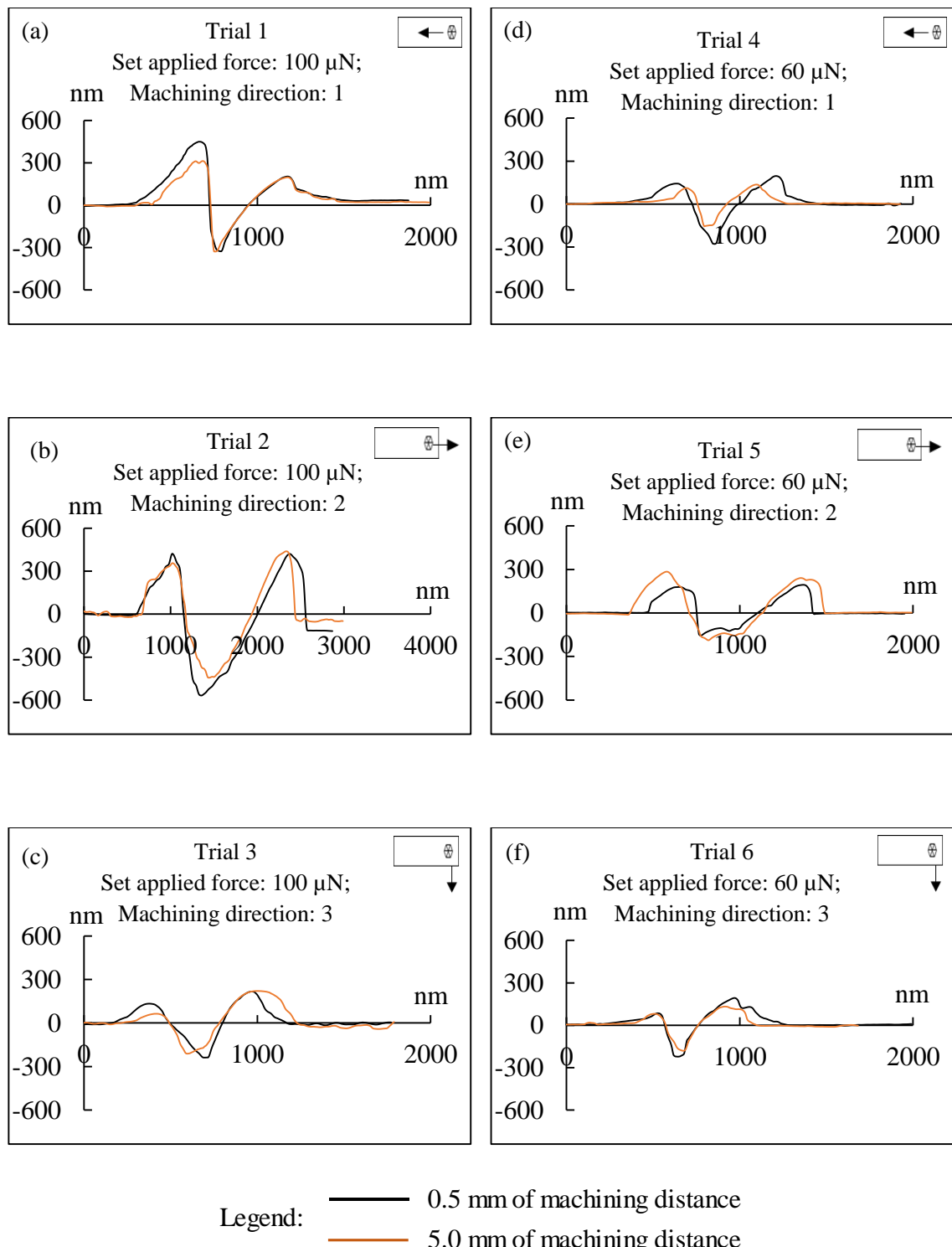


Figure 5.20: Grooves profiles.

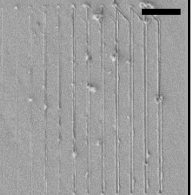
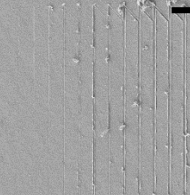
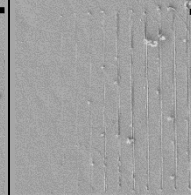
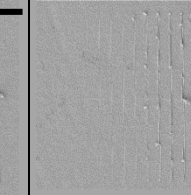
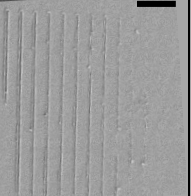
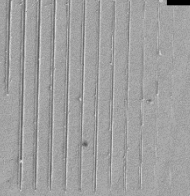
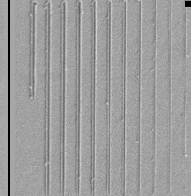
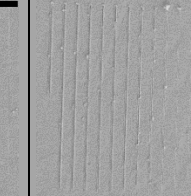
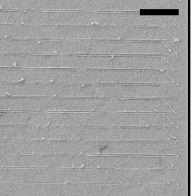
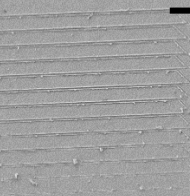
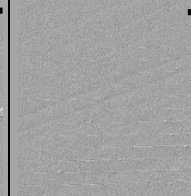
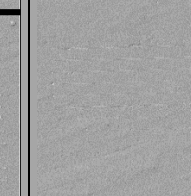
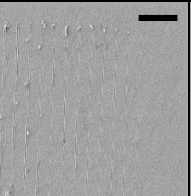
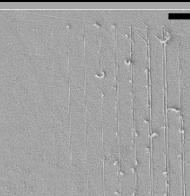
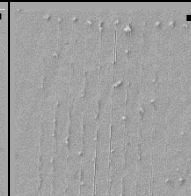
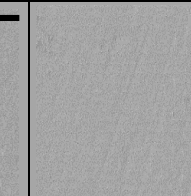
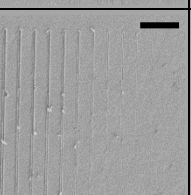
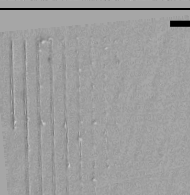
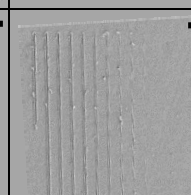
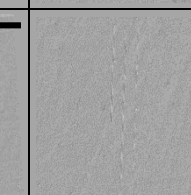
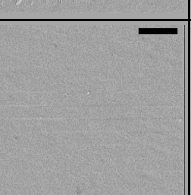
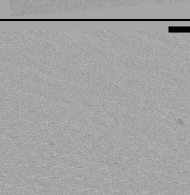
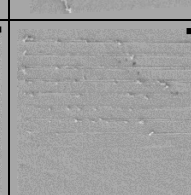
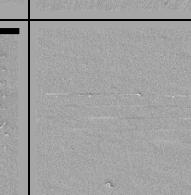
| Trial | Set up applied force ( $\mu\text{N}$ ) | SEM micrographs of grooves  |   |  |   |
|-------|--|---|---|--|---|
|       |  | 0.5 mm  | 1.0 mm  | 1.5 mm   | 3.0 mm  |
| 7     | 20                                     |    |    |    |    |
| 8     |  |    |    |    |    |
| 9     |  |   |   |   |   |
| 10    |  |  |  |  |  |
| 11    | 10                                     |  |  |  |  |
| 12    |  |  |  |  |  |

Table 5.8: SEM micrographs of grooves at the considered machining distances for set applied force of 20  $\mu\text{N}$  and 10  $\mu\text{N}$ . Scale bars: 12  $\mu\text{m}$ .

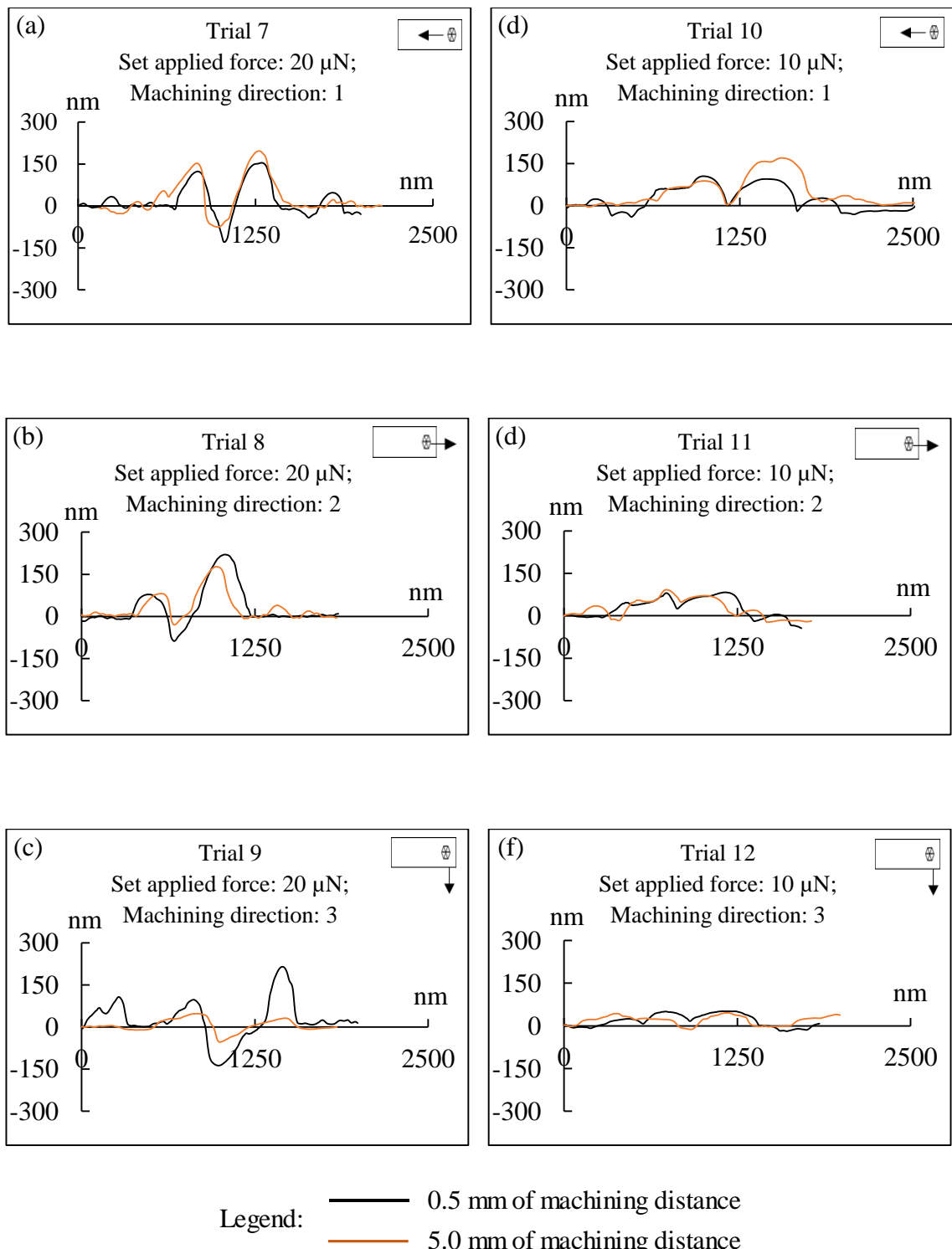


Figure 5.21: Grooves profiles.

| Trial | Applied<br>normal force<br>( $\mu\text{N}$ ) | <i>H/D ratio</i> with standard deviation |  |
|-------|--|--|--|
|       |  | During machining<br>trial until 0.5 mm   | During machining<br>trial until 3.0 mm |
| 1     | 100  | $0.65 \pm 0.12$                          | $1.15 \pm 0.13$                        |
| 2     |  | $0.96 \pm 0.28$                          | $1.12 \pm 0.40$                        |
| 3     |  | $1.07 \pm 0.48$                          | $1.24 \pm 0.30$                        |
| 4     | 60   | $0.64 \pm 0.22$                          | $0.74 \pm 0.65$                        |
| 5     |  | $0.98 \pm 0.84$                          | $1.75 \pm 0.15$                        |
| 6     |  | $5.21 \pm 2.12$                          | $3.25 \pm 0.73$                        |

Table 5.9: *H/D ratios* for set applied force 100  $\mu\text{N}$  and 60  $\mu\text{N}$ .

| Trial | Applied<br>normal force<br>( $\mu\text{N}$ ) | <i>H/D ratio</i> with standard deviation |  |
|-------|--|--|--|
|       |  | During machining<br>trial until 0.5 mm   | During machining<br>trial until 3.0 mm |
| 7     | 20   | $0.95 \pm 0.17$                          | $1.26 \pm 1.50$                        |
| 8     |  | $6.25 \pm 0.04$                          | $6.42 \pm 0.28$                        |
| 9     |  | $3.44 \pm 0.56$                          | $7.48 \pm 0.73$                        |
| 10    | 10   | $4.65 \pm 0.86$                          | $6.23 \pm 0.32$                        |
| 11    |  | $1.18 \pm 1.28$                          | $2.31 \pm 0.52$                        |
| 12    |  | $6.24 \pm 1.17$                          | $7.15 \pm 0.09$                        |

Table 5.10: *H/D ratios* for set applied force 20  $\mu\text{N}$  and 10  $\mu\text{N}$ .

between both chapters along the direction perpendicular to the long axis of the cantilever.

For the lower pre-set values of normal applied force, i.e. 20  $\mu\text{N}$  and 10  $\mu\text{N}$ , Table 5.10 show that the *H/D ratio* values are always more than unity, i.e. 1. This results indicate that the machining process for all the trials was conducted in the ploughing-dominated regime. However, the SEM micrographs reported in Table 5.8 show that in some case, small chips were still formed for this lower applied loads, especially when machining along *Direction 1*. To explain this apparent contradiction between the *H/D ratio* values and the SEM micrographs, it is worth keeping in mind that at the transition between ploughing and cutting the workpiece material is still expected to be subjected to some level of elastic recovery as reported in Elkaseer and Brousseau (2014). In addition, the small chips observed from the SEM micrographs could be the results of the interaction between the single diamond crystal of the Cu material. This means that, while the overall machining process is undertaken via ploughing, it is also possible that some of the diamond grains act as secondary cutting edges. Further investigations should be required to study the validity of this hypothesis. If it proved to be valid, this would mean that the calculation of the *H/D ratio* may not always be suitable when processing with polycrystalline cutting tools at the nanoscale.

Finally, the conclusion made in Chapter 4 stating that machining along *Direction 3* was not so favourable for the groove formation process can also be observed here. For example, at the highest normal applied force of 100  $\mu\text{N}$ , grooves machining in this direction appear to be the shallowest compare to the other Trials (see Table 5.7 and Figure 5.20). The possible reason behind this observation could be due to the tip machining in a more negative rake angle. These phenomena could also be found in Tseng *et al* (2010)

where the profile of the machined groove was shallower compared to the machining directions parallel the long cantilever axis. Similarly, this can be observed for other set normal applied force values.

## 5.6 Conclusions

This chapter started with investigating the reliability of two AFM tip apex characterisation techniques that can be realised in-situ and provide 3D geometric data about the tip shape, namely the ultra-sharp tip scan approach and the reverse imaging method. Based on quantitative and qualitative data obtained with both techniques, it was concluded that the reverse imaging scan method leads to more reliable results. Consequently, this technique was employed in the remainder of this chapter to characterise the geometry of AFM tips, coated with a film of 100 nm polycrystalline diamond, during further AFM probe-based machining experiments. These machining trials were performed to understand further the behaviour and the performance of silicon probes with diamond-coating when considering normal applied loads between 10  $\mu\text{N}$  and 100  $\mu\text{N}$ , which was a larger range than that studied in Chapter 4. The conclusions reached for this additional experimental study for this chapter can be summarised as follows:

- For a given applied load, the silicon diamond-coated probes used here exhibited negligible wear and were less likely to suffer fracture in comparison with the observations made earlier and in particular, with Chapter 4 where silicon tip coated with a diamond film were also employed. As result, the nanomachining process was more likely to be in control for set of experiments reported here. The reasons put forward to explain this difference between both types of probes are related to 1) the larger radius of the tips used in this chapter, which is expected to lead to a reduced

contact stress; 2) the fact that the diamond coating of the probes utilised here was not N-doped and 3) the larger thickness of the diamond coating for the probes considered in this chapter.

- The evolution of the tip radius did not seem to be influenced by the machining direction while the evolution of the volume loss was. More specifically, processing along in a direction away and parallel to the cantilever long axis always resulted in the largest tip volume loss regardless of the normal load applied. In addition, for the majority of results, the wear volume increased with the increase in the normal load. This result appears to be intuitive. It could not be made in former chapters due to the fact that the process was not in control previously.
- When machining in a direction perpendicular to the cantilever, the groove was very shallow compare to the other machining directions that were parallel to the long cantilever axis. This phenomenon could also be observed in Chapters 3 and 4.
- When employing AFM tips coated with a film made of a polycrystalline material, it is possible that the individual grains of the film may act as local cutting edges. If further studies confirmed that this is the case, this would explain how ploughing might be the overall groove formation mechanism, while still observing the formation of small chips.

**CHAPTER 6:**

**CONTRIBUTIONS, CONCLUSIONS AND FUTURE**

**WORK**

## **CHAPTER 6**

### **CONTRIBUTIONS, CONCLUSIONS AND FUTURE WORK**

#### **6.1 Overview**

This chapter discusses the main contributions of this research, presents the most important conclusions and suggests directions for future work.

#### **6.2 Contributions**

This research took place in the field of AFM probe-based nanoscale machining. In particular, it was concerned with the systematic assessment of the geometrical condition of different types of AFM tips when varying two process parameters, namely the applied load and the machining direction. Thus, this study provides additional experimental data with respect to the wear of AFM tips for the growing research community that focusses on nanoscale machining with an AFM instrument. In particular, tip wear studies are still scarce in this field despite the importance of the phenomenon on the process outcomes. The knowledge gaps that were identified in Chapter 2 following the systematic review of the literature are summarised below. The contributions that this study has made to address each of these gaps is also stated below.

Knowledge gap 1: It was not clear whether the tip wear may vary significantly as a function of different nanomachining parameters and particularly, as a function of the tip material, machining direction and applied load.

Contribution: This study shows that the tips in silicon are very prone to initial tip fracture during the AFM probe-based nanomachining process. The same phenomenon could also occur when silicon tips coated with diamond were utilised, although to a lesser

extent compared to silicon tips. For this reason, it was difficult to draw firm conclusions about the influence of the machining direction and applied load on the tip wear from a large number of experimental trials reported here. Indeed, for a substantial amount of trials, the nano-machining process was not in control due to tip fracture. In spite of this, it is still possible to put forward some overall findings with respect to observed machining phenomena as a function of the processing direction. In particular, the employed AFM probes used to machine a single crystal copper workpiece in a direction parallel to the long axis of the cantilever and towards it mostly operated in the cutting-dominated regime. However, in the direction parallel to the cantilever long axis and away from it, as well as in the direction perpendicular to the cantilever, most of the nanomachining operations appeared dominated by ploughing regardless of the applied load. In addition, it can be said that, overall, the machining direction perpendicular to the long axis of the cantilever was less favourable to generate grooves.

**Knowledge gap 2:** Despite the fact that the estimation of the radius of AFM tips is a commonly employed metric in tip characterisation studies, it was not clear whether radius measurements are reliable for determining the condition of AFM tips when used to machine a workpiece.

**Contribution:** In this particular research, the results of the AFM tip radius estimation were reliable only when the probe suffered no fracture during the nanomachining process. In this case, a higher tip radius corresponded to an increase in tip wear.

**Knowledge gap 3:** When recreating the 3D volume of a tip from the 2D profile of a SEM or TEM image, a common assumption is to assume that the tip is made of a stack of

circular disks. Further work should be completed to propose a more accurate discretisation scheme.

Contribution: A method was proposed to estimate the volume an AFM tip from a 2D profile by discretising the tip into a stack of frustums of right circular cones. In addition, it was shown that the error associated with the more common discretisation scheme which uses circular disk-shaped elements was 26%. Thus, it could be said that the suggested method is more accurate compared to the existing approach.

Knowledge gap 4: The identification of the best in-situ 3D measurement technique in terms of accuracy and practical suitability when implementing AFM probe-based nanomachining represents a line of research that needed systematic investigations.

Contribution: Based on the comparative analysis of the quantitative and qualitative data obtained with two different in-situ 3D measurement techniques, namely the ultra-sharp tip scan method and the reverse imaging method, it was concluded that the reverse imaging technique leads to more reliable results. In addition, experience gained during this work showed that implementing the ultra-sharp tip scan technique is not a straight-forward procedure and requires a highly skilled operator such that it can be carried out reliably. In comparison, the reverse imaging approach does not require for the AFM tip under investigation to be removed from the AFM head.

In addition, a further contribution from this study is that the validity of the *H/D ratio* method for assessing the processing regime experienced during nanomachining was realised for a larger range of machining parameters compared to data reported in the literature.

### 6.3 Conclusions

The conclusions that can be drawn based on this research with respect to the AFM tip-based nanomachining process and the AFM probe characterisation experiments can be summarised as follows:

1. When nanomachining operations are affected by tip breakage, the process outcomes are dependent on the resulting tip geometry after such fracture. In particular, the resulting tip geometry influences the contact area between the probe and the sample and thus, the stress concentration at the tip apex. In addition, the tip geometry after breakage also plays a role in determining whether machining is taking place in the ploughing-dominated or cutting-dominated regime, which in turn is expected to influence the machining force and thus, the wear.
2. Negligible wear and a much reduced likelihood of fracture could be achieved when using silicon tips coated with polycrystalline diamond with no nitrogen doping. Thus, the nanomachining process is more likely to be in control in this case.
3. When managing to implement the nanomachining process in a state of control, the results obtained suggest that the evolution of the tip wear was influenced by the machining direction. In particular, processing along a direction parallel and away to the cantilever long axis always leads to the largest tip volume loss regardless of the normal load applied. It is interesting to note that this is also the direction where the process was most likely to be conducted in the ploughing-dominated regime. This result is in-line with the expectation that cutting forces increase when machining is conducted in the ploughing-dominated regime compared to processing with chip

formation. In addition, when the nanomachining process is in control, the wear volume increases with the increase in the normal load for all directions considered.

4. Generally, the validity of the *H/D ratio* as a post-processing metric to distinguish between ploughing and cutting on the nanoscale was verified. However, care should be taken about drawing firm conclusions when this ratio is close to unity and when a tool coated with a polycrystalline material is utilised.
5. The 2D data of the tip geometry obtained from SEM inspections could provide reliable results for characterising the tip apex profile. However, such data have limitations when analysing the tip wear, especially for measuring the wear volume. In addition, the acquisition of SEM micrographs for an AFM probe is a time consuming process which could also result in tip damage when placing the AFM probe in the SEM chamber.
6. Finally, the torsional stiffness of the AFM probe used influences the groove formation process. In particular, the V-shape cantilevers used in this study had less torsional rigidity compared to rectangular cantilevers. This was detrimental to the machining of grooves when processing in a direction perpendicular to the long axis of the cantilever.

#### **6.4 Recommendations for future work**

Further research efforts were identified during this research. These are reported as follows:

1. Even though the characterisation of AFM tips was performed at regular intervals throughout this study, the implemented wear monitoring approaches should be considered as off-line techniques. Indeed, the nanomachining operations needed to be interrupted every time the probe was due for inspection. Thus, further research for developing an online method to monitor the tip wear is still required. Efforts in this direction should focus on techniques which can be easily implemented with any type of commercial probes.
2. The ultra-sharp tip scan approach used in Chapter 4 for characterising the AFM tip apex profile shows that this in-situ technique always overestimates the width of the tip profile. Hence, further comprehensive studies should be carried out to identify the factors that are responsible for this.
3. In this research, most of the AFM probes used for machining operations suffered tip breakage. Thus, a better understanding of tip fracture initiation and propagation may provide some useful guidance for the AFM practitioner when implementing this nanoscale machining process.
4. Further investigation is required to confirm whether the individual grains of the polycrystalline material film may act as local cutting edges when employing AFM tips coated with such films for nanomachining operations.

## Appendix A: Comparison between two discretisation schemes for tip volume calculations from 2D profile data.

For each of the six probes utilised in Chapter 3, Table A.1 provide data between different tip volume estimation methods from 2D profiles. From the results in Table A.1, the graph of the comparison between two discretisation schemes for tip volume calculations from 2D profile data is also illustrated in Figure A.1. The first method relies on representing the tip as a stack of circular disk-shaped elements while the second method is based on a stack of frustums of right circular cones. The formula used to express the volume,  $V_c$ , when using a stack of circular disk shaped elements is given below.

$$V_c = \pi r_c^2 h_c \quad (\text{A.1.0})$$

where  $h_c$  is the height,  $r_c$  is the radius of the circular disk shape as shown in Figure A.1.

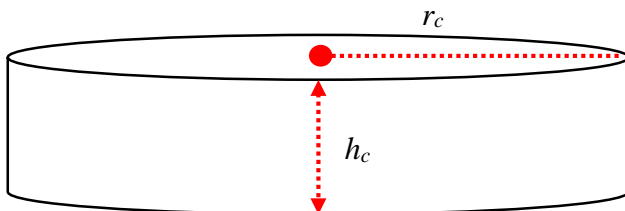


Figure A.1: Circular disk

| Method to calculate volume of the AFM tip | Volume Measurement ( $\text{nm}^3 \times 10^6$ ) |       |       |       |       |       |         |
|---|--|-------|-------|-------|-------|-------|---------|
|   | Probes   |       |       |       |       |       | Average |
|   | 1  | 2     | 3     | 4     | 5     | 6     |         |
| Stack of Circular disk                    | 630.7  | 567.4 | 485.9 | 685.2 | 476.7 | 650.4 | 582.7   |
| Stack Frustum of right circular cone disk | 571.6  | 480.5 | 271.7 | 492.3 | 395.7 | 571.6 | 463.9   |

Table A.1: Volume of the six NSC 15 silicon tips used in Chapter 3 prior to the start of the experimental trials.

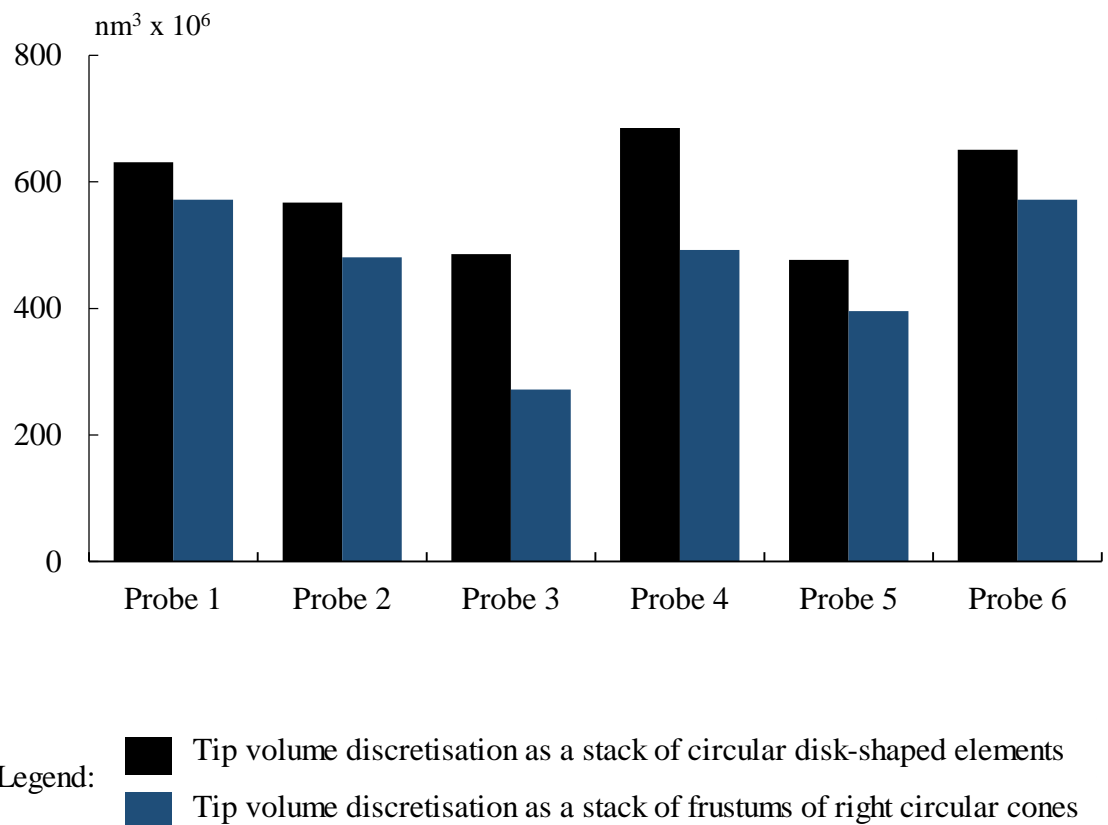


Figure A.2: Comparison between two discretisation schemes for tip volume calculations from 2D profile data

The error,  $V_{error}$ , associated with the discretisation using circular disk-shaped elements was estimated as follows:

$$V_{error} = \frac{V_{average\ circular\ disk} - V_{average\ frustum}}{V_{average\ frustum}} \times 100\% \quad (\text{A } 1.1)$$

where  $V_{average\ circular\ disk}$  and  $V_{average\ frustum}$  are the average volume values, from the six probes employed in Chapter 3, for the stack of circular disk-shaped elements and the stack of frustums of right circular cones discretisation schemes, respectively.

**Appendix B: Fitness agreement for AFM tip profile**

The fitted polynomial of the AFM tip profile was conducted by using Excel software. In particular, the polynomial of degree two trendline profile is formatted to the tip profile as illustrated in Figure B.1. The fitness agreement between these two profiles was between 88% to 97% as shown in Tables B.1 and B.2. In particular, the fitness agreement (R-squared value) which is the estimation values of the trendline profile that correspond to the actual data which in this case is the profile of the AFM probe.

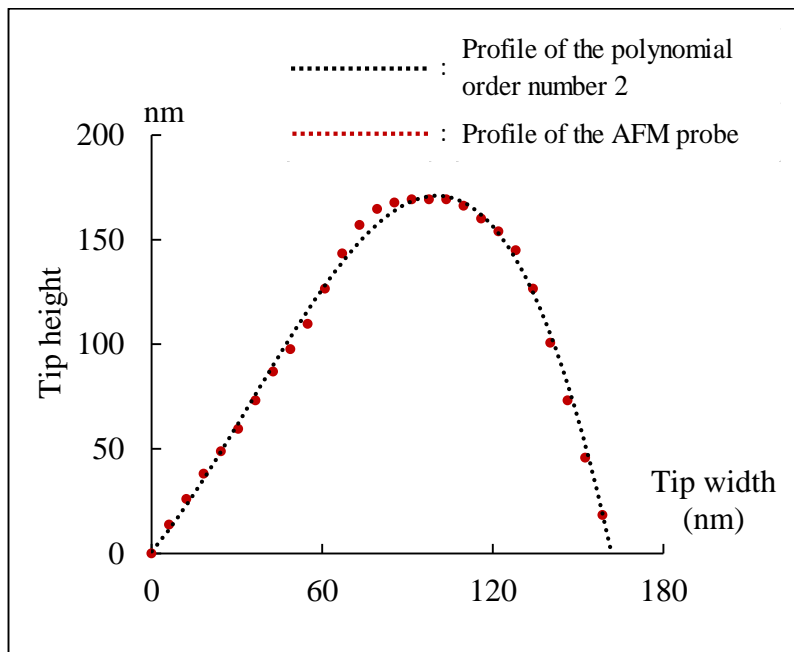


Figure B.1: Profile of the polynomial of degree two fitted to profile of the AFM probe

| <b>AFM probe</b>  | <b>Fitness agreement (%)</b> |          |          |          |          |          |
|---|------------------------------|----------|----------|----------|----------|----------|
|   | <b>1</b>                     | <b>2</b> | <b>3</b> | <b>4</b> | <b>5</b> | <b>6</b> |
| Silicon tip (NSC 15)  | 95.23                        | 97.59    | 96.20    | 91.67    | 97.23    | 88.42    |
| Silicon diamond coated tip with nitrogen doping (DCP 20)        | 96.70                        | 95.69    | 97.44    | 96.57    | 97.16    | 96.61    |
| Silicon diamond coated tip without nitrogen doping (DT-NCHR 10) | 94.08                        | 96.17    | 92.58    | 89.21    | 95.40    | 95.77    |

Table B.1: Fitness agreement (R-squared value) between polynomial degree two profile and AFM tip profile prior to the start of the experimental trials.

| <b>AFM probe</b>  | <b>Fitness agreement (%)</b> |          |          |          |          |          |
|---|------------------------------|----------|----------|----------|----------|----------|
|   | <b>1</b>                     | <b>2</b> | <b>3</b> | <b>4</b> | <b>5</b> | <b>6</b> |
| Silicon tip (NSC 15)  | 84.95                        | 85.54    | 90.20    | 90.10    | 90.10    | 87.33    |
| Silicon diamond coated tip with nitrogen doping (DCP 20)        | 87.32                        | 88.00    | 93.48    | 96.21    | 91.61    | 86.32    |
| Silicon diamond coated tip without nitrogen doping (DT-NCHR 10) | 97.44                        | 94.28    | 88.32    | 85.59    | 89.38    | 95.49    |

Table B.2: Fitness agreement between polynomial degree two profile and AFM tip profile after completing the experimental trials.

**Appendix C: SEM micrograph of AFM silicon tip after breakage occurrence.**

Figure C.1 show SEM micrographs of NSC 15 silicon tips. It believes that the tips exhibited a fracture after 0.5 mm machining distance.

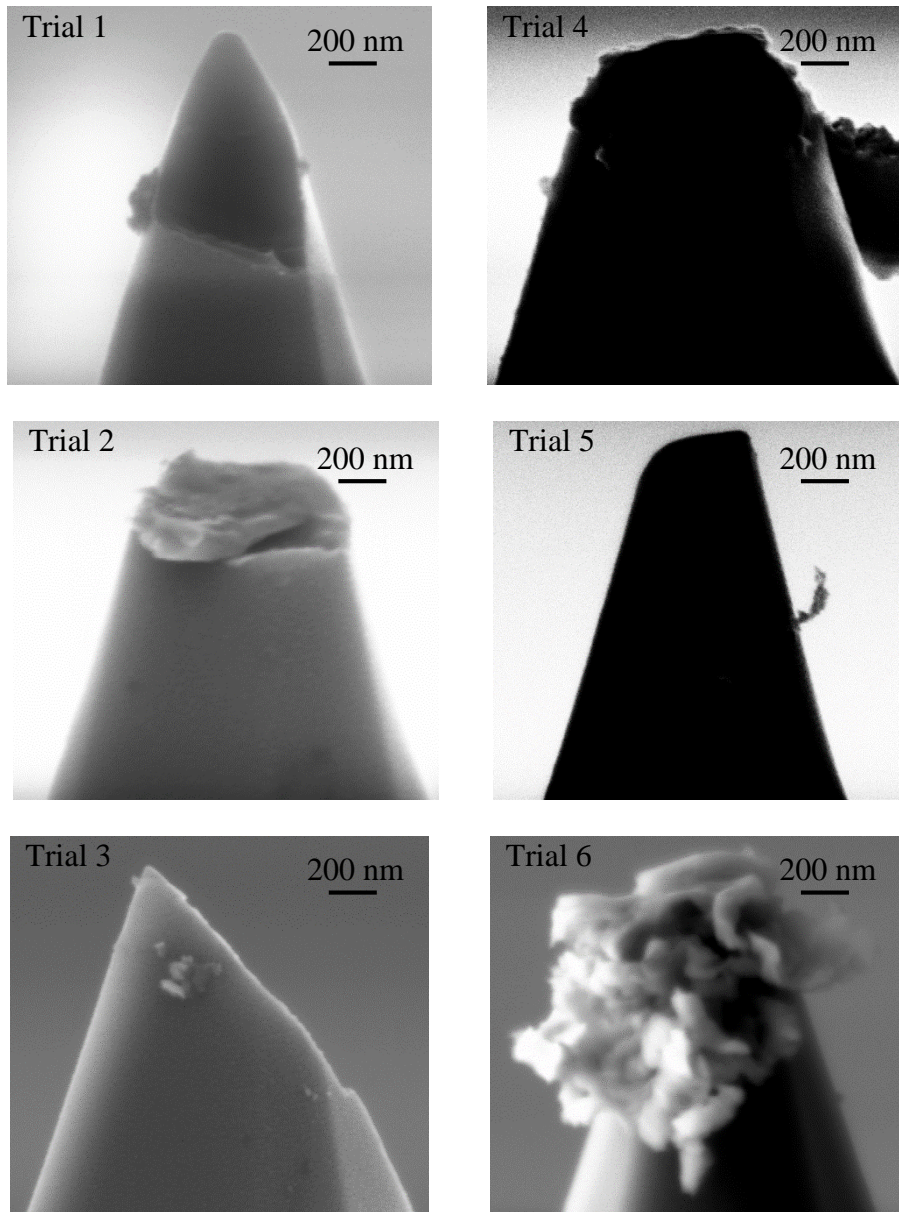


Figure C.1: SEM micrographs of the six NSC 15 silicon tips after machining at 0.5 mm.

**Appendix D: SEM micrograph of AFM silicon diamond coated tip  
after breakage occurrence**

Figure D.1 show a few of SEM micrographs of silicon diamond coated tip with nitrogen doping. It believes that the tips exhibited a fracture during the machining operation.

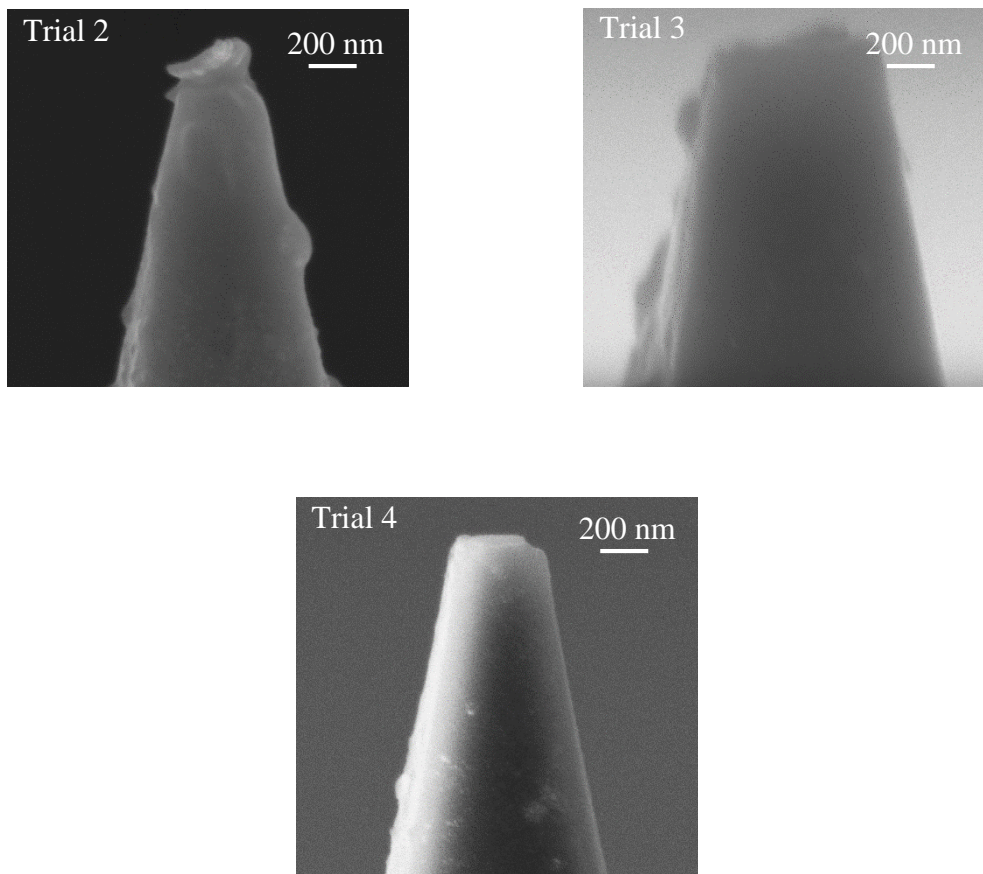


Figure D.1: SEM micrographs of the DCP 20 silicon diamond coated tips with nitrogen doping after machining at 0.5 mm.

Figure D.2: show a SEM micrographs of silicon diamond coated tip with nitrogen doping. It believes that the tips exhibited a fracture during the machining operation.

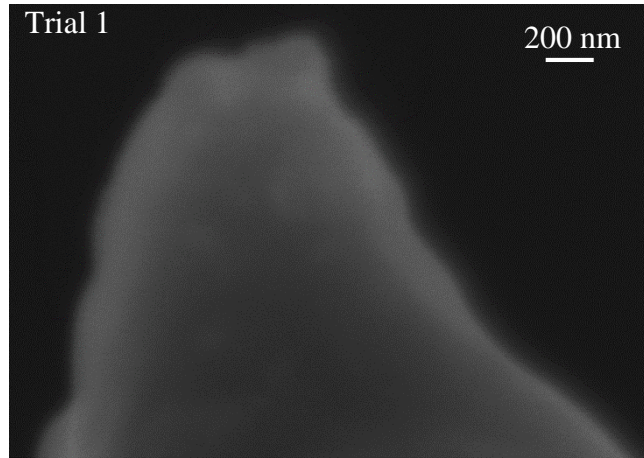


Figure D.2: SEM micrographs of the DT-NCHR 10 silicon diamond coated tips without nitrogen doping after machining at 0.5 mm at set applied force 100  $\mu\text{N}$ .

Figure D.3 shown an image of the single crystal copper with a part of the utilized silicon diamond coated tip with nitrogen doping stuck on the surface of the sample

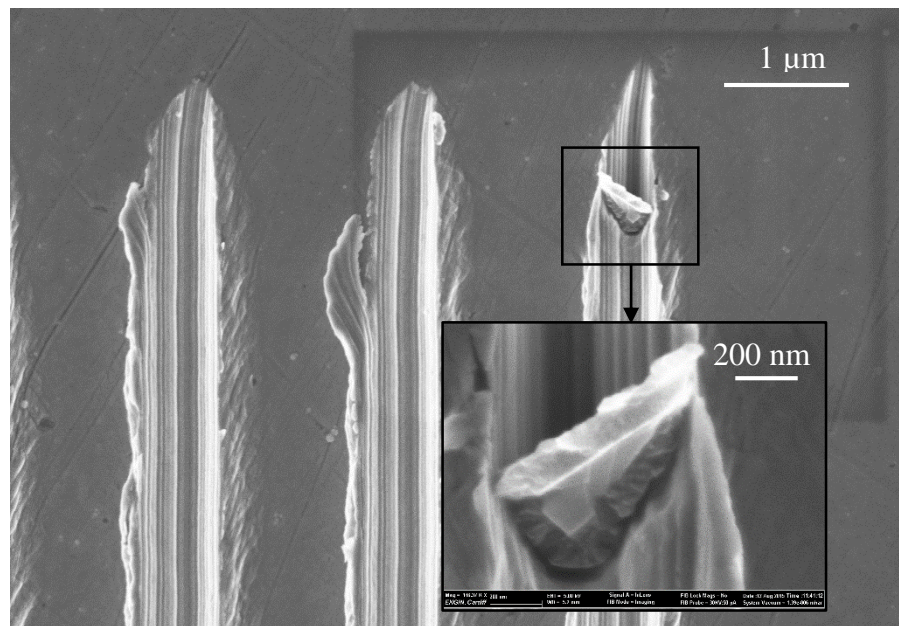


Figure D.3: A part of silicon polycrystalline diamond coated tip without nitrogen doping stuck on the surface of single crystal copper workpiece

## **Appendix E: Evolution of tip radius, area and volume loss value for silicon tip nanomachining experiments.**

Tables E.1, E.2 and E.3 show the measurement values for tip radius, area and volume loss measurement respectively for silicon tip nanomachining experiment.

| Machining distance (mm) | Radius measurement (nm) |       |       |       |       |       |
|-------------------------|-------------------------|-------|-------|-------|-------|-------|
|                         | Trials                  |       |       |       |       |       |
|                         | 1                       | 2     | 3     | 4     | 5     | 6     |
| 0.0                     | 8.0                     | 9.4   | 13.5  | 19.9  | 14.2  | 46.3  |
| 0.5                     | 76.9                    | 325.0 | 86.0  | 352.0 | 227.3 | 151.6 |
| 1.0                     | 128.0                   | 454.6 | 92.0  | 294.0 | 321.5 | 294.1 |
| 1.5                     | 119.1                   | 480.0 | 102.0 | 325.0 | 263.2 | 277.8 |
| 3.0                     | 161.3                   | 492.0 | 119.1 | 337.0 | 263.2 | 357.1 |

Table E.1: Evolution of tip radius measurement for silicon tip.

| Machining distance (mm) | Area loss measurement ( $\text{nm}^2 \times 10^4$ ) |      |      |      |      |      |
|-------------------------|---|------|------|------|------|------|
|                         | Trials  |      |      |      |      |      |
|                         | 1   | 2    | 3    | 4    | 5    | 6    |
| 0.0                     | 0.0   | 0.0  | 0.0  | 0.0  | 0.0  | 0.0  |
| 0.5                     | 13.9  | 47.2 | 70.2 | 64.2 | 20.4 | 20.6 |
| 1.0                     | 14.4  | 53.5 | 73.2 | 77.8 | 30.9 | 24.3 |
| 1.5                     | 18.0  | 54.1 | 73.3 | 84.7 | 31.2 | 29.7 |
| 3.0                     | 21.5  | 55.5 | 79.3 | 88.6 | 33.5 | 31.4 |

Table E.2: Evolution of tip area loss measurement for silicon tip.

Appendix E: Evolution of tip radius, area and volume value for silicon tip nanomachining experiments.

---

| Machining distance (mm) | Volume loss measurement ( $\text{nm}^3 \times 10^6$ ) |       |       |       |       |      |
|-------------------------|---|-------|-------|-------|-------|------|
|                         | Trials  |       |       |       |       |      |
|                         | 1   | 2     | 3     | 4     | 5     | 6    |
| 0.0                     | 0.0   | 0.0   | 0.0   | 0.0   | 0.0   | 0.0  |
| 0.5                     | 47.9  | 159.5 | 211.5 | 119.7 | 63.7  | 35.6 |
| 1.0                     | 59.9  | 175.3 | 218.6 | 147.3 | 83.5  | 44.3 |
| 1.5                     | 70.6  | 182.3 | 220.5 | 166.7 | 99.7  | 52.8 |
| 3.0                     | 73.8  | 190.0 | 232.4 | 185.6 | 118.6 | 57.6 |

Table E.3: Evolution of tip volume loss measurement for silicon tip.

Appendix F: Evolution of tip radius and volume value for silicon diamond coated tip with nitrogen doping nanomachining experiments.

## **Appendix F: Evolution of tip radius and volume loss value for silicon diamond coated tip with nitrogen doping nanomachining experiments.**

Tables F.1 and F.2 show the measurement values for tip radius and volume loss measurement respectively for silicon diamond coated tip with nitrogen doping nanomachining experiment.

| Machining distance (mm) | Radius measurement (nm) |       |       |       |       |       |
|-------------------------|-------------------------|-------|-------|-------|-------|-------|
|                         | Trials                  |       |       |       |       |       |
|                         | 1                       | 2     | 3     | 4     | 5     | 6     |
| 0.0                     | 84.2                    | 77.7  | 81.5  | 110.1 | 94.8  | 102.2 |
| 0.5                     | 84.8                    | 183.4 | 81.6  | 147.2 | 97.6  | 104.8 |
| 1.0                     | 119.3                   | 194.6 | 130.0 | 212.1 | 113.1 | 145.9 |
| 1.5                     | 127.0                   | 196.9 | 146.7 | 212.1 | 123.1 | 159.3 |
| 3.0                     | 145.5                   | 239.2 | 186.4 | 223.5 | 126.9 | 162.6 |
| 5.0                     | 158.7                   | 232.0 | 254.7 | 292.1 | 135.8 | 165.6 |

Table F.1: Evolution of tip radius measurement for silicon diamond coated tip with nitrogen doping.

| Machining distance (mm) | Volume loss measurement ( $\text{nm}^3 \times 10^6$ ) |       |       |       |      |      |
|-------------------------|---|-------|-------|-------|------|------|
|                         | Trials  |       |       |       |      |      |
|                         | 1   | 2     | 3     | 4     | 5    | 6    |
| 0.0                     | 0.0   | 0.0   | 0.0   | 0.0   | 0.0  | 0.0  |
| 0.5                     | 23.9  | 52.1  | 34.4  | 21.4  | 27.7 | 33.8 |
| 1.0                     | 28.8  | 55.0  | 104.8 | 32.5  | 28.9 | 51.2 |
| 1.5                     | 32.1  | 87.7  | 111.9 | 52.3  | 40.9 | 65.8 |
| 3.0                     | 38.5  | 89.4  | 121.3 | 60.8  | 49.0 | 66.4 |
| 5.0                     | 45.6  | 100.5 | 144.9 | 111.6 | 54.9 | 66.4 |

Table F.2: Evolution of tip volume loss measurement for silicon diamond coated tip with nitrogen doping.

## **Appendix G: Evolution of tip radius and volume loss value for silicon diamond coated tip without nitrogen doping nanomachining experiments.**

Tables G.1 and G.2 show the measurement values for tip radius and volume loss measurement respectively for silicon diamond coated tip without nitrogen doping nanomachining experiment.

| Trials | Machining distance (mm) |                    |                         |                    |                         |                    |                         |                    |                         |                    |
|--------|-------------------------|--------------------|-------------------------|--------------------|-------------------------|--------------------|-------------------------|--------------------|-------------------------|--------------------|
|        | 0.0                     |                    | 0.5                     |                    | 1.0                     |                    | 1.5                     |                    | 3.0                     |                    |
|        | Radius measurement (nm) | Standard deviation |
| 1      | 113.0                   | 7.0                | 117.9                   | 10.1               | 122.3                   | 5.6                | 143.0                   | 5.2                | 150.1                   | 4.5                |
| 2      | 95.1                    | 6.4                | 127.0                   | 16.4               | 143.2                   | 21.7               | 145.3                   | 5.6                | 146.2                   | 11.8               |
| 3      | 136.0                   | 33.8               | 143.0                   | 14.1               | 149.0                   | 5.3                | 158.0                   | 2.5                | 161.0                   | 8.8                |
| 4      | 112.2                   | 3.8                | 126.0                   | 9.9                | 128.3                   | 7.8                | 132.1                   | 3.4                | 146.9                   | 5.4                |
| 5      | 173.4                   | 21.6               | 185.0                   | 18.2               | 195.8                   | 17.6               | 201.0                   | 26.0               | 121.3                   | 18.4               |
| 6      | 135.0                   | 2.5                | 143.8                   | 4.1                | 153.2                   | 11.4               | 158.1                   | 2.1                | 161.4                   | 9.6                |
| 7      | 133.1                   | 5.5                | 140.2                   | 6.5                | 143.0                   | 3.2                | 148.0                   | 2.6                | 149.0                   | 2.8                |
| 8      | 127.0                   | 11.2               | 131.0                   | 8.7                | 131.4                   | 6.5                | 134.0                   | 5.8                | 137.9                   | 6.7                |
| 9      | 175.1                   | 1.1                | 178.4                   | 0.8                | 182.0                   | 3.2                | 183.2                   | 2.8                | 187.3                   | 2.3                |
| 10     | 135.0                   | 1.5                | 138.2                   | 4.3                | 142.2                   | 3.2                | 146.0                   | 2.6                | 150.1                   | 1.8                |
| 11     | 120.5                   | 7.8                | 121.2                   | 3.2                | 123.0                   | 3.1                | 126.0                   | 2.7                | 132.0                   | 1.5                |
| 12     | 147.0                   | 1.1                | 152.0                   | 2.1                | 148.3                   | 2.8                | 138.9                   | 3.2                | 135.7                   | 2.4                |

Table G.1: Evolution of tip radius measurement for silicon diamond coated tip without nitrogen doping.

| Trials | Machining distance (mm)                               |                    |   |                    |   |                    |   |                    |   |                    |
|--------|---|--------------------|---|--------------------|---|--------------------|---|--------------------|---|--------------------|
|        | 0.0   |                    | 0.5   |                    | 1.0   |                    | 1.5   |                    | 3.0   |                    |
|        | Volume loss measurement ( $\text{nm}^3 \times 10^6$ ) | Standard deviation | Volume loss measurement ( $\text{nm}^3 \times 10^6$ ) | Standard deviation | Volume loss measurement ( $\text{nm}^3 \times 10^6$ ) | Standard deviation | Volume loss measurement ( $\text{nm}^3 \times 10^6$ ) | Standard deviation | Volume loss measurement ( $\text{nm}^3 \times 10^6$ ) | Standard deviation |
| 1      | 0.000   | 0.000              | 7.520   | 0.015              | 9.500   | 0.014              | 14.500  | 0.017              | 19.500  | 0.001              |
| 2      | 0.000   | 0.000              | 2.540   | 0.001              | 5.560   | 0.011              | 7.520   | 0.004              | 9.520   | 0.055              |
| 3      | 0.000   | 0.000              | 0.080   | 0.011              | 3.820   | 0.012              | 8.060   | 0.020              | 8.800   | 0.013              |
| 4      | 0.000   | 0.000              | 40.086  | 0.048              | 53.000  | 0.129              | 126.400   | 0.159              | 130.000   | 0.133              |
| 5      | 0.000   | 0.000              | 36.000  | 0.428              | 85.000  | 0.136              | 105.000   | 0.186              | 118.000   | 0.208              |
| 6      | 0.000   | 0.000              | 22.000  | 0.105              | 34.000  | 0.571              | 45.000  | 0.127              | 56.000  | 0.058              |
| 7      | 0.000   | 0.000              | 1.500   | 0.146              | 2.200   | 0.138              | 2.800   | 0.165              | 4.200   | 0.076              |
| 8      | 0.000   | 0.000              | 1.100   | 0.107              | 1.500   | 0.113              | 2.200   | 0.037              | 3.100   | 0.140              |
| 9      | 0.000   | 0.000              | 0.500   | 0.107              | 1.200   | 0.120              | 1.500   | 0.196              | 2.200   | 0.128              |
| 10     | 0.000   | 0.000              | 0.005   | 0.001              | 0.006   | 0.001              | 0.008   | 0.002              | 0.013   | 0.001              |
| 11     | 0.000   | 0.000              | 0.004   | 0.001              | 0.007   | 0.001              | 0.011   | 0.000              | 0.012   | 0.001              |
| 12     | 0.000   | 0.000              | 0.002   | 0.001              | 0.005   | 0.001              | 0.007   | 0.002              | 0.010   | 0.001              |

Table G.2: Evolution of tip volume loss measurement for silicon diamond coated tip without nitrogen doping.

## REFERENCES

Ahn B. W. and Lee S. H., 2009, "Characterization and Acoustic Emission Monitoring of AFM Nanomachining", Journal of Micromechanics and Micro engineering, Vol. 19, No. 4, pp. 1-6.

Allen M. J., Hud N. V., Balooch M., Tench R. J., Siekhaus W. J. and Balhorn R., 1992, "Tip-Radius-Induced Artifacts in AFM Images of Protamine-Complexed DNA Fibers", Ultramicroscopy, Vol. 42-44, part 2, pp. 1095-1100.

Atamny F. and Baiker A., 1995. "Direct Imaging of the Tip Shape by AFM", Surface Science, Vol. 323, Issue 3, pp. L314-L318.

Bao G. W., and Li S. F. Y., 1998, "Characterisation of Atomic Force Microscopy (AFM) Tip Shapes by Scanning Hydrothermally deposited ZnO Thin Films", Talanta, Vol. 45, Issue 4. pp. 751-757.

Beegan D., Chowdhury S. and Laugier M. T., 2007, "Comparison between Nanoindentation and Scratch Test Hardness (Scratch Hardness) Values of Copper Thin Films on Oxidised Silicon Substrates", Surface and Coating Technologies, Vol. 201, Issue 12, pp. 5804-5808.

Bhaskaran H., Gotsmann B., Sebastian A., Drechsler U., Lantz M. A., Despont M., Jaroenapibal P., Carpick R. W., Chen Y. and Sridharan K., 2010, "Ultralow Nanoscale Wear through Atom-by-Atom Attrition in Silicon-Containing Diamond-Like-Carbon", Nature Nanotechnology, Vol. 5, pp. 181-85.

Bining G., Quate C. F. and Gerber Ch., 1986, "Atomic Force Microscope", Physical Review Letters, Vol.56, pp. 930-933.

Bloo M. L., Haitjema H. and Pril W. O., 1999, "Deformation and Wear of Pyramidal, Silicon-Nitride AFM tips Scanning Micrometre-Size Features in Contact Mode", Measurement, Vol. 25, Issue 3, pp. 203-211.

Bhushan B. and Kwak K. J., 2007, "Velocity Dependence of Nanoscale Wear in Atomic Force Microscopy", Applied Physics Letters, Vol. 91, Issue 16, pp. 163113-1 - 163113-3.

Bhushan B., 2001, "Nano- to Microscale Wear and Mechanical Characterization using Scanning Probe Microscopy," Wear, Vol. 251, Issues 1-12, pp. 1105-1123.

Bourne K., Kapoor S. G. and Devor R. E., 2010, "Study of a High Performance AFM Probe-Based Microscribing Process", ASME Trans. Journal of Manufacturing Science and Engineering, Vol. 132, Issue No. 3, pp. 309061-3090610.

Brousseau E. B., Krohs F., Caillaud E., Dimov S., Gibaru O. and Fatikow S., 2010, "Development of a Novel Process Chain Based on Atomic Force Microscope Scratching for Small and Medium Series Production of Polymer Nanostructured Components", Journal of Manufacturing Science and Engineering., Vol. 132, Issue 3, pp. 03091-1 – 03091-8.

## References

---

- Brousseau E. B., Arnal B., Thiery S., Gibaru O. and Mayor J. R., 2013, “Towards CNC Automation in AFM Probe-Based Nano Machining”, International Conference on Micromanufacturing 2013, pp. 25-28.
- Bykov V., Gologanov A. and Shevyakov, 1998, “Test Structure for SPM Tip Shape Deconvolution”, Applied Physics A, Vol. 66, issue 5, pp. 499-502.
- Campbell P. M., Snow E. S. and McMarr P. J., 1996, “AFM-based Fabrication of Si Nanostructures”, Physica B, Vol. 227, Issue 1-4, pp. 315-317.
- Chau R., Datta S., Doczy M., Doyle B., Jin B., Kavalieros J., Majumdar A., Metz M. and Radosavljevic M., 2005, “Benchmarking Nanotechnology for High Performance and Low-Power Logic Transistor Applications”, IEEE Transactions on Nanotechnology, Vol. 4., No. 2, pp. 153-158.
- Chen J., 2014, “Nanobiomechanics of Living Cells: A Review”, Interface Focus, Vol 4: 20130055, Issue 2.
- Cheng T.J., Han J. H., Ziwisky M., Lee C. H. and Bhave S. A., 2011, “6.4 GHZ Acoustic Sensor for In-Situ Monitoring of AFM Tip Wear”, IEEE International Conference on Micro Electro Mechanical Systems (MEMS), pp. 521-524.
- Chung K-H. and Kim D-E., 2003, “Fundamental Investigation of Micro Wear Rate using an Atomic Force Microscope”, Tribology Letters, Vol. 15, No. 2., pp. 135-144.

## References

---

- Chung K-H., Lee Y. H. and Kim D-E., 2005, "Characteristics of Fracture during the Approach Process and Wear Mechanism of a Silicon AFM Tip", Ultramicroscopy, Vol. 102, Issue 2, pp. 161-171.
- Crook R., Graham A. C., Smith C. G., Farrer I., Beere H. E. and Ritchie D. A., 2003, "Erasable Electrostatic Lithography for Quantum Components", Nature International Weekly Journal of Science, Vol. 424, pp. 751-754.
- Dongmo L. S., Villarrubia J. S., Jones S. N., Renegar T. B., Postek M. T. and Song J.F., 2000, "Experimental Test of Blind Tip Reconstruction for Scanning Probe Microscopy", Ultramicroscopy, Vol. 85, pp. 141-153.
- Edwards H., McGlothlin R., and Elisa U., 1998, "Vertical Metrology using Scanning-Probe Microscopes: Imaging Distortions and Measurement Repeatability", Journal of Applied Physics, Vol. 83, No. 8, pp. 3952–3971.
- Elkaseer A. M. and Brousseau E. B., 2014, "Modelling the Surface Generation Process during AFM Probe-Based Machining: Simulation and Experimental Validation", Surface Topography: Metrology & Properties, Vol. 2, No. 2, pp. 025001 (12 pages).
- Fang T-H. and Chang W-J., 2003, "Effects of AFM-based Nanomachining Process on Aluminium Surface", Journal of Physics and Chemistry of Solids, Vol. 64, Issue 6, pp. 913-918.

## References

---

Gan Y., 2009, “Atomic and Subnanometer Resolution in Ambient Conditions by Atomic Force Microscopy”, Surface Science Report, Vol. 64, Issue 3, pp. 99-121.

Geng Y., Zhang J., Yan Y., Yu B., Geng L. and Sun T., 2015, “Experimental and Theoretical Investigation of Crystallographic Orientation Dependence of Nanoscratching of Single Crystalline Copper” J. Plos One, Vol. 10.

Glasbey T. O., Batts G. N., Davies M. C., Jackson D. E., Nicholas C. V., Purbrick M. D., Roberts C. J., Tendler S. J. B. and Williams P. M., 1994, “The use of Polymer Film to Estimate AFM Probe Profiles”, Surface Science, Vol. 318, Issue 3, pp. L1219-L1224.

Goel S., Luo X., Reuben R. L. and Pen H., 2012, “Influence of Temperature and Crystal Orientation on Tool Wear during Single Point Diamond Turning of Silicon”, Wear, Vol. 284-285, pp. 65-72.

Gotsmann B. and Lantz M. A., 2008, “Atomistic Wear in a Single Asperity Sliding Contact”, Physical Review Letters, Vol.101, Issue 12-19, pp. 125501-1 - 125501-4.

Gozen B. A. and Ozdoganlar O. B., 2012, “Design and Evaluation of a Mechanical Nanomanufacturing system for Nanomilling,” Precision Engineering, Vol. 36, Issues 1, pp. 19-30.

Gozen B. A. and Ozdoganlar B., 2014, “Wear of Ultrananocrystalline Diamond AFM Tips during Mechanical Nano-Manufacturing by Nano-Milling”, Wear, Vol. 317, Issues 1-2, pp. 39-55.

Griffith J. E., Grigg D.A., Vasile M.J., Russell P.E. and Fitzgerald E.A., 1991, "Characterization of Scanning Probe Microscope Tips for Linewidth Measurement", Journal of Vacuum Science & Technology. B, Microelectronics and Nanometer Structures: Processing, Measurement and Phenomena, Vol. 9, Issue 6, pp. 3586-3589.

Griffith J. E. and Grigg D. A., 1993, "Dimensional Metrology with Scanning Probe Microscopes", Journal of Applied Physics, Vol. 74, Issue 9, pp. 83-109.

Grigg D. A., Russell J. E., Griffith, Vasile M. J. and Fitzgerald E. A., 1992, "Probe Characterization for Scanning Probe Metrology", Ultramicroscopy, Vol. 42-44, Part 2, pp. 1616-1620.

Huang Y-P., Lin S-C. and Lin V T-Y, 2013, "Effects of System Parameters on Tip-Wear in Tapping Mode Atomic Force Microscopy", Surface Topography: Metrology and Properties, Vol. 1, pp. 015003 (8 pages).

Jacobs T. D. B., Lefever J. A. and Carpick R. W., 2015, "A Technique for the Experimental Determination of the Length and Strength of Adhesive Interactions between Effectively Rigid Materials", Tribology Letters, Vol. 59, No. 1, pp. 1-11.

Jacobs T. D. B., Wabiszewski G. E., Goodman A. J. and Carpick R. W., 2016, "Characterising Nanoscale Scanning Probes using Electron Microscopy: A Novel Fixture and a Practical Guide", Review of Scientific Instruments, Vol. 87, pp. 013703\_01 – 013703-10.

## References

---

Jiang X., Wu G., Du Z., Ma K. J., Shirakashi J. and Tseng A. A., 2012, "Nanoscale Scratching of Platinum Thin Films using Atomic Force Microscopy with DLC Tips", Journal of Vacuum Science and technology B, Nanotechnology and Microelectronics: Materials, Processing, Measurement and Phenomena, Vol. 30, pp. 012605.

Jin X., and Unertl W.N., 1992, "Submicrometer Modification of Polymer Surfaces with a Surface Force Microscope," Applied Physics Letters, Vol. 61(6), pp. 657-659.

Junno T., Deppert K. Montelius L., and Samuelson L., 1995, "Controlled Manipulation of Nanoparticles with an Atomic Force Microscope", Applied Physics Letter, Vol. 66, pp. 3627-3629.

Jung T.A., Moser A., Hug H.J., Brodbeck D., Hofer, R., Hidber H.R., and Schwarz U.D., 1992, "The Atomic Force Microscope Used as a Powerful Tool for Machining Surfaces," Ultramicroscopy, Vol. 42-44, Part 2, pp. 1446-1451.

Kim J. and Dornfeld D. A., 2000, "Development of a Drilling Burr Control Chart for Stainless Steel", Journal of Materials Processing Technology, Vol. 28, pp.317-322.

Khurshudov A. and Kato K., 1995, "Wear of the Atomic Force Microscope Tip under Light Load, Studied by Atomic Force Microscopy", Ultramicroscopy, Vol. 60, pp. 11-16

## References

---

Khurshudov A. G., Kato K. and Koide H., 1996, "Nano-Wear of the Diamond AFM Probing Tip under Scratching of Silicon, Studied by AFM", *Tribology Letters*, Vol. 2, Issue 4, pp. 345-354.

King W. P., Kenny T. W., Goodson K. E., Cross G., Despont M., Dürig U., Rothuizen H., Bining G. K. and Vettiger P., 2001, "Atomic Force Microscope Cantilevers for Combined Thermomechanical Data Writing and Reading", *Applied Physics Letter*, Vol. 78, No., 9, pp. 1300-1302.

Klehn B. and Kunze U., 1999, "Nanolithography with an Atomic Force Microscope by Means of Vector-Scan Controlled Dynamic Ploughing", *Journal of Applied Physics*, Vol. 85, No. 7, pp. 3897 – 3903.

Koyanagi H., Hosaka S. and Imura R., 1995, "Field Evaporation of Gold Atoms onto a Silicon Dioxide Film by using an Atomic Force Microscope", *Applied Physics Letter*, Vol. 67, No. 18, pp. 2609-2611.

Li Y., Maynor B. W. and Liu J., 2001, "Electrochemical AFM "Dip-Pen" Nanolithography", *Journal of the American Chemical Society*, Vol. 123, No. 9, pp. 2105-2106.

Liu X., DeVor R. E., Kapoor S. G. and Ehmann K. F., 2004, "The Mechanics of Machining at the Microscale: Assessment of the Current State of the Science ASME Transactions", *Journal of Manufacturing Science and Engineering*, Vol. 126(4), pp. 666-678.

## References

---

- Liu X., DeVor R. E., and Kapoor S. G., 2006, “An Analytical Model for the Prediction of Minimum Chip Thickness in Micromachining”, Journal of Manufacturing Science and Engineering, Vol. 128(2), pp. 474-491.
- Liu J., Notbohm J. K., Carpick R. W. and Turner K. T., 2010, “Method for Characterizing Nanoscale Wear of Atomic Force Microscope Tips”, ACSNano, 4, No. 7, pp. 3763-3772.
- Liu B. H. and Chen C-H., 2011, “Direct Deformation Study of AFM Probe Tips Modified by Hydrophobic Alkylsilane Self-Assembled Monolayers”, Ultramicroscopy, Vol. 111, Issue 8, pp. 1124-1130.
- Losilla N. S., Martinez J., Bystrenova E., Greco P., Biscarini F. and Garcia R., 2010. “Patterning Pentacene Surfaces by Local Oxidation Nanolithography”, Ultramicroscopy, Vol. 110, Issue 6, pp. 729-732.
- Malekian M. Park S. S., Strathearn S., Mostofa D., Md G. and Jun M. B. G., 2010 “Atomic Force Microscope Probe-Based Nanometric Scribing,” Journal of Micromechanics and Microengineering, Vol. 20, pp. 115016 - 115026.
- Mamin H. J. and Rugar D., 1992, “Thermomechanical Writing with an Atomic Force Microscope Tip”, Applied Physics Letter, Vol. 61, pp. 1003-1005.

## References

---

- Maoz R., Frydman E., Cohen S. R. and Sagiv J., 2000, “Constructive Nanolithography: Site -Defined Silver Self-Assembly on Nanoelectrochemically Pattered Monolayer Templates”, Advance Materials, Vol. 12, pp. 424-429.
- Maw W., Stevens F., Langford S. C. and Dickinson J. T., 2002, “Single Asperity Tribocorrosion Wear of Silicon Nitride Studied by Atomic Force Microscope”, Journal of Applied Physics, Vol. 92, No. 9, pp. 5103-5109.
- Mesquida P. and Stemmer A., 2001, “Attaching Silica Nanoparticles from Suspension onto Surface Charge Patterns Generated by a Conductive Atomic Force Microscope Tip”, Advanced Materials, Vol. 13, Issues 18, pp. 1395-1398.
- Miller R., Vesenka J. and Henderson E., 1995, “Tip Reconstruction for the Atomic Force Microscope”, SIAM Journal Applied Mathematics, Vol. 55, No. 5, pp. 1362-1371.
- Montelius L. and Tegenfeldt J. O., 1993 “Direct Observation of the Tip Shape in Scanning Probe Microscopy”, Applied Physics Letter, Vol. 62, No. 21, pp. 2628-2630.
- Mostofa M. G. and Park C. I., 2013, “AFM Probe Based Nano Mechanical Scribing of Soda Lime Glass, Journal of Manufacturing Process, Vol. 15. No. 4, pp. 625-634.
- Neto C. and Craig V. S. J., 2001, “Colloid Probe Characterization: Radius and Roughness Determination”, American Chemical Society, Vol. 17, pp. 2097-2099.

## References

---

Ngunjiri J., and Garno J. C., 2008, “AFM-Based Lithography for Nanoscale Protein Assays,” Analytical Chemistry, Vol. 80(5), pp. 1361-1369.

Notargiacomo A., Foglietti V., Cianci E., Capellini G., Adami M., Faraci P., Evangelisti F., and Nicolini C., 1999, “Atomic Force Microscopy Lithography as a Nanodevice Development Technique,” Nanotechnology, Vol. 10, No. 4, pp. 458-463.

Odin C., Aime J. P., Kaakour Z. E. and Bouhacina T., 1994, “Tip’s Finite Size Effects on Atomic Force Microscopy in the Contact Mode: Simple Geometrical Considerations for Rapid Estimation of Apex Radius and Tip Angle Based on the Study of Polystyrene Latex Balls”, Surface Science, 317, Issue 3, pp. 321-340.

Park J-Y., Yaish Y., Brink M., Rosenblatt S. and McEuen L P., 2002, “Electrical Cutting and Nicking of Carbon Nanotubes using an Atomic Force Microscope”, Applied Physics Letter, Vol. 80, Issue 23, pp. 4446-4448.

Park S. S., Mostafa M. G., Park C. I., Mehrpouya M. and Kim S. 2014, “Vibration Assisted Nano Mechanical Machining Using AFM Probe”, CIRP Annals - Manufacturing Technology, Vol. 63, Issue 1, pp. 537–540.

Pelz J. P. and Koch R. H., 1990, “Tip-related Artifacts in Scanning Tunneling Potentiometry”, Physical Review B, Vol. 41, pp. 1212.

Piner R. D., Zhu J., Xu F., Hong S., Mirkin C. A., 1999, “Dip-Pen Nanolithography”, Science, Vol. 283, Issue 5402 pp. 661-663.

Ponzoni A., Comini E., Sberveglieri G., Zhou J., Deng S. Z., Xu N. S., Ding Y. and Wang X. L., 2006, Ultrasensitive and High Selective Gas Sensors using Three Dimensional Tungsten Oxide Nanowire Networks”, Applied Physics Letter, Vol. 88, pp. 203101-1 – 203101-3.

Pugno N. M, Agrawal R. and Espinosa H. D., 2009, “Nanowear of Atomic Force Microscope Tips: Modelling and Experiments”, Reviews on Advance Material Science, Vol. 19, pp. 73-77.

Quate C.F., 1997, “Scanning Probes as a Lithography Tool for Nanostructures” Surface Science, Vol. 386, Issues 1-3, pp. 259-264.

Requicha A. A. G., Meltzer S., Terán Arce F. P., Makaliwe J. H., Sikén H., Hsieh S., Lewis D., Koel B. E. and Thompson M. E., 2001, “Manipulation of Nanoscale Components with the AFM: Principles and Applications”, IEEE-NANO 2001, pp. 81-86.

Ried R. P., Mamin H. J., Terris B. D., Fan L. S. and Rugar D., 1997, “6 MHz, 2 N/m Piezo-Restive Atomic Force Microscope Cantilevers INCISIVE Tips”, Journal of Microelectromechanical Systems, Vol. 6, No. 4, pp. 294-302.

Rozhok S, Piner R. and Mirkin C. A, 2003, “Dip-Pen Nanolithography: What Controls Ink Transport?”, The Journal of Physical Chemistry B, Vol. 107, pp. 751-757.

## References

---

Sader J. E., Chon J. W. M. and Mulvaney P., "Calibration of Rectangular Atomic Force Microscope Cantilevers", Review of Scientific Instruments, 1999, Vol. 70, Issue 10, pp. 3967.

Schumacher H. W., Keyser U. F., Zeitler, U., Haug R. J. and Eberl K., 2000, "Controlled Mechanical AFM Machining of Two-Dimensional Electron Systems: Fabrication of a Single Electron Transistor", Physica E, Vol. 6(1–4), pp. 860-863.

Schmutz J. C., Fuchs H. and Hölscher H., 2010, "Measuring wear by Combining Friction Force and Dynamic Force Microscopy", Wear. Vol. 268, Issues 3-4, pp. 526-532.

Sheiko S. S., Moller M., Reuvekamp E. M. C. M. and Zandbergen H. W., 1993, "Calibration and Evaluation of Scanning-Force-Microscopy Probes", Physical Review B, Vol. 48, No. 8, pp. 5675-5678.

Shen L. and Chen Z., 2007, "An Investigation of Grain Size and Nitrogen-Doping Effects on the Mechanical Properties of Ultrananocrystalline Diamond Films", International Journal of Solids and Structures, Vol. 44, pp. 3379-3392.

Shen L. and Chen Z., 2009, "A Study of Mechanical Properties of Pure and Nitrogen-Doped Ultrananocrystalline Diamond Films under Various Loading Conditions", International Journal of Solids and Structures, Vol. 46, pp. 811-823.

Snow E. S. and Campbell P. M., 1994, "Fabrication of Si nanostructures with an Atomic Force Microscope", Applied Physics Letters, Vol. 64, Issue 15, pp. 1932-1934.

Snow E. S., Campbell P. M. and McMarr P. J., 1996, “AFM-Based Fabrication of free Standing Si Nanostructures”, Nanotechnology, Vol. 7, No. 4, pp. 434-437.

Sugimura H., 2008, “Scanning Probe Anodization for Nanopatterning: Applied Scanning Probe Methods X”, Nanoscience and Technology, pp. 217-255.

Sundararajan S. and Bhushan B, 2001, “Development of a Continuous Microscratch Technique in an Atomic Force Microscope and its Application to Study Scratch Resistance of Ultrathin Hard Amorphous Carbon Coatings”, Journal of Materials Research, Vol. 16, pp. 437-445.

Takahata K. 2013, “Advances in Micro/Nano Electromechanical Systems and Fabrication Technologies” InTech, ISBN 978-953-51-1085-9.

Tranchida D., Piccarolo S., Deblieck R. A. C., 2006, “Some Experimental Issues of AFM Tip Blind Estimation; The Effect of Noise and Resolution”, Measurement Science and Technology, Vol. 17, pp. 2630-2636.

Tseng A. A., 2011, “Removing Material Using Atomic Force Microscopy with Single- and Multiple-Tip Sources,” Small, Vol. 7(24), pp. 3409-3427

Tseng A. A., Notargiacomo A. and Chen T. P., 2005, “Nanofabrication by Scanning Probe Microscope Lithography: A Review”, Journal of Vacuum Science and Technology

## References

---

B, Nanotechnology and Microelectronics: Materials Processing, Measurement and Phenomena, Vol. 23(3), pp. 877-894.

Tseng A. A., Shirakashi J-I., Nishimura S., Miyashita K and Notargiacomo A., 2009, “Scratching Properties of Nickel-Iron Thin Film and Silicon using Atomic Force Microscope”, Journal of Applied Physics, Vol.106, pp. 044314-1 – 044314-8.

Tseng A. A., Shirakashi J., Nishimura S., Miyashita K. and Li Z., 2010, “Nanomachining of Permaloy for Fabricating Nanoscale Ferromagnetic Structures using Atomic Force Microscope”, Journal of Nanoscience Nanotechnology, Vol. 10, pp. 456-466.

Tseng A. A., Feng C., Kuo J., Nishimura S., and Shirakashi J-C., 2011, “Scratch Direction and Threshold Force in Nanoscale Scratching using Atomic Force Microscopes,” Applied Surface Science, Vol.257, Issue 22, pp. 9293-9250.

Vesenka J., Manne S., Giberson R., Marsh T. and Herderson E., 1993, “Colloidal Gold Particles as an Incompressible Atomic Force Microscope Imaging Standard for Assessing the Compressibility of Biomolecules”, Biophysical Journal, 65, pp. 992-997.

Vettiger P., Fellow, IEEE, Cross G., Despont M., Drechsler U., Dürig U., Gotsmann B., Häberle W., Lantz M. A., Rothuizen H. E., Stutz R., and Binnig G. K., 2002, “The Millipede-Nanotechnology Entering Data Storage” IEEE Transactions on Nanotechnology, Vol. 1, No. 1, pp. 39-55.

## References

---

- Villarubia J. S., 1994, "Morphological Estimation of Tip geometry for Scanned Probe Microscopy", *Surface Science*, Vol.321, Issue 3, pp. 287–300.
- Villarubia J. S., 1996, "Scanned Probe Microscope Tip Characterization without Calibrated Tip Characterizers", *Journal of Vacuum Science and Technology B, Nanotechnology and Microelectronics: Materials, Processing, Measurement and Phenomena*, Vol. 14, pp. 1518.
- Villarubia J. S., 1997, "Algorithms for Scanned Probe Microscope Image Simulation, Surface Reconstruction, and Tip Estimation", *Journal of Research of the National Institute of Standards and Technology*, Vol. 102, No. 4, pp. 425-454.
- Wan J., Xu L., Wu S. and Hu X, 2014, "Investigation on Blind Tip Reconstruction Errors Caused by Sample Features", *Sensors*, Vol. 14, pp. 23159-23175.
- Westra K.L., Mitchell A. W. and Thomson D. J., 1993, "Tip Artifacts in Atomic Force Microscope Imaging of Thin Film Surfaces", *Journal of Applied Physics*, Vol. 74, pp. 3608-3610.
- Xie X. N., Chung H. J., Sow C. H., Adamiak K. and Wee A. T. S., 2005, "Electrical Discharge in a Nanometer-Sized Air/ Water Gap Observed by Atomic Force Microscopy", *Journal of the American Chemical Society*, Vol. 127 (44), pp. 15562-15567.

## References

---

- Xie X. N., Chung H. J., Sow C. H. and Wee A.T.S., 2006, “Nanoscale Materials Patterning and Engineering by Atomic Force Microscopy Nanolithography”, Material Science and Engineering: R: Reports, Vol. 54, Issues 1-2, pp. 1-48.
- Yan Y, Sun T., Liang Y and Dong S., 2007, “Investigation on AFM-based Micro/Nano-CNC Machining System”, International Journal of Machine Tools and Manufacture, Vol. 47, Issue 11, pp. 1651-1659.
- Yan Y., Hu Z., Zhao X., Dong S. and Li X., 2010, “Top Down Mechanical Machining of Three Dimensional Nanostructures by Atomic Force Microscopic”, Small, Vol. 6, No. 6, pp. 724-728.
- Yan Y. D., Geng Y., and Hu Z., 2015, “Recent Advances in AFM Tip-Based Nanomechanical Machining”, International Journal of Machine Tools & Manufacture, Vol. 99, pp. 1-18.
- Yan Y., He Y., Geng Y., Hu Z., and Li H., 2016, “Review on AFM Tip-Based Mechanical Nanomachining: The Influence of the Input Machining Parameters on the Outcomes”, Current Nanoscience, Vol. 12.
- Yano T., Ichimura T., Kuwahara S., H'Dhili F., Uetsuki K., Okuno Y., Verma P. and Kawata S., 2013, “Tip-Enhanced Nano-Raman Analytical Imaging of Locally Induced Strain Distribution in Carbon Nanotubes”, Nature Communication, Vol. 4, pp. 2592 (7 pages).

## References

---

Zhang L. and Dong J., 2012, "High-rate Tunable Ultrasonic Force Regulated Nanomachining Lithography with an Atomic Force Microscope," *Nanotechnology*, Vol. 23, pp. 085303 (9 pages).

Zhang L., Dong J. and Cohen P. H., 2013, "Material-Insensitive Feature Depth Control and Machining Force Reduction by Ultrasonic Vibration in AFM-Based Nanomachining", *IEEE Transactions On Nanotechnology*, Vol. 12(5), pp. 743-750.

Zhao Q. L, Ding S., and Sun T., 2001, "Investigation of an Atomic Force Microscope Diamond Tip Wear in Micro/Nano-Machining", *Key Engineering Materials*, Vol. 202-203, pp. 315-320.

## **PUBLICATIONS AND PRESENTATIONS**

Mukhtar N. F. H., Brousseau E. B. and Prickett P. W., 2014, "Study of Silicon Tip Wear during AFM Probe-Based Machining of Single Crystal Copper", International Conference of Micromanufacturing in Singapore; 25th-28th March 2014, No. 60.

Alraziqi Z. N. R., Mukhtar N. F. H., and Brousseau E. B., 2016, "Comparison of Two AFM Probe Inspection Techniques for Three-Dimensional Tip Characterisation", International Conference and Exhibition of 16<sup>th</sup> European Society for Precision Engineering and Nanotechnology (EUSPEN) in Nottingham UK; 30<sup>th</sup> May – 03<sup>rd</sup> June 2016.

Alraziqi Z. N. R., Mukhtar N. F. H., and Brousseau E. B., 2016, "Comparison of Two AFM Probe Inspection Techniques for Three-Dimensional Tip Characterisation", Presentation at Cardiff University Postgraduate Conference in Cardiff University, UK; 08<sup>th</sup> February 2016.